Caveolae control intercellular tension during cytokinesis and promote successful abscission

Virginia Ribeiro De Andrade

Thèse de doctorat - Sorbonne Université

École doctorale : Complexité du vivant

Caveolae control intercellular tension during cytokinesis and promote successful abscission

Présentée par

Virgínia da Conceição RIBEIRO DE ANDRADE

Pour obtenir le grade de :

Docteur en Biologie Cellulaire de Sorbonne Université

Dirigée par Dr. Arnaud ECHARD

Unité de Trafic Membranaire et Division Cellulaire

Institut Pasteur - CNRS UMR3691

Présentée et soutenue publiquement le 14 Octobre 2021

Devant un jury composé de :

Dr. Joëlle SOBCZAK-THEPOT	Présidente
Dr. Ulrike EGGERT	Rapportrice
Dr. Richard LUNDMARK	Rapporteur
Dr. Christophe LAMAZE	Examinateur
Dr. Marie-Émilie TERRET	Examinatrice
Dr. Arnaud ECHARD	Directeur de thèse

Aknowledgments

In the last 4 years, being a PhD student gave me the opportunity to dig-in and grow my scientific knowledge, to express my creativity in the design of experiments and in preparing oral presentations, and importantly, to understand how scientific research works. The work I have developed that culminated in the writing of this thesis and in the preparation of a scientific article, have shaped my scientific personality. This work would not have been achieved without centuries of scientific advancement, from the continuous everyday rustle of scientific papers coming out. As perfectly said by Isaac Newton in a letter to Robert Hooke in 1675 "If I have seen further it is by standing on the shoulders of giants". Indeed, ideas, creativity, innovation in research (and in all domains of life), are based on previous knowledge, and that is great! I will not extend myself on this topic, but as written by Virginia Woolf in her book, A room of one's own, "For masterpieces are not single and solitary births; they are the outcome of many years of thinking in common". In addition, I want to remember and thank all the brave women that followed what they believed was their right, and thus among other rights, were given the right to enter University. In 1866, Mary Putman was the first woman registered in a University in France. Though not allowed to enter the scholarly path, some women before had been able to pursue scientific "careers", and contributed to the scientific advancement, however their discoveries and research more often stay in the shadows and are not always mentioned. Fortunately, we are in times of change.

I would like to thank my PhD supervisor Arnaud Echard, for giving me the opportunity to do the PhD thesis in his lab, as well as for his supervision, advice and lively discussions during these last years.

I would like to thank the members of the jury: Ulrike Eggert, Richard Lundmark, Marie-Émilie Terret, Christophe Lamaze, and Joëlle Sobczak-Thepot for the critical reading of the manuscript and for accepting to be a part of the jury. I would also like to thank my thesis advisory committee, *comité de suivi de thèse*, Cédric Delevoye, Matthieu Piel et Flora Llense for productive discussions and advice.

A big thank you to Ana Jimenez for teaching me how to do laser ablation and Vincent Fraisier, from the Cell and Tissue Imaging facility (PICT-IBiSA), and the Nikon Imaging Centre at Institut Curie for allowing me to perform there the laser ablation experiments. I also thank Cédric Delevoye for the beautiful electron microscopy images of caveolae in intercellular bridges, and for the discussions during my project.

I would like also to thank the Flow Cytometry Platform at the Institut Pasteur, especially to Pierre-Henri Commere and Sandrine Schmutz for the sorting of the cells. In addition, I would like to thank Audrey Salles and Maryse Moya-Nilges for their effort and patience in trying to develop a SIM-SEM correlation protocol!

The TMDC team is a special environment to work on, the sense of teamwork is very marked and helping others when experiments might not be working is part of our day. The lunch tradition at 12h (or 11h40!), the little celebrations when experiments work, the big celebrations of papers and thesis, the lab day retreat, and the beers after work are all special moments that I will bear with me. That said I want to thank Jian Bai that first taught me in the lab when I was an intern, Ronan Shaughnessy, Tamara Advedissian, Neetu Gupta, Fréderique Cuvelier, Nathalie Sassoon, Clémentine Rouyère, Cyril Addi, Adrien Presle, Stéphane Frémont, Murielle Serres and Reine Bouyssie.

I would like to thank all the teachers that I have had during my school and university path, which have always urged me to curiosity, to knowledge and culture, as well as all the friends I have made along with it. Life without my family and the friends would not make sense. I would like to thank my friends that have closely spent with me this thesis adventure, in Paris, and bore with me the not so easy moments of the PhD life, Leonor, Hudson, Alicia, Noelia, Isadora, Lia (thank you for the caveolae discussions!), Mercedes and Alexandra. I have to thank Mafalda for her endless support, advice and patience especially through the challenging times of the PhD.

Finally, I have to thank my family for they are the ones that shaped me to be courageous in life in order to become who I want to, and to fight for my future. Even though we are all far away, their support is continuous. Obrigada mãe, pai, Guida, Ricardo, Samuel.

Résumé

La cytocinèse est le processus par lequel une cellule mère est physiquement séparée en deux cellules filles après la mitose. Elle commence en anaphase par la contraction d'un anneau d'actomyosine associé à la membrane de la cellule au niveau du plan médian, ce qui conduit à l'invagination d'un sillon de clivage. L'invagination du sillon entraine la formation d'un pont intercellulaire, au centre duquel se localise le *midbody*, responsable du recrutement de la machinerie qui assurera la coupure physique du pont - l'abscission. Même si toutes les étapes menant à l'abscission ne sont pas entièrement comprises, les filaments d'ESCRT-III jouent un rôle clé. Ils s'assemblent tout d'abord au niveau du *midbody*, puis se polymérisent sur le côté du *midbody* en constrictant la membrane plasmique au niveau du "site d'abscission". Les voies moléculaires responsables de l'assemblage des filaments d'ESCRT-III au niveau du pont intercellulaire ont fait l'objet d'une caractérisation intensive. En revanche, les aspects mécaniques jouent également un rôle puisque le pont intercellulaire est sous tension (du fait de force de traction) et que l'abscission ne peut avoir lieu qu'après la diminution de cette tension. Comment ces contraintes mécaniques sont régulées au moment de l'abscission reste largement inconnu.

L'abscission se produit successivement des deux côtés du *midbody*, libérant ainsi un *midbody remnant*. Notre laboratoire a récemment purifié et analysé par spectrométrie de masse le contenu protéique des *midbody remnants*. Cette analyse a permis de découvrir un enrichissement de plus de 400 protéines dans les *midbody remnants*, révélant des protéines qui n'ont jamais été associées à la cytocinèse, parmi lesquelles des protéines des cavéoles.

L'objectif de ce travail a ainsi été de déterminer si les cavéoles régulent la tension au niveau du pont intercellulaire pendant la cytocinèse. Cette hypothèse découle du fait que les cavéoles ont été décrites comme des réservoirs membranaires qui tamponnent la tension de la membrane plasmique dans les cellules en interphase.

Des expériences d'immunofluorescence et des vidéos de cellules vivantes ont révélé que la Caveoline1 et la Cavine1, les principaux composants des cavéoles, sont localisées de façon dynamique au niveau du sillon de clivage, du midbody, et à l'interface pont/cellule. En utilisant la microscopie électronique, nous avons confirmé que des cavéoles sont effectivement localisées au niveau *midbody* et à l'interface du pont/cellule. D'un point de vue

fonctionnel, la perte des cavéoles entraîne un retard d'abscission et une altération de la polymérisation de l'ESCRT-III au site d'abscission. Ces défauts observés après la déplétion des cavéoles sont associés à une augmentation de la tension du pont d'un facteur deux, mesurée par ablation laser du pont intercellulaire. De plus, l'absence des cavéoles conduit à une activation accrue de la myosine II à l'interface du pont/cellule. Tous ces défauts sont corrigés après réduction de la tension corticale en inhibant la kinase ROCK.

Nous proposons que les cavéoles limitent la tension transmise au pont intercellulaire pendant la cytocinèse, favorisant ainsi l'assemblage de ESCRT-III au site d'abscission et la coupure finale des cellules.

Abstract

Cytokinesis is the process by which a mother cell is physically separated into two daughter cells after mitosis. It starts in anaphase with the contraction of a membrane-associated actomyosin ring at the midplane of the cell leading to the ingression of a cleavage furrow. Ingression of the furrow forms an intercellular bridge, at the centre of which localizes the midbody that is responsible to recruit the machinery that will mediate the physical cut of the bridge – abscission. Even if not all steps leading to abscission are fully understood, the ESCRT-III filaments drive abscission. ESCRT-III filaments assemble first at the midbody and then polymerize to the side of the midbody, which constricts the plasma membrane at the "abscission site". The molecular pathway leading to the assembly of the ESCRT-III filaments at the intercellular bridge has been the subject of intensive characterization. However, cell mechanics also play a role since the intercellular bridge is under tension due to pulling forces and abscission only occurs when the tension decreases. How this is regulated remains largely elusive.

Abscission happens successively on both sides of the midbody, releasing a "midbody remnant". Our laboratory recently purified midbody remnants and analysed their protein content by mass spectrometry. This analysis revealed an enrichment of more than 400 proteins in midbody remnants, showing proteins that have never been associated with cytokinesis, among which caveolae-associated proteins.

Thus, the aim of this work was to determine whether caveolae regulate the tension at the intercellular bridge during cytokinesis. This hypothesis stems from the fact that caveolae have been described to serve as membrane reservoirs that buffer plasma membrane tension in interphase cells.

Immunofluorescent stainings and live-cell imaging revealed that Caveolin1 and Cavin1, the main components of caveolae, are dynamically localized at the furrow, midbody and at the bridge/cell interface. Electron microscopy confirmed that *bona-fide* caveolae are localized at the midbody and at the bridge/cell interface. Functionally, the loss of caveolae led to an abscission delay and impaired ESCRT-III polymerization at the abscission sites. These defects are associated with an increase in the tension of the bridge, since depletion of caveolae led to 2-fold increase in the tension at the intercellular bridge, as measured by laser ablation, and increased myosin II activation at the bridge/cell interface. All these defects were corrected after lowering cortical tension by inhibiting the ROCK kinase.

Altogether we propose a mechanism in which caveolae limit the tension transmitted to the intercellular bridge during cytokinesis favouring ESCRT-III assembly at the abscission sites and successful abscission.

Table of Contents

Part I: Introduction

Cell division has interested biologists ever since the cell theory was proposed by Schleiden and Schwann in 1833 [32]. It took another 30 years for the first clear drawings of cell division in animals to be published by Walter Flemming [33]. His work on cell division was a landmark for the development of cell biology, *e.g.* coining the term chromatin, and he was the first to report the appearance of the midbody at the centre of the intercellular bridge connecting the daughter cells in the late stages of cytokinesis, in 1891 [32]. Cytokinesis is the last step of cell division leading to the physical separation of the daughter cells. The stepping stone discovery that actomyosin drives furrow ingression in the 1970s [34, 35, 36] was followed by the discovery of important proteins for cytokinesis using mutants in animal models [37-39], and later on from RNAi screens *in vivo* [40-42]. These studies started to unveil the composition of the midbody and several proteins required for cytokinesis, demonstrating that the midbody was not a cellular junk, and showed that the post-furrowing steps of cytokinesis must be tightly regulated. Today, even though the midbody maturation and the final steps of cytokinesis are still not fully understood, we know that trafficking, cytoskeleton and lipid remodelling, together with the recruitment of the ESCRT machinery have to occur at the intercellular bridge, in order to promote the physical cut of the bridge– also called abscission, as it will be described further ahead. Abscission of the intercellular bridge occurs on the both sides of the midbody and releases a free midbody remnant. Finding new proteins that may play a role during abscission can be done using proteomic studies, taking advantage of purified midbody remnants. Recently, our lab has revealed more than 400 proteins enriched in purified and intact (detergent free) midbody remnants [1]. Among them, caveolae proteins were found, suggesting that they localize at the midbody and could play a role during cytokinesis. Caveolae are small plasma membrane invaginations that have been described in interphase cells to buffer membrane tension [20]. Tension at the intercellular bridge has been described as a negative regulator of cytokinesis, since high tension delays cytokinesis [29]. However, whether there are proteins capable of actively regulating tension at the intercellular bridge during cytokinesis remains elusive. Thus, we wanted to determine whether caveolae could regulate tension during cytokinesis and play a role in the final steps of cell division.

In the following chapters, I will first introduce cytokinesis and the molecular mechanisms required from furrow ingression to complete abscission. Next, I will review what is known about caveolae: their protein components, their biogenesis and dynamic behaviour, as well as their ability to buffer membrane tension. Finally, in the third chapter, I will summarize what is known about the regulation of tension at the intercellular bridge during cytokinesis.

Chapter I: Animal cell cytokinesis

I.1 **Cytokinesis overview**

In this introduction, I will address only the animal cell cytokinesis. Some of its mechanisms are conserved across eukaryotes but not all since, *e.g.* yeast, and plants have a cell wall. During cytokinesis, the mother cell is physically separated into two daughter cells. At the onset of anaphase, the degradation of proteins of the cyclin B family [43] by the E3 ubiquitin ligase anaphase promoting complex (APC), and the consequent inactivation of CDK1 [44], leads to the sister chromatids segregation, and is the trigger to cytokinesis initiation, thus ensuring faithful genome inheritance [45]. The rearrangement of the microtubules at the spindle midzone leads to the formation of the central spindle that will specify the localization and regulate the contraction of the actomyosin II ring in the plasma membrane, at the midplane of the cell (Fig. 1a). As a consequence, actomyosin II-dependent constriction of the plasma membrane - furrow ingression- (Fig. 1b), happens until it reaches 1-2 μm in diameter, leading to the formation of the intercellular bridge (Fig. 1c) that will connect the two daughter cells for several hours until abscission occurs. Note that at this stage the daughter cells re-enter into the G1 phase and have thus exited mitosis. At the centre of the bridge localizes the midbody (Fig. 1c), an electron dense structure derived from the mitotic spindle, that orchestrates the final steps of cytokinesis by recruiting the abscission machinery. Abscission itself is driven by the Endosomal Sorting Complex Required for Transport (ESCRT) machinery that assembles at the midbody and then polymerizes from the midbody to the abscission site (~1 μm away from the midbody), where abscission takes place. Next, the same process occurs on the other side of the midbody, leading to the release of the two daughter cells as well as a midbody remnant [46]. The latter can either wander in the extracellular media or be engulfed, usually by one of the daughter cells (Fig. 1d-e).

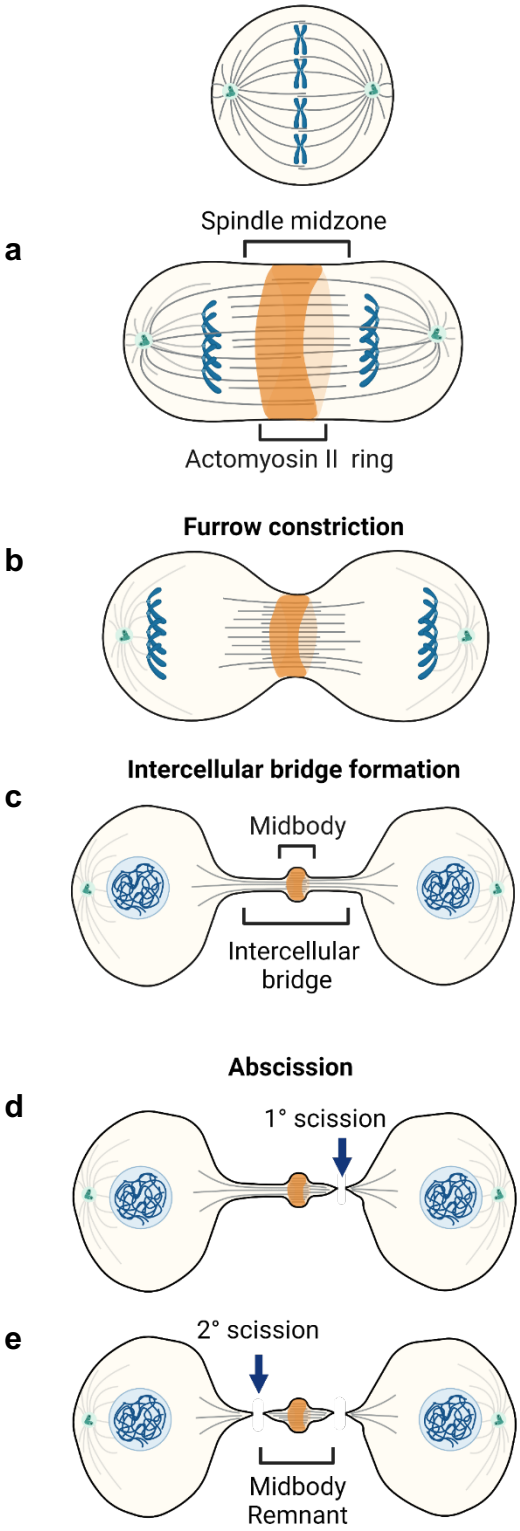

Figure 1 – Schematic of the sequential steps of animal cytokinesis that lead to the separation of the two daughter cells.

I.2 **Early steps of cytokinesis**

I.2.1 From central spindle formation to furrow ingression

During anaphase, when the chromosomes are moving poleward, the microtubules at the spindle midzone rearrange to form an antiparallel dense array with their "+" end overlapping at the centre of the spindle to form the **central spindle** (Fig. 2a). The central spindle assembly requires the recruitment of several proteins to the midzone to bundle the microtubules, and to establish a signalling platform that will be important for different stages of cytokinesis.

Beside microtubules, the central spindle is composed of:

a. **PRC1 and KIF4A** – the protein regulator of cytokinesis 1 (PRC1) is a non-motor microtubule-associated protein that binds to KIF4A (kinesin family member 4A), which is a + end directed kinesin.
b. **Centralspindlin**, which is a heterotetrameric complex composed of two molecules of Mitotic kinesin-like protein 1 (MKLP1) and two molecules of Rho-family GTPase activating protein (GAP) MgcRacGAP (also known as CYK4).
c. **The Chromosomal Passenger Complex (CPC)** that is constituted by the kinase Aurora B, INCENP (Inner centromere protein), Borealin and Survivin.

At the onset of anaphase, the decline of CDK1 (in combination with active phosphatases) promotes the removal of CDK1-mediated phosphorylations from:

- PRC1, allowing its homodimerization. PRC1 dimers are then able to recognize antiparallel microtubules and crosslink them [47, 48]. PRC1 is transported to the central spindle by KIF4A, which, in turn, limits the microtubule + end dynamics and controls the central spindle length [49, 50];
- the motor domain of MKLP1, to allow its phosphorylation by the kinase Aurora B. This promotes the clustering of centralspindlin and its transport to the spindle midzone [51, 52];
- INCENP, allowing its binding to the Mitotic kinesin-like protein 2 (MKLP2 also known as Rabkinesin-6), and translocation of the complex from the centromeres to the spindle midzone [53,54]. Once at the midzone, Aurora B phosphorylates PRC1 and MKLP1[55].

The central spindle and the centralspindlin are important for the **specification of the division plane** (Fig. 2b). Indeed, the Polo-like kinase 1 (PLK1) phosphorylates MgcRacGAP that binds to the RhoA GTPase activator GEF-ECT2 and translocates it to the spindle midzone to convert RhoA-GDP into activated RhoA-GTP at the plasma membrane [12, 56-58]. Afterwards, the RhoA GTPase directs the assembly of an actomyosin II ring at the cortex of the cell equator by promoting the polymerization of unbranched actin filaments, via the activation of the formin mDia1 and profilin. At the same time, RhoA promotes the phosphorylation of the regulatory myosin light chain (MRLC), leading to myosin II activation and contraction of the ring [12] (Fig. 2c). Importantly, the assembled contractile ring is physically attached to the plasma membrane via the scaffolding protein Anillin and Septins (GTP binding proteins that polymerize into filaments) [12, 59].

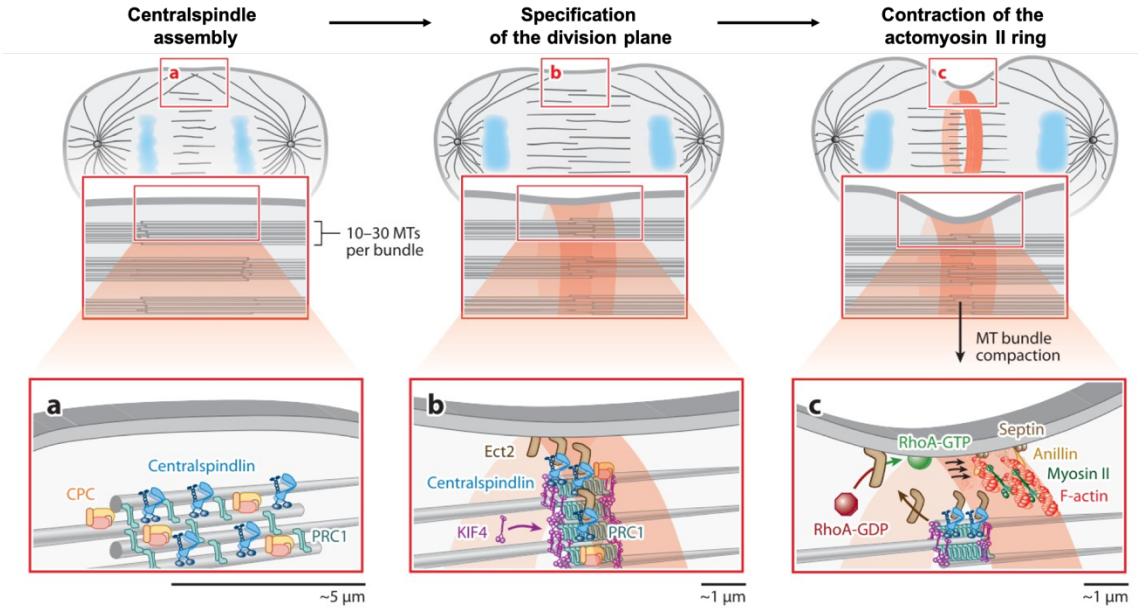

Figure 2 – Assembly of the central spindle and division plane specification. a) The formation of the central spindle. b)-c) division plane specification and actomyosin II ring formation. Adapted from [12]

The constriction of the actomyosin II ring that is connected to the plasma membrane of the cell leads to **furrow ingression** at the equator, and partitions the cytoplasm into two, with correct localization of the chromosomes at each pole of the mother cell. Furrow ingression leads to the formation of an intercellular bridge filled with microtubules, derived from the central spindle, that connects the two daughter cells. At its centre, where the + ends of the overlapping microtubules lie, the midbody is formed and is stabilized by Septins and Anillin [60]. Indeed, depletion of either protein leads to the regression of the intercellular

bridge, hence cytokinesis failure and binucleation. Therefore, at this stage the stability of the bridge no longer depends on actin, as first demonstrated in *Drosophila* cells [42].

In human cells, the intercellular bridge will be physically cut in the next few hours, and the midbody serves as a platform for the recruitment of the abscission machinery, namely the ESCRT proteins. This machinery will assemble at the midbody and polymerize to the future abscission sites (secondary ingression sites) to fuse and scission the plasma membrane of the bridge from the inside. Interestingly, it has recently been purposed that the early localization of Septins at the midbody primes the localization of ESCRT in later stages of cytokinesis [61].

In the next section, which focuses on the process of abscission, I will first describe how the ESCRT machinery is capable of driving abscission. I will then review the role of trafficking and cytoskeleton remodelling required in the late stages of cytokinesis for successful abscission.

I.3 **Maturation of the intercellular bridge and abscission**

I.3.1 ESCRT-III recruitment at the midbody and polymerization towards the abscission site

Successful abscission requires the physical cut of the intercellular bridge from the inside (*i.e.* using cytosolic machineries). What was known from previous transmission electron microscopy (TEM) done in the 1960s/1970s [62-64] and that had been confirmed by several labs, was the localization of a constriction zone with ripples at the plasma membrane (Fig. 3a).

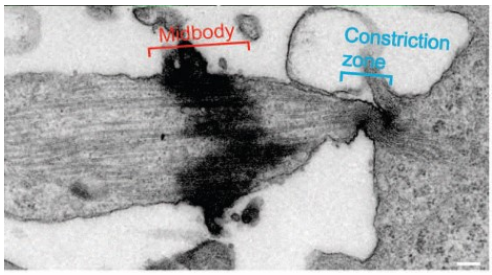

Figure 3 – TEM of an intercellular bridge where the highly electron dense dark area corresponds to the midbody and on the side localizes the constriction sites. Adapted from [3]

These were located approximately 1 µm from the midbody, where abscission would likely take place. No proteins were known to drive this process and it was believed that traction on the bridge would drive abscission. Therefore, the discovery that the Endosomal Sorting Complex Required for Transport (ESCRT) machinery is implicated in abscission, was a major finding in 2007 [65, 66]. Abscission was then proposed to be topologically equivalent to the other membrane fission events executed by ESCRTs namely during multivesicular bodies' formation, and HIV budding [67, 68]. The ESCRT components were shown to localize at the midbody, and later on, in 2011, several components of the ESCRT complex were found precisely at the abscission sites. This is a necessary condition to constrict the intercellular bridge and to successfully complete abscission [5, 29, 69]. More functions of ESCRTs have been then discovered, notably in the plasma membrane, lysosomal membrane and nuclear membranes repair, as well as in the re-sealing of the nuclear envelope, in the closure of autophagosome and in neuron pruning [70-75].

I.3.2 The ESCRT machinery orchestrates the final cut

The ESCRT machinery is evolutionary conserved, from prokaryotes to eukaryotes, having homologues in both eucaryotes and archaea, as well as in bacteria as recently show [76-78]. This machinery is composed in humans of 27 proteins classified in four multimeric protein complexes: the ESCRT-0 (that is not involved in abscission and will not be discussed here), ESCRT-I, ESCRT-II and ESCRT-III [79]. The subunits composing each ESCRT complex are shown in Table 1 bellow.

Complex	Yeast protein	Alternative names (yeast)	Metazoan protein	Alternative names (metazoan)
ESCRT-I	Vps23	Stp22	TSG101	
	Vps28		VPS28	
	Vps37	Srn2	VPS37A, B, C, D	
	Mvb12		MVB12A, B, UBAP1	
ESCRT-II	Vps22	Snf8	EAP30	
	Vps25		EAP20	
	Vps36		EAP45	
ESCRT-III	Vps2	Did4 Chm2	CHMP2A, B	
	Vps20	Chm6	CHMP6	
	Vps24		CHMP3	
	Snf7	Vps32	CHMP4A, B, C	Shrub
	Vps60	Chm5	CHMP5	
	Did2	Chm1 Vps46	CHMP1A, B	
			CHMP7	
	Ist1		IST1	
Vps4-Vta1	Vps4		VPS4A, B	SKD1
	Vta1		VTA1	LIP5
Bro1/ALIX	Bro1	Vps31	ALIX	AIP1

Table 1 - The ESCRT complex is constituted by ESCRT-I/-II/-III, VPS4 and ALIX. Each ESCRT complex is composed of several subunits that have conserved homology. Names in yeast and the corresponding in Metazoan are shown. From [19]

Remodelling and fission of membranes by the ESCRTs are driven by the complex ESCRT-III, which polymerizes into filamentous helices that constrict the attached plasma membrane, as was shown *in vivo* and *in vitro* [79].

The ESCRT-III family comprises 7 members, the Charged Multivesicular body Proteins 1-7 (CHMP1-7) that can co-polymerize (Table 1). Specifically, during cytokinesis, several proteins of the ESCRT-III complex polymerize at the midbody and abscission site

(CHMP2A/B, CHMP3, CHMP4A/B, CHMP5, CHMP6, IST1), to drive membrane constriction and abscission [79]. The localization of these proteins at the bridge have been observed by many labs working in cytokinesis, using immunofluorescence of selected ESCRT-III proteins, or fluorescent tagged proteins [1, 29, 69]. Remarkably, high resolution 3D Stochastic Optical Reconstruction Microscopy (STORM) showed that the ESCRT-III protein IST1 first localizes at the midbody, and starts to form a spiral that, while elongating, constricts the plasma membrane creating an abscission site 1 μm away from the midbody (Fig. 4a) [14]. These spirals form a cone-like structure from the midbody to the abscission site. This is in agreement with images obtained from electron tomograms of high-pressure frozen cells, from the Gerlich and Müeller-Reichardt labs, showing the localization of 17 nm diameter filaments at the constriction sites (Fig. 4b, c). These helices likely drive abscission, since RNAi of CHMP2A prevents the formation of these helices and membrane constriction. However, there is no definitive proof that the helices are made of ESCRT-III although this is very likely.

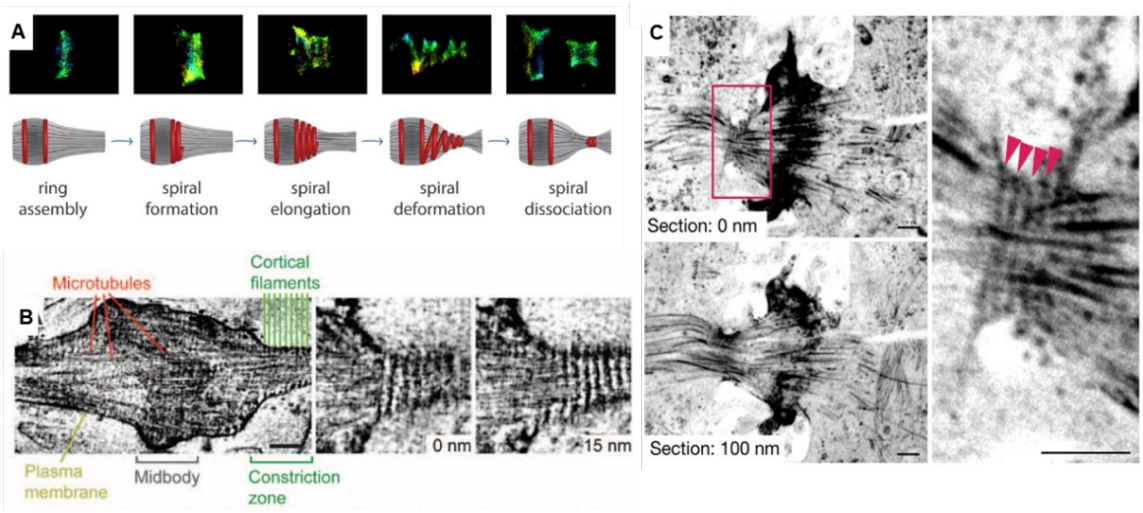

Figure 4 – ESCRT-III filaments form spirals. a) The several stages of IST1 endogenous localization and spiral formation seen using 3D STORM. b) Electron tomography of high-pressure frozen cells, showing the microtubules at the midbody and the 17 nm diameter cortical filaments at the side of the midbody. c) Like b) showing spaced helices localized at the constriction sites. Adapted from [4-6]

I.3.3 Sequential recruitment of the ESCRT-III machinery to the midbody and abscission sites

The ESCRT-III machinery recruitment during cytokinesis happens in two sequential phases, one aiming to enrich ESCRT-III at the midbody, and a second one involving ESCRT-III polymerization towards the abscission sites. During anaphase, PLK1 negatively

regulates the Centrosomal Protein of 55 kDa (CEP55) by phosphorylating it, preventing CEP55 from localizing at the central spindle. This mechanism ensures timely recruitment of CEP55, since its premature recruitment to the spindle halts abscission [80]. Thus, once the midbody is formed, MKLP1 can correctly recruit CEP55, at the right time [81, 82]. Next, CEP55 recruits through direct interactions both ALIX and the tumour-susceptibility gene 101 (TSG101 / ESCRT-I) that act in parallel to fully recruit ESCRT-III to the midbody [66, 83-86] (Fig. 5a). On the one hand, phosphorylated (activated) ALIX directly interacts with CHMP4B (subunit of ESCRT-III) (Fig. 5a). On the other hand, TSG101 and the Vacuolar protein sorting-associated protein 28 homolog (VPS28) recruit ESCRT-II proteins which, in turn, will finally recruit CHMP4B to the midbody (Fig. 5a).

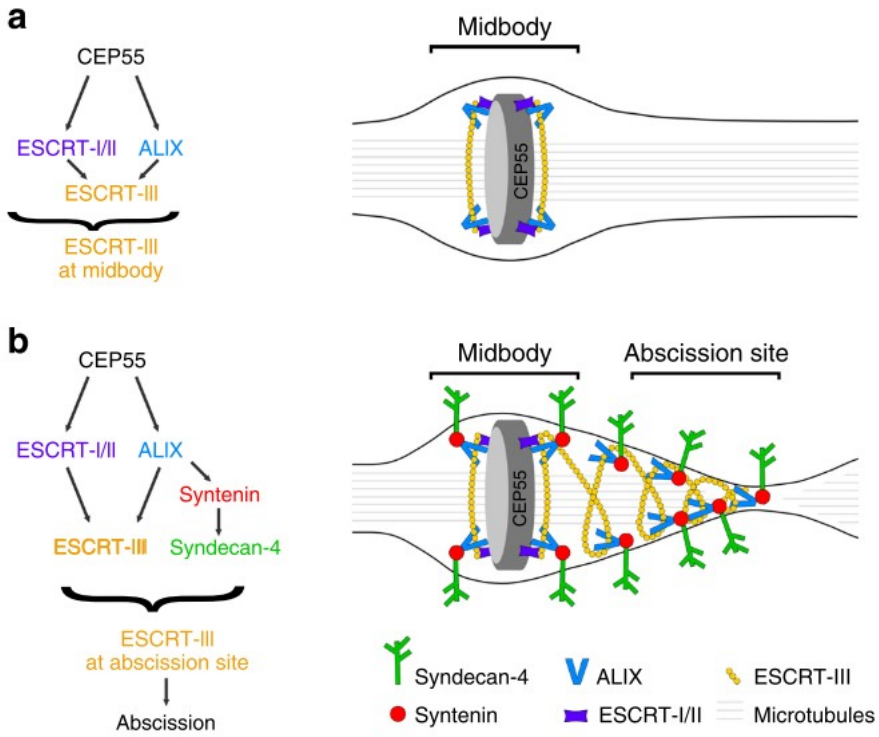

Figure 5 – Schematic representation of the mechanism of ESCRT-III recruitment at the midbody a) and towards the abscission sites in b). Adapted from [1]

Co-depletion of TGS101 and ALIX induces a strong delay in abscission [1, 87]. However, these two pathways are not equivalent since the depletion of ALIX alone leads to a clear delay in abscission and to binucleation, whereas the depletion of TSG101 leads to a moderate delay in abscission and a small increase in binucleated cells [1, 65, 66, 87]. Besides the localization of ESCRT-III at the midbody, polymerization to the abscission site has to occur, and this step is CEP55-independent, since CEP55 is not found at the abscission sites. The formation of the abscission site was proposed to be promoted by the Rab11-FIP3 (Rab11

Family interacting proteins3) endosomes. These vesicles localize at the bridge to form the secondary abscission site and promote the localization of ESCRT-III there [88]. But how does the ESCRT-III appear or relocate to the abscission sites? Recently, our lab described a key additional role of ALIX to recruit Syntenin, which itself recruits the transmembrane protein Syndecan-4 at the bridge (Fig. 5b) [1]. The tripartite ALIX-Syntenin-Syndecan-4 module was previously shown to be important in MVBs formation and exosome production [89, 90]. At the bridge ALIX-Syntenin-Syndecan-4 couples the ESCRT-III machinery to the plasma membrane, stabilizing ESCRT-III filaments at the abscission site until abscission happens. Consistently, depletion of Syntenin, or Syndecan-4, significantly delays abscission, and moderately increases binucleation. Mechanistically, depletion of ALIX, or Syntenin, or Syndecan-4 leads to a transient and unstable CHMP4B-GFP cone, often an abortive one that afterwards manages to re-polymerize to the abscission sites [1]. Therefore, ESCRT-III recruitment to the abscission sites takes longer and is unstable, which delays abscission. It is noteworthy that Syndecan-4 is the first transmembrane protein described to be required for cytokinesis. This shed new light on the mechanisms required for successful abscission, explaining why previous authors had found that the depletion of ALIX had little effect on the ESCRT-III recruitment at the midbody but had an impact in abscission.

I.3.4 Dynamic remodelling of the ESCRT-III subunits is required for polymerization of the filaments, constriction of the membrane and fission

Filament polymerization from the midbody to the abscission sites requires a dynamic turnover of the ESCRT-III subunits. Indeed, the ESCRT-III polymerization is an active process that requires ATP, and the AAA-ATPase VPS4 is in charge of the remodelling of the helices, to promote its elongation and constriction [17]. The spatio-temporal analyses of the localization of CHMP4B-GFP (the main polymerizing subunit of the ESCRT-III) and VPS4-GFP in stable cell lines, revealed that their localization is synchronized (Fig. 6a), contrary to the initial thought [73]. In addition, FRAP experiments demonstrated that the majority of the CHMP4B subunits at the midbody have a half-life of 20 seconds, and this rapid turnover depends on VPS4 [17, 18] . Depletion of VPS4 leads to a delay in abscission and failed constriction of the abscission sites, even though the helices are still present there, demonstrating that filament turnover is essential for ESCRT-III function. Interestingly, further dissection of the polymerization process *in vitro,* using purified yeast homologues in liposomes, recently revealed that Snf7 (CHMP4B), VPS24 (CHMP3) and VPS2

(CHMP2A/B) co-polymerize together and form double stranded filaments of 15 nm width (Fig. 6b) [17].

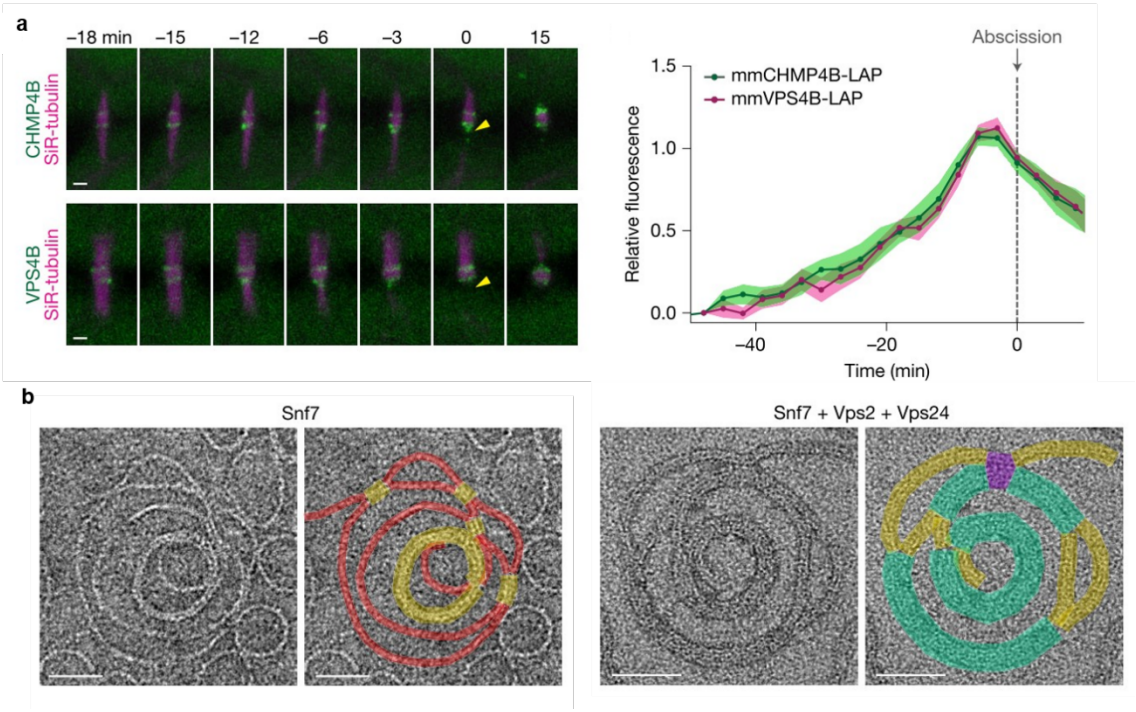

Figure 6 – a) Stable HeLa cell lines expressing VPS4-GFP and CHMP4B-GFP and fluorescence quantification. Abscission is marked by the yellow arrowhead. b) Left: TEM of Snf7 spirals polymerized on liposomes. Right: Snf7 polymerization on liposomes, followed by the addition of Vps2 and Vps24. Red overlay indicates 1 stranded filament; yellow 2 stranded filaments; green 4 stranded filaments and purple 6 stranded filaments. Adapted from [17]

This filament size is close to the 17 nm diameter filaments previously observed by EM described in Fig. 4b. Additionally, measurements using high-speed Atomic Force Microscopy (AFM) showed that Snf7-VPS24-VPS2 filaments, in the presence of VPS4 and ATP, are remodelled: pre-existing spirals shrunk, while several other spiral filaments started to polymerize. This strongly suggests that VPS4-dependent and continuous remodelling of the ESCRT-III spirals is a key feature for constriction. It is noteworthy that the shrinkage of the filaments by VPS4 occurred to no less than 200 nm [17], which is also the average size of helices spotted by EM at the constriction sites [91]. Could this be because the following constriction and fission are very fast, hence it is a step difficult to catch by EM? Or does this mean that the VPS4 constriction is limited until this size and that after this point other machineries, or proteins, are recruited to further constrict the plasma membrane [60].

Continuous attempts have been made to understand which components of the ESCRT machinery are required for the constriction of the membrane to a critical point such

that fission occurs. Spontaneous fission is believed to occur when membranes are closer than approximately 3 nm. Recent *in vitro* studies from the Weissenhorn lab, showed that VPS4 induces membrane constriction and cleavage of CHMP2A/CHMP3 filaments (note that CHMP4B was not included), using high-speed AFM. [30]. The authors propose that VPS4 hexamers localize in-between the CHMP2A/CHMP3 helices and rotate in a clockwise or anticlockwise way to thread the substrate via its central pore (Fig. 7) [92].

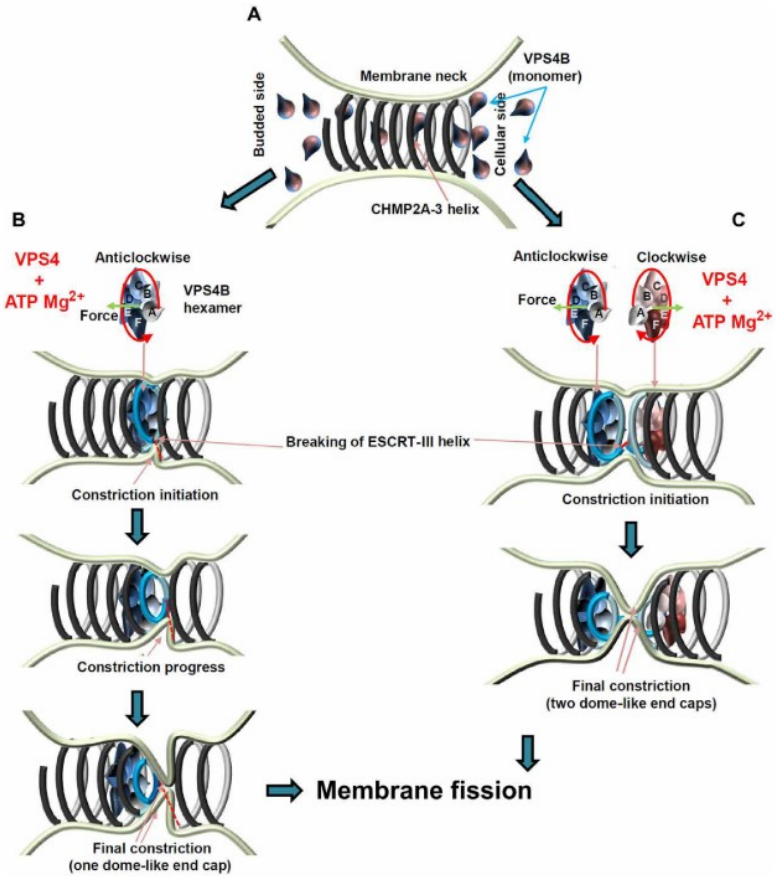

Figure 7 – Model purposed in *Maity et al.*, where CHMP2A-CHMP3 filaments cleavage induced by VPS4 leads to membrane constriction and eventual fission. (A) CHMP2A-CHMP3 helical filaments assemble within a membrane neck structure such as a vesicle or virus bud or at the midbody. Currently, we do not know how many turns assemble in vivo. (B) VPS4 forms an asymmetric hexamer structure in the presence of ATP and Mg2+. This structure needs to assemble on functional ESCRT-III filaments, and ATP-driven rotation threads the substrate via its central pore. Because CHMP2A-CHMP3 polymer assembly is directional, the assembly of VPS4 acting clockwise or anticlockwise is likely to be important. The assembly of one VPS4 complex might be sufficient to induce CHMP2A-CHMP3 constriction, which often starts asymmetrically (middle). This can lead to membrane constriction and cleavage of the CHMP2A-CHMP3 filament. (C) Alternatively, two adjacent VPS4B complexes remodel CHMP2A-CHMP3 filaments acting clockwise and anticlockwise, thereby leading to the generation of two dome-like end caps and cleavage of the CHMP2A-CHMP3 filament. In both scenarios, constriction of CHMP2A-CHMP3 could prime the site for fission, and cleavage of the filament might play an important role in tension release as proposed in [28]. From [30].

This will lead to an asymmetrical constriction of the filament and the adjacent plasma membrane, and the formation of a dome-like end cap (seen by cryo-EM). This eventually results in the constriction of CHMP2A/CHMP3 tubes from a diameter of 45 nm to < 10 nm. In addition, the formation of the dome is likely to be important for membrane constriction, as proposed in [93]. Thus, the authors propose that these domes within a bud neck *in vivo* could prime ESCRT-III to perform membrane fission.

Last year, the Frost Lab showed, using cryo-EM, that the ESCRT-III accessory CHMP1B polymerizes in positively curved membranes (liposomes), in a single stranded filament that is capable of generating a moderately curved tube. Interestingly, addition of IST1 (ESCRT-III protein) to the system induces further constriction of the membrane tube up to 4.8 nm (distance between the inner leaflets) [94]. This was the first ESCRT-III polymer that was reported with constriction sizes near the size required for spontaneous fission. More recently, findings from the Roux Lab demonstrate that during ESCRT-III polymerization, sequential subunit exchange leads to constriction of the filaments, and consequent membrane deformation and fission (Fig. 8) [18]. Importantly, in late stages of the polymer remodelling, the VPS2 subunit in the filament VPS2 – Did2 (CHMP1) is exchanged by Ist1 (yeast homolog of IST1) to form a Did2-Ist1 (CHMP1B-IST1 in humans) filament. Polymerization of Did2-Ist1 on the inside of membranes leads to the constriction of the membrane to a diameter of 12 nm (filament + membrane). Interestingly, Did2-Ist1 can also polymerize in the reverse topology, on the outside of a membrane neck, leading to the constriction of the membrane and fission. (Fig. 8). Remarkably VPS4 is required for all steps: subunits exchange, polymer constriction and fission. Of interest, subunit exchange in the filaments was found not to be dependent on membrane curvature. This is the first *in vitro* reconstitution of a membrane remodelling process that requires sequential subunit recruitment. Altogether, these findings should inspire future works to address the ESCRT-III dynamic polymerization and membrane fission in cytokinetic bridge, with potential exchanges of ESCRT-III subunits within filaments of increasing curvature.

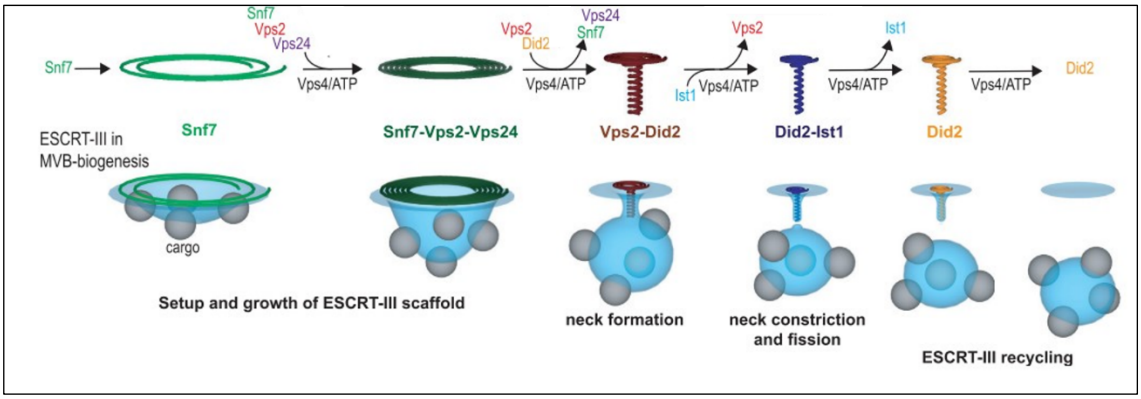

Figure 8 – ESCRT-III sequential polymerization by subunit exchange can constrict and fission membrane necks *in vitro*, using Yeast ESCRT-III subunit homologs. Snf7 (CHMP4B), VPS2 (CHMP2), VPS24 (CHMP3), Did2 (CHMP1), Vps4 (VPS4), Ist1 (IST1). Adapted from [18]

I.3.5 Trafficking towards the intercellular bridge promotes F-actin clearance from the abscission site

I.3.5.1 Summary of the working mechanism of Rab GTPases

Before jumping into the trafficking towards the intercellular bridge, I will briefly remind the working mechanism of the Rab proteins. The Rab and Arf GTPase family are key regulators of intracellular traffic. They define specific routes in the secretory and endocytic pathways as shown in Fig. 9.

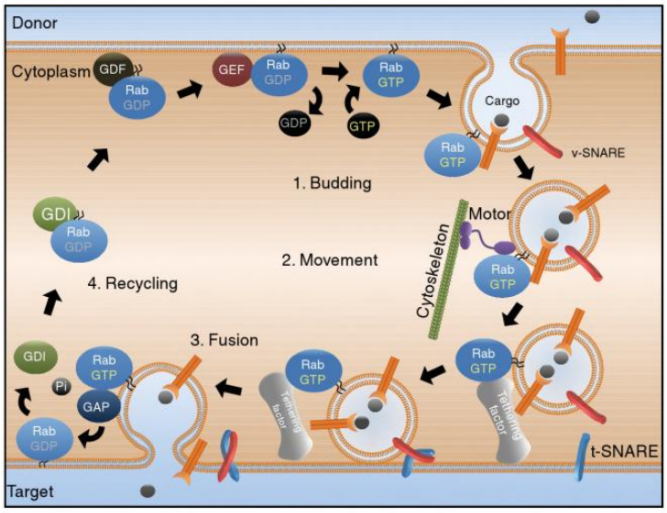

Figure 9 - Functional mechanism of Rab GTPases. Adapted from [9]

One of the most important findings in the field in the 1990s was to understand that Rabs decorate specific compartments [95]**.** The singularity of Rabs draws from the multi-step control of vesicle formation, scission, motility, docking, and fusion. How do Rab GTPases function? Rab proteins can cycle between inactive-soluble form (GDP-bound), and an active form (GTP-bound) that is membrane associated (Fig. 9). After protein synthesis, GDP-bound Rabs are prenylated with a geranylgeranyl group at the C-terminal, to allow association of the protein with the membrane [9]. This complex will be escorted to a membrane where a Guanine nucleotide Exchange Factor **(GEF)** will catalyse the replacement of GDP by GTP forming a GTP-bound Rab. The latter has the capacity to recruit effector proteins. After membrane fusion, a GTP activating protein **(GAP)** induces the hydrolyses of GTP by the Rab. This leads to a GDP-bound Rab that is extracted from the membrane by a GDP dissociation inhibitor (GDI) protein, thus becoming soluble at the cytosol. The GDI displacement factor (GDF) will recycle the GDP-bound Rab by leading it to a specific membrane [9]. The GTP-bound state enables the direct recruitment of effector proteins, and interestingly one effector can bind to different Rabs, or have several Rab

binding sites depending on the task to perform [96]. The Rab-effector interaction will in particular help Rabs regulate the **targeting of the vesicle** to another organelle (e.g. Rab-FIP3); the recruitment of **molecular motors** for transport (kinesin, dynein or myosin); the recruitment of **tethering factors** (for docking) that will bring the two membranes in close proximity (e.g. exocyst complex) and the **fusion** thanks to the SNARE complex - interaction of the cognate vesicular SNAREs (v-SNARE proteins) with the target SNAREs (t-SNAREs) on the acceptor membrane (Fig. 9).

I.3.5.2 Trafficking towards the intercellular bridge

In the early 2000s, genome wide screens (using RNAi or drugs to inhibit specific trafficking pathways) [41, 42, 97] showed that the intracellular trafficking is important for completion of cytokinesis, re-opening this venue in the field that had been put aside. Rab GTPases are key regulators of membrane trafficking in eukaryote cells, and among the 62 human Rabs, several localize at the furrow or at the intercellular bridge (Rab1, Rab8, Rab10, Rab11 Rab14, Rab21, Rab24 and Rab35) [98]. Trafficking of vesicles to the ingressing furrow and later within the intercellular bridge is required for cytokinesis, as summarized in Fig. 10.

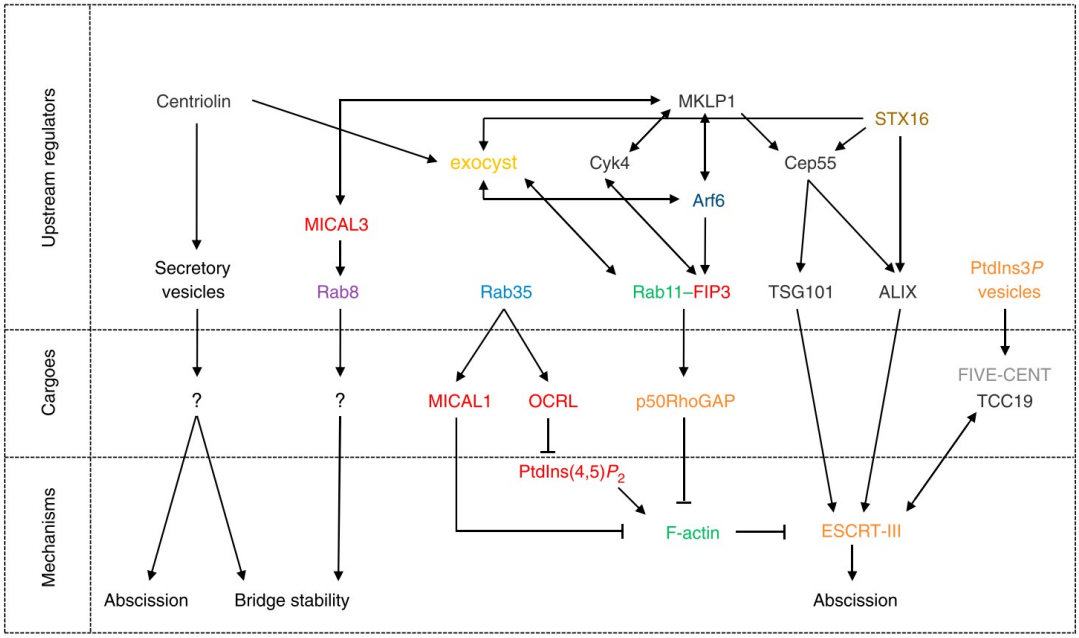

Figure 10 - The several pathways known to connect membrane traffic and cytokinesis. Adapted from [96]

Although important for abscission, vesicle trafficking doesn't drive it *per se* as initially proposed [99]. Most of the functional studies have focused on the roles of Rab11 and Rab35

and their effectors due to their ability to increase cytokinesis failure when knocked-down. It is well known that these two Rabs promote abscission by ensuring low levels of F-actin at the intercellular bridge as it will be described in the next section I.3.5.3.

I.3.5.3 F-actin clearance from the bridge is required for cytokinesis

After furrow ingression, F-actin from the furrow disassembles. This happens due to Rho A inactivation by the Protein Kinase C ε (PKCε) and 14-3-3 protein complex during cytokinesis [100, 101]. Actin continues to be cleared from the intercellular bridge, and this is accompanied by lipids remodelling. As described in section I.3.1, the ESCRT machinery constricts the plasma membrane to drive abscission. This process can be impaired if too much actin is localized in the bridge. Thus F-actin must not accumulate and even be cleared for successful abscission.

How does F-actin not accumulate and even disassemble at the bridge? F-actin levels and clearance at the bridge are controlled by capping proteins, Rab35 and Rab11.

Recently, it has been shown that the actin capping protein (CP) that binds to the barbed end of growing actin filaments, is important for completion of cytokinesis [102]. The loss of both α- and β-CP leads to an increase of the number of multinucleated cells to 20% and 10% respectively. Indeed, depletion of CP leads to a 2.4-fold increase of F-actin in cytokinetic cells, and its capping function is required for proper cytokinesis. This is consistent with the fact that introducing a CP mutant that cannot bind to the barbed end of F-actin does not rescue the number of multinucleated cells resulting from CP depletion. In addition, loss of CP leads to impaired ESCRT-III machinery assembly at the midbody. Together these data suggest that controlling the filament size of F-actin in late stages of cytokinesis is important for successful cytokinesis.

The role of Rab35 in cytokinesis was first demonstrated in 2006, in a systematic Rab RNAi screen in *Drosophila* S2 cells. After Rab35 depletion, the defects in cytokinesis (measured by the number of binucleated cells) were much higher than those observed in Rab5 or Rab11 deficient cells (Rab35 20%, Rab5 and Rab11 6%) [103]. Rab35 is involved in fast endocytic recycling [103]. Interestingly, in this paper the authors show that Rab35 colocalizes with PI(4,5)P2 at the furrow and in early bridges. Functionally, the overexpression of the dominant negative Rab35 S22N delocalizes PI(4,5)P2 and Septin2 from the

intercellular bridges [103] . Later on, yeast two-hybrid and protein pulldown assays from our lab showed that Rab35 directly binds to the PI(4,5)P2 lipid phosphatase OCRL (Lowe oculocerebrorenal syndrome protein) [104] (Fig. 11).

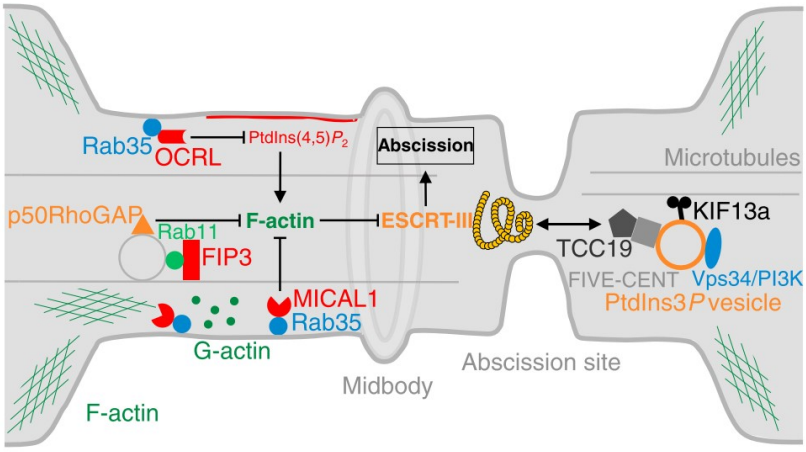

Figure 11 – Schematic showing the actin cytoskeleton remodelling by the Rab11 and Rab35 effectors, to promote ESCRT-III assembly at the abscission sites and successful abscission.

GTP bound Rab35 directly interacts and recruits OCRL to the intercellular bridge. It is noteworthy that phosphoinositide PI(4,5)P2 regulates actin dynamics and promotes high actin polymerization [105]. At the bridge, OCRL hydrolyses PI(4,5)P2 into PI(5)P subsequently promoting the depolymerization of F-actin [104] . Indeed, depletion of OCRL or Rab35 induces an increase of F-actin levels at the bridge and consequently a significant delay in abscission. Importantly, it was shown that treating Rab35 or OCRL depleted cells with low doses of Latrunculin-A (to restore normal levels of F-actin at the bridge) rescued the abscission defects, directly proving that excess of F-actin at the bridge prevents abscission. In conclusion, in late intercellular bridges Rab35-OCRL prevents F-actin polymerization/accumulation by reducing PI(4,5)P2 levels (Fig 11).

Still, it remained unknown how actin was being actively depolymerized at the intercellular bridge. In 2017, S. Frémont in our lab described that GTP bound Rab35 binds directly to and activates MICAL1 (Molecule Interacting with CasL), recruiting it to the intercellular bridge [106]. MICAL1 is a redox enzyme that oxidizes specific methionine residues of F-actin and promotes filament disassembly *in vitro* [106]. At the bridge, MICAL1 oxidizes actin filaments promoting their depolymerization, thus leading to effective F-actin clearance and successful abscission [106]. Consistently, siMICAL1 delayed abscission and induced a massive accumulation of F-actin at the intercellular bridge. Importantly,

accumulation of F-actin at the bridge prevents ESCRT-III recruitment to the abscission sites, therefore contributing to the delay in abscission. In addition, treatment of wild type cells with Jasplakinolide (an F-actin stabilizing drug) also decreases ESCRT-III recruitment to the abscission site. This suggests that stabilization of F-actin impairs the recruitment of the abscission machinery. One possibility is that F-actin may serve as a physical barrier obstructing the recruitment of ESCRT-III at future the abscission site. Alternatively, stabilization of actin may perturb tension at the bridge, and thus inhibit ESCRT-III polymerization as described in section III.2.

In parallel to the Rab35/OCRL/MICAL1 pathway, the Rab11 pathway is also important to promote cytokinesis and actin clearance.

Rab11 is involved in endosomal recycling and is required for normal cytokinesis across species: in *Drosophila* and mammalian cells via Rab11-FIP3 (Rab11 Family Interacting Protein 3), and in *C. elegans* via Rab11 GEF REI-1 [88, 107-110] . During cytokinesis Rab11-FIP3 endosomes are docked at the intercellular bridge and can then interact with other proteins to help form the midbody and stabilize the bridge. More precisely Rab11-FIP3 interacts with Sec15 (also an effector of Rab11) of the exocyst complex. FIP3 links Rab11 to Arf6 that is in its turn in contact with the exocyst. Finally, FIP3 binds to MgcRacGAP/Cyk4 that is enriched at the midbody [107, 110, 111].

Rab11-FIP3 positive endosomes are important to deliver at the bridge the p50RhoGAP cargo, which is a GAP for RhoA. Thus, proper p50RhoGAP delivery at the bridge should limit RhoA activation and therefore F-actin polymerization at the bridge (Fig 11). In addition, it was recently shown that Rab11-FIP1 is recruited to the intercellular bridge to promote Rab35 localization at the midbody, thus ensuring that high levels of Rab35 are maintained at the bridge [112]. Indeed, depletion of RAB11-FIP1 leads to decreased levels of Rab35 at the intercellular bridge. Moreover, loss of Rab11-FIP1 and Rab35 depletion leads to similar phenotypes: increased binucleation, delay in cytokinesis and accumulation of actin at the intercellular bridges. Similar to what was reported after Rab35 depletion [104], the delay in abscission in Rab11-FIP1-depleted cells could be restored to normal values using low levels of Lantraculin A. To conclude, this study revealed intimate connections between the Rab11-FIP3 and the Rab35 pathway in F-actin clearance and abscission.

I.3.6 Microtubule cut at the abscission site promotes abscission

As mentioned in section I.2 above (and Fig. 2), the intercellular bridge is filled with microtubules that mostly originate from the central spindle. The microtubules at the intercellular bridge undergo post translational modifications and are highly acetylated [113]. This has been proposed to stabilize the microtubules at the bridge. Interestingly, immunofluorescence and time-lapse video microscopy of the ending binding protein 3 (EB3), usually localized in the + end of the microtubules, showed that it is localized at the midbody, and has been suggested to stabilize the midbody [114, 115]. This seems to be required for cytokinesis since depletion of EB3 leads to an increased number of binucleated cells [114].

Successful abscission nevertheless requires microtubule clearance at the abscission site, as shown in Fig. 6a, and appears concomitant with the ESCRT-III polymerization to the abscission sites [1, 29, 116]. The microtubule severing is mediated by the AAA-ATPase Spastin that is recruited by CHMP1B to the abscission sites [117]. Indeed, Spastin-depleted cells exhibit a strong delay in abscission and defective IST1 helices [5, 14], shown by 3D STORM (Fig. 12). Depolymerizing microtubules using a drug (Batabulin) in Spastin-depleted cells restores normal abscission [4], demonstrating the importance of microtubules clearance for abscission [91]. These data also highlight an important coordination between microtubule severing and the ESCRT-III polymerization. It is noteworthy that microtubule remodelling is local, since the microtubules at the midbody are not severed and are still present in the midbody remnant after abscission has occurred.

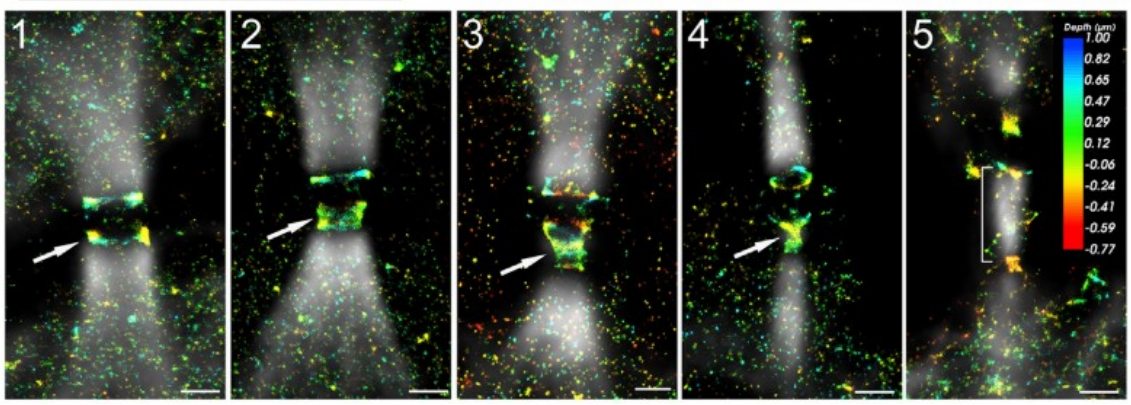

Figure 12 – IST1 localization at the midbody and abnormal helices in Spastin depleted cells. From [14].

I.4 **What happens if abscission fails?**

Cytokinesis leads to the separation of the daughter cells with the correct chromosomes number. Cytokinesis defects are associated with several diseases (such as Lowe syndrome or female infertility) and is implicated in tumorigenesis [118]. Indeed, it is now well established that failure in cytokinesis can favor tumor development *in vivo* through the formation of genetically unstable tetraploid cells. Therefore, understanding the mechanisms of cytokinetic abscission is of both fundamental and medical importance.

I.4.1 Inhibiting abscission in physiological conditions

Polyploidization is not always a pathological condition, since it is characteristic of several types of cells or tissues, like in syncytiotrophoblasts, Purkinje cells, hepatocytes, cardiomyocytes, vascular smooth muscle cells, megakaryocytes and germ cells [15] (Fig. 13).

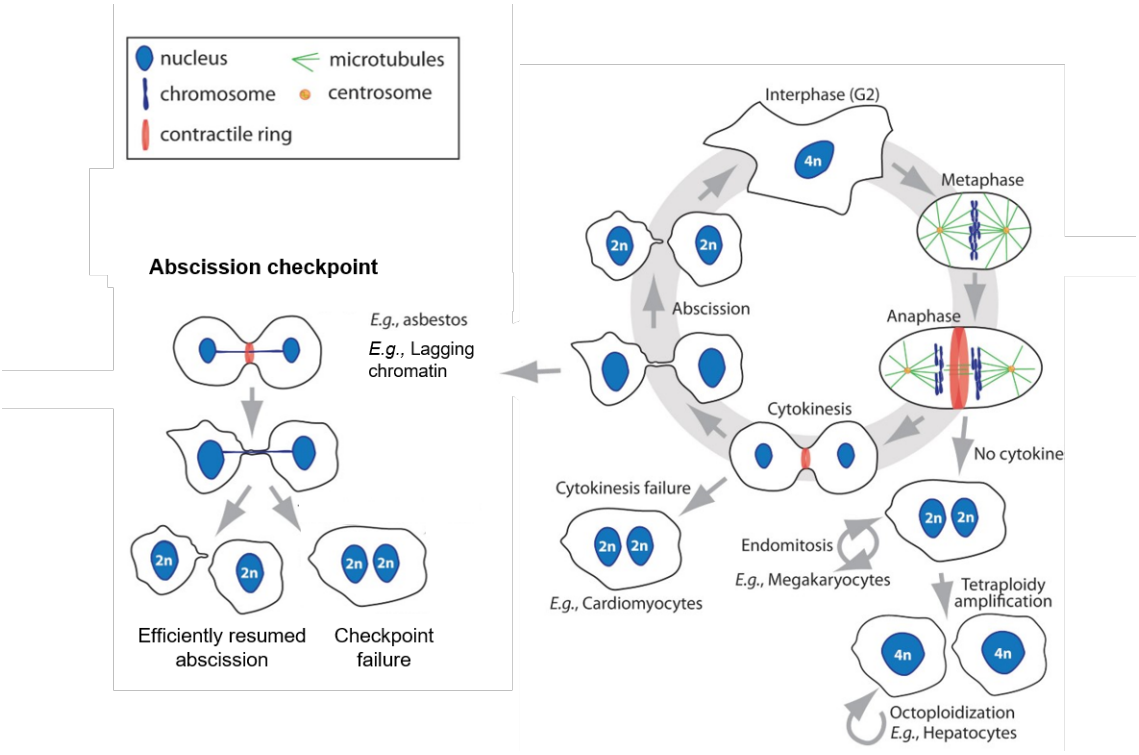

Figure 13 – Cell division and consequences of failure or efficient abscission. Abscission checkpoint activation leads to abscission delay to resolve the errors efficiently, and consequence of checkpoint failures is aneuploidy. Arrows: leading out from the normal cycle show different ways of cytokinesis failure leading to polyploidy. Normal physiological pathways: hepatocytes, megakaryocytes and cardiomyocytes formation. From [15]

Interestingly, cardiomyocytes, megakaryocytes, and hepatocytes undergo abscission failure, even if triggered by different mechanisms. In particular, halting ESCRT-III recruitment to delay abscission is a physiological mechanism used during meiosis in mouse spermatogenesis. In this case, TEX14, that is only expressed in the testes, binds CEP55, thus preventing the recruitment of ALIX/TSG101[119, 120]. Therefore, cytokinesis is paused since the ESCRT-III machinery cannot be recruited to the intercellular bridge. Depletion of TEX14, or overexpression of CEP55 leads to abscission and spermatogenesis failure. In addition, in *Drosophila* spermatogenesis and in the female germline stem cells differentiation abscission is also impaired for the normal development of the tissue [121, 122].

I.4.2 Inhibiting abscission to solve errors at the intercellular bridge – the abscission checkpoint

Cytokinesis is a multi-step and tightly regulated process and cytokinetic defects may arise from non-corrected error in these steps. First, cells might not be able to form a cleavage furrow, for instance as a result of the inactivation of RhoA, of a RhoA activator or a RhoA effector at the onset of anaphase [123]. Second, the ingressing furrow might fail and regress if an important component of central spindle is not correctly recruited, as in the case of loss of PRC1. Third, cells can fail abscission if CEP55, ALIX, or several other components of the ESCRT-III are not present, as well as if there is too much actin at the intercellular bridge, as described in section I.3.2. Finally, environmental factors, like the presence of the mineral asbestos in cells can physically obstruct the abscission site. This can contribute to their carcinogenic effect in humans [123]. As a result of the aforementioned failure in cytokinesis, the proliferation of binucleated (tetraploid) cells might be eliminated by a p53-dependent pathway, limiting the risks of tumorigenesis[118].

When errors at the intercellular bridge occur, abscission can be strategically delayed through the activation of the **abscission checkpoint**, or "NoCut Checkpoint" [50], until the errors are resolved and abscission can resume. Several errors can trigger the abscission checkpoint including lagging chromatin and ultrafine anaphase bridges (induced after inhibition of the topoisomerases) within the intercellular bridge; replication stress; high membrane tension at the bridge, or nuclear pore defects [45].The abscission checkpoint depends on several important regulators of cytokinesis, like Aurora-B and CHMP4C [124]. More specifically, Aurora-B-mediated phosphorylation of CHMP4C activates the checkpoint [124].It has been suggested that CHMP4C and ANCHR may sequester VPS4 at the midbody

inhibiting its localization at the abscission site, and thus abscission [125]. Therefore, activation of the checkpoint delays abscission for several hours, apparently to give the cells time to solve the cytokinetic defects, and therefore prevent tetraploidization, or chromosome breaks and DNA damage. Failure in solving these errors, can lead to furrow regression and binucleation [50]. In addition, mutations in CHMP4C that cannot bind to ALIX and thus disrupt this checkpoint promotes genome instability and is associated with cancer development [126]. A new regulator of the abscission checkpoint has been described recently in our lab. The human Methionine sulfoxide reductase B2 (MSRB2) protein reduces actin and is a key component of the cytokinetic abscission checkpoint [127]. MSRB2 is a cytosolic protein that relocates to the midbody in the presence of lagging chromatin. MsrB2 promotes actin polymerization at the intercellular bridge which delays abscission. Interestingly, MsrB2 selectively reduces oxidized actin monomers, counteracting the MICAL1 enzyme that oxidizes actin filaments (see section I.3.2.3 above). Consistently, depletion of MSRB2 leads to decreased actin levels at the bridge, and 90% of the bridges with lagging chromatin become binucleated, while only accelerating abscission in cells without chromatin bridges [127].

I.4.2.1 The unexpected case of CEP55-knockout mice

As mentioned above, depletion of the ESCRT-III machinery leads to strong delays in abscission that can cause bridge regression and binucleation (section I.3.1). Surprisingly, it has been reported that deletion of the CEP55 in mice is necessary for apical progenitor cells (precursors of neurons) but is dispensable for other dividing cells [128]. The authors report that Cep55-knockout mice progress through embryogenesis and are born alive. However, Cep55-knockout newborns showed several brain abnormalities: severe microcephaly; reduced brain and cortical thickness; binucleated neurons as well as kidney abnormalities. Importantly, similar anomalies have been reported in the MARCH syndrome (multinucleated neurons, anhydramnios, renal dysplasia, cerebellar hypoplasia and hydranencephaly) and the Meckel syndromes, that are both associated with mutations in CEP55 in humans [129, 130]. In addition, depletion of Cep55 or Chmp4B in cultured neural mouse progenitors induces abscission delay and binucleation [128]. The authors finally show that neural progenitor cells depend on ESCRT-III for abscission. Similarly, another study in mice showed that loss of CEP55 impairs abscission in neural stem cells concomitant with mice developing microcephaly at birth [131]. In addition, cultured primary fibroblasts of the Cep55-knockout

mice do not recruit ALIX, TSG101, CHMP2B, nor CHMP4B to the midbody as expected. However, these cells can successfully divide, even when ESCRT-III components are depleted. These results are intriguing but often binucleated cells are not detectable in culture or tissue because they are cleared in a p53-dependent manner, or can undergo cytofission generating mononucleated cells [132, 133]. Nonetheless, this provocative result in fibroblasts suggests an ESCRT-III independent cytokinesis and that delayed cytokinesis is detrimental only in a subset of cells *in vivo*. Other researchers have proposed that intercellular bridges can break after several hours, in an ESCRT-III-independent way, especially in stiff environments [134]. Many questions remain regarding why some cells require or not ESCRT-III-mediated abscission and whether other unknown proteins can lead to abscission in ESCRT-deficient cells.

I.5 **The midbody remnant: a product of cytokinetic abscission**

I.5.1 Overview of the fate and functions of the midbody remnant

The majority of cells undergo abscission successively on both sides of the midbody (Fig. 1d-e), generating a free midbody remnant (MBR) [46]. This was an important finding since previous studies had suggested that abscission would occur only once, and that the arm of the bridge always retracted into the cytoplasm with subsequent degradation of the midbody by autophagy [29, 135-137]. Scanning Electron Microscopy (SEM) images of HeLa cells revealed that MBRs localize at the surface of the cell and display no connection with the daughter cells, hence showing that the bridge underwent two abscissions [46], (Fig 14a). In addition, the MBR can tightly associate with the cell surface via Ca^{2+} / Mg^{2+} dependent receptors [46], possibly integrins [138], together with the tethering factor BST2/tetherin [139].

The MBR can follow two very different fates (shown in Fig 14b):

- Be engulfed – the MBR can wander on the cell surface for several hours until it is engulfed in a phagocytosis-like event that is dependent on actin, and can enter the lysosomal degradation pathway [46 , 140-142]. Interestingly, in *C. elegans,* it has been shown that MBR engulfment can occur via the cell death protein, ced-1, because the MBR contain phosphatidylserine in the outer leaflet [140]. In mammalian cells this engulfment process is less characterized, but it may also require the exposure of phosphatidylserine to be phagocytosed-like [138].
- Be released into the media – just after abscission or after being at the cell surface, the midbody can detach and be released into the extracellular media. This has been observed by live-cell video microscopy, where the midbodies can be followed being taken away to the media [139, 143]. These free MBR have been observed *in vivo* in the cerebrospinal fluid of mouse and in *in vitro* in cultured cells [140, 142, 144-146]. Interestingly, the free MBRs can be engulfed by a non-daughter cell or even by a different cell type [46, 136].

The MBR has been implicated in several post-abscission functions, for instance in mammalian brain development; primary cilia formation; specification of the Dorsal-Ventral axis in *C. elegans*, and cell proliferation [144, 145, 147, 148]. Recently in our lab, the MBR attachment to the surface of the cells was found to be promoted by the viral restriction factor tetherin (BST2) revealing a new parallel between viral biology and cytokinesis, since BST2 is known for tethering viral particles to the infected cell during HIV release [139]. Hopefully, in the next years more studies will help to understand the mechanism of internalization of the MBR, and whether the MBR can play other roles or trigger specific signalling cascades once it is internalized.

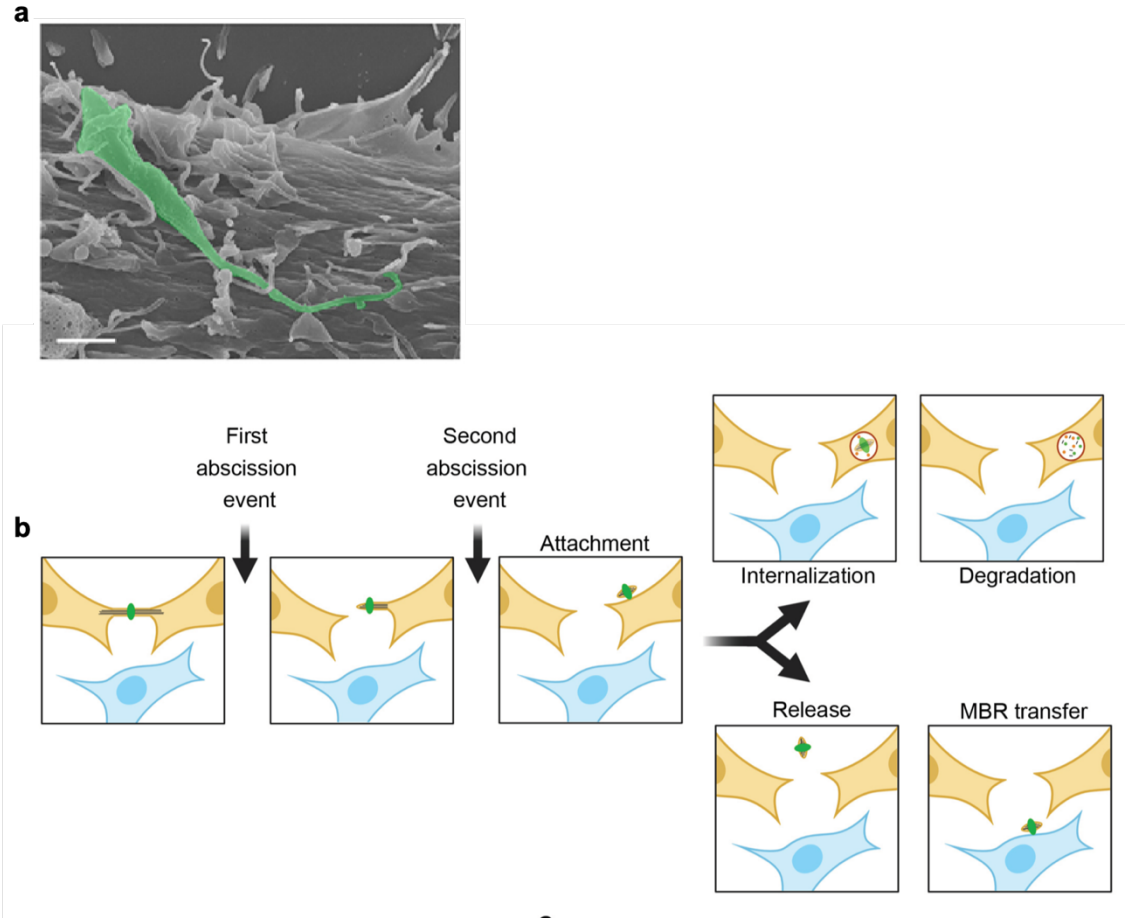

Figure 14 - Schematic of the MBR release and its fate in the cells. a) MBR at the cell surface. b) MBR is freed after two consecutive cuts on the side of the midbody. The MBR can then be internalized by the cells or released to the extracellular media. From [44, 137]

I.5.2 The midbody remnant proteome: finding potential new actors in cytokinesis

As the MBRs are released into the extracellular medium, they can be purified to subsequently assess their protein composition by several methods, like immunofluorescence or mass-spectrometry. Our lab has recently set up a purification protocol to isolate pure, intact midbody remnants using flow cytometry (FACS) [1]. The sophistication of methodologies to purify MBRs are important to improve protein recovery and solubilization for mass spectrometry. Notably, no cell synchronization was done and the purification of MBRs did not involve the use of detergents in this study. This allows the potential identification of transmembrane proteins and membrane associated proteins. MBRs were detached from the cells using only EDTA that chelates $Mg^{2+}$and Ca^{2+}, and midbody remnants from cells endogenously expressing GFP-MKLP2 were FACS sorted. In addition to collecting MBR for mass-spectrometry, sorted MBR can be pelleted and spread in coverslips to perform immunofluorescence and SEM as shown in Fig. 15a.

The resulting midbody proteome, named the *Flemmingsome* as a tribute to Walter Flemming, revealed almost 500 proteins enriched at the midbody (Fig. 15b). Proteins involved in membrane trafficking, actin cytoskeleton, microtubule related proteins, and CPC proteins were found as expected, such as MKLP1, MKLP2, RacGAP1, KIF4A, PRC1, CEP55, CHMP4B (Fig. 15a). Surprisingly, proteins from the ubiquitin-dependent proteasome and the translation machinery were also found, raising the question whether translation is an active process during cytokinesis, and whether this machinery is activated when the MBR is engulfed by the cells. Furthermore, caveolae proteins were among the hits, namely Cavin1, CAV1, EHD2, Pacsin2-3. Caveolae and the description of its different proteins components as well as their role in cells will be the subject of chapter II.

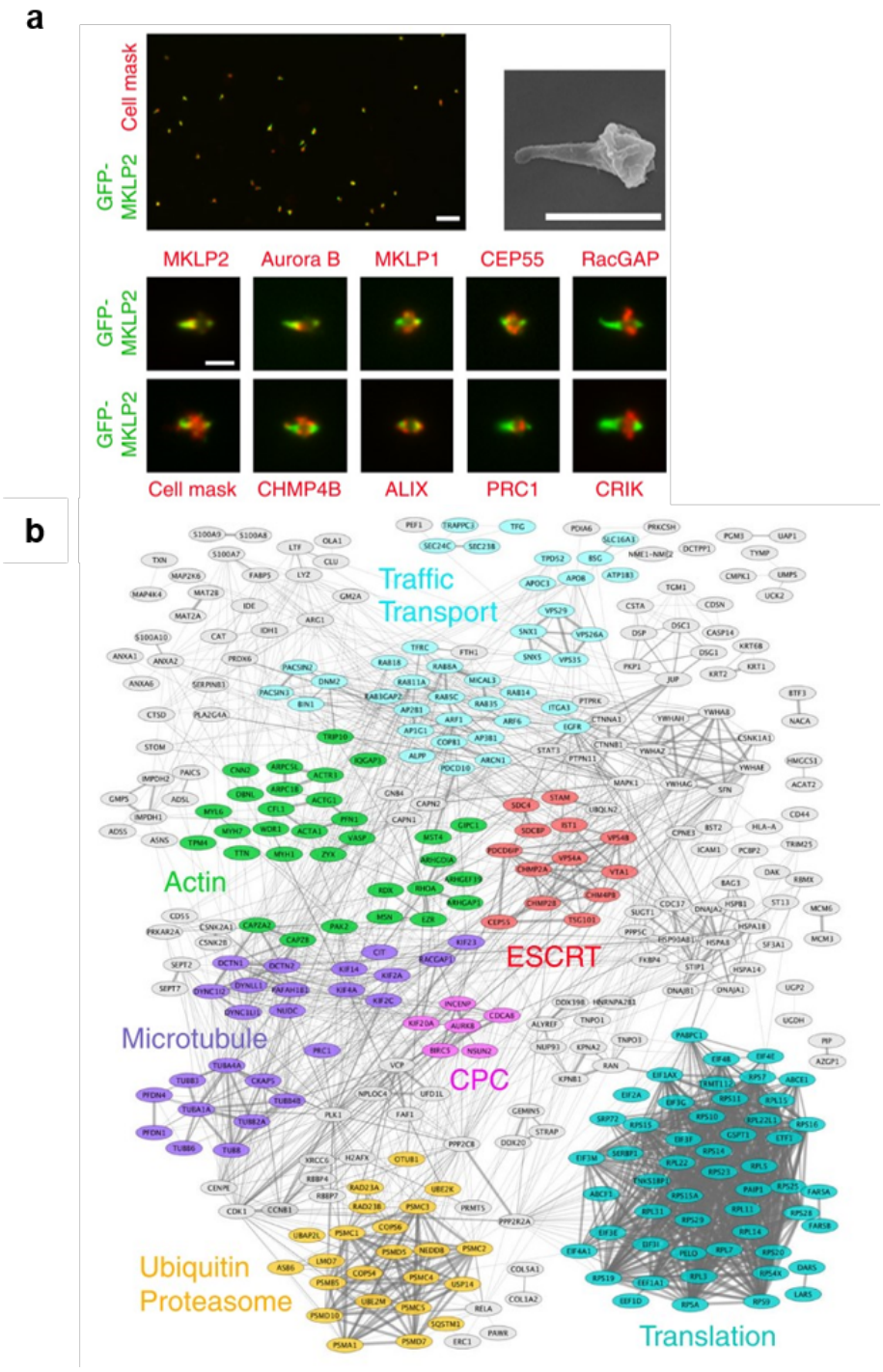

Figure 15 – Midbody remnants proteome – the *Flemmingsome*. a) MBR+ population analysed with cell mask membrane marker. Each individual midbody is positive for GFP-MKLP2 (green) and cell mask (red). Scanning electron microscopy (SEM) of an isolated MBR. b) STRING functional association network for the enriched proteins in the proteome. From [1]

Chapter II: Caveolae

II.1 **Caveolae: the little "caves" discovered in the 1950s**

In 1953, George Palade described for the first time in endothelial cells of blood capillaries in the heart, spherical membrane invaginations with a regular shape and size [149] that he named plasmalemmal vesicles (Fig. 16a) to suggest they could transport molecules across the endothelial plasma membrane. In later work on blood vessel capillaries of the tongue (rat), Palade showed that these plasmalemmal vesicles are localized and "open" to the blood front of the endothelium, as well as in the tissue front, as shown in a handmade 3D model [16] (Fig. 16b). In 1955, Eichi Yamada coined the term caveolae describing "caveolae intracellulares" after their resemblance with little "caves" at the plasma membrane of gallbladder epithelial cells in mice [150].

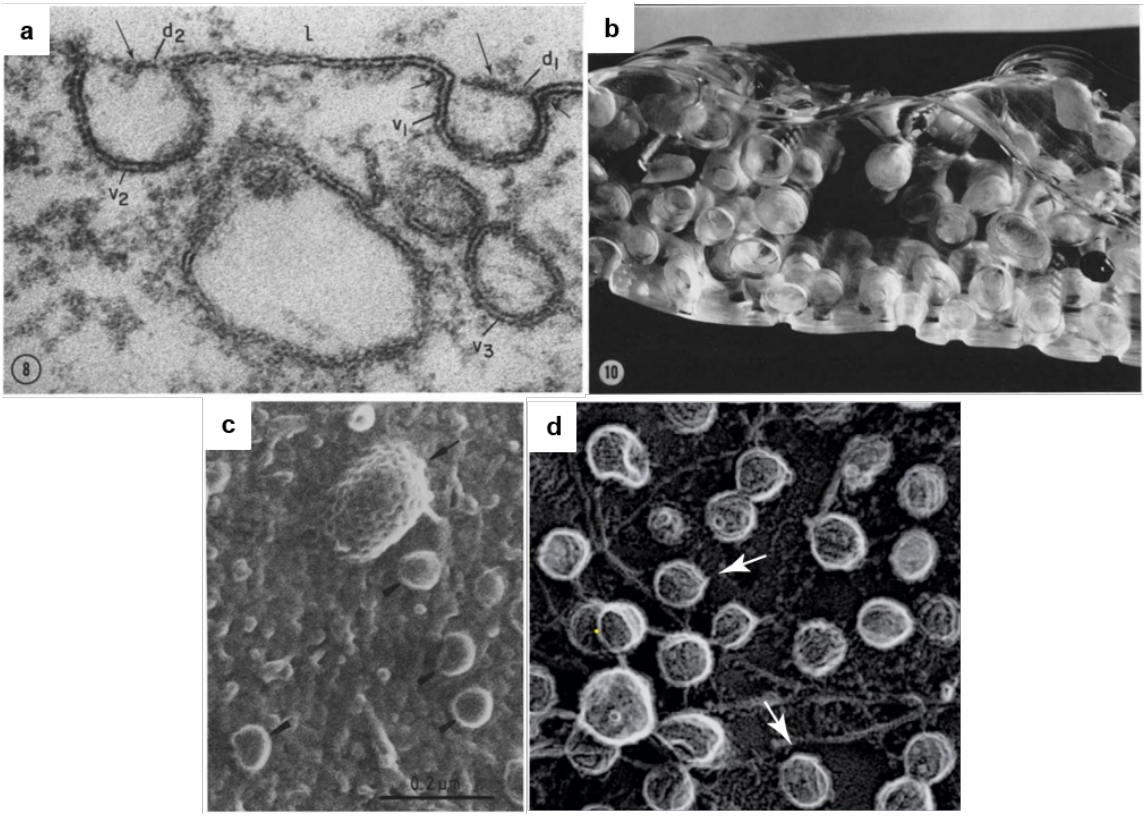

Figure 16 - Caveolae morphology see by transmission electron microscopy (TEM) and by rapid freeze deep-etch microscopy. a) TEM of in blood vessels capillaries showing caveolae. b) Handmade 3D reconstruction carved in lucite of an endothelial cell with caveolae pits. c) Scanning electron microscopy of fragments of dorsal caveolae detached upon adhesion to poly-lysine-coated silicon chips d) Caveolae observed using rapid-freeze deep-etch electron of the inner surface of the plasma membrane from T24 human bladder carcinoma cells. Adapted from [16].

Since then, caveolae have been morphologically described as cup- or Ω-shaped plasma membrane invaginations of 50-100 nm diameter, with a striated coat (Fig. 16c, d) and devoid of a clathrin coat [25]. Caveolae can be identified as single invaginations or as "rosettes", in which several caveolae are connected into one supra-caveolae structure which, in turn, can either be connected to the plasma membrane or located close to it. These invaginations are only found in vertebrates, being virtually present in all mammalian cells. They are especially enriched in skeletal muscle cells, adipocytes and endothelial cells, but are absent from neurons and lymphocytes [25]. Caveolae are believed to form subdomains at the plasma membrane, composed of a specific sub-set of lipids and proteins that are required for their assembly. The progress made in the last years in the discovery of the protein composition of caveolae shed new light into their functions in signalling, trafficking, lipid homeostasis and mechanoprotection in cells. Specifically, caveolae are constituted by Caveolins, Cavins, and Pacsins (in some cell types), which are required for caveolae formation, and accessory proteins like EHD2 and Dynamin2 required for their dynamics. This molecular machinery required for proper caveolae assembly and stability will be described more in detail in the next section.

II.2 **The caveolae protein composition**

In 1992, **Caveolin1** (CAV1) was the first constitutive protein of caveolae identified. *Rothberg. et al.* described that CAV1 localizes in caveolae in fibroblasts as shown by immunoelectron microscopy [151] (Fig. 17a). In 1993, Dupree and colleagues described VIP21 (Vesicular integral-membrane protein of 21 kDa), a membrane protein localizing in the trans-Golgi network and in caveolae in MDCK cells [152]. The comparison of the sequences showed these two proteins were the same, and the name CAV1 prevailed [153, 154]. Two other isoforms of Caveolin encoded by separate genes were identified in the following years, CAV2 through microsequencing of adipocyte-CAV1 enriched membranes, and CAV3 by database search for homologues of CAV1 and subsequent molecular cloning [155-157]. CAV1 and CAV2 are expressed predominately in non-muscle cells, such as endothelial cells, fibroblasts and adipocytes, whereas CAV3 is a muscle specific isoform expressed in skeletal and cardiac muscles [156]. Cells that do not express CAV1, such as lymphocytes, lack caveolae, and its expression in these cells is sufficient to induce their formation, which strongly suggested that CAV1 is a constitutive protein of caveolae [158].

In 2008, two studies from the Parton and Pilch labs formally demonstrated that **Cavin1** is a constitutive protein of caveolae required for their formation in mammalian cells (zebrafish and mice) [159, 160, 161]. Previous studies had already identified Cavin1 as a protein localizing in caveolae in adipocyte cells by screening for antibodies recognizing epitopes present in caveolae, and by mass-spectrometry of caveolae enriched membranes [162], [163]. Ectopic expression of Cavin1 in PC3 cells that express CAV1 but do not form caveolae, was sufficient to induce caveolae formation [159]. In addition, Cavin1 knock-out mice revealed the loss of caveolae in all tissues, and decreased protein levels of all three caveolin isoforms [161]. The Cavin family comprises **Cavin1**, **Cavin2** or SDPR (serum deprivation response protein), **Cavin3** or SRBC (serum deprivation response factor-related gene product that binds to C-kinase), and **Cavin4** or MURC (muscle-restricted coiled coil). Cavin1, Cavin2 and Cavin3 are mainly expressed in caveolae in non-muscle cell [164, 165], and were found by mass-spectrometry, while Cavin4 is a muscle-specific isoform [166], found in a sequence homology screen. Other proteins important for caveolae stability and dynamics have been described in 2011, namely **Pacsin2 and Pacsin3** (Protein kinase C And casein kinase Substrate in Neurons protein 2 -3) [167-169], which contains an F-BAR (Bin/Amphiphysin/Rvs) domain; and the ATPase **EHD2** (Eps-15 homology domain-containing protein 2), in 2012 [10, 170]. In addition, **Dynamin2** was found in caveolae and proposed to induce membrane fission during caveolae internalization [171, 172]. Cavins and Caveolins localize in the bulb of caveolae, whereas EHD2 localizes at the neck of caveolae. The localization of Pacsins in caveolae has not been precisely described but immunogold EM suggests that they mostly localize near the neck of caveolae (Fig. 17c).

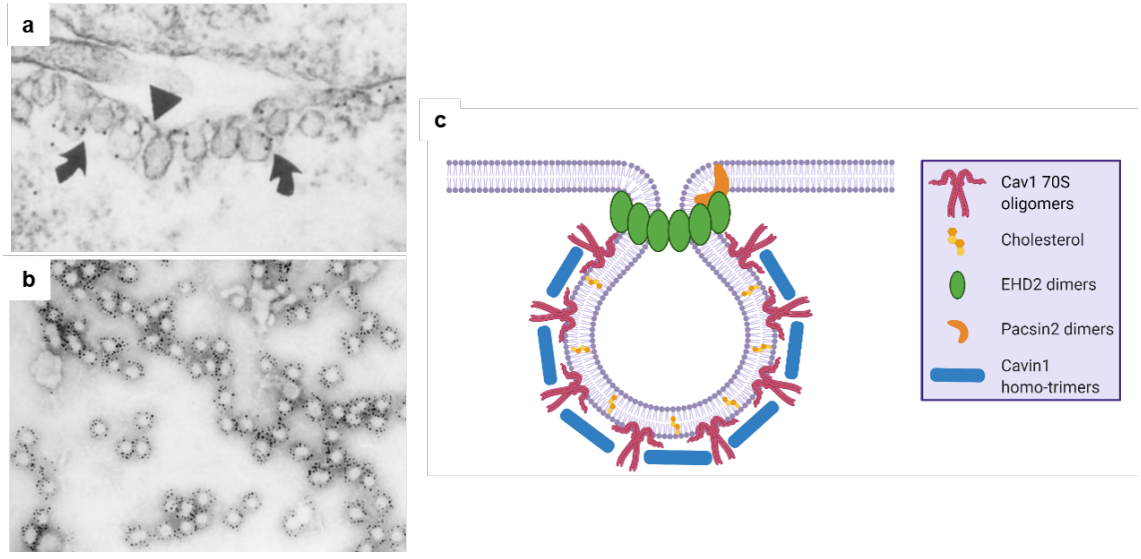

Figure 17 – Caveolae-associated proteins. Immunogold labelling of CAV1 in human fibroblasts a), and Cavin1 in adipocyte plasma membrane b). c) Schematic of caveolae and the proteins known to localize there. Adapted from [151, 173].

II.2.1 Caveolins: structure and function in caveolae assembly

Caveolins are small proteins of 16-22 kDa with four characteristic domains (Fig. 18a):

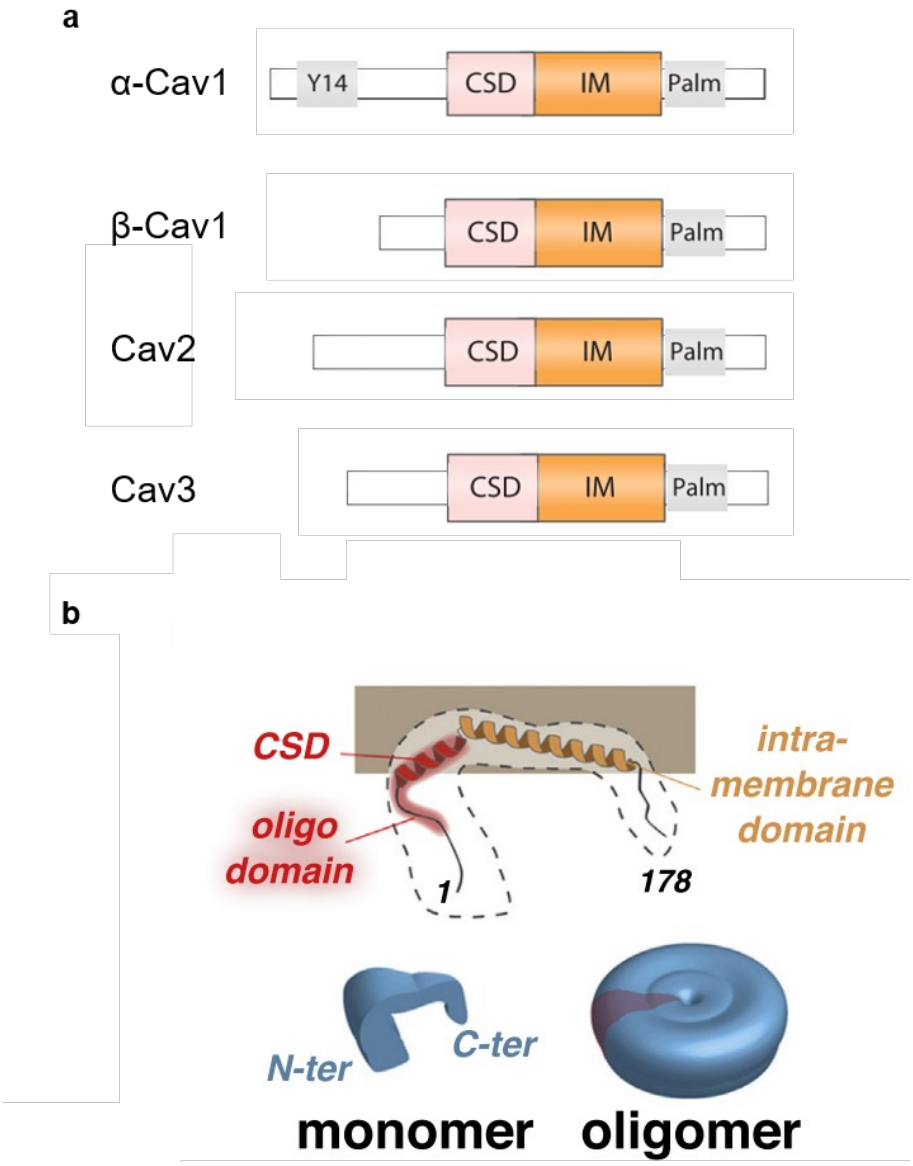

Figure 18 – The Caveolin protein family. a) The caveolin family domains and features. b) CAV1 topology in a membrane. CAV1 monomers assemble into oligomeric complexes. CSD (CAV1 scaffolding domain). IM (Intramembrane domain). Palm (Palmitoylation sites). Y14 (Tyrosine 14). Adapted from [13, 25]

- **the N-terminus domain (residues 1-81 in CAV1)** – mutations in residues 49-58 impair CAV1 targeting to the plasma membrane [174]. This domain contains a Cavin1-interacting region that is a disordered region (residues 30-60);

- **the scaffolding domain (CSD) (residues 82-102 in CAV1)** – the CAV1 CSD has been described to bind directly to cholesterol through a cholesterol binding domain [175], [176]. This domain is involved in oligomerization and protein-protein interactions that are associated with signalling pathways, as it will be described further in section II.5.2.;
- **the transmembrane domain** (residues 103-133 in CAV1) – is a hydrophobic α-helix embedded in the lipid bilayer;
- **C-terminus domain** (residue 102-134 in CAV1) – can be palmitoylated and might be involved in oligomer-oligomer interactions [13].

The Caveolin family has a sequence signature constituted by a single stretch of eight amino acids (aa) 68FEDVIAEP75 in the N-terminus [155, 156]. In addition, Caveolins can homo- or hetero-oligomerize forming high-order oligomers of 300 kDa [177]. No complete atomic structure of Caveolins is available, however, circular dichroism (CD), nuclear magnetic resonance (NMR) and computational analysis studies suggest Caveolins have an unusual topology with the N- and C- termini facing the cytosol. This happens due to two hydrophobic alpha helixes (residues 87-128 CAV1) localized in the scaffolding domain and transmembrane domain that form a hairpin-like structure that is embedded in the lipid bilayer. In-between the two helixes, there is GIP aa sequence that serves as a hinge allowing the two helixes to adopt a U-like shape, thus implying that both C- and N-termini are cytoplasmic (Fig. 18b) [152, 178, 179].

CAV1 is the most studied protein from the caveolin family. It has two isoforms, α-CAV1 and β-CAV1, the latter being 31 amino acids (aa) shorter than α-CAV1, and both localize in caveolae [180]. The N-terminus domain of α-CAV1 can be phosphorylated on the Tyrosine 14 after activation with insulin, the Rous Sarcoma virus, or the Src-Kinase [181-183]. CAV1 has also been described to be phosphorylated on the Serine 80 in the endoplasmic reticulum, and this seems to be important for the secretion of CAV1 [184]. The C-terminus domain of CAV1 can be palmitoylated on cysteine residues (C133, C143, and C156) [185, 186], and even though these do not seem to be required for the anchoring of CAV1 to the plasma membrane it may be important for its oligomerization [185, 186].

The length of N-terminus of Caveolins varies, with CAV1 having the longest, while CAV2 lacks 16 amino acids (aa) and CAV3 27 aa [179], thus neither of them can be phosphorylated at the Tyrosine 14. CAV3 and CAV1 have a high degree of sequence homology, whereas CAV2 does not, particularly in the scaffolding domain [179]. CAV1 and

CAV3 are required for caveolae formation. In addition, CAV1 and CAV3 are able to hetero-oligomerize in cardiac myocytes [187].

CAV2 is usually co-expressed with CAV1 and both can form hetero-oligomers [155, 188]. CAV2 does not seem to be required for caveolae assembly, since CAV2-deficient mice still form caveolae (but show skeletal muscle anomalies), and expression of CAV2 in model systems does not lead to the formation of caveolae [189]. Rather, CAV2 has been proposed to help caveolae assembly [190]. CAV2 also has two isoforms but not much is known about whether they have different functions in caveolae formation.

II.2.2 Cavins: structure and function in caveolae assembly

Cavins are peripheral membrane proteins that can bind to lipids. They belong to a unique protein family with a particular electrostatic alternating pattern: two basic conserved homologous regions positively charged, α-Helical Regions1-2 (HR1-2), that are flanked by three acidic negatively charged, Disorder Regions1-3 (DR1-3) (Fig 19a) [191].

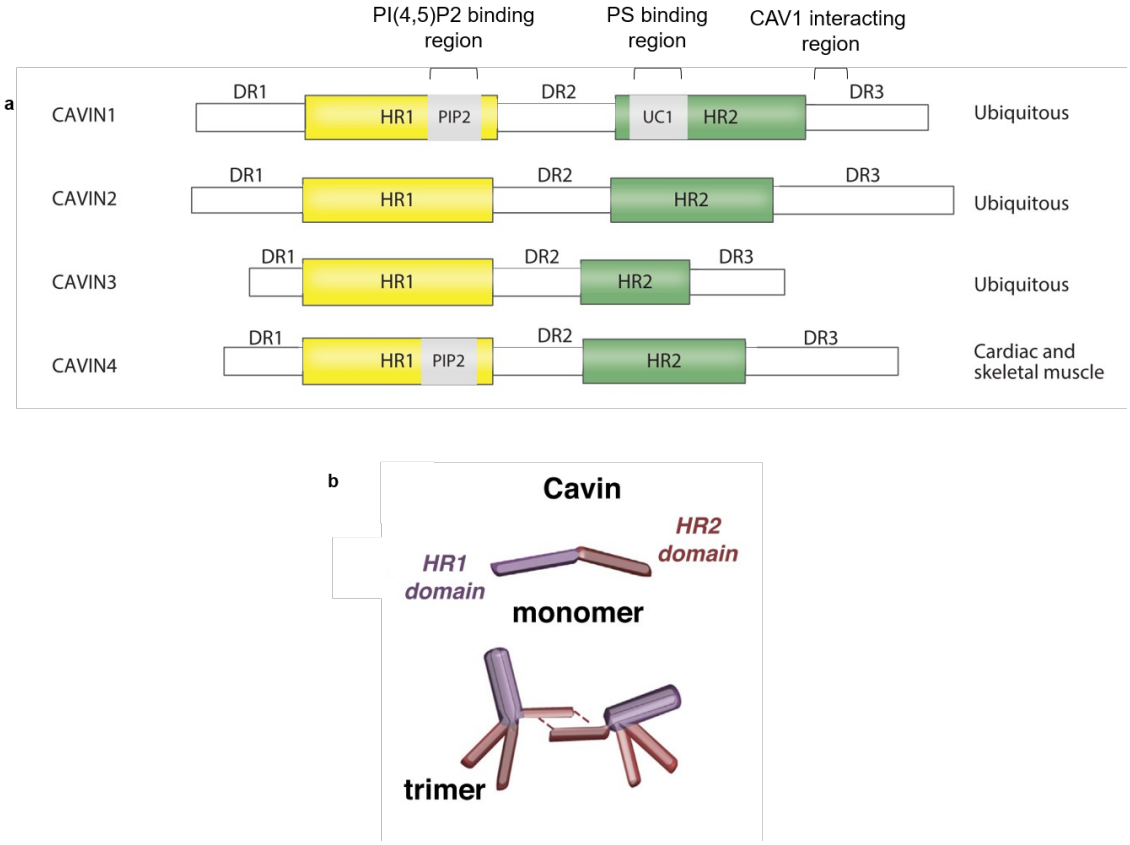

Figure 19 – The Cavin protein family. a) Cavin1 domains and features. b) Cavin1 monomers assemble into trimers that further interact. DR1-2-3 (Disordered Regions 1-2-3). HR1-2(Helical region 1-2). PIP2 (Binding site of PI(4,5)P2). UC1 (Undecad domain 1) Adapted from [13, 25].

These disordered regions are not well conserved at the sequence level but are all predicted to have a disordered secondary structure. The Cavin family is conserved only in vertebrates, whereas the Caveolin family has been described both in vertebrate and in invertebrates like *C. elegans,* but caveolae are not present in these organisms [191].

Proteins of the Cavin family have PEST motifs (sequences enriched in proline, glutamic acid, serine and threonine) located in the disorder regions which can be targeted to proteolysis [163, 173]. Cavins can also be SUMOylated and ubiquitinated [191]. This may

suggest that Cavin protein degradation is important for their turnover and function. In addition, Cavins contain several phosphorylation sites, however none of these have been reported to be important for caveolae formation [191, 192]. An exception to this is the phosphorylation at Ser365 and/or Ser366 that were suggested to enhance caveolae assembly [191].

Cavin1 can form homo- or hetero- trimers with Cavin2, Cavin3, through their well conserved HR1 domain, three Cavin1 or two Cavin1 proteins connected with one Cavin2 or one Cavin3 protein (Fig. 19b) [193]. The HR2 of Cavin1 has been proposed to allow homo- or hetero-trimers interaction, to form high-order and stable complexes in caveolae [194] (Fig. 19b). Though this complex assembly, only Cavin1 is essential for caveolae formation, and for the recruitment of the Cavin complex to caveolae [166]. Cavin2 and Cavin3 have been described to modulate the shape and the dynamics of caveolae, respectively [25]. Cavin1 is the only Cavin that once oligomerized can interact with CAV1 at the plasma membrane to assemble caveolae [166], via the residues 310-345 in the Cavin1 DR3 (Fig. 19a). Therefore, even if Cavin2 - 3 - 4 are able to oligomerize, they are not targeted to caveolae unless they hetero-oligomerize with Cavin1. Indeed, this agrees with the fact that deletion of Cavin1 in mice is sufficient to block caveolae formation in all tissues [161]. In addition, Cavin2 and Cavin3 cannot hetero-oligomerize together. It has been shown that these two Cavins compete for the binding site on Cavin1 and hence they may be localized in different domains of caveolae. Interestingly, even though Cavin4 is a muscle cells-specific isoform, the other Cavins are also expressed in these cells, suggesting that Cavin4 may function as a regulatory protein there. The strict requirement of Cavin1 to form caveolae may arise from the fact that it is the only Cavin that contains an 11 residue (undecad) repeat (240-269 residue) in the HR2 domain [195]. This domain has been shown to be important for caveolae formation and stability, both in cell lines and *in vivo*. Indeed, Cavin1-GFP mutants lacking this region are localized in the cytosol and are not able to form caveolae [195]. Additionally, the lesions in the notochord of zebrafish observed upon Cavin1 depletion were not rescued with the undecad deletion mutant [195].

Cavin proteins can interact electrostatically with the anionic lipids phosphatidylinositol 4,5 bisphosphate (PI(4,5)P2) and phosphatidylserine (PS), via HR1 and HR2 domains, respectively, to assemble caveolae [159, 193, 194, 196, 197]. This will be further detailed the section II.3.

II.2.3 EHD2 structure and function in caveolae stabilization

EHD (Eps-15 homology domain-containing protein) proteins (~60kDa) belong to the Dynamin superfamily of large GTPases proteins. EHDs have two helical regions, a conserved ATP-binding domain (G domain), a linker region and a carboxy-terminal EH domain (Fig. 20a). EHDs contain an NPF (asparagine- proline-phenylalanine) motif that interacts with the EH domain. In addition, the EH domain and the NPF motif can interact with target proteins. The function of EHDs is associated with membrane sculpture: while EHD1, EHD3 and EHD4 are implicated in endocytic pathways, EHD2 has been described to localize at the plasma membrane in caveolae, thus hereafter I will focus on EHD2 [10, 170, 198]. EHD2 induces membrane tubulation in liposomes *in vitro* [199], forming an oligomerized ring-like structure around lipid tubules [199]. Consistently, the localization of EHD2 has been shown to be restricted to the neck of caveolae. EHD2 was first thought to play a role in the scission of caveolae, but most of the studies point out to a role in stabilizing caveolae at the plasma membrane that will be further described in section II.4.2.

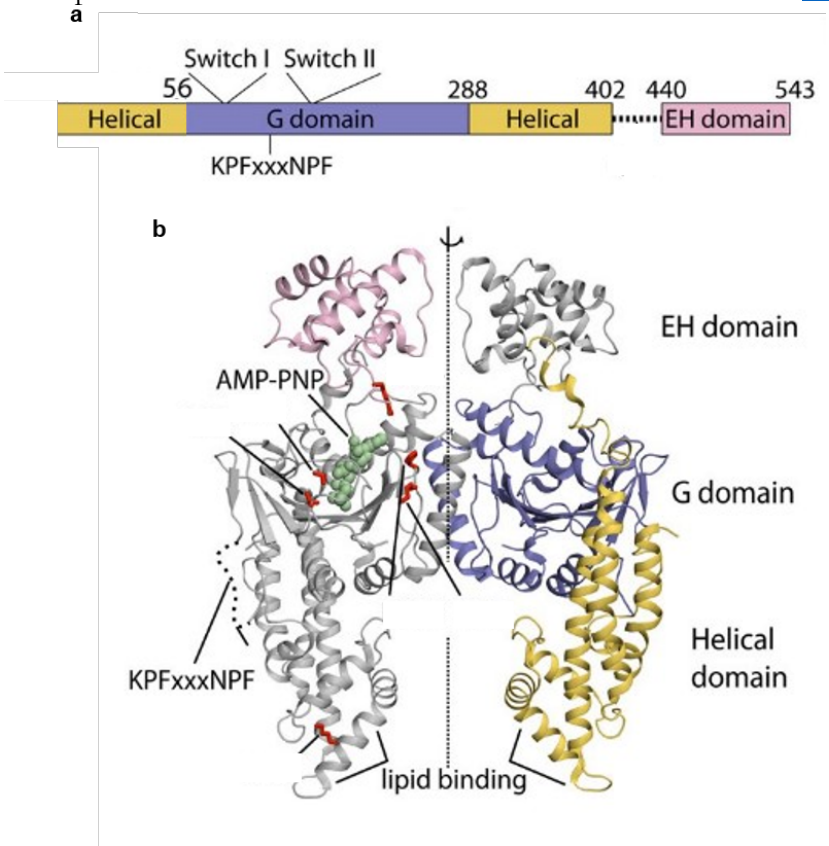

Figure 20 – The EHD2 protein family. a) EHD2 domains and structure in (b). Adapted from [10]

II.2.4 Pacsin2 and Pacsin3 structure and function in caveolae assembly

Proteins of the Pacsin/Syndapin family (56-61 kDa) are very conserved in their structure domain and sequences [200]. The Pacsin1/SyndapinI is only expressed in neurons (and will not be addressed in this manuscript), the Pacsin2/SyndapinII is ubiquitously expressed, and Pacsin3/SyndapinIII is expressed only in skeletal muscles [200]. Proteins of this family contains an F-BAR domain, an Src-homology 3 domain (SH3) spaced by a linker region that contains an NPF (asparagine-proline-phenylalanine) binding motif (Fig. 21a) [27]. Pacsins form homo-dimers, and the F-BAR domain gives to these proteins the ability to sense curvature, serving as a scaffold to induce high-curvature on membranes (Fig. 21b) [27]. The SH3 and the NPF domains allow Pacsins to bind to specific partners, like Dynamin2 and EHD2 respectively [200]. Pacsin2 and Pacsin 3 seem to be required to form caveolae, and to sculpt the membrane morphology of caveolae. The importance of Pacsin proteins for caveolae formation will be detailed in section II.4.2.

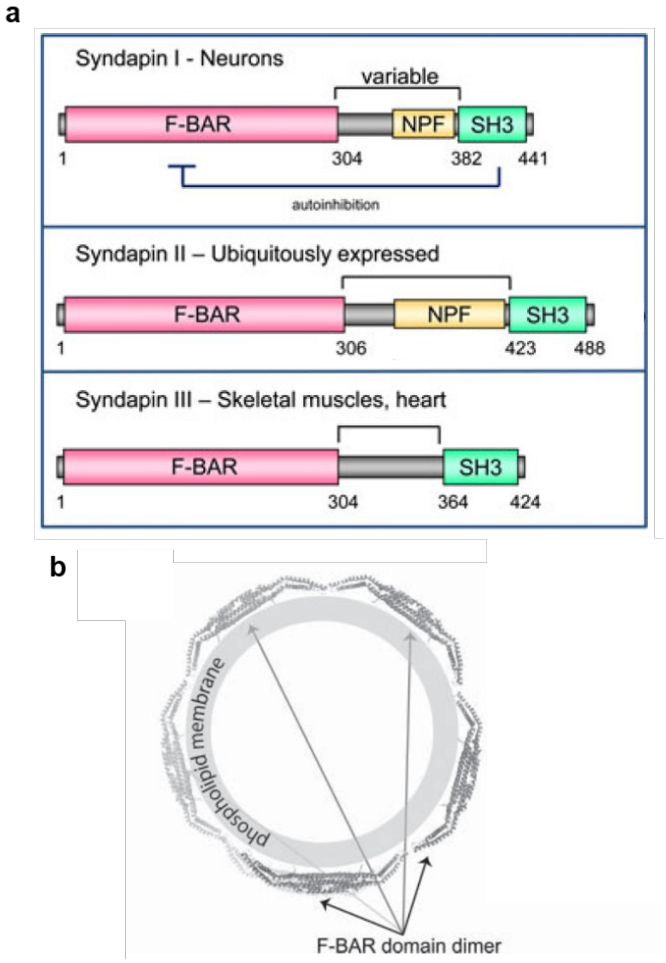

Figure 21 – The Pacsin protein family. a) Domain organization of the three Pacsin/Syndapin isoforms. b) Topology of Pacsin2 oligomers around a lipid bilayer. Adapted from [26, 27]

II.3 **The distinct lipid composition of caveolae**

Caveolae have a characteristic lipid composition, likely representing a specialized lipid domain at the plasma membrane [13]. Quantitative lipid analyses of purified caveolae vesicles from primary rat adipocytes showed a significant enrichment of sphingomyelin and cholesterol, of 2- and 3-fold, respectively, when compared to the surrounding plasma membrane [201]. Glycerophospholipids were also present, notably the ganglioside GM3 and GD3. This specific lipid enrichment could be, on the one hand, due to the fact that the caveolae proteins have lipid binding motifs, such as CAV1 which interacts with cholesterol, and Cavin1 with PI(4,5)P2 and phosphatidylserine (PS) [175, 202, 203]. Thus, the clustering of these proteins when caveolae assemble at the plasma membrane could drive lipid rearrangement. On the other hand, it has also been proposed that the different curvatures present in a caveolae pit may induce a preferential accumulation of lipids with a specific molecular shape to accommodate these curvature changes [25].

CAV1 binds directly to cholesterol, as mentioned in section II.2, and one caveola can bear up to 22.000 molecules of cholesterol as quantified in [201]. Cholesterol and CAV1/caveolae localization at the plasma membrane seem to be tightly regulated. Depletion of cholesterol using inhibitors (nystatin or methyl-ß-cyclodextrin) flattens caveolae (Fig. 22) [151] and disperses CAV1 at the plasma membrane, as shown by freeze fracture immunolabeling of CAV1 [204].

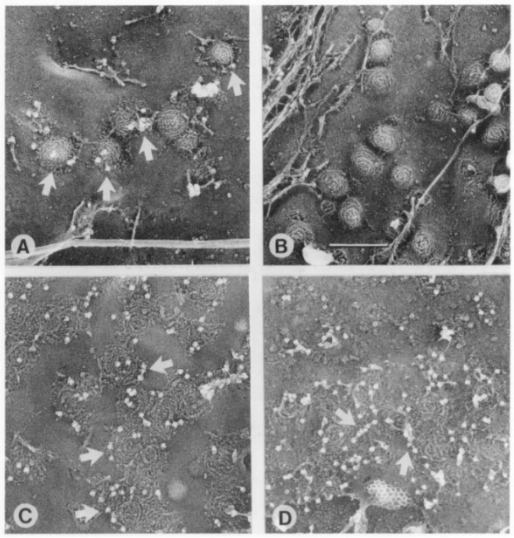

Figure 22 - Effect of cholesterol drug inhibition in cells. a-b) Deep-etched EM shows budded caveolae (white arrows). c-d) Caveolae are lost after cholesterol inhibition. Adapted from Rothberg 1992.

Conversely, the localization of cholesterol in the Golgi and at the plasma membrane depends on CAV1 expression [205, 206]. Caveolae may also be involved in regulating lipid trafficking, since depletion of CAV1 causes a mis-sorting of internalized glycosphingolipid to late endosomes or lysosomes to accumulate there. In addition, *Shvets et al.* showed that upon loss of CAV1 a pool of dehydroergoesterol, an analogue of cholesterol, accumulates in lysosomes along with glycosphingolipids [207]. Furthermore, addition of glycosphingolipids and cholesterol to the cells was shown to stimulate caveolae budding from the plasma membrane in adipocytes, as further described in section II.4.3

The scaffolding domain of CAV1 bears 3 cationic residues that are able to interact with negatively charged headgroups of PI(4,5)P2 and PS, via electrostatic interactions. Interestingly, *in vitro* studies in large unilamellar vesicles, showed that CAV1 peptides corresponding to the scaffolding region (residue 82-101) are able to induce the formation of membrane domains enriched in PS, PI(4,5)P2 and cholesterol. As mentioned earlier, this suggests that CAV1 can rearrange lipid domains on bilayer. Like CAV1, Cavin1 proteins also bind to lipids, as stated in section II.2, namely PI(4,5)P2 and PS. Indeed, depletion of PS leads to the loss of caveolae at the plasma membrane shown by electron microscopy [203]. In addition, pharmacological induction of PS scrambling at the plasma membrane inhibits the formation of caveolae since it drastically decreases CAV1-GFP puncta at this location and the remaining ones are more diffusive [203]. This suggests an important function of PS in the formation and lipid clustering of caveolae. This is not the case for the Cavin1 binding to PI(4,5)P2 since it has been proposed that this interaction is not essential for caveolae formation, serving rather as a sensor of Cavin1 membrane association. Indeed, the Cavin1 binding site to PI(4,5)P2 contains lysine residues that can be ubiquitinated and target Cavin1 for proteasomal degradation [191, 208]. Thus, when Cavin1 is bound to the membrane via PI(4,5)P2, the ubiquitination site is not accessible. Once Cavin1 is released from the plasma membrane, it is quickly ubiquitinated and targeted for degradation. These data suggest a mechanism to regulate the amount of cytosolic versus caveolae-associated Cavin1.

While it is clear that the caveolae formation depends on the localization of specific lipids, the presence of certain lipids at the plasma membrane may also halt caveolae formation. For instance, in endothelial cells of the central nervous system, little transcytosis occurs, a phenomenon that helps maintaining the impermeability of the blood brain barrier. In these cells, caveolae are almost absent. Interestingly, it has been shown that endothelial cells at the blood brain barrier are rich in fatty-acid containing phospholipids, which inhibits caveolae formation [209]. Indeed, depletion of the lipid transporter Msfd2a that transports

fatty acids into the brain, leads to the appearance of caveolae and blood brain barrier permeability.

The lipid composition of caveolae affects also the balance of caveolae connected or scissed from the plasma membrane, as it will be described in the section II.4.

Altogether, these findings indicate a tight coupling between caveolae proteins and specific lipids in the assembly and dynamics of caveolae. In the next section, I will explain how this assembly occurs.

II.4 **Caveolae biogenesis and dynamic behaviour at the plasma membrane**

II.4.1 CAV1 synthesis and trafficking to the plasma membrane

CAV1 is synthesized in the endoplasmic reticulum, and the CAV1 monomers oligomerize there into 14-16 CAV1 complexes that may correspond to 8S complexes (Fig. 23) [177, 178]. It has been shown that these oligomers are important for subsequent caveolae assembly, since CAV1 mutants, which cannot oligomerize are not able to form caveolae [210]. These oligomers are next transported to the Golgi via a COP-II-dependent pathway [190]. At the Golgi, the preassembled 8S complexes will further oligomerize into 70S units (containing ~ 140-160 molecules of CAV1) that are enriched in cholesterol [190]. This corresponds to a the steady-state pool of CAV1 at the Golgi. Maturation of the CAV1 oligomers in the Golgi seems to depend on cholesterol since its depletion inhibits the exit of CAV1-containing vesicles from the Golgi, and conversely its overexpression accelerates this process. These Golgi cholesterol-rich membranes containing CAV1 70S oligomers are then targeted to the plasma membrane [190].

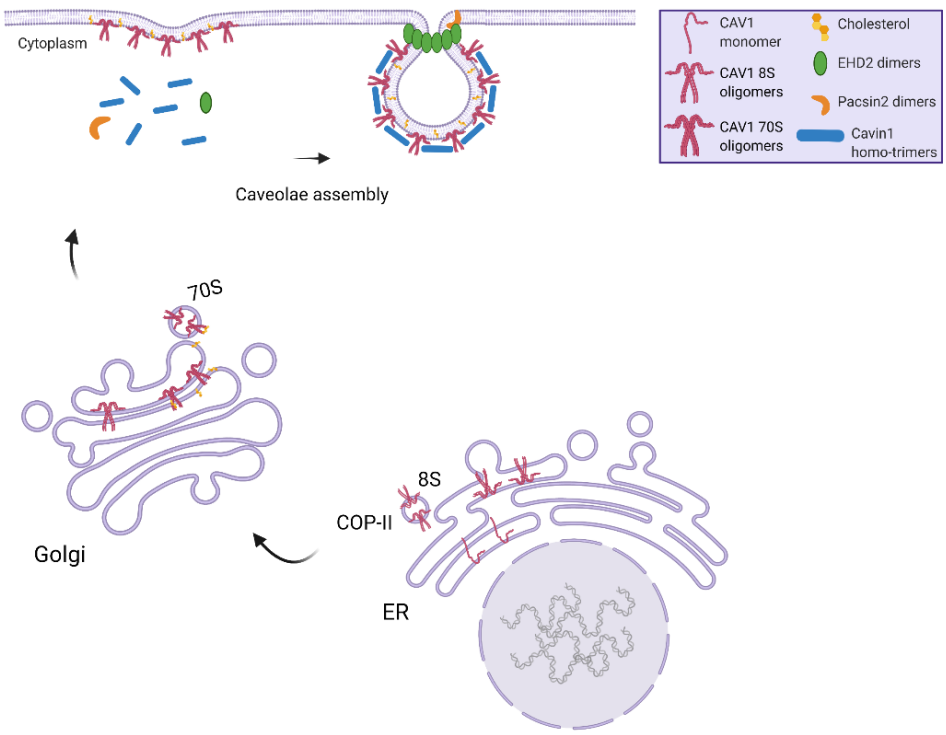

Figure 23 – Biogenesis of caveolae: (1) Trafficking of CAV1 and cholesterol to the plasma membrane, (2) recruitment of caveolae proteins, (3) assembly of caveolae

Upon insertion of the CAV1 vesicles at plasma membrane, the CAV1 oligomers do not disperse in the plasma membrane but rather form a domain where lipids can be clustered [210]. At this stage, Cavins, EHD2, Pacsins can be recruited to the CAV1 domains at the plasma membrane to fully assemble caveolae.

II.4.2 Caveolae assembly at the plasma membrane

The observation of a striated coat around caveolae using EM and X-Ray crystallography has suggested that Cavins may be responsible for the organization this structure, rather than Caveolin oligomers as initially proposed. Unroofing of cells for deep-etched microscopy reveals the different topology states of caveolae, from flat to fully budded. One caveola is estimated to contain 150-200 CAV1 monomers and 50-60 Cavins (~15-20 trimers) [194, 211-213].

Recruitment of Cavins to the plasma membrane to form caveolae was thought to occur through CAV1 but it may be, in fact, be recruited via PS [166, 193, 194]. Actually, Cavin1 purified 60 S complexes can induce membrane deformation in liposomes enriched in PS. It has been also shown that PS stabilizes CAV-Cavin1 interactions. Therefore, Cavin1 binding to PS can generate CAV1-PS-Cavin1 domain at the plasma membrane, that can further cluster specific lipids.

The exact mechanism of how caveolae assemble has not been formerly described, but a model has been proposed. As mentioned in section II.2.2., the Cavin molecules can form trimers via their HR1 domain [193]. Upon association with CAV1 at the plasma membrane, these trimers further oligomerize into higher-order structures that interact between them via the Cavin1 HR2 domain [13, 193, 194, 211, 214](Fig. 20b). Thus, the caveolae coat composed of Cavins and Caveolins were suggested to form a polyhedron structure (Fig. 24). In detail, CAV1 oligomers (Fig. 24a) would be located at the pentagon's face, and the Cavins would hold the structure together by aligning with the edges of the polygon covering the CAV1 oligomers [13, 194] (Fig. 24c). Indeed, Cavin1 60S complexes are shown to form polyhedron patches of protein lattices in liposomes seen by cryo-EM [194]. Similar polyhedron lattice structures (a striated coat) are observed using Cavin3-GFP 80 S complexes purified from cultured cells and visualized by cryo-EM, which revealed an overall size of 66 nm (consistent with caveola size) [211]. Apart from the importance of the HR1 and HR2 coiled coil domains to promote oligomerization of Cavins, a new study

demonstrated that the disorder domains of Cavin1 are essential to promote fuzzy electrostatic interactions with the plasma membrane, which is important for inducing membrane curvature [215]. While Cavin1 mutants lacking the DR1 (N-terminal) or DR3 (C-terminal) were not able to tubulate liposomes *in vitro,* they could bind to the membrane, suggesting that the disorder domains are required to sculpt membranes. In addition, the authors showed that DR1 and DR3 are required to form caveolae, and that the C-terminal disorder domain is required for Cavin1 co-localization with CAV1. Altogether, these findings improved the caveolae assembly model, where the coiled coil positive HR1 and HR2 domains bind to the lipid bilayer, while the negatively charged disorder domains are electrostatically repulsed to the outside and can interact with the membrane, thus promoting membrane curvature and interaction with CAV1.

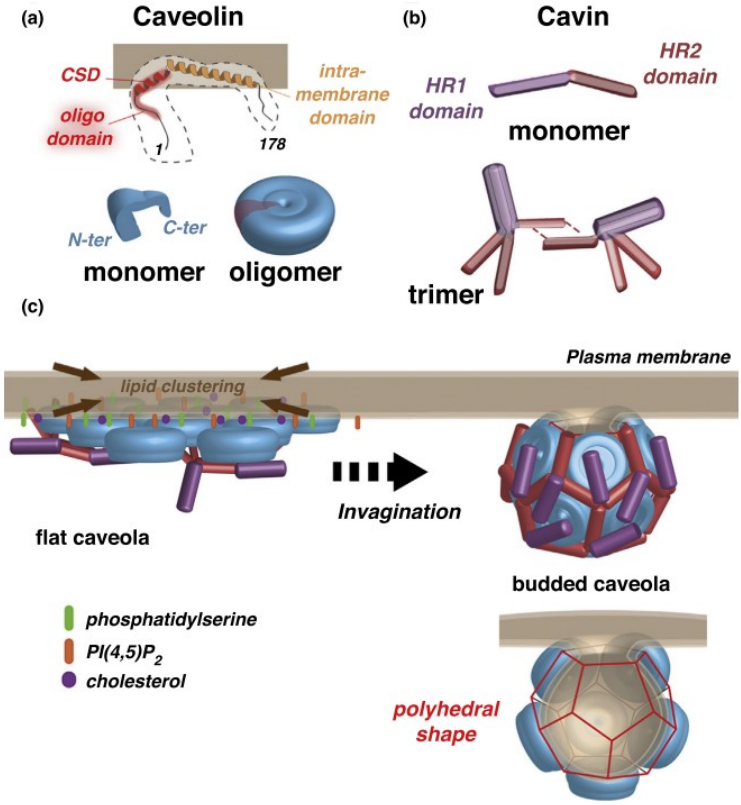

Figure 24 – Schematic model of caveolae assembly. a) CAV1 structure and oligomerization same as in Fig. 18b) Cavin1 monomer and oligomerization, same as in Fig. 19b. c) Proposed model for caveolae assembly. Adapted from [13]

Fully mature caveolae require the recruitment of Pacsins and EHD2, which regulate both caveolae dynamics and morphology. Pacsin2 partially co-localizes with CAV1 at the plasma membrane and may help the formation of *bona-fide* caveolae [167, 168] since its

depletion leads to a large decrease in caveolae in cultured cell lines, HeLa and NIH 3T3 [167]. The authors performed immunogold EM showing that Pacsin2 localizes in the bulb and /or neck of caveolae. In addition, loss of Pacsin2 leads to the formation of morphologically abnormal CAV1-associated plasma membrane invaginations [168]. Mechanistically, the F-BAR domain of Pacsin1 is sufficient to co-localize with CAV1, and the F-BAR domain co-immunoprecipitates with CAV1 (N-terminal) [168]. In addition, the Pacsin2 SH3 domain binds Dynamin2. Similarly, the muscle-specific isoform Pacsin3 seems to be important for caveolae formation [165]. Pacsin3 knocked-out mice showed loss of deep invaginated caveolae pits in cardiomyocytes [169]. Despite the loss of deep caveolae, the density of CAV3 at the plasma membrane remained the same, and, strikingly, Cavin1 formed more clusters at the plasma membrane, shown with electron immunogold labelling of freeze-fractured cardiomyocytes. These findings suggest that Pacsins and its membrane-sculpting F-BAR domain could facilitate caveolae formation by inducing curvature at the membrane.

EHD2 is recruited to the neck of caveolae, where ATP binding allows the insertion of EHD2 into the plasma membrane and oligomerization [216]. By doing so, EHD2 has been proposed to stabilize caveolae at the plasma membrane [10, 163, 173, 217]. Indeed, the depletion of EHD2 leads to more motile CAV1-GFP dots at the plasma membrane [170]. Consistently, CAV1-GFP recovery after bleaching was much faster in EHD2 depleted cells. In fact, EHD2-GFP itself undergoes fast dynamic exchange (half-life 3 min) in bleaching experiments, while Cavin1-GFP recovery is very slow (<20% recovery in 12 min) in normal conditions. Furthermore, it has been shown that loss of EHD2 does not lead to caveolae disappearance, but altered neck morphology. Finally, depletion of EHD2 leads to more fission events of caveolae from the plasma membrane, accompanied by more dynamic and short-lived caveolae [10]. Altogether, these data suggest that EHD2 helps stabilizing caveolae at the plasma membrane, and that Cavin1 is tightly associated to caveolae. In terms of binding partners in caveolae, EHD2 interacts with Cavin1 by co-immunoprecipitation, and the EH domain of EHD2 directly binds to NPF binding pocket of Pacsin2 [10]. It is noteworthy that when EHD2 is depleted, the homologues EHD1 and EHD4 can associate with caveolae to compensate for the EHD2 loss [217]. Consistently, loss of these 3 EHDs does not lead to the loss of caveolae but alters their morphology, and strikingly decreases the number of rosettes found in the cells. Altogether, this suggests that EHDs are also important in the stabilization of these high-order assembly of caveolae.

II.4.3 Caveolae disassembly and scission

Assembled caveolae at the plasma membrane can be short-lived (~20s) or long-lived (>100s) [218]. Caveolae can bud-off the plasma membrane to form an endocytic vesicle (Fig. 25) [171]. Fission of caveolae has been suggested to occur via the GTPase Dynamin2, as in clathrin mediated endocytosis. Dynamin2 localizes at the neck of caveolae and is recruited by Pacsin2. Even though the clear recruitment, assembly and role of Dynamin2 in caveolae has not been clarified, knock down or inhibition of Dynamin (using Dynasore) or overexpression of the GTPase mutant K44A, leads to immobilization of caveolae at the plasma membrane [172, 218-220]. Since EHD2 stabilizes caveolae at the plasma membrane, it was proposed that for fission to occur, it has to be replaced by Dynamin2 at the neck [221]. In addition, depletion of Cavin3 increases the number of stable caveolae at the plasma membrane and leads to the loss of highly dynamic caveolae [222]. Thus, Cavin3 is also key regulator of caveolae dynamics.

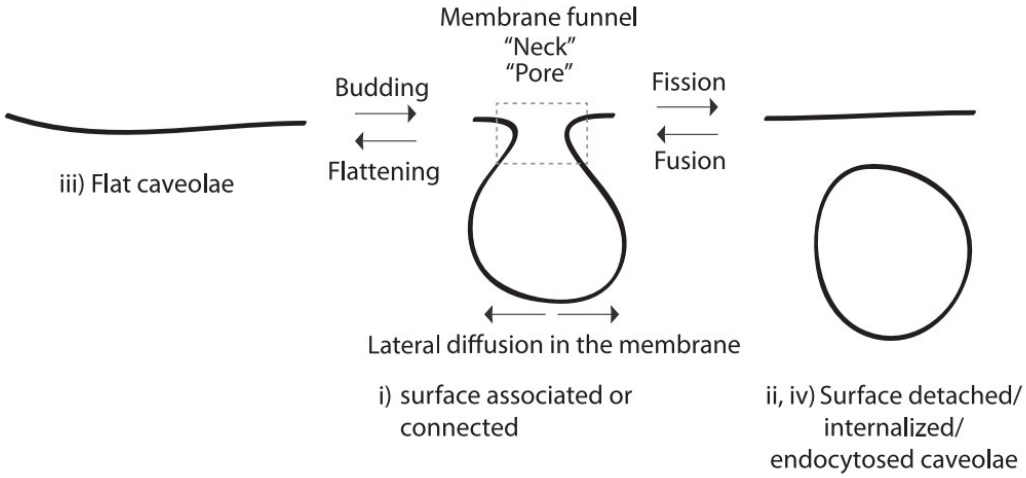

Figure 25 – Schematic of the dynamic behaviour of caveolae. Transition in between flat, Ω-shaped and scissioned caveolae as well as lateral diffusion of caveolae is depicted by arrows. i–iv correlates to the states of caveolae. From [22]

Besides proteins, lipids may also play a role in regulating the dynamics of caveolae at the plasma membrane. Recently, the Lundmark lab has demonstrated a mechanistic link between caveolae and their ability to sense lipid composition at the plasma membrane, showing that the concentration of certain lipids may induce caveolae scission. More specifically, sphingomyelin (SM) was shown to stabilize caveolae at the cell surface, while the localization of cholesterol and glycosphingolipids promotes caveolae scission [22]. Interestingly, these scission events could be counteracted by EHD2.

When fully invaginated caveolae disassemble, they release Cavins and EHD2 into the cytosol, whereas CAV1 stays "freely" at the plasma membrane. Cavins can undergo subsequent proteasomal degradation (see section II.3), whereas EHD2 can be SUMOylated and translocated into the nucleus [223].

II.4.4 Caveolae localization at the plasma membrane is promoted by the actin cytoskeleton.

Trafficking of CAV1 containing vesicles to the plasma membrane, and caveolae formation seems to depend on the β1-integrin/integrin-linked kinase (ILK) signalling complex [224]. ILK null-mice display reduced numbers of caveolae by EM. In addition, CAV1 vesicles associate more with dynamic microtubules and are not able to fuse with the plasma membrane. The authors show that ILK promotes the recruitment of IQGAP1 (F-actin binding protein) and its downstream effector mDia1 to the cell cortex. This could stabilize the microtubules and allow efficient CAV1 vesicles insertion into the plasma membrane. Caveolae has been proposed to associate with actin filaments via Filamin-A localized in caveolae [225]. Other studies have shown that caveolae rosettes internalization depends on actin-binding protein filamin-1, mDia1 and Ab1 tyrosine kinase. Caveolae may be anchored to the plasma membrane to allow ERK activation. This was proposed to happen through myosin1c that co-immunoprecipitated with Cavin3, Cavin1 and CAV1 [226]. The actomyosin association with caveolae with be further detailed in the discussion.

Now that we know the molecular machinery fundamental for the caveolae formation, let's see what are the functions of caveolae.

II.5 **Caveolae functions**

II.5.1 Role of caveolae in the endocytic pathway

Fission of caveolae from the plasma membrane can form an endocytic vesicle that fuses with early-endosomes in a Rab5-dependent manner, as shown in fibroblasts [227]. Interestingly, when a caveola fuses with endosomes it forms a specific structure that maintains the caveolae signature (positive for Cavin1 and CAV1). This domain can be recycled from the endosome and fuse back with the plasma membrane [213, 218]. Furthermore, in genome edited cells, caveolae have been described to colocalize with internalized cargo in transferrin-negative vesicles, in structures that are not early endosome, and are thought to be caveolae clusters detached from the plasma membrane [207].

Early studies on caveolae have proposed that several proteins and infectious agents could be endocytosed via caveolae. However, subsequent works showed that internalization of these agents rarely depended on caveolae. This is the case, for example, for the simian virus 40 (SV40) and cholera toxin that were thought to be endocytosed via caveolae. However, loss of caveolae does not impair these pathogens or toxins from entering, and in the case of SV40 it was even better internalized [25]. During the cell cycle, caveolae internalization and recycling is regulated. In metaphase, caveolae are mainly internalized and re-appear at the plasma membrane during cytokinesis [218], as further discussed in section II.7. So far, no cargo has been found to be specifically internalized in caveolae-dependent way. Thus, scission and recycling of caveolae from the plasma membrane may act as a regulatory mechanism to fine tune caveolae density, rather than acting as an endocytic carrier such as clathrin coated vesicles.

II.5.2 Role of Caveolae in mechanosensing and mechanoprotection

Caveolae have the unique ability to flatten out, which has been proposed to regulate membrane tension in the cells. The idea that caveolae could provide extra membrane in muscles had been proposed in the 1970s in a study where muscle fibres from frogs were extremely stretched and the caveolae neck opening was observed using freeze-fracture EM. [228]. A similar study performed *in vitro* in the smooth muscle cells of the of the sea slug *A. californica* reported as well the flattening of caveolae upon stretching of the cells, using freeze fracture EM [229]. This hypothesis was revisited in cultured cells and *in vivo,* and a more

detailed mechanism was proposed [20, 230]. The Lamaze Lab described in 2011 that caveolae flatten out upon mechanical stretch or hypo-osmotic shock to buffer the sudden increase in membrane tension [20]. Indeed, upon a hypo-osmotic shock that increased by 35% the cell volume, the number of caveolae at the plasma membrane decreased, as shown by cryo-EM. This was concomitant with the loss of co-localization of tagged CAV1-Cavin1 at the plasma membrane. Furthermore, following hypo-osmotic shock, deep-etch EM of unroofed cells showed several structures with loose striated coat reminiscent of caveolae (Fig. 26). After iso-osmolarity recovery, these "flattened" structures recovered to budded caveolae. In addition, it was found that the disassembly of caveolae releases Cavin1 and CAV1 to the cytosol. This mechanism is ATP- and actin-independent [20]. This suggests a mechanism of rapid disassembly of caveolae when the cell needs to cope with mechanical stress. Recovery of budded caveolae at the plasma membrane however may not occur in the same way, since it is ATP- and actin-dependent [20].

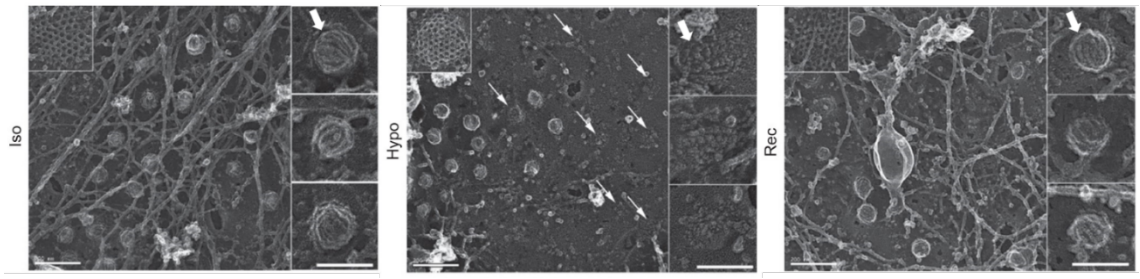

Figure 26 – Caveolae disassembly and recovery after hypo-osmotic shock. Deep-etched EM images of MLEC cells under iso-osmotic, hypo-osmotic and recovered iso-osmotic conditions. Scale bar, 200 nm. Upper left insets depict representative images of clathrin-coated pits. Right images show representative images of caveolae. Scale bars (insets), 100 nm. From [20].

Caveolae flattening upon mechanical stress has been described in fibroblasts, endothelia, skeletal muscle, cardiomyocytes *in vitro* and in zebrafish *in vivo* [13]. In particular, deleting the Cavin1 homologue in zebrafish, leads to notochord (a structure rich in caveolae that serves as scaffold for formation of the vertebrate spine during development) lesions characterized by cells that are necrotic, damaged and membrane permeable [231]. In addition, inducing increased mechanical stress in the notochord leads to an increase in the number of severe lesions in this tissue. Similar studies in which cells are imposed to a physical challenge have commonly shown that the lack of caveolae leads to damages in the plasma membrane or to membrane rupture. This indicates a role for caveolae in the preservation of the plasma membrane integrity and in the mechanoprotection of the cell. In agreement with this is the fact that cells that show abundant caveolae, such as adipocytes, endothelial and muscle cells

are frequently exposed to mechanical stresses: endothelial cells are exposed to shear stress caused by the blood flow; muscle cells undergo repeated cycles of elongation and relaxation, and adipocytes increase their volume to store lipids [13].

II.5.3 Role of Caveolae in intracellular signalling

Caveolae have long been implicated in signalling regulation. Several signalling pathways seem to relate to caveolae through CAV1 and its potential binding partners. Indeed, several growth factors, signalling receptors, and kinases were found to be localized in caveolae and co-immunoprecipitated with CAV1 such as: eNOS (endothelial nitric oxide synthase), insulin, EGF, TGF-b, Src tyrosine kinase, H-Ras and K-Ras [183 , 232 , 233-236]. Furthermore, caveolae have been associated with mechanosignaling pathways: MAP kinase, Akt, Src Kinases, Rho and Rac GTPases. CAV1 contains the CSD motif (see section II.2.1) that binds directly to a putative corresponding Caveolin binding motif (CBM) in Caveolin binding partners: H-Ras, the Src kinase, Fyn tyrosine kinases and eNOS [13] (Fig. 27).

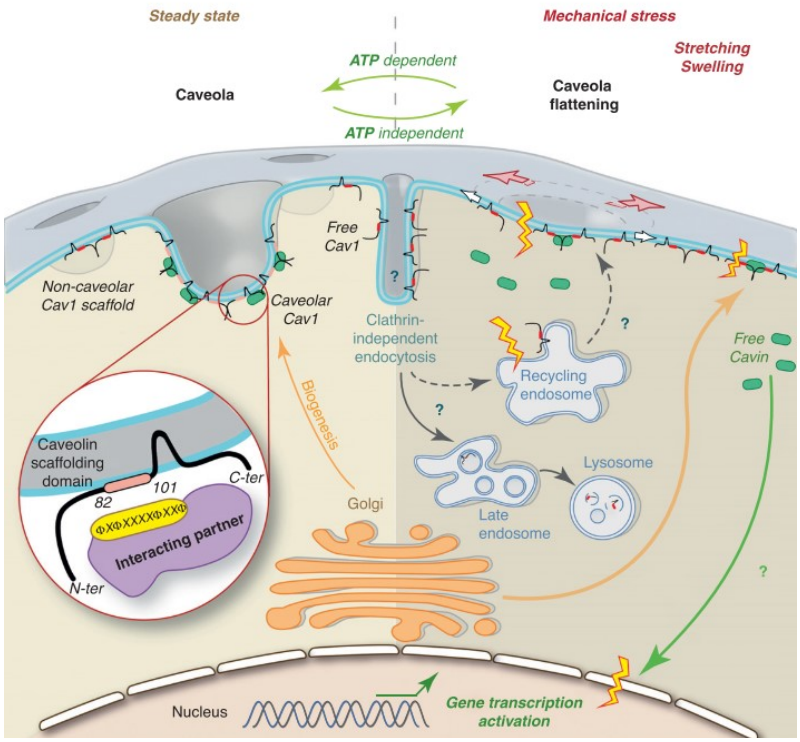

Figure 27 - Molecular and cellular consequences of caveolar flattening induced by mechanical stress. Adapted from [11]

In fact, the CSD exerts an inhibitory effect on Caveolin signalling effectors. In the case of eNOS, the binding of CAV1 through the CSD allows the phenylalanine 92 to extend its lateral chain and to reach the hydrophobic pocket of eNOS, thus inhibiting its catalytic activity [237, 238] even though the CBM might not be specific for CAV1 partners, since it can be found in species where Caveolins are not expressed (e.g. *S. cerevisae*), the CSD has been proposed to have a dynamic behaviour, being able to transit from fully helical to partly unstructured, thus likely changing its accessibility to bind other proteins. In addition, the fact that caveolae can flatten and release CAV1 freely at the plasma membrane may change its accessibility to the CSD [13].

As we have seen in the previous sections, caveolae can contribute to lipid rearrangement in the plasma membrane creating specialized lipid nanodomains. This can potentially be key for the clustering and activation of transmembrane receptors in caveolae [239]. Interestingly, this feature has been proposed to be actively regulated by the dynamic assembly/disassembly of caveolae upon mechanical stress [11, 20]. Indeed, caveolae disassembly provokes the redistribution of CAV1, sphingolipids, and the activation of c-Src at the plasma membrane [230]. In addition, loss of CAV1 leads to perturbations in Ras signalling and its spatial organization on the plasma membrane [152, 240]. This happens due to a change in the lipid composition and distribution at the plasma membrane in CAV1-depleted cell. Thus, cycling between flattened and budded caveolae leads to the exposure or the hiding of receptors, respectively, at the plasma membrane that translates into an activation or inhibition of cellular responses (*e.g.* insulin receptors, JAK/STAT pathway). Calcium pumps can also localize in caveolae and the mechanical disassembly of caveolae leads to reduced calcium responses due to changes in lipids and CAV1 localization [241, 242]. In addition, it has been recently shown that the coupling of caveolae mechanics with signalling in melanocytes (cells of the epidermis that produce melanin) is required for human skin pigmentation [243]. Loss of caveolae leads to upregulation of cAMP; shape changes in melanocytes; and impaired pigment transfer from melanocytes to keratinocytes (the most abundant cells in the epidermis). In addition, loss of CAV1 leads to membrane rupture in mechanically stressed melanocytes. This study thus underlines the capacity of caveolae to serve as molecular hubs that coordinate intercellular communication that is key to skin pigmentation and tissue homeostasis.

In addition, caveolae can act as mechanosensors that transmit mechanical-induced signals, through at least three different described mechanisms:

i. increased mechanical stress flattens caveolae, and releases EHD2 to the cytosol that can be SUMOylated and subsequently translocated into the nucleus. Here EHD2 regulates gene transcription including caveolae related genes. Accordingly, intrinsic loss of EHD2 in a breast tumour cell line impairs caveolae mechanosensing and gene transcription, which are restored upon EHD2 expression. Therefore, EHD2 might be key in mechanotransduction connecting the disassembly of caveolae with gene transcription under mechanical stress [223];
ii. disassembled caveolae releases Cavins which can potentially interact with proteins in a non-caveolar manner. A recent interactome of cytosolic Cavin1, Cavin2 and Cavin3 found 47 potential partner proteins that may lead to new Cavin roles in metabolism and stress-signalling. This led to the finding that the protein phosphatase 1 alpha (PP1α) interacts with Cavin3 in the cytosol when caveolae disassemble upon UV treatment. This interaction stimulates apoptosis via increased histone H2A phosphorylation. This study identified a pro-apoptotic signalling pathway that may depend on the mechanosensing of caveolae [244];
iii. in migrating A2780 cells, caveolae might serve as a sensor for low tension, since they are localized at the rear of the cell (area of low tension) in fast migrating cells. Caveolae here was shown to recruit the RhoA GEF Ect2 to hyperactivate RhoA. This leads to actomyosin rearrangement, which induces rear retraction and forward migration of the cells [245]

Finally, modulation of signalling in caveolae can also happen through CAV2, since it is required for the activation of the estrogen receptor and insulin signalling; and through Cavin-3 which has been reported to mediate ERK and Akt signalling [13].

II.6 **Caveolae-associated diseases**

II.6.1 Muscle dystrophy

Several forms of muscular dystrophy and cardiomyopathy are associated with mutations in the caveolae proteins CAV3, Cavin1 and Cavin4, leading to severe defects in muscle physiology [8]. As mentioned in section II.5.2., tissues that are exposed to continuous mechanical stress commonly have abundant caveolae. Therefore, mutations that lead to the impairment of the mechanoprotection function given by caveolae is also linked to several diseases, including cancers and muscle dystrophies as summarized in Table 2. Indeed, loss of caveolae due to mutations in CAV3 leads to membrane damage in myotubes [246]. Zebrafish lacking the Cavin1 homologue or overexpression of the dominant-acting CAV3, increases plasma membrane damage [231]. In addition, increased mechanosensitive defects due to loss of caveolae are associated with damages in the sarcolemma, as well as with membrane rupture in endothelial cells during increased cardiac output.

Pathology	Caveola disorders
Cancers	Decreased Cav1 and Cavin-1 in breast tumors; increased or decreased Cav1 in breast cancer stroma; increased Cav1 in prostate tumors; loss of Cav1 from prostate cancer stroma
Muscular dystrophies: Limb Girdle Muscular Dystrophy (LGMD), Rippling Muscle Disease (RMD), Distal Myopathy (DM), Familial HyperCKemia (FHCK), Duchenne Muscular Dystrophy (DMD)	Thirty human Cav3 mutations identified in MDs; decreased Cav3 in LGMD1-C, FHCK, RMD and DM; increased Cav3 in DMD; Cav3 mislocalization in LGMD (dysferlin mutants); two reported Cavin-1 mutations
Lipodystrophies	Cavin-1 and Cav1 mutations; absence of Cav1 expression
Pulmonary hypertension in chronic obstructive pulmonary disease (COPD)	Increased Cav1 in endothelial and medial smooth muscle cells
Bladder smooth muscle hypertrophy	Decreased Cav1

Table 2 - Table summarizing human pathologies that could be linked to impaired caveola-dependent mechanoresponse. Adapted from [11]

II.6.2 Lipodystrophy

In 2008, the first patients discovered with total loss of caveolae due to mutations in CAV1 displayed severe lipodystrophy and hypertriglyceridemia [247-249]. Patients lacking Cavin1 also display lipodystrophy (and loss of caveolae in muscles) [250];Ardissone, 2013 #4571}. Cavin1 and CAV1 deletion in mice leads to similar lipodystrophy defects, meaning a striking loss of fat mass, small adipocytes, as well as high levels of fatty acids triglycerides

in the blood [161, 251]. This is due to the loss of caveolae-dependent lipid storage capacity by adipocytes, since even under high fat acid diet mice lacking caveolae stay lean. On the other hand, since CAV1 localizes at the plasma membrane of adipocytes and lipid droplets (where lipids are stored), the depletion of CAV1 affects lipid uptake/caveolae-dependent signalling and lipid droplet composition. In addition, CAV1 null mice are insulin resistant. Finally, Cavin1 has been shown to directly regulate both lipolysis and ribosome synthesis, which is required for adipocyte maturation. Interestingly, EHD2 null mice show increased lipid droplets' size and fat tissue, as well as augmented fatty acid uptake, in a caveolae-dependent manner [252]. In addition, in obese patients and mouse models, EHD2 expression was found to be down-regulated. Hence, the negative regulation of caveolae in adipocytes by EHD2 is required for regulating lipid storage and fatty acids uptake.

II.6.3 Cancer

The role of caveolae in cancer seems to be complex, since CAV1 has been described as a tumour suppressor but also as an oncogene [253]. The effect of CAV1 on tumours may depend on the type and stage of the cancer and could be linked with altered regulation of pathways involving CAV1 [254]. Early stages of tumour progression are associated with low CAV1 expression, whereas CAV1 is overexpressed in advanced cancer stages and metastasis. During tumour development, cells can be exposed to many different forces in their microenvironment, be it compressive, tensile, fluid shear stress or hydrostatic pressure. In recent years, more evidence shows that alterations in the tissue and cell mechanics may alter tumour progression [255]. It has been proposed that this biphasic expression of CAV1 could be modulated by the mechanosensing properties of caveolae in response to the microenvironment of the tumour (Fig. 28) [7]. This model proposed for carcinomas states that while the carcinoma is still "in situ", confined by the basal membrane cells, the cells can respond to mechanical stress due to the caveolae flattening and budding at the plasma membrane [7] (Fig 28). Then, in invasive carcinomas, the cells break the basal membrane and tumour cells are stiffer. Therefore, these metastatic cells become exposed to the mechanical forces of the extracellular matrix. This may alter the caveolae mechanosensing response and impair CAV1 dependent mechano-signalling, hence promoting migration and metastasis.

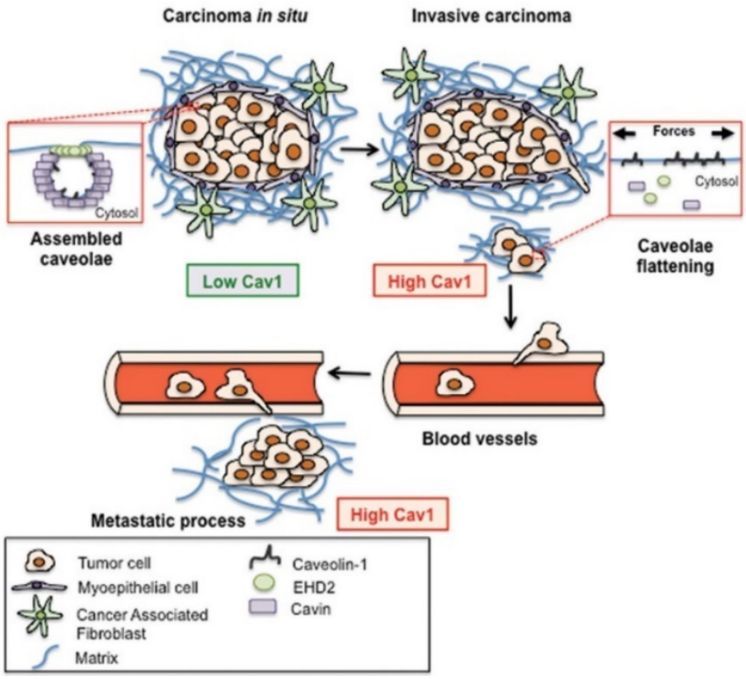

Figure 28 - Potential role of caveolae in tumour progression. Adapted from [7].

II.7 **What is known about caveolae in cell division?**

The first report of Caveolin protein in dividing cells happened 20 years ago. CAV1 proteins were found to be enriched in Zebrafish blastomeres, as shown by immunofluorescence (Fig. 29b) and in MDCK II diving cells using time-lapse video microscopy and fluorescently tagged α-/β-CAV1 (Fig. 29a). However, no functional studies were reported in these articles.

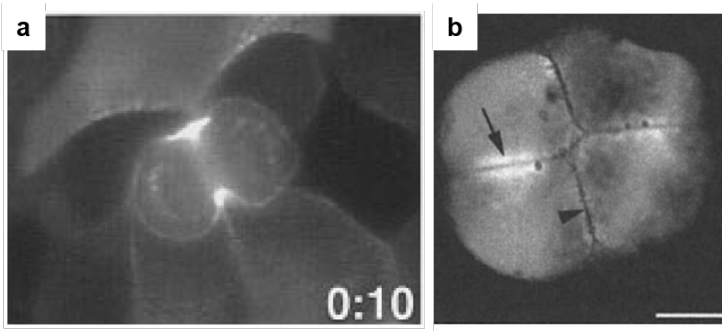

Figure 29 – Localization of Caveolins in ingressing furrows. a) α-CAV1-GFP localization in MDCK II cells 10 min after mitotic round-up. b) Zebrafish blastomeres immunostained with pan-Caveolin antibody recognizing the CAV1, CAV2 and CAV3. Note that the Caveolin labelling occurs mostly at older furrows (arrow) rather than in earlier furrows (arrowhead) *in vivo*. From [2, 3]

In 2011 *Boucrot et al.,* described that CAV1-GFP undergoes massive internalization at the onset of mitosis (Fig. 30a) [218]. Specifically, the authors described that the number of "arrivals" vs "departures" of CAV1-GFP at the plasma membrane is decreased in metaphase (internalization) and is increased in anaphase (re-appearance at the plasma membrane). This has been shown by following CAV1-GFP puncta at the plasma membrane during from interphase to anaphase using live-cell imaging (Fig. 30a) and quantification of the number of CAV1-GFP puncta/caveolae at the plasma membrane using TIRF microscopy (Fig. 30b). Again, a potential functional role of caveolae and caveolae recycling has not been investigated in this paper.

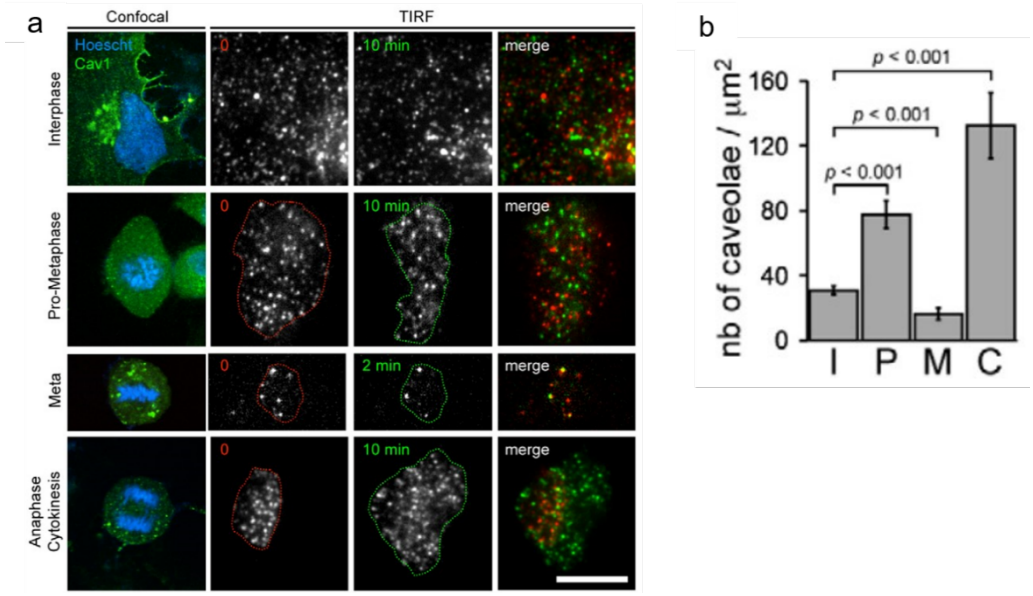

Figure 30 - Representative still TIRF images acquired every 10 min at the plasma membrane of BSC1 cells stably expressing Cav1–EGFP. The cells were in interphase, rounding-up phase (pro-metaphase), metaphase and membrane recovery phase during daughter cell formation (anaphase–cytokinesis), as illustrated by confocal images on the first column. DNA was stained using the membrane- permeant dye Hoechst 33342. Note also that only one of the two daughter cells was followed in this capture. To emphasize the dynamics of most of the Cav1–EGFP structures during all stages of the cell cycle, the first image '0' was colored in red and the last 10 min (2 min for metaphase) in green in the overlay panel. To facilitate comparisons, we used here for interphase the same capture than in Fig. 1B. The full time-series of the interphase and cytokinesis cell are visible in supplementary material Movies 1 and 2, respectively. Scale bar: 10 µm. (B) Surface density of Cav1–EGFP-containing structures at the plasma membrane during interphase (I), pro-metaphase (P), metaphase (M) and cytokinesis (C). From [218]

In a more recent study, CAV1 was proposed to translate the adhesion geometry of the cell to the spindle orientation during mitotic round-up (Fig. 31) [24]. The authors showed that the cell division axis correlates with cellular edge retraction, and CAV1 localizes at the cortical region of retracted fibres. The localization of CAV1 at this location is dependent on RhoA, Ect2 and diaphanous mDia1, since the depletion of these proteins impairs the enrichment of CAV1 at the cell cortex. In addition, the depletion of β1-integrin suppressed the cortical localization of CAV1 in pro-meta/metaphase cells, albeit having a minor effect on the expression of caveolin-1 protein. The fact that CAV1 localizes in the cortical region leads to the targeting of the complex Gαi1–LGN–NuMA (which regulates spindle orientation) to guide the spindle positioning. Indeed, depletion of CAV1 impairs correct spindle orientation.

In addition, budded caveolae localize at the cortex near the retracted fibres in GFP-CAV1 cells as seen by EM. Altogether these data suggest that CAV1 at the plasma membrane may provide a link between the interphase adhesion geometry to the mitotic spindle orientation. However, whether this is a CAV1-dependent or caveolae associated mechanism remains to be investigated.

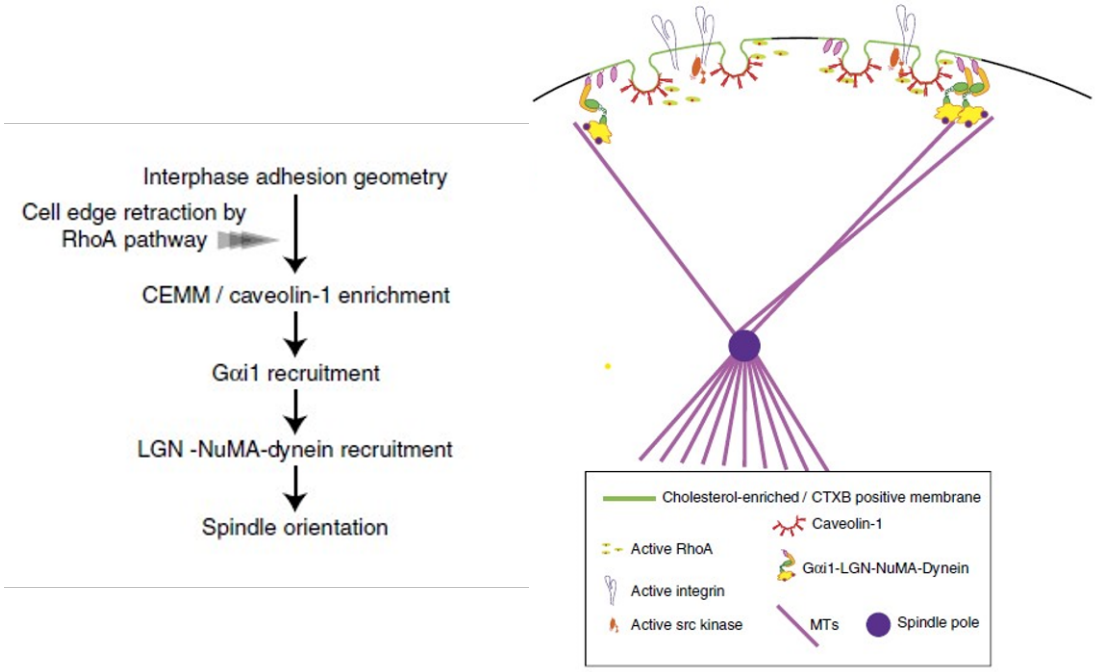

Figure 31 - A model for the mechanisms that translate interphase adhesion geometry to the mitotic spindle orientation. The translation starts at the onset of mitotic cell rounding, when the heterogeneity of interphase adhesion geometry leads to anisotropic activation of RhoA. The regions with high RhoA activation rapidly retract the cell edge, and generate the caveolin-1-associated CEMM at the proximal end of retraction fibres. Gai1 is preferentially localized within the CEMM that guides the Gai1 cortical crescent to the proximal end of the retraction fibres. Consequently, Gai1/LGN/NuMA complexes direct the spindle axis towards the cortex enriched with retraction fibres. Adapted from [24]

Chapter III: The intercellular bridge is under tension

III.1 **General considerations about membrane tension and cortical tension**

The plasma membrane of mammalian cells is composed of a lipid bilayer and (glycol)proteins, and defines the limit between the cell and the extracellular space. It holds together the cellular contents and can accommodate size and shape changes of the cell. In addition, it allows the cell to interact with the environment [256]. Importantly, the plasma membrane is linked to the intracellular cytoskeleton. Thus, any mechanical stress at the plasma membrane will induce changes in the underlaying cytoskeleton. Conversely, changes in the cytoskeleton architecture subject the plasma membrane to mechanical stress, such as in during cell shape changes. Thus it is important to take into account the mechanical properties that characterize the cell membrane, such as the membrane bending stiffness, k, and the membrane tension σ [256].

The **membrane tension** is the force needed to stretch a lipid bilayer [256]. The plasma membrane tension has two components: the in-plane tension of the lipid bilayer and the adhesion energy between the membrane and the underlying, cortical cytoskeleton [11]. Typically, this tension is in the order of a hundred pN μm^{-1} [256]. Indeed, the cell cortex is linked to the plasma membrane via molecular linkers, such as proteins of the ERM family (Ezrin, Radixin, Moesin) that bind both the actin cytoskeleton (directly) and the plasma membrane (indirectly). The cell membrane tension depends on the area of the membrane relative to the cell volume. Increasing the surface area of the lipid bilayer, such as during cell adhesion to the substate or hypo-osmotic shock treatment (which provokes the swelling of the cells) increases the membrane tension. Conversely, the de-adhesion from the substrate or hyper-osmotic shock treatment (shrinkage of the cell) lowers the membrane tension. In addition, membrane tension can be modulated by the lipid composition of the membrane, the lipid's shape and the density of membrane-associated proteins [257]. Until recently, membrane tension was thought to spread rapidly across the cell, but it seems that the cytoskeleton resists to membrane flow. Thus, along the membrane surface the cell can locally bear different membrane "tensions". Notably, membrane tension is important for a variety

of cell functions such as cell migration, division and spreading; endocytosis and exocytosis; membrane repair and osmoregulation.

The cell cortex comprises a network of myosin II, actin filaments (branched and unbranched) and actin-binding proteins localized below the plasma membrane. **Cortical tension** is the tension of the actomyosin network that arises from the motor activity of the myosin II filaments [258]. This renders the network contractile, hence the higher the myosin II activity the higher the cortical tension. Changes in the molecular composition, as well as in the organization and dynamics of the actomyosin II network modulate cortical tension. Cell shape changes depend on the actomyosin cortex, such as during mitotic cell rounding; furrow ingression during cytokinesis; cell body retraction during migration, as well as apical constriction in epithelial cells during morphogenesis [257]. For instance, cortical tension can trigger, during anaphase, the accumulation of actomyosin II at the cell equator [259]. This accumulation leads to a local increase in cortical tension, 3 folds higher than in the cell poles, which is required for efficient cytokinetic furrow ingression [260]. In the cases where the plasma membrane moves away from the cortex, the cytoskeleton-plasma membrane linkers, such as the ERMs, are under tension to hold both structures together. Distinguishing the cortical tension from the membrane tension is not straightforward and it has been proved to be experimentally challenging to develop methods enabling to measure the in-plane tension separately from pure cortical tension. Thus, one may rather consider the **cell tension** that takes into account both the cortical tension and the membrane tension and which is more easily accessible experimentally. The cell tension is thus the sum of the membrane and cortical tensions ($\sigma_{cell} = \sigma_{membrane} + \sigma_{cortex}$), and it has been shown that both tensions counteract the large-scale cellular deformations [256].

The intricate relationship between the cell cortex and the plasma membrane leads to a mutual response. For instance, in resting neutrophils, inhibition of myosin II using blebbistatin (which thus decreases cortical tension) and increases membrane tension [261]. On the other hand, in migrating zebrafish keratinocytes and in the *Dictyostelium* during cytokinesis, artificially increasing the membrane tension by micropipette aspiration leads to a local recruitment of the actin cytoskeleton and myosin II, respectively [262, 263]. In *Dictyostelium*, Myosin II was only recruited to the tensed membrane present in the micropipette during cytokinesis and not during interphase, suggesting that this may be a specific mechanism to regulate the shape of the cells while dividing. Indeed, it has been proposed that cortex contraction regulates cell shape during cytokinesis [264]. This is of physiological importance since, for example, during development in mouse oocytes, extra-

soft cells are a common defect in the cell population that leads to early development failure [265]. Importantly, the authors showed that reducing cortical tension of the oocytes promotes aneuploidy, due to chromosome alignment defects.

III.2 **Tension release at the intercellular bridge triggers abscission**

The molecular machinery that leads to abscission has been well studied, as described in Chapter I. However, the mechanical context of this process and whether the recruitment of the abscission machinery depends on tension remains understudied. In 2011, the Piel Lab proposed that the release of tension at the intercellular bridge leads to ESCRT-III polymerization and abscission [29]. This represents an unexpected finding, since it was believed that pulling on the intercellular bridge would, on the contrary, favour membrane scission. **For which reason is the intercellular bridge under tension?** During cytokinesis, the daughter cells respread on the substrate and pull on the substrate [29]. Part of this force is transmitted to the intercellular bridge. This pulling of the daughter cells on the intercellular bridge has an inhibitory effect on abscission since the more the cells pull on it the longer abscission takes (Fig 32a).

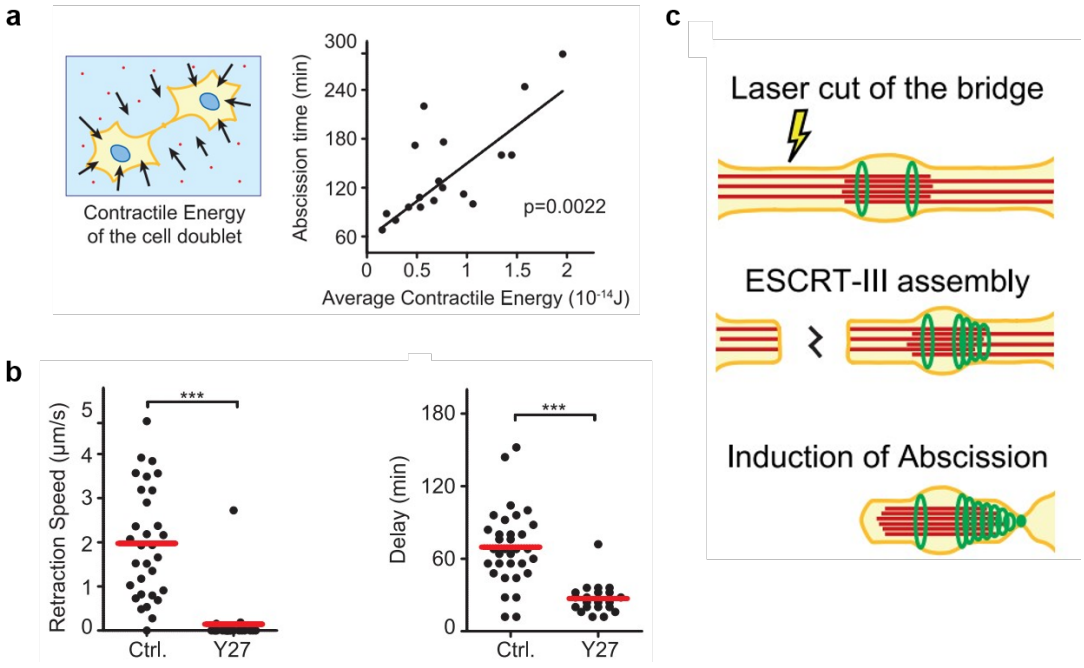

Figure 32 - Decreasing tension at the intercellular bridge triggers ESCRT-III assembly and abscission. a) Abscission time depends on the contractility of the daughter cell doublet measured by TFM. b) Left: Bridge tension (retraction speed) in control and cells treated by Y27632. Right: Delay between drug treatment and abscission in control and treated cells with Y27632. c) Proposed model: Releasing tension at the intercellular bridge triggers ESCRT-III assembly and subsequently induces abscission. Adapted from [29]}.

Indeed, combining traction force microscopy (TFM) and laser ablation of the cytokinetic bridge to measure the forces applied by the daughter cells on the substrate revealed that the intercellular bridge bears forces of around 1.4 nN. Mechanistically, the cortex contractility can pull on the bridge. It has been shown that inhibition of the ROCK kinase both decreases contractility of the daughter cells and leads to shorter abscission times. However, whether the pulling of the daughter cells on the substrate is enough to induce tension at the bridge, or whether there is preferential accumulation of the actomyosin II in areas near the bridge is not known. Furthermore, membrane tension can account for 0.4 to 0.8 pN of the forces at the intercellular bridge. This was measured using membrane tubule pulling experiments. Strikingly, the ROCK kinase inhibitor was shown to also decrease membrane tension at the intercellular bridge and the cell body in the membrane tubule pulling experiments [29].

Is tension always constant at the cytokinetic bridge? This does not seem to be the case, as it has been shown that bridges on the brink of abscission are under lower tension than average bridges [29]. In addition, incubating cells with ROCK inhibitors decreases tension at the bridge and accelerates abscission (Fig. 32b). These data suggest that abscission is triggered by a reduction of tension at the intercellular bridge.

What is the relationship between tension and the ESCRT-III machinery at the intercellular bridge? Low tension at the bridge was found to favour ESCRT-III polymerization to the abscission site [29]. Laser ablating the bridge on one side of the midbody provokes the microtubule cut (see section I.3.3.) and tension release, which induces abscission on the other side of the midbody within 25 min. Indeed, using CHMP4B-GFP cells to perform laser ablation the same experiment revealed that the ESCRT-III cone (see section I.3.1.2.) forms rapidly on the side of the midbody opposite to the cut 10 min after ablation. In addition, depletion of CHMP2A (an essential component of the ESCRT-III polymers), (see section I.3.2) does not trigger the formation of the ESCRT-III cone after ablation. This agrees with recent data in non-dividing cells showing that ESCRT-III recruitment to endosomes occurs when membrane tension is reduced [266]. It is noteworthy that ablation of the bridge before the recruitment of the ESCRT-III at the midbody leads to a transient recruitment of ESCRT-III at the midbody but without the subsequent cone formation. These results suggest that the artificial release of tension on the bridge induces abscission by promoting the assembly of the ESCRT-III helices from the midbody to the abscission sites (Fig. 32c). Altogether, these data suggest that lowering tension at the intercellular may be one of the most upstream events leading to cytokinesis conclusion.

This study provided an insightful working model for the effect of tension at the intercellular bridge. Still, many questions remain like what is the effect of high tension on other molecular machineries at the bridge, such as in F-actin, or Septins recruitment. Importantly, no protein has been described to help or regulate tension at the intercellular bridge so far.

Chapter IV: Rational and aims of the thesis

Cytokinesis is controlled by both molecular and mechanical inputs. The molecular machinery that leads to abscission has been intensely studied in last 20 years. In contrast, the importance of the mechanical regulation in of the cytokinetic cells, in particular during abscission, remains understudied. Thanks to the work of *Janvore-Laufaurie et al.*, [29] (Chapter III.2) we know that the cytokinetic bridge is under tension during cytokinesis and that abscission requires a tension relieve at the bridge. Mechanistically, tension on the bridge seems to inhibit the ESCRT-III filament assembly at the abscission sites, and thus delay abscission [29]. However, whether there are active mechanisms regulating the tension at the intercellular bridge has not been investigated and remains unknown.

The quantitative proteome of purified midbody remnants performed in the lab (the *Flemmingsome* [1]) is an opportunity to identify proteins that might be involved on the tension regulation in the post furrowing steps of cytokinesis. Unexpectedly, several proteins of caveolae were either present (CAV1, EHD2, Pacsin2) or highly enriched (Cavin1, Pacsins3) in the *Flemmingsome* of HeLa cells. Most of the functions of caveolae have been described in interphase cells (see section II.5). Importantly, in the last years, the role of caveolae in buffering plasma membrane tension and as mechanosensers has shown to be important in several cell types, *in vitro* and *in vivo*, with a role to prevent diseases in humans, such as muscle dystrophy.

Previous studies have shown that at the onset of mitosis, CAV1, a constitutive protein of caveolae (sections), is enriched at the cortical regions of the rounded cell (Chapter II.7). This localization is β1- integrin-dependent and seems to guide the spindle orientation. In addition, *Boucrot et al.,* described that caveolae are massively internalized during metaphase, and re-distributes again to the plasma membrane of the daughter cells in telophase. Finally, the CAV1 proteins were found to localize at the furrow ingression of MDCK and blastomeres (Chapter II.7). However, no specific functions of caveolae in cytokinesis have been described so far.

Thus, the main objectives of my thesis were initially the following:

- Assess the localization of the essential caveolae proteins CAV1 and Cavin1, at each step of cytokinesis, and whether budded caveolae exist at the intercellular bridge.

- Describe the dynamics of the caveolae-associated proteins during cytokinesis.

- Investigate the role of caveolae in cytokinesis by analysing the abscission time of wild type and caveolae-depleted cells.

- Test whether the role of caveolae is related to tension by analysing the impact of the loss of caveolae in the ESCRT-III localization at the intercellular bridge.

- Understand how caveolae might control tension during cytokinesis.

The main results obtained during my thesis are included in the manuscript in the Results section (article close to submission). In addition, the characterization of the Cavin1 knock-out is presented in the paper in Annex I (submitted).

Part II: Results

Manuscript:

Caveolae control intercellular tension during cytokinesis and promote successful abscission

Summary

Cytokinesis is the last step of cell division and leads to the separation of the daughter cells. Failure in cytokinesis results in the formation of genetically unstable tetraploid cells that have been shown to promotes tumorigenesis *in vivo* [267]. While dividing, the daughter cells pull on the intercellular bridge, which was shown to bear forces on the nN (nano-Newton) range. What are the consequences of the tension sensed at the intercellular bridge to cytokinesis? It has been previously shown that high tension at the bridge inhibits ESCRT-III polymerization to the abscission sites, thus delaying abscission [27]. Thus, a drop in tension is required for triggering abscission. However how tension is controlled is not known and has not been investigated.

Detection of Cavin1, CAV1, EHD2 and Pacsin2-3 in the midbody remnants proteome caught our attention, since these are well established caveolae-associated proteins. Caveolae are small plasma membrane invaginations that were shown to buffer plasma membrane tension in interphase cells. Cytokinetic cells undergo dramatic shape changes, and no function of caveolae in cell division had been described so far.

Thus, we sought out to study the potential function of caveolae in cytokinesis. First, using immunofluorescence we have observed that CAV1 and Cavin1 are localized at the ingressing furrow, at the midbody and at the bridge/cell interface, the "entry points". Further studies using EM revealed that budded caveolae are indeed localized at the midbody and entry points (manuscript Fig. 1)

Next, using live-cell imaging we have observed that Cavin1 and CAV1 dynamically colocalize at the midbody at all stages of cytokinesis (late furrow, early and late bridges). Interestingly, the Cavin1/CAV1 pool at the entry points decreases as the cells progress towards abscission. In addition, we also identified a transient CAV1/Cavin1 pool localized at the tip of the CHMP4B cone on the side of the midbody, both in the live-cell imaging studies as well as using immunofluorescence (manuscript Fig. 1 and 2)

What is the function of caveolae during abscission? To answer this question, we have used Cavin1 knock-out HeLa cells that I have generated in the lab (see characterization in Annexe I, Fig. 11). The loss of caveolae led to the following cytokinetic defects: (1) delayed abscission; (2) halted localization of ESCRT-III filaments at the abscission sites; (3) increase in binucleation (manuscript Fig. 3). The defects observed on the ESCRT-III machinery

seemed to be reminiscent of high tension at the intercellular bridge, in agreement with the study of [29].

Pursuing this hypothesis, laser ablation of the cytokinetic bridge revealed a 2-fold increase in the bridge tension in caveolae-depleted cells. Since the cortical and membrane tension are intricately connected, we investigated the architecture of the cytoskeleton. Caveolae-depleted cells revealed increased F-actin and activated myosin II (pMRLC II) levels at the entry points. In addition, in the entry points of wild type cells, caveolae and pMRLC II showed to be excluded from each other (manuscript Fig. 4).

Finally, to prove that the cytokinetic defects observed were due to the increased tension on the cytokinetic bridge, we decreased the global contractility of the cell using an inhibitor of the ROCK kinase (which phosphorylates the MRLC). Lowering the contractility in the caveolae-depleted cells diminished the levels of pMRLC at the entry points, restored normal abscission time and relocalized ESCRT-III at the abscission site (manuscript Fig. 5).

Based on these results, we propose that caveolae buffer intercellular bridge tension by limiting the cortical and membrane tension. This mechanism promotes ESCRT-III polymerization and successful abscission (manuscript Fig. 6)

Caveolae promote successful abscission

by controlling intercellular bridge tension during cytokinesis

Virginia Andrade,[1,2] Jian Bai,[1,2] Neetu Gupta-Rossi,[1] Ana Jimenez,[3] Cédric Delevoye,[4,5] Christophe Lamaze,[6] Arnaud Echard[1, *]

[1] Membrane Traffic and Cell Division Unit, Institut Pasteur, UMR3691, CNRS, 25-28 rue du Dr Roux, F-75015 Paris, France

[2] Sorbonne Université, Collège doctoral, F-75005 Paris, France

[3] Dynamics of Intracellular Organization Laboratory, Institut Curie, PSL Research University, CNRS UMR 144, Sorbonne Université, 75005 Paris, France

[4] Institut Curie, PSL Research University, CNRS, UMR144, Structure and Membrane Compartments, 75005 Paris, France

[5] Institut Curie, PSL Research University, CNRS, UMR144, Cell and Tissue Imaging Facility (PICT-IBiSA), 75005 Paris, France

[6] Institut Curie, PSL Research University, INSERM U1143, CNRS UMR 3666, Membrane Mechanics and Dynamics of Intracellular Signaling Laboratory, 26 rue d'Ulm, 75005 Paris, France

[*] Corresponding Author: arnaud.echard@pasteur.fr

Keywords:

Cytokinesis, Cell division, Caveolae, Membrane tension, ESCRT, Myosin II

ABSTRACT

During cytokinesis, the intercellular bridge (ICB) connecting the daughter cells experiences pulling forces, which delay abscission by preventing the assembly of the ESCRT scission machinery. Abscission is thus triggered by tension release, but how ICB tension is controlled is unknown. Here, we report that caveolae, which are known to control membrane tension upon mechanical stress in interphase cells, are located at the midbody, at the abscission site and at the ICB/cell interface in dividing cells. Functionally, the loss of caveolae delays ESCRT-III recruitment during cytokinesis and impairs abscission. This is the consequence of a 2-fold increase of ICB tension measured by laser ablation, associated with a local increase in myosin II activity at the ICB/cell interface. We thus propose that caveolae buffer membrane tension and limit contractibility at the ICB to promote ESCRT-III assembly and cytokinetic abscission. Altogether, this work reveals an unexpected connection between caveolae and the ESCRT machinery and the first role of caveolae in cell division.

TEASER

Caveolae limit the tension in the intercellular bridge during cytokinesis to enable ESCRT-III assembly and successful abscission.

INTRODUCTION

Cytokinesis is the last step of cell division and physically separates the daughter cells. In animal cells, cytokinesis is driven by local and highly coordinated

polymerization/depolymerization of different types of cytoskeleton and filaments (*1, 2*). First, the ingression of the cleavage furrow depends on the contraction of an acto-myosin ring at the cell equator. Then, the intercellular bridge (ICB) connecting the daughter cells is stabilized by septins. Finally, the midbody at the center of the ICB recruits the abscission machinery that pinches the membrane on one side of the midbody at the future abscission site (**Fig. S1A**) (*1, 2*). This last step requires the local disassembly of microtubules and actin filaments (*2-6*), as well as the timely polymerization of ESCRT-III filaments at the abscission site (*7-10*). The ESCRT-III-driven constriction of the plasma membrane eventually leads to the scission of the ICB (*2, 7*).

What triggers ESCRT-III filament assembly at the right place and time, first at the midbody then at the abscission site remains largely unknown. While several biochemical components, such as CEP55, MKLP1, ALIX, TSG101, Syndecan-4, are key for the proper recruitment, localization and polymerization of the ESCRT-III machinery (*2, 7*), it has been shown that mechanical inputs play a critical role as well. Indeed, after furrow ingression, the daughter cells exert nano-Newton (nN)-range pulling forces on the bridge, which is thus under tension (*11*). Rather than favoring abscission, this, on the contrary, delays ESCRT-III recruitment at the abscission site (*11*). It has thus been proposed that abscission requires a tension release in the ICB (*11*), but how this is controlled remains elusive. Understanding the regulation of the intercellular forces in the ICB should thus reveal one of the most upstream events that initiates abscission.

Here, we identified caveolae as a key regulator that limits ICB tension and promotes abscission. Caveolae are characteristic cup-shaped 60-80 nm invaginations of the plasma membrane, discovered in the 1950's (*12-16*). The formation of caveolae requires two types of structural components: Caveolins, which are partially embedded in the plasma membrane, and Cavins that form a coat around caveolae (*14, 15*). In addition, accessory proteins such as EHD2 and PACSINS regulate caveolae dynamics (*14-16*). In vertebrates, caveolae are

particularly abundant in cells that experience chronical mechanical constraints, such as muscle cells, endothelial cells and adipocytes (*14, 15*). Caveolae define nanometer scale lipid compartments at the plasma membrane and have been involved in the regulation of many signaling events (*17*). Over the past decade, it also emerged that caveolae constitute a membrane reservoir that plays a critical role in buffering membrane tension in non-dividing cells experiencing mechanical stress, through their ability to flatten out (*18-21*). This is particularly important to maintain tissue integrity in adult tissues, during development and in pathological situations such as cancers (*22-27*).

Cells experience dramatic forces and shape changes during cell division, but little is known about caveolae during mitosis or cytokinesis. At the onset of mitosis, before chromosome segregation, caveolin-1 is enriched at cortical regions and guides spindle orientation (*28*). Later, in metaphase, caveolin-1 redistribute from the plasma membrane to internal compartments, accompanied with fission of caveolae from the plasma membrane (*29*). Conversely, caveolin-1 reappears at the membrane during telophase in HeLa cells (*29*). Furthermore, it is known for long that caveolin-1 concentrate at the cleavage furrow in MDCK cells and in early zebrafish embryos (*30, 31*). However, the significance of this dynamic redistribution of caveolin-1 during mitotic exit, and whether caveolae have a role in cell division remains unknown.

Using a variety of approaches, from endogenous immunostaining, high resolution spinning disk confocal microscopy, electron microscopy, CRISPR-Cas9 KO cells to laser ablation for measuring tension, we report that 1) *bona fide* caveolae are present at the midbody as well as at the sides of the ICB after furrow ingression, 2) caveolae regulate acto-myosin II-dependent contractility at the ICB and ICB mechanical tension, and 3) by limiting ICB tension, caveolae promote both ESCRT-III assembly and abscission. This work thus reveals the first function of caveolae in cell division, whereby caveolae buffer tension in the ICB, a physical parameter that is critical for successful cytokinesis.

RESULTS

Caveolae are present at the midbody and at the ICB/cell interface

In many cell types, abscission occurs on both sides of the midbody and releases a midbody remnant (MBR) (*11, 32-36*) (**Fig. S1A**). We recently developed a new method for isolating pure, intact MBRs from HeLa cells and provided the quantitative proteome of this organelle that we termed the *Flemmingsome* (*37*). Data analysis led to the intriguing discovery that several proteins constitutive of caveolae were either present (caveolin-1, PACSIN2, Cavin3 and EHD2) or enriched (Cavin1/PTRF and PACSIN3, >3.5 fold and >3 fold compared to control fractions, respectively) in the *Flemmingsome* (**Fig. S1B**). In this study, we chose to focus on Cavin1 and caveolin-1 (Cav1), as both are essential structural components of caveolae (*14, 15*).

Immunostaining of purified MBRs from HeLa cells expressing the midbody marker GFP-MKLP1 showed endogenous Cavin1 and Cav1 localization on dotty structures (**Fig. 1A and S1C**), consistent with the proteomic data. During cytokinesis, we also observed an enrichment in similar structures containing Cavin1 (**Fig. 1B**) and Cav1 (**Fig. S1D**) at the cytokinetic furrow when ingressed, as previously reported for Cav1 in other cell types (*30, 31*). In addition, we found that both proteins localized to the midbody in 80-90% of both early and late ICBs (characterized by thick and thin tubulin staining, respectively (*33, 37*)) (**Fig. 1B and S1D**), which had not been previously reported thus far. The presence of Cavin1 dots suggested the existence of caveolae at the midbody, since Cavin1 at the plasma membrane is only present on fully budded caveolae at the plasma membrane (*16*). To determine whether *bona fide* caveolae were present at the midbody, we turned to electron microscopy (EM). Using scanning EM (SEM), we observed small open structures at the midbody ring that likely correspond to membrane invaginations (arrows, **Fig. 1C**). Transmission EM on ultrathin 2D sections further demonstrated the presence at the

midbody (MB) of small (60-100 nm) plasma membrane invaginations with typical morphology of caveolae (arrow, **Fig. 1D**).

After furrow ingression, we also frequently observed an accumulation of dotty Cavin1- and Cav1-positive structures at one or both sides of the ICB (**Fig. 1E and S1E**). These flanking regions of the ICB correspond to the interface between the ICB and the daughter cell, and we thus named them "entry points" (EPs). Transmission EM confirmed that caveolae were present at the plasma membrane at the EPs (**Fig. 1F**). In late cytokinetic bridges, secondary constrictions with decreased microtubule staining are found ~1 μm away from midbody and correspond to the tip of the ESCRT-III cone that constrict at the presumptive abscission site (*4, 33, 37*) (see **Fig. S1A**). Interestingly, the enrichment of caveolae at EPs was observed in approximately 40% of late ICBs without secondary constrictions but only in 10% of ICBs with secondary constrictions (which correspond to ICBs temporally closer to abscission) (**Fig. 1E and S1E**). This indicates that the number of caveolae at the EPs decreases as cells progress towards abscission. Altogether, we conclude that *bona fide* caveolae are present at the midbody and transiently at the ICB/cell interface after furrow ingression.

Cavin1 and Cav1 dynamically colocalize at the midbody and at the ICB/cell interface

To reveal the dynamics of the caveolae during cytokinesis, we monitored their localization in live cells using time-lapse spinning-disk confocal microscopy in cells expressing both Cav1-RFP and Cavin1-NG (mNeonGreen). As shown in **Fig. 2A** and **Movie 1**, punctate structures positive for both Cavin1 and Cav1 localized at the ingressed furrow (190 min before abscission, time -190 min). As the ICB matured, pools of Cavin1 and Cav1 were found at the midbody (**Fig. 2A**, bracket, times -120, -70 and 0 min) and accumulated at EPs (**Fig. 2A**, squared regions, time -160 min). Interestingly, quantification of Cavin1-NG intensity at EPs (**Fig. 2B, Fig. S2A** and **Movie 2**) revealed that 1) one EP is

consistently more labeled than the other, suggesting an asymmetry in caveolae localization at EPs; 2) Cavin1 intensity starts to decrease at both EPs approximately 100 minutes before abscission, with a sharper decrease 50 min before abscission; 3) abscission occurs approximately 20 minutes after both EPs have reached their minimal Cavin1 intensity. Since ESCRT-III starts to polymerize as a cone from the midbody toward the abscission approximately 30 min before abscission (*37*) (see **Fig. S1A**), ESCRT-III polymerization is thus concomitant with low levels of Cavin1 at EPs. Importantly, Cavin1-positive dots detected in live cell imaging were almost always positive for Cav1 (**Fig. 2A**, lower panel) indicating that they correspond to caveolae (*14-16*), which is consistent with our EM data in fixed cells.

Beside the midbody and EPs, we also noticed the presence of discrete Cavin1- and Cav1-positive punctate structures at the future abscission site (**Fig. S2B**, arrowheads). These structures contained both Cavin1 and Cav1, and were localized at the distal tip (**Fig. 2C**, arrowhead) of the ESCRT-III cone labelled by CHMP4B (**Fig. 2C**, arrow). Remarkably, time lapse microscopy demonstrated that this pool of caveolae disappeared prior to abscission, while the ESCRT-III cone polymerized toward the abscission site (100% of cases, n= 13 movies and **Fig. 2D**).

In summary, caveolae are found at the midbody throughout cytokinesis. They are also found at the ICB/cell interface (*i.e.* entry points) and at the tip of the ESCRT-III machinery, and progressively disappear from these locations as cells progress toward abscission.

Loss of caveolae impairs abscission and ESCRT-III localization

To investigate the function of caveolae in cytokinesis, we took advantage of a HeLa cell line KO for Cavin1 that we recently generated using CRISPR-Cas9 strategy (*38*). Westernblots confirmed the absence of Cavin1 protein expression in these cells (**Fig. 3A**).

In addition, we observed the loss of Cavin1 dots by immunofluorescence (**Fig. S3A**). As expected, this was accompanied with a strong reduction of Cav1-positive dots upon Cavin1 KO (**Fig. S3B**), since Cavin1 and Cav1 protein levels are correlated (*39, 40*)**.** Using transmission EM, we did not detect the presence of caveolae in Cavin1 KO cells, contrary to control KO cells (**Fig. 3B**, arrows). We conclude that caveolae are absent in the Cavin1 KO cells that we generated.

Most noteworthy, the lack of caveolae was associated with a 3-fold increase in the number of binucleated cells in the Cavin1 KO cell population (**Fig. 3C**), indicating cytokinetic defects. Furthermore, using time-lapse phase contrast microscopy, we observed that abscission was delayed in Cavin1 KO cells compared to control cells (**Fig. 3D**). Importantly, re-expression of Cavin1 in the KO cells fully rescued the cytokinetic defects, ruling out off target artifacts (**Fig. 3C and S3C**). Similarly, depletion of Cav1 by siRNAs resulted in the loss of Cav1-positive structures in the ICB (**Fig. S3D**) and delayed abscission as well (**Fig. S3E**).

To understand the origin of the cytokinetic defects induced by the loss of caveolae, we next investigated the ESCRT scission machinery by monitoring the key ESCRT-III subunit CHMP4B. In fixed cells, Cavin1 KO led to a decrease in the proportion of ICBs with CHMP4B both at the midbody and at the abscission site, accompanied by an increase in the proportion of less mature ICBs characterized by the presence of CHMP4B only at the midbody (**Fig. 3E**). This suggested a defect in ESCRT-III assembly at the abscission site upon removal of caveolae. As expected, the abnormal localization of CHMP4B was fully rescued by re-expressing Cavin1 (**Fig. 3E**). Spinning-disk confocal microscopy further demonstrated delayed arrival of CHMP4B-GFP both at the midbody (t1, **Fig. 3F**) and at the abscission site (t2, **Fig. 3F**) upon Cavin1 KO. These results indicate that caveolae are required for the proper assembly of ESCRT-III at the midbody and at the abscission site.

Altogether, this explains, at the mechanistic level, the abscission defects observed upon caveolae loss.

Caveolae limit acto-myosin II contractility at the ICB/cell interface and control ICB tension during cytokinesis

High tension in ICBs during cytokinesis delays ESCRT-III polymerization (*11*). Since membrane tension was found to contribute to half of the bridge tension (*11*) and caveolae can buffer membrane tension in interphase cells (*19, 41*), we hypothesized that the loss of caveolae may increase ICB tension during cytokinesis. Changes in ICB tension can be measured by laser ablation. Indeed, when the ICB is transversally cut by a UV-laser (**Fig. 4A**), the initial speed of retraction was previously shown to be proportional to the forces exerted by the daughter cells on their ICB (*11*). Remarkably, using this approach, we found a two-fold increase of ICB tension in Cavin1 KO cells compared to control KO cells (**Fig. 4B and Movie 3**). These results demonstrate that caveolae are functionally required to limit the ICB tension during cytokinesis.

Tension measured in the ICB can result from an entangled combination of membrane tension and cell contractility transmitted to the ICB by the acto-myosin system (*42*). We thus examined the activity of myosin II by measuring the levels of phosphorylated Myosin II Regulatory Light Chain (pMRLC) and F-actin localization upon Cavin1 depletion. First, we observed that the proportion of cytokinetic cells with F-actin accumulation at both EPs increased in Cavin1 KO cells (**Fig. 4C**). Conversely, the proportion of cytokinetic cells without F-actin accumulation at either EPs decreased in Cavin1 KO cells (**Fig. 4C**). Second, as seen for F-actin, the proportion of cytokinetic cells with accumulation of endogenous pMRLC at both EPs increased in Cavin1 KO cells (**Fig. 4D**). Conversely, the proportion of cytokinetic cells without pMRLC accumulation at either EPs decreased in Cavin1 KO cells

(**Fig. 4D**). However, neither the total levels of MRLC nor the percentage of activated myosin II (ratio pMRLC/total MRLC) was changed in Cavin1 KO cells synchronized in cytokinesis (**Fig. S4A**). Altogether, the loss of caveolae results in a higher proportion of ICBs displaying F-actin and activated myosin II in the EP regions.

Interestingly, in wild type cells, we observed that structures with high levels of activated myosin II and high levels of Cavin1 were inversely correlated (and often mutually exclusive) within EP regions: high intensity Cavin1-positive structures (**Fig. 4E** green peaks and **Fig. 4F box b**) were negative or weak for pMRLC (**Fig. 4E** magenta peaks and **Fig. 4F box b**) and vice-versa (**Fig. 4E and Fig. 4F box a**). This suggests that the presence of caveolae locally restricts myosin II activation at EPs during cytokinesis, a hypothesis consistent with increased pMRLC at EPs found in the absence of Cavin1.

Altogether, we conclude that the presence of caveolae both limits the presence of F-actin/active myosin II at the cell/ICB interface and the ICB tension during cytokinesis.

Increased ICB tension is responsible for the cytokinetic defects induced by the loss of caveolae

Our data raised the possibility that, upon Cavin1 depletion, the local increase in F-actin and activated myosin II at EPs could contribute to the observed increase in ICB tension, thus explaining the defects in ESCRT-III assembly and the abscission delay. To test this hypothesis, we treated Cavin1 KO cells with Y27632, a pharmacological inhibitor of ROCK, a kinase that activates myosin II through direct phosphorylation of MRLC. Upon ROCK inhibition, the increase in the proportion of ICBs with both EPs positive for pMRLC observed in Cavin1 KO cells was abolished (**Fig. 5A**). Concomitantly, ROCK inhibition restored ICB tension to normal levels in Cavin1 KO cells (**Fig. 5B**), suggesting that activated myosin II at EPs contributes to the ICB tension increase measured upon Cavin1 depletion. Remarkably, the treatment of Cavin1 KO cells with Y27632 was also sufficient to restore the

correct assembly of ESCRT-III at the abscission site (**Fig. 5C**). Furthermore, reducing membrane tension by incubating the cells in a moderately hyper-osmotic medium (400 mOsm) also restored the proper assembly of ESCRT-III at the abscission site in Cavin1 KO cells (**Fig. S4B**). These results show that reducing either membrane tension or acto-myosin II-dependent contractility is sufficient to correct the abnormal localization of ESCRT-III at the abscission site observed upon the loss of caveolae. Accordingly, Y27632 treatment also rescued the abscission defects observed in Cavin1 KO cells (**Fig. 5D**). Noteworthy, in wild type cells, we observed that the polymerization of ESCRT-III at the abscission site occurs concomitantly with a decrease in the accumulation of pMRLC at EPs (**Fig. S4C**). This suggests that during normal cytokinesis, the drop in ICB tension known to promote abscission (*11*) depends on the decrease of acto-myosin II contractility at EPs.

We conclude that the increase of tension in the ICB induced by the absence of caveolae is the cause of the defects in ESCRT-III assembly, which in turn impairs normal abscission. Therefore, caveolae are functionally required to promote ESCRT-III polymerization and successful abscission by limiting intercellular bridge tension during cytokinesis.

DISCUSSION

The decrease in ICB tension after furrow ingression is one of the most upstream mechanical determinants that controls the assembly of the abscission machinery. Yet, no regulator of ICB tension has been reported so far. Here, we establish the first functional role

of caveolae in cell division, which were found to buffer ICB tension to promote cytokinetic abscission.

Our proteomic analysis of MBRs revealed the presence or the enrichment of several structural and regulatory components of caveolae (Cav1, Cavin1, Cavin3, EHD2, PACSIN2-3), leading to the hypothesis that caveolae could play an active role during cytokinesis. Indeed, proteins involved either in furrow ingression or in late cytokinetic stages often accumulate at the midbody and can be identified by mass spectrometry in purified MBRs. This recently allowed us to reveal the role of ALIX/syntenin/Syndecan-4 and BST2/tetherin in abscission and post-abscission MBR capture, respectively (*37, 43*).

While a role of caveolae in cytokinesis has not been reported so far, the structural caveolae component Cav1 had been previously localized at the furrow (*30, 31*). We confirmed and extended these observations using endogenous staining for both Cav1 and Cavin1 (Fig. 1B, S1D) as well as fluorescently-tagged proteins (Fig. 2A). We also revealed the presence of caveolae components 1) at the midbody itself, 2) at the "entry points" (EPs), which correspond to the interfaces between the ICB and the daughter cells (Fig. 1E, S1E, 2A, S2A) and 3) at the tip of the ESCRT-III cone while polymerizing toward the abscission site (Fig. 2C-D). The extensive colocalization between Cavin1 with Cav1 in these structures (Fig. 2A), together with EM data (Fig. 1D,F) demonstrated that these are *bona fide* caveolae present at the plasma membrane.

What could determine the localization of caveolae at these specific locations during cytokinesis? Intense recycling of caveolae components during mitotic exit and telophase has been reported (*29*), and it is thus possible that this contributes to the localization of caveolae at the cytokinetic furrow, EPs and midbody. Alternatively, individual caveolae could diffuse from the cell body to the furrow, EPs and midbody in the plane of the plasma membrane. Finally, caveolae could as well form *in situ* due to the peculiar lipid composition of the furrow

and midbody membrane that is known to promote caveolae formation in non-dividing cells (*44-49*). We also noticed that caveolae are particularly abundant at EPs when the plasma membrane adopts a funnel shape (as in Fig. 1E, "EP1 enriched" right panels), possibly indicating that particular curvature might favor caveolae formation or retention. Regarding the intriguing presence of caveolae at the tip of the ESCRT-III cone, we noticed that the ESCRT-III subunit CHMP4B had been found in complex with several caveolae components (Cavin1, Cav1 and PACSIN3) using mass spectrometry (*50*). This could provide a molecular connection explaining the remarkable coupling between caveolae and ESCRT-III at the abscission site.

What is the role of caveolae during cytokinesis? Following furrow ingression, daughter cells exert nano Newton-range pulling forces on the ICB that must be reduced to favor abscission (*11*). Accordingly, high tension inhibits ESCRT-III polymerization at the abscission site during cytokinesis (*11*) and prevents membrane scission in reconstitution assays (*51*). Our results point to a key role of caveolae in limiting ICB tension, which in turn promotes ESCRT-III polymerization and consequently abscission. Indeed, the depletion of Cavin1 results in 1) a 2-fold increase in ICB tension (Fig. 4B); 2) a delay in ESCRT-polymerization at the midbody and at the abscission site (Fig. 3E-F) and 3) a delay in abscission (Fig. 3D) or cytokinetic failure (Fig. 3C). In addition, Cav1 depletion leads to similar defects in cytokinesis (Fig. S3E). Importantly, the increase in ICB tension upon caveolae loss is the cause of the cytokinetic failure, since decreasing membrane tension through a moderate hyperosmotic shock (Fig. S4B) or by decreasing acto-myosin II-dependent contractility through ROCK inhibition (Fig. 5C) restores the proper polymerization of ESCRT-III at the abscission site in Cavin1 KO cells. Remarkably, ROCK inhibition also rescues the abscission defects in these cells (Fig. 5D). To our knowledge, caveolae thus appear as the first regulator of ICB tension during cytokinesis.

How could caveolae control ICB tension during cytokinesis? ICB tension results from a combination of membrane tension and cortical tension due to acto-myosin II-dependent contractility exerted on the ICB (*11, 42*). We envision two, non-mutually exclusive, mechanisms to explain how caveolae might control both components of ICB tension.

First, the pool of caveolae present at the EPs could contribute to the decrease in membrane tension at the ICB by flattening out (**Fig. 6**, wild type cells), as shown previously in non-dividing cells (*18, 42*). Consistently, using both fixed cells (Fig. 1E, S1E) and 10-min frequency time-lapse microscopy (Fig. 2A, 2B and S2A), we found that caveolae progressively disappeared from EPs as cells progressed through abscission. The enrichment of caveolae precisely at the interface between the ICB and the cell body would constitute a membrane reservoir ideally located for reducing membrane tension at the ICB. The caveolae-mediated membrane tension reduction would then promote ESCRT-III polymerization at the abscission site and thus abscission. In agreement with the idea that caveolae flattening at EPs reduces ICB tension, it is known that ESCRT-III starts to polymerize as a cone at the presumptive abscission site approximately 30 min before abscission occurs, and this corresponds to the time when caveolae at the EPs intensity reaches a minimum (Fig. 2B). Interestingly, previous quantitative measurements showed that the tension at the ICB also diminishes at that time (*11*). Beside caveolae flattening at EPs, caveolae flattening at the plasma membrane of the daughter cells, outside the EP regions, could also contribute to the reduction of ICB tension that precedes abscission. In addition, the flattening of the caveolae localized at (or close to) the tip of the ESCRT-III cone (Fig. 2C-D) could also help the constriction of the plasma membrane at the abscission site by locally reducing membrane tension.

Second, caveolae at EPs could also negatively regulate acto-myosin II-dependent contractility at or close to the ICB. Indeed, depleting Cavin1 leads to an increase of the proportion of ICBs with activated myosin II at EPs, associated with a 2-fold increase in ICB tension (Fig. 4B, D). This regulation appears local, since global myosin II activation during cytokinesis is unchanged after caveolae depletion (Fig. S4A). Furthermore, pharmacological inhibition of ROCK in Cavin1 KO cells enabled to restore both normal pMRLC patterns at the EPs as well as normal ICB tension (Fig. 5A-B). This suggests that the abnormally high ICB tension observed after caveolae loss results from the local increase in acto-myosin II activity at the EPs. How the presence of caveolae at EPs seen in wild type cells locally regulates this previously undescribed pool of activated myosin II to restrict ICB tension is not known and would require future investigation. Nonetheless, the inverse correlation between high levels of activated myosin II and high levels of Cavin1 at EPs is remarkable (Fig. 4E-F) and might involve complex biochemical reciprocal inhibitory signals between caveolae and the acto-myosin system. Interestingly, there is increasing evidence that caveolae regulate both membrane tension and acto-myosin II activity at the plasma membrane (*26, 52-55*), in particular during rear-to-front retraction during durotaxis-mediated migration (*54*) and in cell-cell contacts involved in melanin pigment transfer from melanocytes to keratinocytes (*55*). Furthermore, caveolae have been recently implicated in the negative regulation of F-actin polymerization and thereby intercellular tension through adherent junctions between non-dividing epithelial cells (*26*). The parallel with the role of caveolae as a negative regulator of ICB tension during cell division is striking, although the functional consequence —ESCRT-III polymerization and membrane scission— is very different. Thus, the local regulation of acto-myosin-dependent contractility coupled to the buffering of membrane tension might be a general function of caveolae.

In summary, we propose that the presence of caveolae at EPs and at the abscission site buffers membrane tension and limits myosin II activation at the ICB in wild type dividing cells (Fig. 6, right panels). This promotes the decrease of the ICB tension, thus favoring the polymerization of ESCRT-III at the abscission site to allow abscission. In cells without caveolae, the lack of the caveolae membrane reservoir and the increased activation of myosin II at EPs leads to an increase of ICB tension that is detrimental for ESCRT-III polymerization and abscission (Fig. 6, left panels). This could be particularly relevant in tumorigenesis, since caveolae promote both elimination of cancer cells through extrusion (*26*) and formation of binucleated cells (this study), a well-established starting point for tumor formation (*56, 57*). The unexpected connection between caveolae and the ESCRT machinery should also stimulate investigation on how caveolae might control key other ESCRT-III-dependent processes beyond cell division, such as the budding of enveloped viruses and plasma membrane repair.

MATERIALS AND METHODS

Cell Culture

HeLa CCL-2 (ATCC), HeLa Control KO (HeLa CCL-2 transfected with a plasmid encoding Cas9 without gRNA described in *(38)*) and HeLa Cavin1 KO (HeLa CCL-2 transfected with a plasmid encoding Cas9 and a gRNA targeting *Cavin1* described in *(38)*) were grown in Dulbecco's Modified Eagle Medium (DMEM) GlutaMax (#31966 Gibco, Invitrogen Life Technologies). All culture media were supplemented with 10 % fetal bovine serum (FBS, #500105R1 Dutscher) and 1 % Penicillin/Streptomycin (#15140122 Gibco) and cultured in 5 % CO_2 condition at 37 °C. CHMP4B-GFP stable cell lines were generated by lentiviral transduction of HeLa Control KO and Cavin1 KO cells and selected by flow cytometry (FACS) sorting. For the ROCK inhibitor experiments, HeLa Control KO and Cavin1 KO were treated with Y27632 (Calbiochem) at 20 μM overnight (Fig. 5B, 5D) or 50 μM for 3h (Fig. 5A, 5C).

Plasmid constructs

Cavin1-GFP and Cav1-RFP were described previously in (*58*). To construct Cavin1-mApple, the Cavin1 CDS was subcloned into Gateway pENTR plasmids. The transient

expression vector was generated by LR recombination (Thermo Fisher) of Cavin1-pENTR and pDEST mApple N1.

Cell transfections and siRNAs

For live cell imaging, HeLa cells, were transfected with 200 ng of plasmids for 48 h using X-tremeGENE 9 DNA reagent (Roche, Fig. 2A), or electroporated with 2 μg of plasmid using Lonza's nucleofection protocol (Fig. S2A). HeLa CHMP4B-GFP cells were transfected with 80 ng Cavin1-mApple for 48h using X-tremeGENE 9 DNA reagent (Fig. 2D). For the rescue experiments, Control KO and Cavin1 KO cells were transfected with 200 ng of plasmids (Fig. 3C, S3C) or 120 ng of plasmid for 24h (Fig. 3E) for 24h using X-tremeGENE 9 DNA reagent (Roche).

Depletion of Cav1 was achieved by RNAi using siRNAs with the following sequence: 5' GCAUCAACUUGCAGAAAGA 3' (Merck), and Control siRNA Luciferase: 5' CGUACGCGGAAUACUUCGA 3' (Merck). HeLa cells were transfected on two consecutive days with 20 nM Cav1 siRNAs using Lipofectamine RNAiMAX (Invitrogen), following the manufacturer's instructions and recorded 3 days later.

Western Blots

siRNAs-treated HeLa cells and Control KO and Cavin1 KO cells were directly lysed in 1x Laemmli (Bio-Rad Laboratories) with Benzonase nuclease (#70664 Millipore) and migrated in 10 % SDS-PAGE gels (Bio-Rad Laboratories). Control KO and Cavin1 KO cells used in the rescue experiments were detached with trypsin (Gibco), collected and lysed with NP-40 extract buffer (50 mM Tris, pH 8, 150 mM NaCl, 1 % NP-40) containing protease inhibitors (#11873580001 Roche) and 30 μg of lysate was migrated in 10 % SDS-PAGE gels (Bio-Rad Laboratories). In both cases, the migrated gels were transferred onto PVDF membranes (Millipore) and incubated overnight at 4 °C with corresponding primary antibodies (Table S1) in 50 mM Tris-HCl pH 8.0, 150 mM NaCl, 0.1 % Tween-20, 5 % milk. This was followed by incubation with horseradish peroxidase (HRP)-coupled secondary antibodies (1:10,000, Jackson ImmunoResearch) for 1 h at room temperature (RT) and revealed by chemiluminescence using Immobilon Crescendo or Forte Western HRP substrate (Millipore Merck).

For western blots against pMRLC, MRLC and actin, cells were lysed with 1x Laemmli (Bio-Rad Laboratories) with Benzonase nuclease and phosphatase inhibitors (Sigma-Aldrich p2850, Merck), and the lysates were migrated in 4–15 % gradient SDS-PAGE gels (Bio-Rad Laboratories). Gels were transferred onto nitrocellulose membranes (Whatman Protran), incubated overnight with primary antibodies in 50 mM Tris-HCl pH 8.0, 150 mM NaCl, 0.1 % Tween-20, 5 % BSA. fluorescently-coupled secondary antibodies (1:10,000, Jackson ImmunoResearch) were incubated for 30 min in Tris-HCl pH 8.0, 150 mM NaCl, 0.1 % Tween-20, 3 % milk at RT and revealed by LI-COR (Biosciences).

Immunofluorescence and image acquisition

Midbody remnants were purified as described in (*37*) and fixed with pure methanol (#32213 Sigma-Aldrich) at -20 °C for 3 minutes. HeLa cells were grown on coverslips, and fixed with either 4 % paraformaldehyde (PFA, #15714 Sigma-Aldrich) for 20 min (Table S1) or pure methanol (#32213 Sigma-Aldrich) at -20 °C for 3 minutes (Table S1). Cells and midbody remnants were permeabilized with 0.1 % Triton X-100 and blocked with PBS containing 1% BSA for 1 h at RT, then incubated with the corresponding primary antibodies (Table S1) diluted in PBS containing 1% BSA for 1 h at RT. This was followed by an incubation with the secondary antibodies diluted in PBS containing 1% BSA for 1 h at RT. Cells were additionally stained with DAPI (0.5 mg/mL, Serva) for 10 minutes at RT. Cells and midbody remnants were finally mounted in Mowiol (Calbiochem). Image acquisition was done with an inverted Eclipse Nikon Ti-E microscope, using a 100x 1.4 NA PL-APO objective lens or a 60x 1.4 NA PL-APO VC objective lens, coupled to a CCD camera (Photometrics Coolsnap HQ) or Retiga R6 CCD Camera – Teledyne Photometrics and MetaMorph software (MDS), or using a CSU-X1 spinning disk confocal scanning unit (Yokogawa) coupled to a Prime 95S sCMOS Camera (Teledyne Photometrics) and CSU 100x objective. Images were then converted into 8- bit images using Fiji software (NIH) and mounted in Photoshop CS6.

Osmotic shock experiments

Mild hyper-osmotic shocks were performed as in (*51*). Cells were seeded on glass coverslips the day before the experiment, and treated for 90 min either with isotonic cultured media (DMEM, 10 % FBS, 300 mOsm) or with DMEM, 10 % FBS media containing D-Glucose (#G5767 Sigma-Aldrich) to obtain a final osmotic pressure of 400 mOsm. Cells were then fixed and immunostained.

Time-lapse microscopy

For time-lapse phase-contrast imaging (abscission times), cells were plated on glass bottom 12-well plates (MatTek) and put in an open chamber (Life Imaging) equilibrated in 5 % CO_2 and maintained at 37 °C. Time-lapse sequences were recorded every 10 min for 48 h using an inverted Nikon Eclipse Ti-E microscope with a 20x 0.45 NA Plan Fluor ELWD controlled by Metamorph software (Universal Imaging).

For time-lapse fluorescent imaging, images were acquired using an inverted Nikon Eclipse Ti-E microscope equipped with a CSU-X1 spinning disk confocal scanning unit (Yokogawa) and with a EMCCD Camera (Evolve 512 Delta, Photometrics) or a Prime 95S sCMOS Camera (Teledyne Photometrics). Images were acquired with CSU 100x or CSU 60x 1.4 NA PL-APO VC objectives and MetaMorph software (MDS).

Laser ablation

Laser ablation experiments were performed using a pulsed 355 nm ultraviolet (UV) laser (Roper Scientific) controlled by Metamorph and the iLas2 system (GATACA systems). The laser ablation system was connected to an inverted Nikon Eclipse Ti microscope confocal spinning disk equipped with a Yokagawa CSU-X1 spinning head, coupled to an EM-CCD

camera (Evolve, Photometrics) and a 100x objective (Nikon S Fluor 100x 0.5-1.3 NA). The 355 nm UV laser is sufficient for membrane and microtubule cut, as described and demonstrated in [11]. To record the movement of the midbody following laser ablation, fast acquisition movies (20 ms time-lapse) were made using only transmitted light. The displacement of the midbody was then tracked using the software Icy (*59*). The midbody displacement after laser ablation follows a double exponential function as described in [11], and the retraction speed of the midbody was obtained from a linear regression of the first hundreds of ms after ablation.

Cells synchronization

For EM and western blots for detecting pMRLC, MRLC and actin, a mitotic shake-off was performed to synchronize the cells in mitosis. Two days before the experiment, 2 million HeLa cells were seeded in T75 flasks. First, mitotic and dead cells were shaken-off and the remaining cells were further incubated for 2 h with fresh filtered media (DMEM GlutaMax supplemented with 10 % FBS and 1 % Penicillin/Streptomycin). Cells were again shaken-off, and the supernatant containing the mitotic cells was collected and centrifuged (900 xg for 3 min) in 15 mL tubes. The pellet of cells was then resuspended and added to collagen I (#A10483 Gibco) coated glass coverslips (50 μg/mL, for EM), or p6 well-plate (50 □g/mL, for WB) and incubated for 2 h at 5 % CO_2 and 37 °C to allow them to exit mitosis and to progress into cytokinesis.

Electron Microscopy

Glass coverslips with synchronized cytokinetic cells were chemically fixed for 2 h at RT in cacodylate buffer (0.1 M, pH 7.2) supplemented with 2.5 % (v/v) glutaraldehyde and 2 % (v/v) paraformaldehyde, then washed in cacodylate buffer (3 times), post-fixed with 2 % (w/v) osmium tetroxide supplemented with 1.5 % (w/v) potassium ferrocyanide (45 min for 4 °C), washed in water (3 times), dehydrated in ethanol (increasing concentration from 30 to 100 %), and finally embedded in Embed812/ Araldite (Epon) resin as described in (*60*). Microtomy of embedded cell monolayers was performed on a Reichert UltracutS ultramicrotome (Leica Microsystems) for 70 nm thin sections collected on formvar-coated cupper/ palladium grids, then contrasted with uranyl acetate and lead citrate. Electron micrographs acquired with a Transmission Electron Microscope (Tecnai Spirit G2; ThermoFischer Scientific, Eindhoven, The Netherlands) equipped with a 4k CCD camera (Quemesa, EMSIS, Muenster, Germany) using ITEM software (EMSIS).

Image and Data Analyses

All images and videos were minimally processed to adjust the intensity levels, reduce image noise, and rotate the images with Fiji software. The kymographs (Fig. 4B) were obtained using an ROI (straight line) along the intercellular bridge at a fixed position over the entire movie, using Icy software. The scan lines were obtained using an ROI (straight line), with a width corresponding to the bridge or EP height, along the objects of interest,

using Fiji. Pixel intensities values were extracted from the entry points defined with an ROI (square) for each channel of interest, using Fiji.

Statistical Analyses

All the plots and statistical tests were performed using GraphPad prism software. The presented values are displayed as mean ± SD (Standard Deviation) for at least three independent experiments (as indicated in the figure legends). The significance was calculated using unpaired, one-sided/two-sided t-tests, as indicated. For comparing the distribution of the abscission times, a nonparametric Kolmogorov–Smirnov test was used. In all statistical tests, a $P > 0.05$ was considered as non-significant. *P* values are indicated in the Figures.

REFERENCES

1. R. A. Green, E. Paluch, K. Oegema, Cytokinesis in Animal Cells. *Annual review of cell and developmental biology*, (2012).
2. C. Addi, J. Bai, A. Echard, Actin, microtubule, septin and ESCRT filament remodeling during late steps of cytokinesis. *Current opinion in cell biology* **50**, 27-34 (2018).
3. D. Dambournet *et al.*, Rab35 GTPase and OCRL phosphatase remodel lipids and F-actin for successful cytokinesis. *Nature cell biology* **13**, 981-988 (2011).
4. J. A. Schiel *et al.*, FIP3-endosome-dependent formation of the secondary ingression mediates ESCRT-III recruitment during cytokinesis. *Nature cell biology* **14**, 1068-1078 (2012).
5. S. Fremont *et al.*, Oxidation of F-actin controls the terminal steps of cytokinesis. *Nat Commun* **8**, 14528 (2017).
6. S. Fremont, A. Echard, Membrane Traffic in the Late Steps of Cytokinesis. *Current biology : CB* **28**, R458-R470 (2018).
7. B. Mierzwa, D. W. Gerlich, Cytokinetic Abscission: Molecular Mechanisms and Temporal Control. *Developmental cell* **31**, 525-538 (2014).
8. P. P. D'Avino, L. Capalbo, Regulation of midbody formation and function by mitotic kinases. *Seminars in cell & developmental biology* **53**, 57-63 (2016).
9. C. L. Stoten, J. G. Carlton, ESCRT-dependent control of membrane remodelling during cell division. *Seminars in cell & developmental biology*, (2017).
10. E. J. Scourfield, J. Martin-Serrano, Growing functions of the ESCRT machinery in cell biology and viral replication. *Biochemical Society transactions* **45**, 613-634 (2017).
11. J. Lafaurie-Janvore *et al.*, ESCRT-III assembly and cytokinetic abscission are induced by tension release in the intercellular bridge. *Science* **339**, 1625-1629 (2013).
12. G. E. Palade, The fine structure of blood capillaries. *J Appl phys* **24**, 1424 (1953).
13. E. Yamada, The fine structure of the gall bladder epithelium of the mouse. *J Biophys Biochem Cytol* **1**, 445-458 (1955).
14. R. G. Parton, Caveolae: Structure, Function, and Relationship to Disease. *Annual review of cell and developmental biology* **34**, 111-136 (2018).
15. R. G. Parton *et al.*, Caveolae: The FAQs. *Traffic* **21**, 181-185 (2020).
16. R. G. Parton, V. Tillu, K. A. McMahon, B. M. Collins, Key phases in the formation of caveolae. *Current opinion in cell biology* **71**, 7-14 (2021).
17. N. Ariotti *et al.*, Caveolae regulate the nanoscale organization of the plasma membrane to remotely control Ras signaling. *The Journal of cell biology* **204**, 777-792 (2014).
18. P. Sens, M. S. Turner, Budded membrane microdomains as tension regulators. *Phys Rev E Stat Nonlin Soft Matter Phys* **73**, 031918 (2006).
19. B. Sinha *et al.*, Cells respond to mechanical stress by rapid disassembly of caveolae. *Cell* **144**, 402-413 (2011).
20. O. L. Gervásio, W. D. Phillips, L. Cole, D. G. Allen, Caveolae respond to cell stretch and contribute to stretch-induced signaling. *J Cell Sci* **124**, 3581-3590 (2011).
21. M. A. Del Pozo, F. N. Lolo, A. Echarri, Caveolae: Mechanosensing and mechanotransduction devices linking membrane trafficking to mechanoadaptation. *Current opinion in cell biology* **68**, 113-123 (2021).
22. H. P. Lo *et al.*, The caveolin-cavin system plays a conserved and critical role in mechanoprotection of skeletal muscle. *The Journal of cell biology* **210**, 833-849 (2015).

23. J. Garcia *et al.*, Sheath Cell Invasion and Trans-differentiation Repair Mechanical Damage Caused by Loss of Caveolae in the Zebrafish Notochord. *Current biology : CB* **27**, 1982-1989.e1983 (2017).
24. Y. W. Lim *et al.*, Caveolae Protect Notochord Cells against Catastrophic Mechanical Failure during Development. *Current biology : CB* **27**, 1968-1981.e1967 (2017).
25. M. Dewulf *et al.*, Dystrophy-associated caveolin-3 mutations reveal that caveolae couple IL6/STAT3 signaling with mechanosensing in human muscle cells. *Nat Commun* **10**, 1974 (2019).
26. J. L. Teo *et al.*, Caveolae Control Contractile Tension for Epithelia to Eliminate Tumor Cells. *Developmental cell* **54**, 75-91.e77 (2020).
27. V. Singh, C. Lamaze, Membrane tension buffering by caveolae: a role in cancer? *Cancer Metastasis Rev* **39**, 505-517 (2020).
28. S. Matsumura *et al.*, Interphase adhesion geometry is transmitted to an internal regulator for spindle orientation via caveolin-1. *Nat Commun* **7**, ncomms11858 (2016).
29. E. Boucrot, M. T. Howes, T. Kirchhausen, R. G. Parton, Redistribution of caveolae during mitosis. *J Cell Sci* **124**, 1965-1972 (2011).
30. H. Kogo, T. Fujimoto, Concentration of caveolin-1 in the cleavage furrow as revealed by time-lapse analysis. *Biochemical and biophysical research communications* **268**, 82-87 (2000).
31. B. Feng, H. Schwarz, S. Jesuthasan, Furrow-specific endocytosis during cytokinesis of zebrafish blastomeres. *Experimental cell research* **279**, 14-20 (2002).
32. V. Dubreuil, A. M. Marzesco, D. Corbeil, W. B. Huttner, M. Wilsch-Brauninger, Midbody and primary cilium of neural progenitors release extracellular membrane particles enriched in the stem cell marker prominin-1. *The Journal of cell biology* **176**, 483-495 (2007).
33. N. Elia, R. Sougrat, T. A. Spurlin, J. H. Hurley, J. Lippincott-Schwartz, Dynamics of endosomal sorting complex required for transport (ESCRT) machinery during cytokinesis and its role in abscission. *Proceedings of the National Academy of Sciences of the United States of America* **108**, 4846-4851 (2011).
34. E. F. Crowell, J. Y. Tinevez, A. Echard, A simple model for the fate of the cytokinesis midbody remnant: implications for remnant degradation by autophagy: modeling remnant production and degradation enables re-interpretation of published data and improves design of future experiments. *Bioessays* **35**, 472-481 (2013).
35. E. F. Crowell, A. L. Gaffuri, B. Gayraud-Morel, S. Tajbakhsh, A. Echard, Midbody remnant engulfment after cytokinesis abscission in mammalian cells. *J Cell Sci* **127**, 3840-3851 (2014).
36. E. Peterman *et al.*, The post-abscission midbody is an intracellular signaling organelle that regulates cell proliferation. *Nat Commun* **10**, 3181 (2019).
37. C. Addi *et al.*, The Flemmingsome reveals an ESCRT-to-membrane coupling via ALIX/syntenin/syndecan-4 required for completion of cytokinesis. *Nat Commun* **11**, 1941 (2020).
38. C. Roffay *et al.*, Passive coupling of membrane tension and cell volume during active osmotic cell response. (in revision).
39. M. M. Hill *et al.*, PTRF-Cavin, a conserved cytoplasmic protein required for caveola formation and function. *Cell* **132**, 113-124 (2008).
40. L. Liu *et al.*, Deletion of Cavin/PTRF causes global loss of caveolae, dyslipidemia, and glucose intolerance. *Cell Metab* **8**, 310-317 (2008).
41. A. Echarri *et al.*, An Abl-FBP17 mechanosensing system couples local plasma membrane curvature and stress fiber remodeling during mechanoadaptation. *Nat Commun* **10**, 5828 (2019).

42. P. Sens, J. Plastino, Membrane tension and cytoskeleton organization in cell motility. *J Phys Condens Matter* **27**, 273103 (2015).
43. A. Presle *et al.*, The viral restriction factor tetherin/BST2 tethers cytokinetic midbody remnants to the cell surface. *Current biology : CB* **31**, 2203-2213.e2205 (2021).
44. M. M. Ng, F. Chang, D. R. Burgess, Movement of membrane domains and requirement of membrane signaling molecules for cytokinesis. *Developmental cell* **9**, 781-790 (2005).
45. G. E. Atilla-Gokcumen *et al.*, Dividing cells regulate their lipid composition and localization. *Cell* **156**, 428-439 (2014).
46. C. Cauvin, A. Echard, Phosphoinositides: Lipids with informative heads and mastermind functions in cell division. *Biochimica et biophysica acta* **1851**, 832-843 (2015).
47. U. Ortegren *et al.*, Lipids and glycosphingolipids in caveolae and surrounding plasma membrane of primary rat adipocytes. *Eur J Biochem* **271**, 2028-2036 (2004).
48. M. Hubert *et al.*, Lipid accumulation controls the balance between surface connection and scission of caveolae. *eLife* **9**, (2020).
49. Y. Zhou *et al.*, Caveolin-1 and cavin1 act synergistically to generate a unique lipid environment in caveolae. *The Journal of cell biology* **220**, (2021).
50. M. Y. Hein *et al.*, A human interactome in three quantitative dimensions organized by stoichiometries and abundances. *Cell* **163**, 712-723 (2015).
51. V. Mercier *et al.*, Endosomal membrane tension regulates ESCRT-III-dependent intra-lumenal vesicle formation. *Nature cell biology* **22**, 947-959 (2020).
52. A. Grande-García *et al.*, Caveolin-1 regulates cell polarization and directional migration through Src kinase and Rho GTPases. *The Journal of cell biology* **177**, 683-694 (2007).
53. A. Echarri, M. A. Del Pozo, Caveolae - mechanosensitive membrane invaginations linked to actin filaments. *J Cell Sci* **128**, 2747-2758 (2015).
54. J. H. R. Hetmanski *et al.*, Membrane Tension Orchestrates Rear Retraction in Matrix-Directed Cell Migration. *Developmental cell* **51**, 460-475.e410 (2019).
55. L. Domingues *et al.*, Coupling of melanocyte signaling and mechanics by caveolae is required for human skin pigmentation. *Nat Commun* **11**, 2988 (2020).
56. T. Fujiwara *et al.*, Cytokinesis failure generating tetraploids promotes tumorigenesis in p53-null cells. *Nature* **437**, 1043-1047 (2005).
57. S. M. A. Lens, R. H. Medema, Cytokinesis defects and cancer. *Nature reviews. Cancer* **19**, 32-45 (2019).
58. D. K. Sharma *et al.*, Selective stimulation of caveolar endocytosis by glycosphingolipids and cholesterol. *Molecular biology of the cell* **15**, 3114-3122 (2004).
59. F. de Chaumont *et al.*, Icy: an open bioimage informatics platform for extended reproducible research. *Nat Methods* **9**, 690-696 (2012).
60. I. Hurbain, M. Romao, P. Bergam, X. Heiligenstein, G. Raposo, Analyzing Lysosome-Related Organelles by Electron Microscopy. *Methods Mol Biol* **1594**, 43-71 (2017).

ACKNOWLEDGMENTS

We thank Matthieu Piel and the Echard Lab members for critical reading of the manuscript; Matthieu Piel, Aurélien Roux and Pierre Sens for helpful discussions throughout this project; the Recombinant antibodies platform (TAb-IP, Institut Curie, Paris) for antibodies. We thank our lab members Adrien Presle and Nathalie Sassoon for the preparation of purified midbody remnants. We thank Audrey Salles from UTechS PBI, Institute Pasteur for discussions and advice in image acquisition; Maryse Moya-Nilges from UTechS PBI, Institute Pasteur for SEM training and help in image acquisition; Quentin Gaia Gianetto for making Fig. S1B; Pierre-Henri Commere from Cytometry and Biomarkers Utechs, Institut Pasteur for FACS sorting and Vincent Fraisier, the Cell and Tissue Imaging facility (PICT-IBiSA), and the Nikon Imaging Centre @ Institut Curie-CNRS for laser ablation experiments.

Funding

Institut Pasteur (AE)
CNRS (AE)
ANR Cytosign, ANR SeptScort (AE)
French National Research Agency through the “Investments for the Future” program, France-BioImaging, ANR-10-INSB-04 (CD)
Cell and Tissue Imaging core facility (PICT-IBiSA), member of the France-BioImaging national research infrastructure, supported by the Labex Cell(n)Scale (ANR-10-LBX-0038) part of the IDEX PSL (ANR-10-IDEX-0001-02 PSL) (CD)
Doctoral School Complexité du Vivant ED515, contrat n° 2828/2017 (VA)
La Ligue Contre le Cancer (4éme année de thèse) (VA)
Pasteur-Paris University (PPU) international PhD program (JB)
Fondation ARC pour la recherche sur le cancer (DOC20180507410) (JB)

Author contributions

VA carried out and analyzed all the experiments except mentioned otherwise. CD performed, analyzed and interpreted the electron microscopy imaging experiments. JB obtained initial observations for Cavin1 localization. AJ taught laser ablation experiments to VA. NGR obtained initial data of the *Flemmingsome*. VA, CD, CL and AE designed the experiments. A.E. secured funding, analyzed and supervised the work. VA and AE wrote the manuscript with the help of CL and CD.

Competing interests

Authors declare that they have no competing interests

Data and materials availability

All data are available in the main text or the supplementary materials

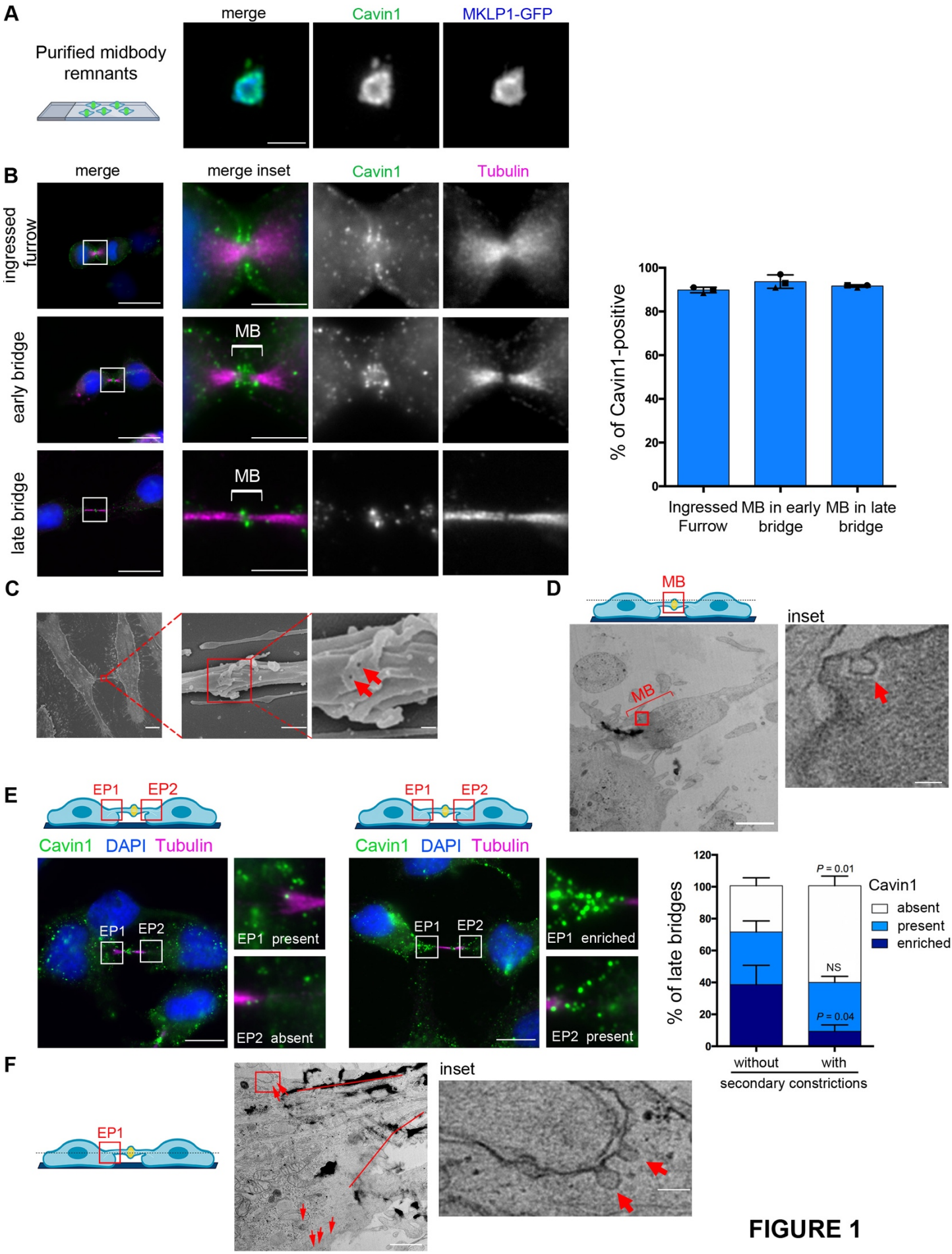
A
Purified midbody remnants
merge
Cavin1
MKLP1-GFP
B
merge
merge inset
Cavin1
Tubulin
ingressed furrow
early bridge
late bridge
MB
MB
% of Cavin1-positive
100
80
60
40
20
0
Ingressed Furrow
MB in early bridge
MB in late bridge
C
D
MB
MB
inset
E
EP1
EP2
Cavin1 DAPI Tubulin
EP1 present
EP2 absent
EP1 enriched
EP2 present
% of late bridges
120
100
80
60
40
20
0
P = 0.01
NS
P = 0.04
Cavin1
absent
present
enriched
without
with
secondary constrictions
F
EP1
inset

FIGURE 1

Figure 1 – Caveolae are present at the midbody and at the Entry Points (EPs) during cytokinesis.

(A) Purified midbody remnants from HeLa cells that stably express MKLP1-GFP were immunostained for endogenous Cavin1. Scale bar, 2 µm.

(B) *Left panels:* Localization of endogenous Cavin1 in HeLa cells stained with α-tubulin + acetylated- tubulin (hereafter "Tubulin") and DAPI at the indicated stage of cytokinesis. Scale bars, 10 µm (general views), 2 µm (insets). *Right panel:* Percentage of the indicated structures positive for endogenous Cavin1. Mean ± SD, n> 20 cells per condition. N = 3 independent experiments. MB: midbody.

(C) Scanning electron microscopy pictures of the intercellular bridge (left) and midbody (successive insets) at different magnifications of the indicated boxed regions. Red arrows point to membrane invaginations at the midbody. Scale bars, 10 µm (left), 500 nm (middle) and 100 nm (right).

(D) *Upper panel:* Scheme highlighting the position of the midbody (MB) within the intercellular bridge (approximately 5 µm above the substrate). *Bottom panels:* Transmission electron microscopy (TEM) pictures of a midbody (MB, electron dense part within the ICB) with the inset from the indicated boxed region showing caveolae (red arrow). Scale bars, 10 µm (left) and 100 nm (inset).

(E) *Upper panels:* Schemes highlighting the localization of the entry points (EP1, EP2), which correspond to the regions (red squares) at the intercellular bridge/cell interfaces. *Lower panels:* Two examples of endogenous staining for Cavin1, together with Tubulin and DAPI, in late bridges. Insets show different categories of Cavin1 localization at EPs: enriched, present or absent, as indicated. Scale bars, 10 µm. *Right panel:* Percentage of late bridges with/without secondary constriction where Cavin1 is enriched, present or absent at EPs, as indicated. Mean ± SD, n> 30 cells per condition. N = 3 independent experiments. One-sided Student's *t* tests. NS nonsignificant (P > 0.05).

(F) *Left panel:* scheme highlighting the localization of an EP region chosen for EM analysis. *Right panels:* TEM pictures of an EP region with the membrane of the ICB highlighted with red lines and caveolae marked with red arrows. The inset shows caveolae (red arrows) of the indicated boxed region. Scale bars, 10 µm and 100 nm (inset). In (D, F) the electron-dense (black) spots represent deposits of contrasting agents.

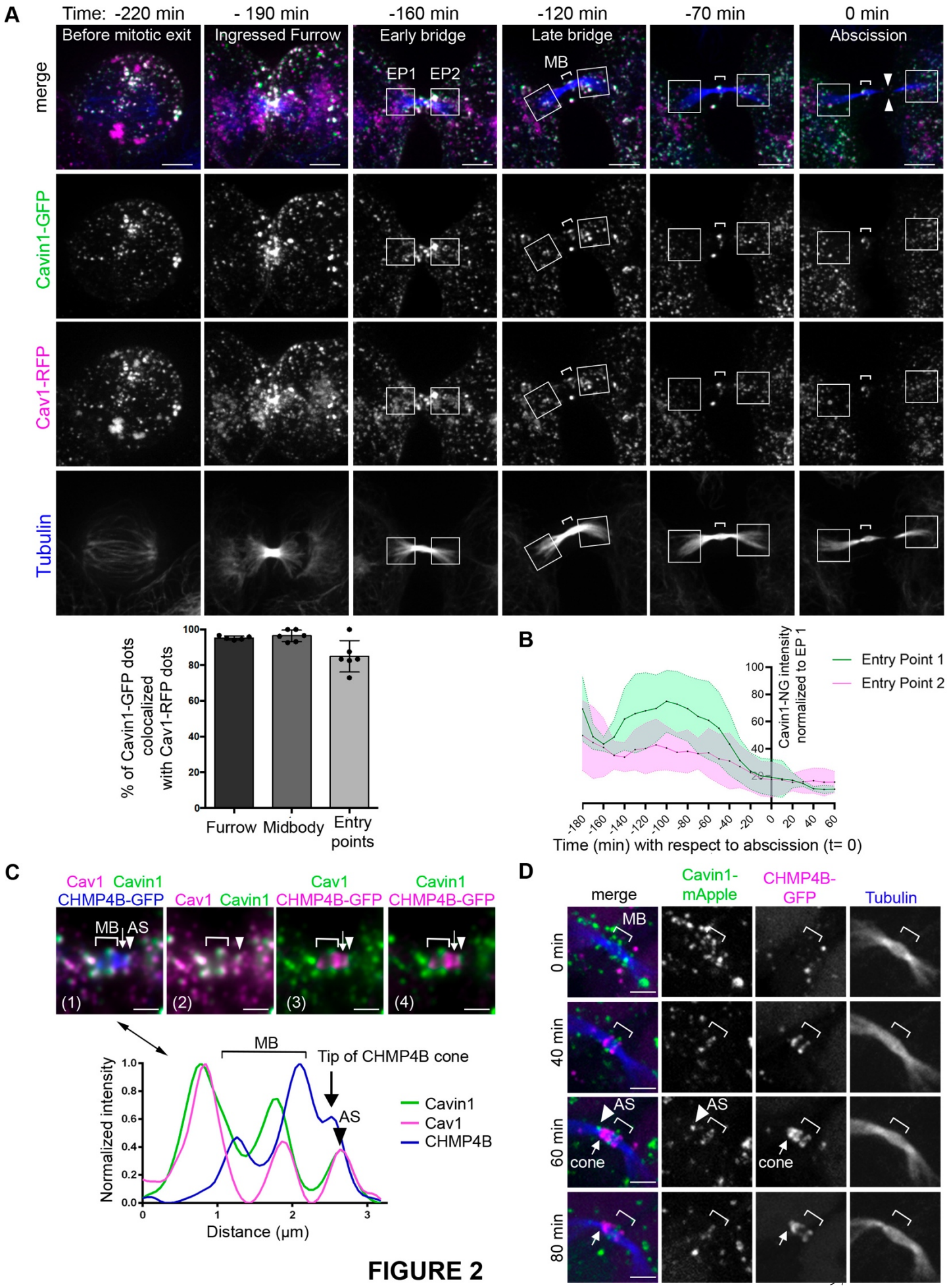
A
Time: -220 min
- 190 min
-160 min
-120 min
-70 min
0 min
Before mitotic exit
Ingressed Furrow
Early bridge
Late bridge
Abscission
EP1
EP2
MB
merge
Cavin1-GFP
Cav1-RFP
Tubulin
% of Cavin1-GFP dots colocalized with Cav1-RFP dots
Furrow
Midbody
Entry points
B
Cavin1-NG intensity normalized to EP 1
Entry Point 1
Entry Point 2
Time (min) with respect to abscission (t= 0)
C
Cav1 Cavin1 CHMP4B-GFP
Cav1 Cavin1
Cav1 CHMP4B-GFP
Cavin1 CHMP4B-GFP
MB
AS
(1)
(2)
(3)
(4)
Tip of CHMP4B cone
Normalized intensity
Distance (μm)
Cavin1
Cav1
CHMP4B
D
merge
Cavin1-mApple
CHMP4B-GFP
Tubulin
0 min
40 min
60 min
80 min
cone

FIGURE 2

Figure 2 – Cavin1 and Cav1 dynamically colocalize at the midbody, the EPs and the abscission site.

(A) *Upper panels:* Snapshots of a spinning-disk confocal microscopy movie of cells co-expressing Cavin1-GFP and Cav1-RFP. SiR-Tubulin was added for microtubule visualization. Squares delimit each EP and brackets indicate the position of the midbody (MB). Facing arrowheads mark the abscission site. Time 0 indicates the time of abscission. Note the progressive disappearance of Cavin1/Cav1 in EP regions as cells progress to abscission and their persistence at the MB. Scale bars, 5 µm. *Lower panel:* Percentage of Cavin1-GFP dots colocalizing with Cav1-RFP dots at the furrow, midbody and EPs. Mean ± SD, n= 6 movies of dividing cells.

(B) Intensity of Cavin1-GFP staining as a function of time at EP1 and EP2 in n= 10 cells throughout cytokinesis (see snapshots of a representative video in Fig. S2A). The brightest EP was defined as EP1 and the values of EP1 (green) and EP2 (magenta) were normalized to the maximum intensity observed in EP1 during cytokinesis for each cell analyzed. For comparison, all movies were registered with respect to the time of abscission (t= 0). Mean ± SD, n= 10 movies.

(C) *Upper panels:* Endogenous staining for Cav1 and Cavin1 in cells stably expressing CHMP4B-GFP, with a zoom centered on the ICB (1). Same bridge with only Cav1 and Cavin1 (2), Cav1 and CHMP4B (3) and Cavin1 and CHMP4B (4) channels displayed. Bracket: midbody (MB). Arrow: CHMP4B-GFP polymerizing cone. Arrowhead: abscission site where Cavin1/Cav1 dots co-localize at the tip of the CHMP4B cone. *Lower panels:* Intensity profiles along the bridge of the merged picture (1) with matched colors and symbols. Scale bars, 1 µm.

(D) Snapshots of a spinning-disk confocal microscopy movie of a cell expressing Cavin1-mApple and CHMP4B-GFP. SiR-Tubulin was added for microtubule visualization. Bracket: midbody (MB). Arrow: CHMP4B-GFP polymerizing cone. Arrowhead: abscission site (AS). Note that the Cavin1 dot at the tip of the CHMP4B cone disappears while the cone constricts the microtubules at the future abscission site. Scale bars, 2 µm.

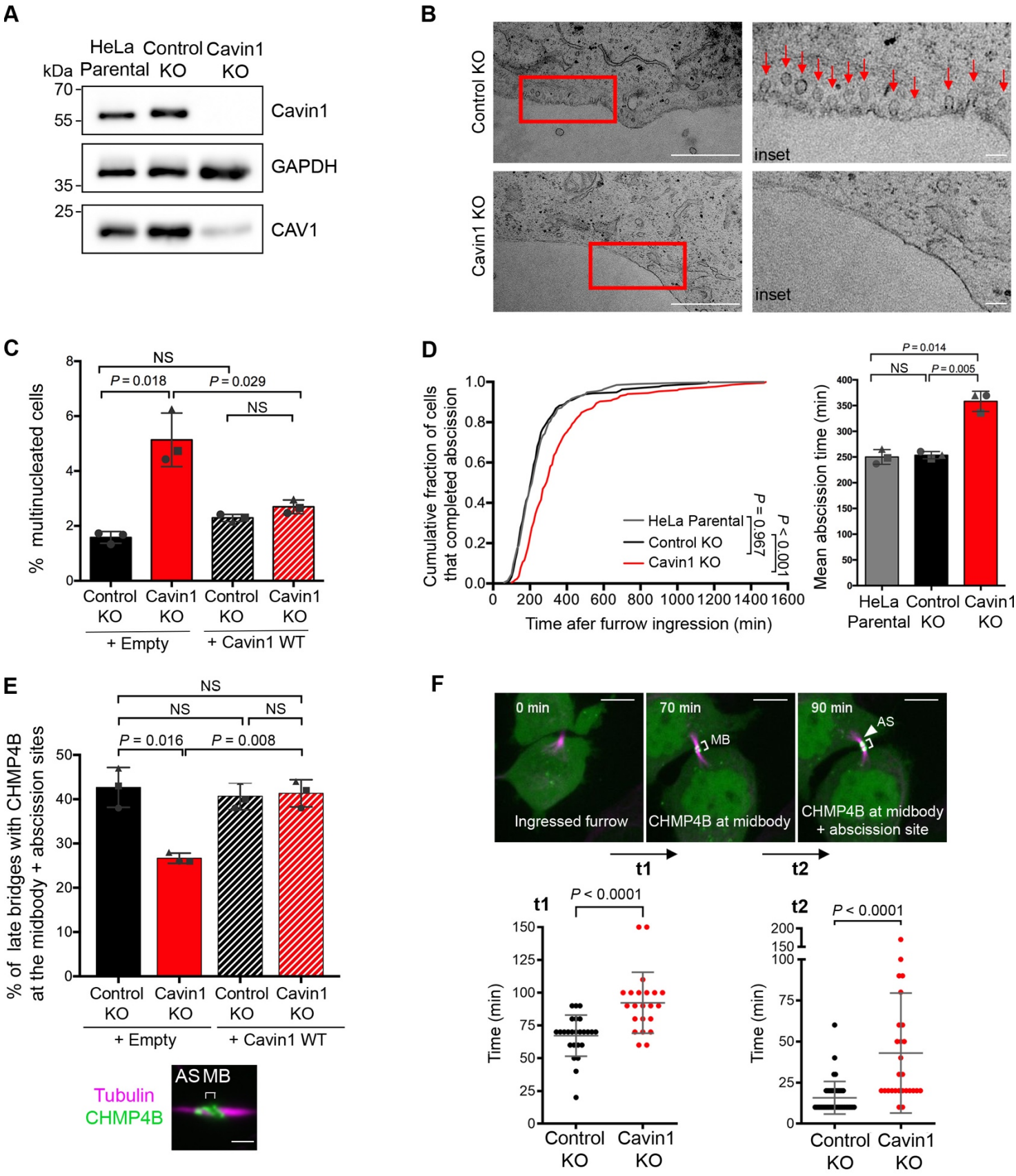
A
HeLa Parental
Control KO
Cavin1 KO
kDa
70
55
35
25
Cavin1
GAPDH
CAV1
B
Control KO
Cavin1 KO
inset
inset
C
% multinucleated cells
NS
P = 0.018
P = 0.029
NS
Control KO
Cavin1 KO
Control KO
Cavin1 KO
+ Empty
+ Cavin1 WT
D
Cumulative fraction of cells that completed abscission
HeLa Parental
Control KO
Cavin1 KO
P = 0.967
P < 0.001
Time afer furrow ingression (min)
Mean abscission time (min)
P = 0.014
NS
P = 0.005
HeLa Parental
Control KO
Cavin1 KO
E
% of late bridges with CHMP4B at the midbody + abscission sites
NS
NS
NS
P = 0.016
P = 0.008
Control KO
Cavin1 KO
Control KO
Cavin1 KO
+ Empty
+ Cavin1 WT
Tubulin
CHMP4B
AS
MB
F
0 min
70 min
90 min
AS
MB
Ingressed furrow
CHMP4B at midbody
CHMP4B at midbody + abscission site
t1
t2
t1
P < 0.0001
Time (min)
Control KO
Cavin1 KO
t2
P < 0.0001
Time (min)
Control KO
Cavin1 KO

FIGURE 3

Figure 3 – Depletion of Cavin1 impairs ESCRT-III localization and abscission.

(A) Lysates from parental HeLa cells, CRISPR/Cas9 Control KO and CRISPR/Cas9 Cavin1 KO were blotted for Cavin1, Cav1 and GAPDH (loading control).

(B) TEM micrographs of ultrathin sections of Control KO and Cavin1 KO cells. Insets from the boxed regions highlight the presence of caveolae (red arrows) in Control KO cells and absence of caveolae in Cavin1 KO cells (at least 10 individual cells were analyzed). Scale bars, 1 µm and 100 nm (insets).

(C) Percentage of Bi-/Multi-nucleated cells in Control KO and Cavin1 KO cells transfected with the indicated plasmids. Mean ± SD, n> 500 cells per condition. N = 3 independent experiments.

(D) *Left panel:* Cumulative distribution of the fraction of cells that completed abscission, measured by phase-contrast time lapse microscopy in HeLa Parental, Control KO and Cavin1 KO cells. *P* values from nonparametric and distribution-free Kolmogorov–Smirnov [KS] tests. *Right panels:* Mean abscission times (min) ± SD in indicated cells, with n> 60 cells per condition. N = 3 independent experiments.

(E) The proportion of late cytokinetic bridges with endogenous CHMP4B localized both at the midbody and at the abscission site (see representative image) was quantified in Control KO and Cavin1 KO cells transfected with indicated plasmid. Mean ± SD, n > 30 cells per condition. N = 3 independent experiments. Arrowhead: abscission site (AS); midbody (MB): bracket. Scale bar, 2 µm.

(F) *Upper panels:* Control KO and Cavin1 KO cells stably expressing CHMP4B-GFP were recorded by spinning-disk confocal time-lapse microscopy. The time taken from cleavage furrow ingression (t= 0 min) to CHMP4B-GFP recruitment at the midbody defines **t1;** and time from CHMP4B-GFP at the midbody to CHMP4B-GFP at midbody + abscission site defines **t2.** Brackets: midbody (MB). Arrowhead: CHMP4B polymerizing toward the future abscission site. Scale bars, 5 µm. *Lower panels:* Times (min) ± SD for t1 and t2 in Control KO and Cavin1 KO. n> 23 cells per condition. N = 4 independent experiments.

In (C), (D) and (E): Two-sided Student's *t* tests. In (F): Unpaired Student's *t* tests. NS non-significant (P > 0.05).

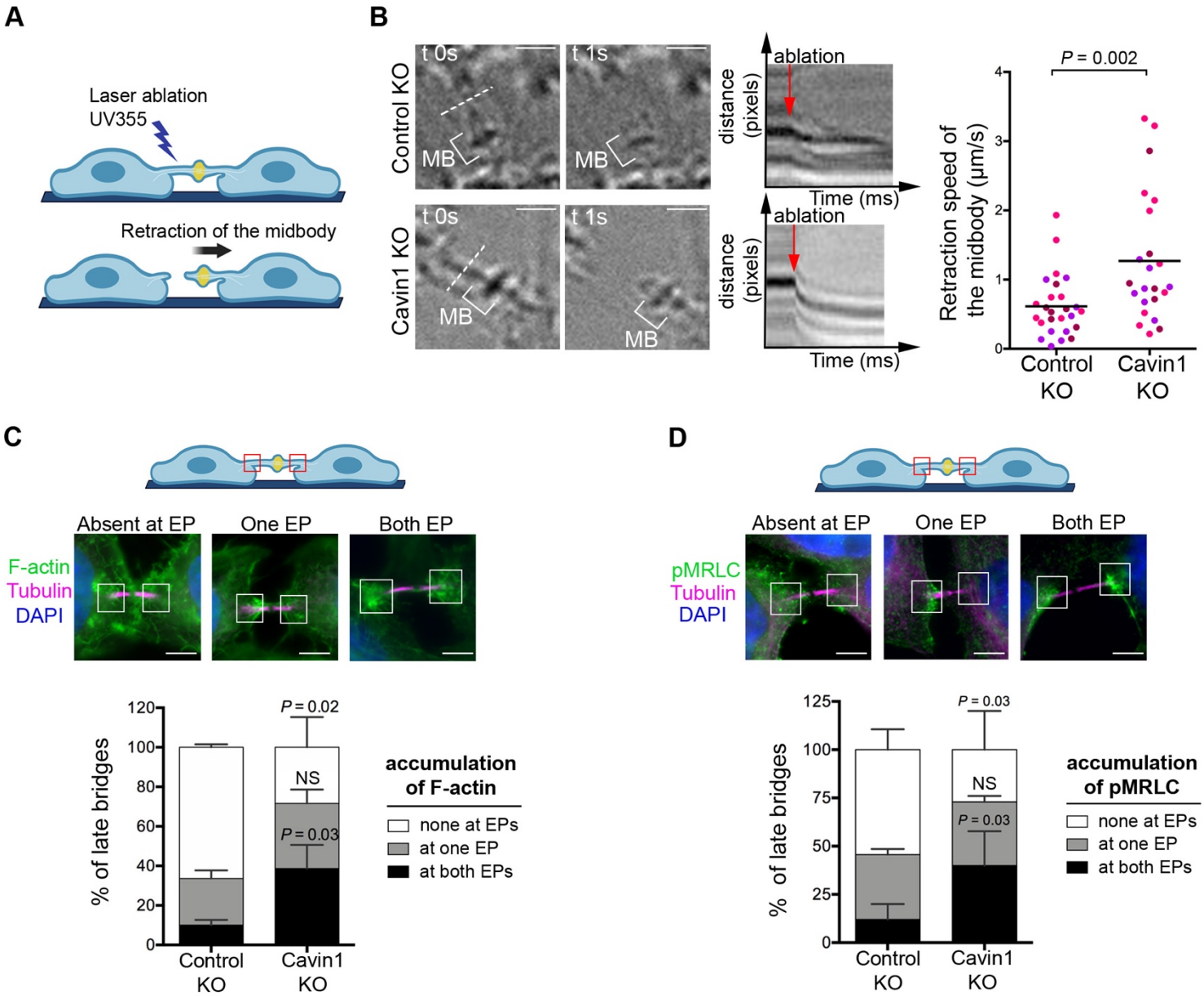
A
Laser ablation
UV355
Retraction of the midbody
B
Control KO
Cavin1 KO
t 0s
t 1s
MB
ablation
distance (pixels)
Time (ms)
P = 0.002
Retraction speed of the midbody (µm/s)
Control KO
Cavin1 KO
C
Absent at EP
One EP
Both EP
F-actin
Tubulin
DAPI
% of late bridges
P = 0.02
NS
P = 0.03
accumulation of F-actin
none at EPs
at one EP
at both EPs
Control KO
Cavin1 KO
D
Absent at EP
One EP
Both EP
pMRLC
Tubulin
DAPI
% of late bridges
P = 0.03
NS
P = 0.03
accumulation of pMRLC
none at EPs
at one EP
at both EPs
Control KO
Cavin1 KO
E
Cavin1-NG pMRLC Tubulin
EP1
EP2
Cavin1-NG
pMRLC
EP1 * **
EP2 * **
Normalized intensity
distance (pixels)
pMRLC
Tubulin
Cavin1-NG
F
Pixel intensity pMRLC (a.u)
Pixel intensity Cavin1-NG (a.u.)
a
b

FIGURE 4

Figure 4 – Caveolae limit acto-myosin II at the Entry Points and control ICB tension during cytokinesis.

(A) Scheme illustrating the laser ablation experiment. A laser-induced ablation of a tensed ICB results in a retraction of the midbody toward the side opposite to the cut.

(B) *Left Panels:* Snapshots of ICBs from Control KO and Cavin1 KO cells, before (t0) and after the laser ablation (t0 + 1 sec). The corresponding kymographs are displayed, with red arrows marking the moment of ablation. Dotted line: position of the laser cut. Brackets: midbody (MB). Scale bars, 2 µm. *Right Panel:* Retraction speed (µm/s) of midbodies in Control KO and Cavin1 KO ablated bridges. Horizontal bar: Mean, n= 23-24 ICBs from N = 3 independent experiments (represented with different colors). Unpaired Student's *t* tests.

(C) *Upper Panels:* The accumulation of endogenous F-actin staining (fluorescent phalloidin) in EPs in late cytokinetic bridges was classified in three categories: none, at one EP and at both EPs, as shown in representative images. Scale bar, 5 µm. *Lower Panels:* Percentage of late bridges for each F-actin category in Control KO and Cavin1 KO cells. Mean ± SD, n > 20 cells per condition. N = 3 independent experiments. Paired Student's *t* tests. NS nonsignificant (P > 0.05).

(D) *Upper Panels:* The accumulation of endogenous pMRLC staining in EPs of late cytokinetic bridges was classified in three categories: none, at one EP and at both EPs, as shown in representative images. Scale bars, 5 µm. *Lower Panels:* Percentage of late bridges for each pMRLC category in Control KO and Cavin1 KO cells. Mean ± SD, n > 30 cells per condition. N = 3 independent experiments. Paired Student's *t* tests. NS nonsignificant (P > 0.05).

(E) *Left panels:* Endogenous pMRLC and Tubulin staining in a Cavin1-NeonGreen stable cell line, with a zoom centered on the ICB. Scale bars, 2 µm. *Right panels:* intensity profiles of the EP1 and EP2 regions, as in indicated in the merged picture with matched colors symbols.

(F) Pixel intensity of pMRLC (y axis) and Cavin1-NG (x axis) at the whole EP1 and EP2 from (E).

Box a: high pMRLC/low Cavin1 intensity pixels; Box b: high Cavin1/low pMRLC intensity pixels.

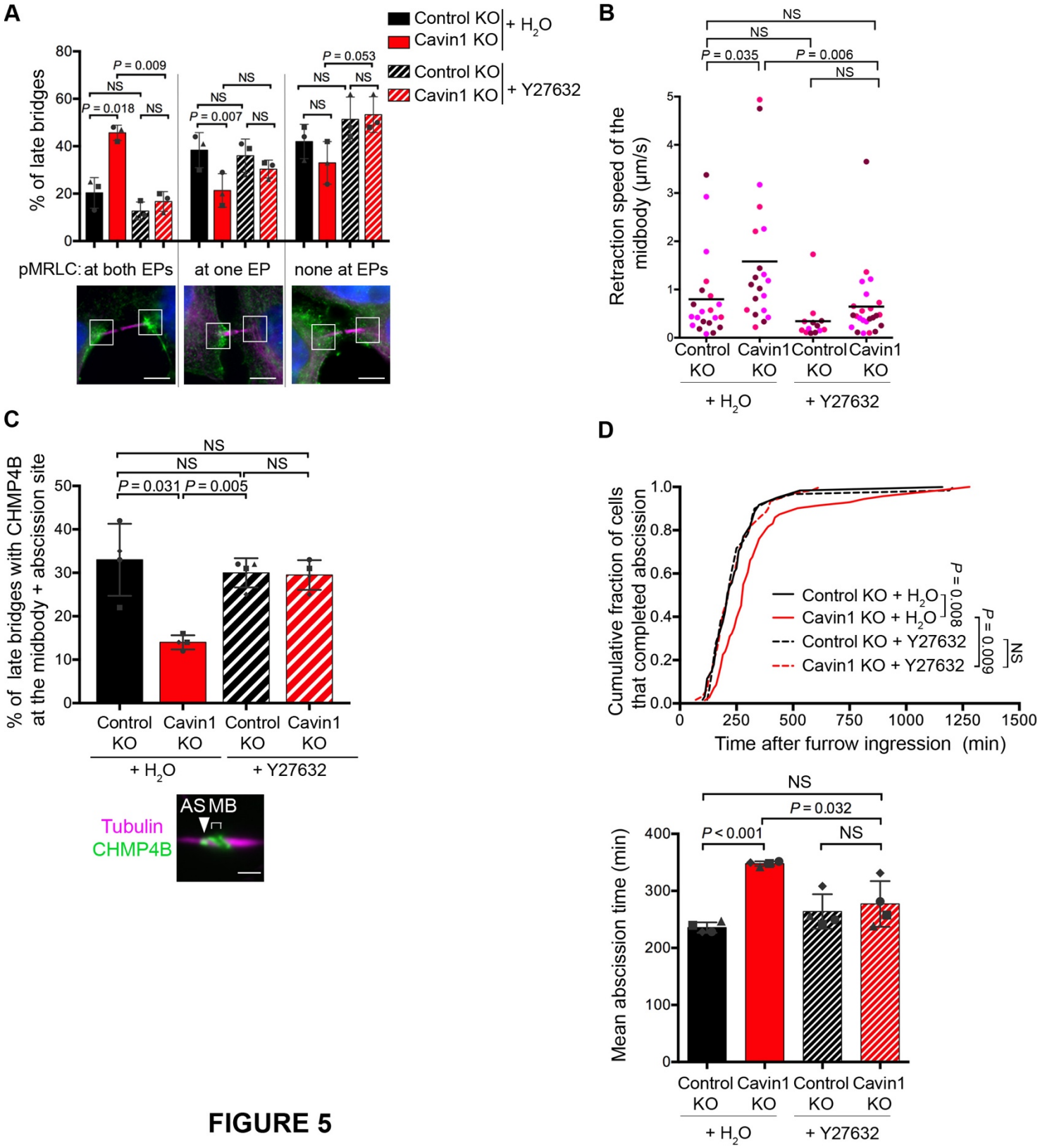
A
Control KO
Cavin1 KO
+ H2O
Control KO
Cavin1 KO
+ Y27632
% of late bridges
P = 0.009
NS
P = 0.018
NS
NS
P = 0.007
NS
NS
P = 0.053
NS
NS
NS
pMRLC: at both EPs
at one EP
none at EPs
B
Retraction speed of the midbody (µm/s)
NS
NS
P = 0.035
P = 0.006
NS
Control KO
Cavin1 KO
Control KO
Cavin1 KO
+ H2O
+ Y27632
C
% of late bridges with CHMP4B at the midbody + abscission site
NS
NS
NS
P = 0.031
P = 0.005
Control KO
Cavin1 KO
Control KO
Cavin1 KO
+ H2O
+ Y27632
Tubulin
CHMP4B
AS
MB
D
Cumulative fraction of cells that completed abscission
Control KO + H2O
Cavin1 KO + H2O
Control KO + Y27632
Cavin1 KO + Y27632
P = 0.008
P = 0.009
NS
Time after furrow ingression (min)
Mean abscission time (min)
NS
P = 0.032
P < 0.001
NS
Control KO
Cavin1 KO
Control KO
Cavin1 KO
+ H2O
+ Y27632

FIGURE 5

Figure 5 – Increased ICB tension upon Cavin1 depletion is responsible for the cytokinetic defects.

(A) Quantification of pMRLC localization at the EP as in Fig. 4D (same representative pictures, Scale bars, 5 µm) in Control KO and Cavin1 KO cells, treated or not with the ROCK inhibitor Y27632. Horizontal bar: Mean ± SD, n> 30 cells per condition. N = 3 independent experiments (represented with different colors).

(B) Retraction speed (µm/s) of midbodies in Control KO and Cavin1 KO ablated bridges, treated or not with the ROCK inhibitor Y27632. Mean, n> 12 ICBs from N = 3 independent experiments. Unpaired Student's *t* tests. NS non-significant (P > 0.05).

(C) CHMP4B localization was quantified as in Fig. 3E (same representative pictures, Scale bars, 2 µm) in Control KO and Cavin1 KO cells, treated or not with the ROCK inhibitor Y27632. Mean ± SD, n> 30 cells per condition. N = 3 independent experiments.

(D) *Upper panel:* Cumulative distribution of the fraction of cells that completed abscission, measured by phase-contrast time lapse microscopy in Control KO and Cavin1 KO cells, treated or not with the ROCK inhibitor Y27632. *P* values from nonparametric and distribution-free Kolmogorov–Smirnov [KS] tests. NS non-significant (*P* > 0.05). *Lower panel:* Mean abscission times (min) ± SD in indicated cells, with n> 60 cells per condition. N = 4 independent experiments.

In (A), (C) and (D): paired Student's *t* tests. NS non-significant (*P* > 0.05).

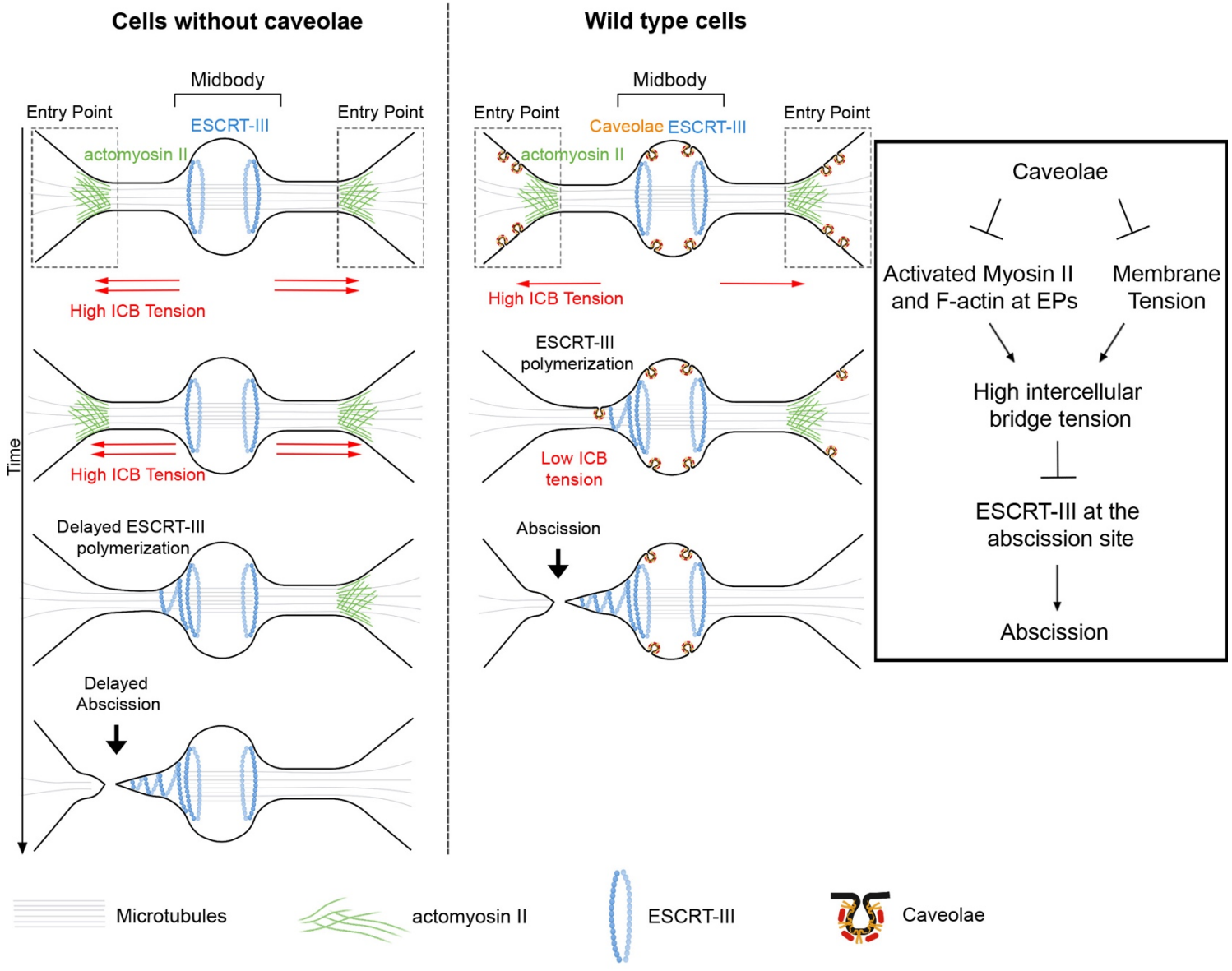
Cells without caveolae
Wild type cells
Midbody
Entry Point
ESCRT-III
Caveolae
actomyosin II
High ICB Tension
Time
Delayed ESCRT-III polymerization
Delayed Abscission
ESCRT-III polymerization
Low ICB tension
Abscission
Caveolae
Activated Myosin II and F-actin at EPs
Membrane Tension
High intercellular bridge tension
ESCRT-III at the abscission site
Abscission
Microtubules
actomyosin II
ESCRT-III
Caveolae

FIGURE 6

Figure 6 – Model: Caveolae limit ICB tension by limiting the F-actin/myosin II-dependent contractility and membrane tension, thereby promoting ESCRT-III polymerization and successful abscission.

Left panel: situation in cells without caveolae (e.g. Cavin1 KO cells). Right panels: situation in cells with caveolae (wild type cells). *Box:* proposed mechanism for the control of abscission by caveolae.

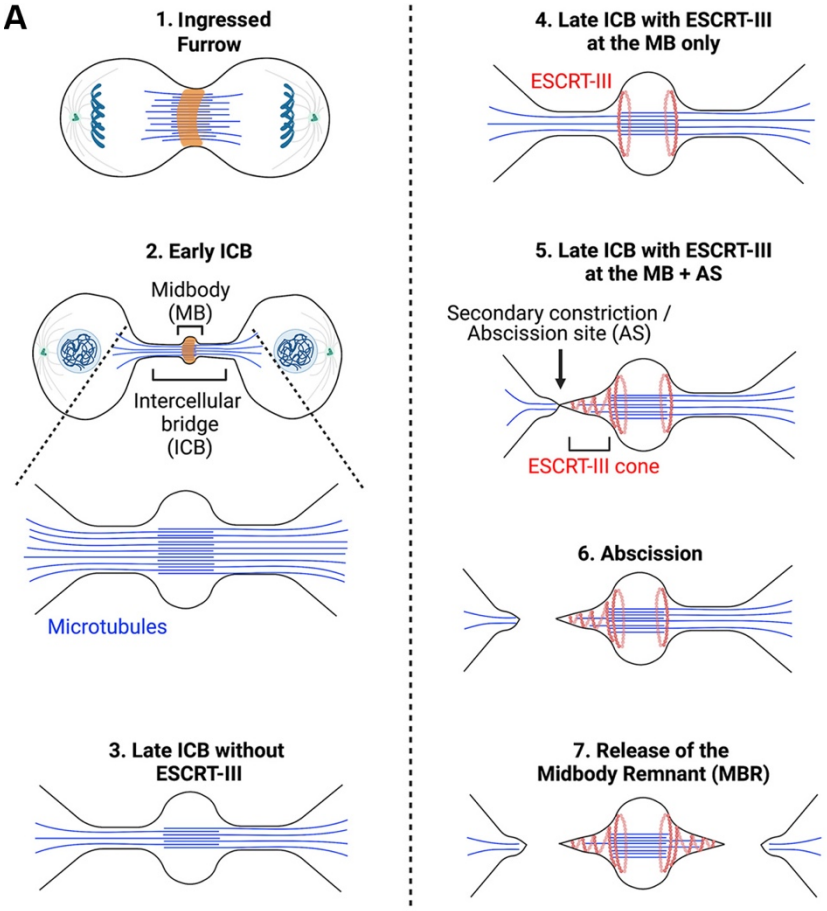

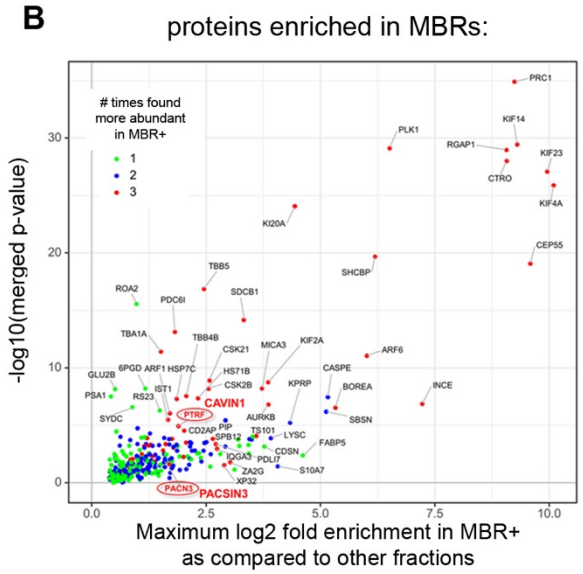

caveolae components present in MBRs:

caveolin-1
PACSIN2
Cavin3
EHD2

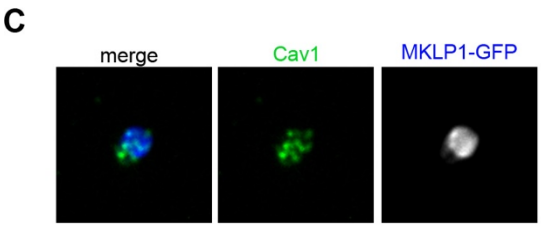

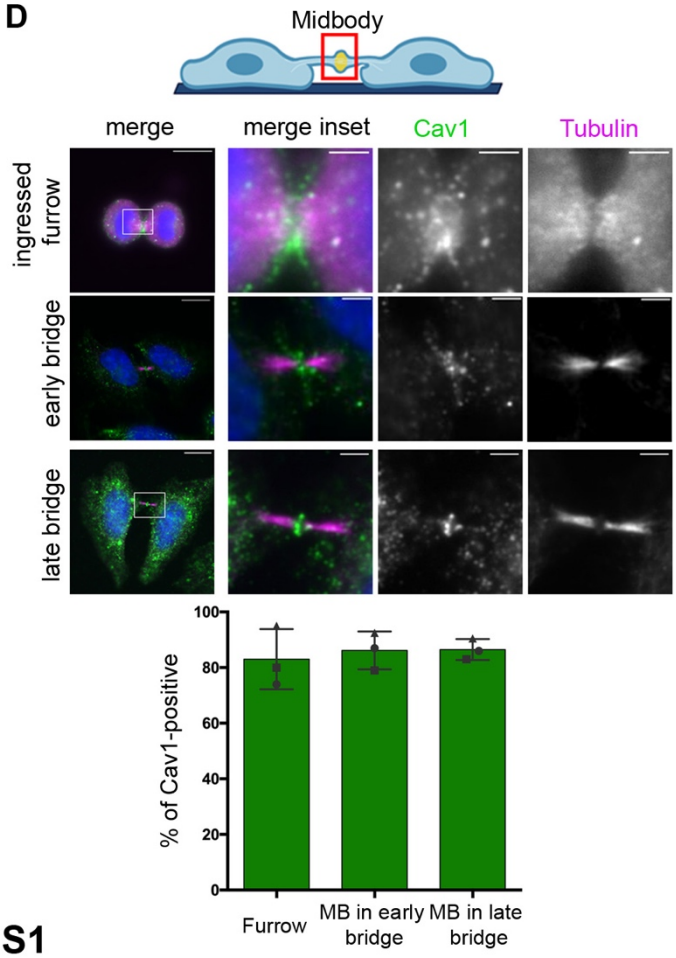

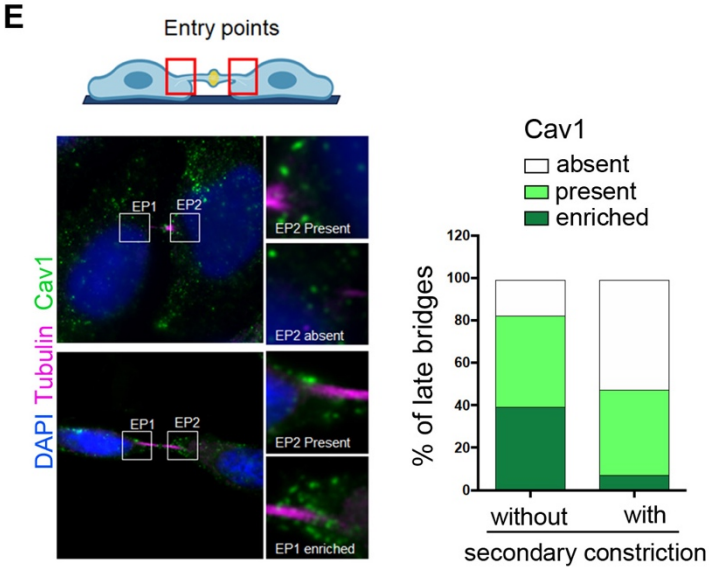

FIGURE S1

Figure S1 – Cavin1 and Cav1 localization during cytokinesis.

(A) Scheme depicting the successive phases of cytokinesis and the main definitions used in this paper. Note the different steps of ESCRT-III polymerization until abscission. A midbody remnant (MBR) is released after abscission on both sides of the midbody.

(B) Merged volcano plot of the mass spectrometry analysis described and showing the *Enriched Flemmingsome* of HeLa cells. See details in (*37*). The caveolae components CAVIN1 and PACSIN3, which have been found enriched in MBRs are highlighted in red. Briefly, MBRs have been purified by flow cytometry from HeLa cells expressing the midbody marker MKLP1-GFP (MBR+ fraction). The plot shows the maximum log2(fold change) in *x*-axis measured between MBR+ purified fractions and the other fractions (either total cell lysates, MBRs enriched by centrifugation but not pure or GFP-negative fraction) and the corresponding –log10(merged p value) in *y*-axis. Color code: proteins significantly enriched in MBR+ when compared with 3 (red), 2 (blue), or 1 (green) of the other fractions. The other components of caveolae that are present but not enriched in the MBRs are listed on the right.

(C) Purified midbody remnants from HeLa cells that stably express MKLP1-GFP were immunostained for endogenous Cav1. Scale bar, 2 µm.

(D) *Upper panels:* Localization of endogenous Cav1, Tubulin, DAPI in HeLa cells at the indicated stage of cytokinesis. Scale bars, 10 µm (general views), 2 µm (inset). *Lower panel:* Percentage of the indicated structures positive for endogenous Cav1. Mean ± SD, n> 30 cells per condition. N = 3 independent experiments.

(E) *Left panels:* Endogenous staining for Cav1, together with Tubulin and DAPI, in late bridges. Insets show different categories of Cav1 localization at EPs: enriched, present or absent, as indicated. Scale bars, 10 µm. *Right panel:* Percentage of late bridges with/without secondary constriction where Cavin1 is enriched, present or absent at EPs, as indicated. Mean ± SD, n> 40 cells per condition.

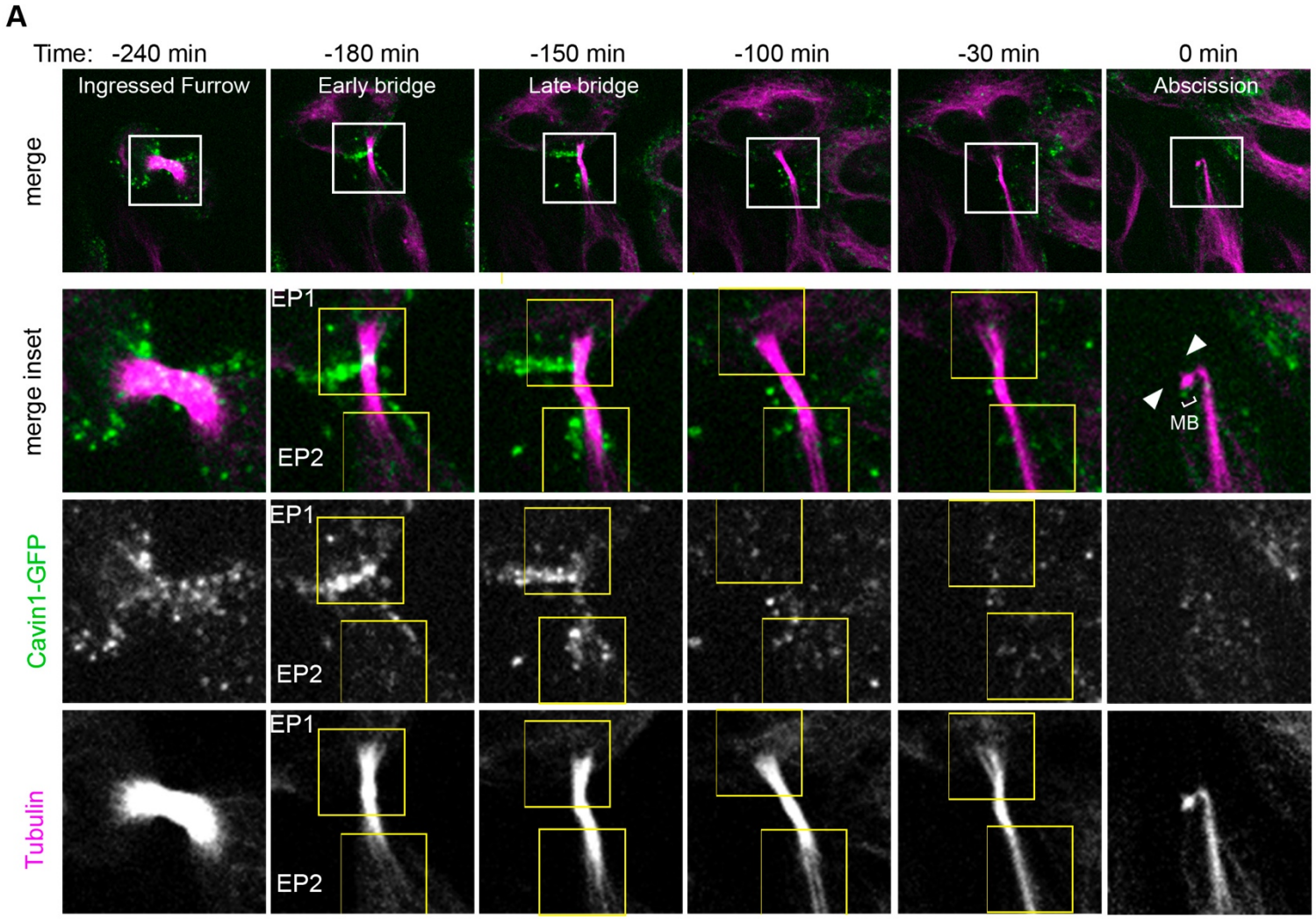
A
Time: -240 min
-180 min
-150 min
-100 min
-30 min
0 min
Ingressed Furrow
Early bridge
Late bridge
Abscission
merge
merge inset
Cavin1-GFP
Tubulin
EP1
EP2
MB

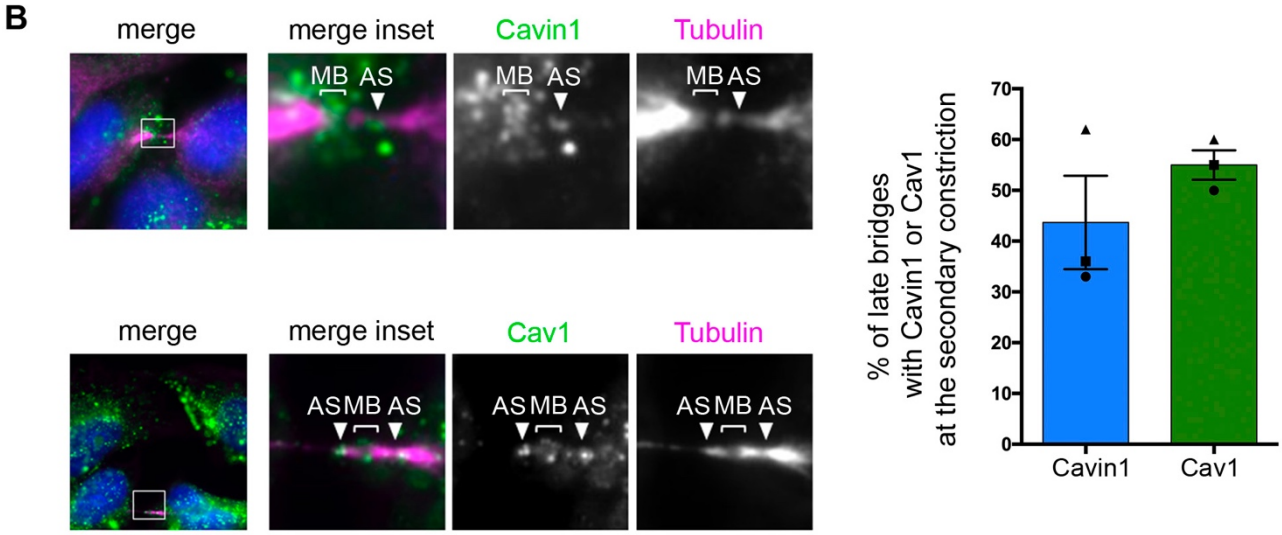
B
merge
merge inset
Cavin1
Tubulin
MB AS
Cav1
AS MB AS
% of late bridges with Cavin1 or Cav1 at the secondary constriction
70
60
50
40
30
20
10
0
Cavin1
Cav1

FIGURE S2

Figure S2 – Cavin1 disappears from the EPs and the abscission site before abscission.

(A) Snapshots of a spinning-disk confocal microscopy movie of cells expressing Cavin1-GFP. SiR-Tubulin was added for microtubule visualization. Regions shown in the insets correspond to the white boxes. Abscission occurred at Time 0 min. Yellow squares delimit each EP and facing arrowheads mark the microtubule cut. Note the progressive disappearance of Cavin1 from EPs as cells progress to abscission and Cavin1 persistence at the MB. Scale bars, 5 µm.

(B) *Upper left panels:* Endogenous staining for Cavin1, showing its localization at the midbody (bracket, MB) and at the future abscission site (arrowhead, AS) denoted by the pinch in the Tubulin at this location Scale bars, 5 µm. *Lower left panels:* Endogenous staining for Cav1, showing its localization at the midbody and at abscission sites. Scale bars, 5 µm. *Right panel:* Percentage of late bridges with Cavin1 or Cav1 localized at the future abscission site / secondary constriction. Mean ± SD, n> 30 cells per condition. N = 3 independent experiments.

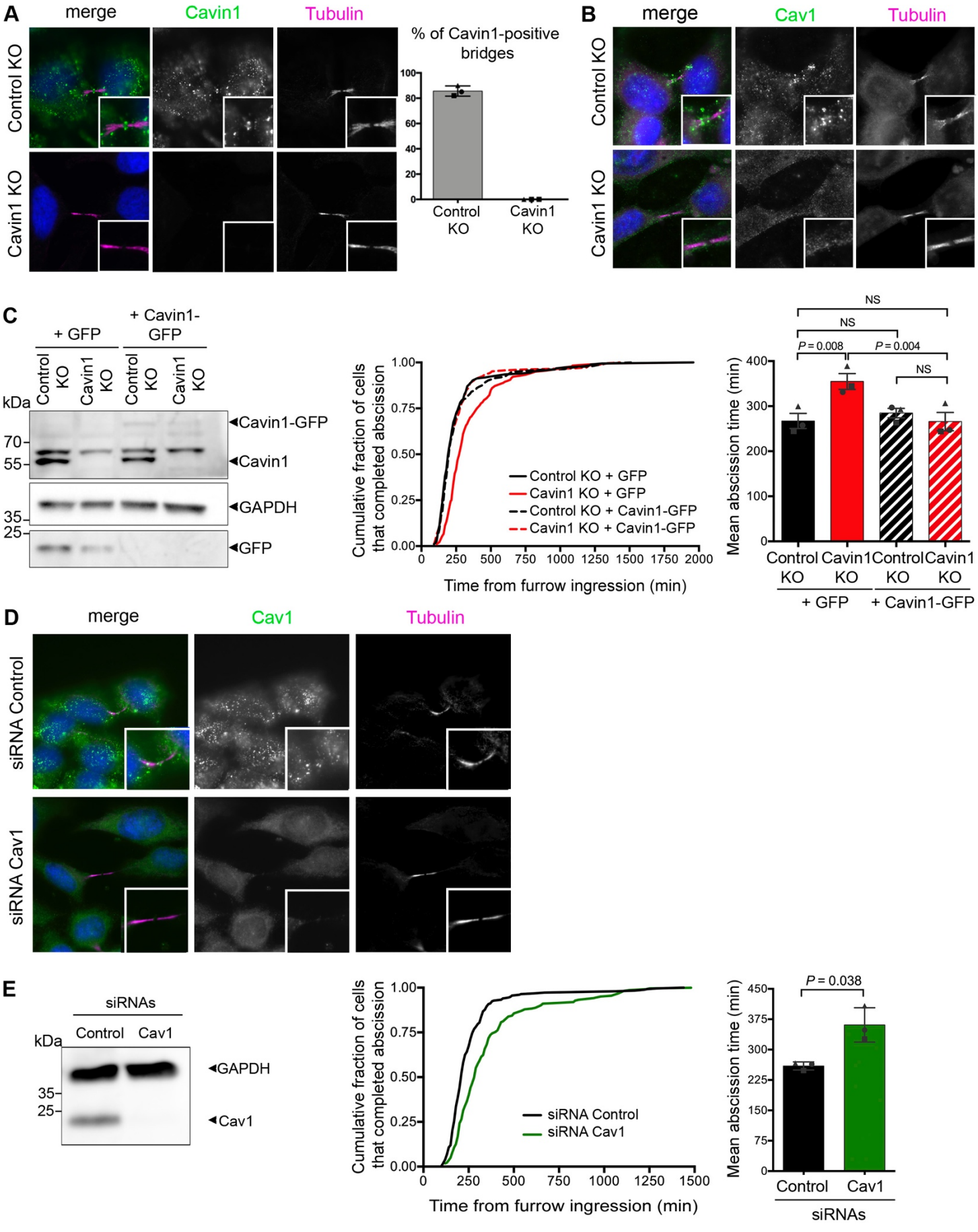
A
merge
Cavin1
Tubulin
Control KO
Cavin1 KO
% of Cavin1-positive bridges
100
80
60
40
20
0
Control KO
Cavin1 KO
B
merge
Cav1
Tubulin
Control KO
Cavin1 KO
C
+ GFP
+ Cavin1-GFP
Control KO
Cavin1 KO
Control KO
Cavin1 KO
kDa
70
55
35
25
Cavin1-GFP
Cavin1
GAPDH
GFP
Cumulative fraction of cells that completed abscission
1.00
0.75
0.50
0.25
0.00
0
250
500
750
1000
1250
1500
1750
2000
Time from furrow ingression (min)
Control KO + GFP
Cavin1 KO + GFP
Control KO + Cavin1-GFP
Cavin1 KO + Cavin1-GFP
NS
NS
P = 0.008
P = 0.004
NS
Mean abscission time (min)
400
300
200
100
0
Control KO
Cavin1 KO
Control KO
Cavin1 KO
+ GFP
+ Cavin1-GFP
D
merge
Cav1
Tubulin
siRNA Control
siRNA Cav1
E
siRNAs
Control
Cav1
kDa
35
25
GAPDH
Cav1
Cumulative fraction of cells that completed abscission
1.00
0.75
0.50
0.25
0.00
0
250
500
750
1000
1250
1500
Time from furrow ingression (min)
siRNA Control
siRNA Cav1
P = 0.038
Mean abscission time (min)
450
375
300
225
150
75
0
Control
Cav1
siRNAs

FIGURE S3

Figure S3 – Cav1 depletion delays abscission. Specificity of the staining and rescue experiments.

(A) *Left panels:* Endogenous staining for Cavin1, Tubulin and DAPI in Control KO cells and Cavin1 KO cells. Insets of the intercellular bridge are displayed. *Right panel:* Percentage of midbodies at the intercellular bridge that are positive for Cavin1 in Control KO and Cavin1 KO cells. N = 3 independent experiments, n> 20 cells per condition. Scale bars, 10 µm.

(B) Endogenous staining for Cav1, Tubulin and DAPI in Control KO cells and in Cavin1 KO cells. Insets of the intercellular bridge are displayed. Scale bars, 10 µm.

(C) *Left panel:* Lysates from Control KO cells and Cavin1 KO cells transfected with either GFP or Cavin1-GFP, as indicated, were blotted for Cavin1 (upper part), GFP (lower part) and GAPDH (loading control). *Middle panel:* Cumulative distribution of the fraction of cells that completed abscission, measured by phase-contrast time lapse microscopy in Control KO and Cavin1 KO cells transfected with either GFP or Cavin1-GFP, as indicated. *P* values from nonparametric and distribution-free Kolmogorov–Smirnov [KS] tests. NS non-significant ($P > 0.05$). *Right panel:* Mean abscission times (min) ± SD in indicated cells, with n> 60 cells per condition. N = 3 independent experiments. Paired Student's t tests. NS non-significant ($P > 0.05$).

(D) Endogenous staining for Cav1, Tubulin and DAPI in Control and Cav1 siRNAs transfected cells. Scale bars, 10 µm.

(E) *Left panel:* Lysates from HeLa cells transfected with Control or Cav1 siRNAs were blotted for Cav1 and GAPDH (loading control). *Middle panel:* Cumulative distribution of the fraction of cells that completed abscission, measured by phase-contrast time lapse microscopy in Control and Cav1 depleted cells. *P* values from nonparametric and distribution-free Kolmogorov–Smirnov [KS] tests. NS non-significant ($P > 0.05$). *Right panel:* Mean abscission times (min) ± SD in indicated cells, with n> 60 cells per condition. N = 3 independent experiments. Two-sided paired Student's t tests. NS non-significant ($P > 0.05$).

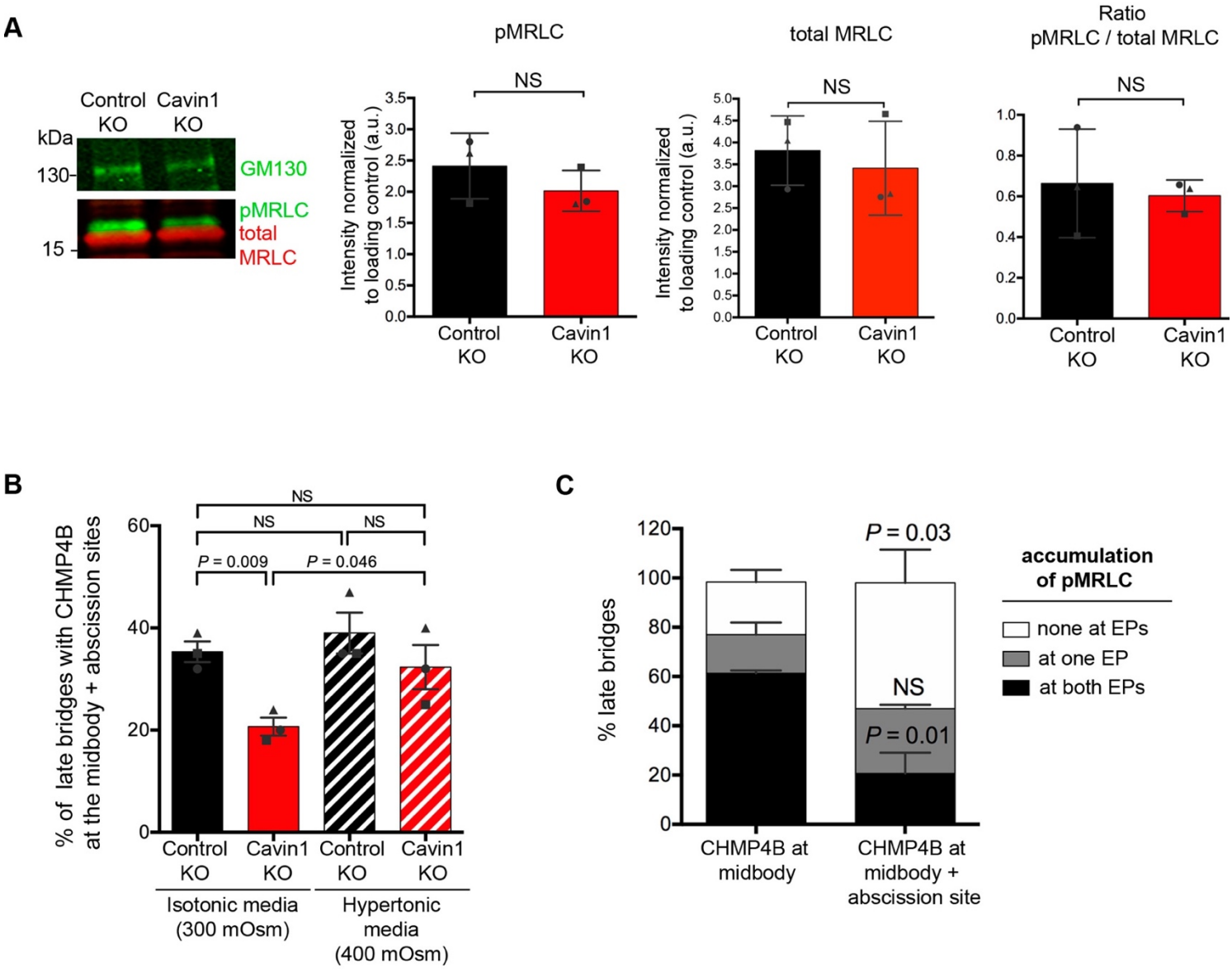
A
Control KO
Cavin1 KO
kDa
130
GM130
15
pMRLC
total MRLC
pMRLC
total MRLC
Ratio pMRLC / total MRLC
Intensity normalized to loading control (a.u.)
NS
Control KO
Cavin1 KO
B
% of late bridges with CHMP4B at the midbody + abscission sites
NS
NS
NS
P = 0.009
P = 0.046
Isotonic media (300 mOsm)
Hypertonic media (400 mOsm)
C
% late bridges
P = 0.03
NS
P = 0.01
CHMP4B at midbody
CHMP4B at midbody + abscission site
accumulation of pMRLC
none at EPs
at one EP
at both EPs

FIGURE S4

Figure S4 – Global levels of activated myosin II and actin are unchanged in the Cavin1 KO cells. Hyperosmotic shock rescues ESCRT-III localization at the abscission site in Cavin1 KO cells.

(A) *Left panel:* Lysates from Control KO cells and Cavin1 KO cells were blotted for pMRLC, total MRLC and GM130 (loading control). *Right panels:* quantification of the fluorescent westernblots presented above: pMRLC (normalized to GM130), total MRLC (normalized to GM130) and the ratio pMRLC / total MRLC. Mean ± SD, N = 3 independent experiments. Two-sided paired Student's t tests. NS non-significant ($P > 0.05$).

(B) Percentage of late bridges with CHMP4B localized both at the midbody and abscission site in Control KO cells and Cavin1 KO cells, either in isotonic media (300 mOsm) or hypertonic media (400 mOsm), as indicated. Mean ± SD, n> 34 bridges per condition. N = 3 independent experiments. Paired Student's t tests. NS non-significant ($P > 0.05$).

(C) Percentage of late bridges with pMRLC accumulation at one EP, two EPs or none at EPs, when CHMP4B is localized at the midbody only or both at the midbody and abscission site, in wild type HeLa cells. Mean ± SD, n= 11-28 bridges per condition. N = 3 independent experiments. Paired Student's t tests. NS non-significant ($P > 0.05$).

Protein	Company	Host	Name / clone	Dilution WB	Dilution IF	Fixation IF
Cavin1	Proteintech	rabbit	18892-1-AP	1/4000	1/2000	PFA, MeOH
CAV1	SantaCruz	mouse	(7C8) sc-53564		1/100	MeOH
CAV1	Abcam	rabbit	ab2910	1/4000		
CHMP4B	Proteintech	rabbit	13683-1-AP		1/500	MeOH
GAPDH	Proteintech	mouse	60004-1-Ig (1E6D9)	1/40 000		
GM130	Abcam	rabbit	EP892Y	1/2000		
RMLC	Sigma	mouse	M4401	1/1000		
pMRLC	Cell Signaling	rabbit	antibody #3671	1/1000	1/100	PFA
Actin	Chemicon, Merck		MAB1501	1/2000		
Tubulin	Institut Curie: Therapeutic recombinant antibodies platform	human	F2C-hFc2, VHHD5-hFc1, C3B9-hFc		1/200	PFA, MeOH
Phalloïdin 488	ThermoFisher Scientific	N/A	N/A	N/A	1/200	PFA
Phalloïdin 642	Cell Signaling Technology	N/A	N/A	N/A	1/200	PFA

Table S1

Table S1 – Antibodies and fluorescent probes used in this study.

MeOH: methanol fixation.

PFA: paraformaldehyde fixation.

Part III: Discussion

In this work, we have shown that the caveolae associated proteins CAV1 and Cavin1 are localized at the ingressed furrow, at the midbody and at the bridge/cell interface (entry points). Importantly, EM revealed the presence of *bona-fide* caveolae at these locations. Interestingly, caveolae at the bridge and entry points during cytokinesis proved to be important for successful cytokinesis. More specifically, the depletion of Cavin1 led to several cytokinetic defects: impaired ESCRT-III recruitment to the midbody and abscission site; delayed abscission and increased number of binucleated cells; increased tension at the intercellular bridge. These defects were corrected by the inhibition of the ROCK kinase to decrease the cortical tension of the daughter cells. Moreover, depletion of Cavin1 led to an increase of the actomyosin II network localized at the entry points. Similarly, this defect was rescued by the inhibition of ROCK. Altogether these data suggest that caveolae can buffer the tension at the intercellular bridge and limit the amount of actomyosin II recruited to the EP, which is important for effective ESCRT-III recruitment, subsequent abscission and successful cytokinesis. The mechanical regulation of cytokinesis remains largely unexplored, and our data reveal a mechanism that controls tension at the intercellular bridge. Finally, the regulation of the intercellular tension by caveolae represents one of the most upstream events that regulates the conclusion of cytokinesis.

I. Caveolae-associated proteins and caveolae localize at the intercellular bridge and entry points during cytokinesis

We have found that the minimal components to form caveolae, CAV1 and Cavin1 localize in the midbody remnants (manuscript Fig. 1A, S1A). This is consistent with their presence and enrichment in the midbody remnant proteomic study [1]. The localization of CAV1 at the ingressing furrow had been previously reported in Zebrafish blastomeres by immunofluorescence and in time-lapse video microscopy of MDCK II dividing cells using fluorescently tagged CAV1 but no further investigations were done. We characterized the spatio-temporal localization of Cavin1 and CAV1 during cytokinesis, performing endogenous stainings as well as time-lapse video microscopy. We found that not only CAV1 localizes at the furrow but also Cavin1. In addition, we found an unnoticed pool of these two proteins at the midbody in both early and late bridges (manuscript Fig. 1B and S1D), as well as at the bridge/cell interface, the "entry points". The localization Cavin1 and CAV1 at the entry points was striking and these two proteins are often enriched there (manuscript Fig. 1E). Importantly, the large extent of colocalization of Cavin1 with CAV1 at the midbody and entry points strongly suggested the presence of caveolae. Thanks to EM studies we confirmed that, indeed, *bona-fide* caveolae localize in these regions (manuscript Fig. 1D, F). Surprisingly, no previous studies had reported the localization of caveolae at intercellular bridges by EM, even though several electron micrographs have been done over the years in intercellular bridges [315]. This might be due to the use of stringent electron microscopy fixation that may have not preserved well the plasma membrane and thus did not allow visualization of caveolae at the midbody. In addition, since the midbody measures around 1.5 μm in diameter, and caveolae are invaginations of 50-100 nm, it is often difficult to find the correct section showing caveolae connected to the plasma membrane and not only a portion of the budded caveolae, which may look like a vesicle. We have not investigated whether other Cavin proteins or Caveolins are also present at the intercellular bridge. It would be interesting to study this by immunofluorescence and time-lapse video microscopy to understand whether there is a specific pool of caveolae-associated proteins localized at the bridge, or whether all components, Cavin2, 3 and Caveolin2 localize at the intercellular bridge. Although Cavin2, 3 and Caveolin2 have not been identified in the midbody remnant proteome by mass

spectrometry [1], they might be present albeit in low amounts and this remains to be experimentally investigated.

The pools of caveolae localized at the midbody and at the entry points seem to have different kinetics. Following the localization of CAV1 and Cavin1 in 10 min interval time-lapse video microscopy revealed that the pool of caveolae at the midbody seems to be stable and persist during cytokinesis (manuscript Fig. 2A). On the other hand, the caveolae at the entry points seem to be more dynamic, as they progressively disappear as the bridge matures towards abscission (Fig. 1E, 2A, B). Contrary to what was initially thought in the caveolae field, caveolae are dynamic structures that can display a kiss-and-run behaviour and be short-lived (such as 2 seconds, representing 1/3 caveolae population at the plasma membrane), or can be long-lived (localizing at the plasma membrane for more than 100 seconds) [218, 316]. In this study however, we did not assess the kinetics of caveolae at the midbody or entry points below the 10 min interval (cytokinesis takes about 250 min and we were interested in following the localization of the proteins all along cytokinesis). This would be an interesting point to address in order to understand whether the caveolae at the midbody are static (*i.e.* can be individually followed for long periods of time), and thus represent a new long-lived pool of caveolae at the plasma membrane. Another possible scenario is that the caveolae undergo recycling at the midbody and entry points, but maintain a consistent amount of caveolae there (or decreasing over time in the case of the entry points), and this cannot be measured in our 10 min interval time-lapse movies. Thus, performing fast acquisition movies (*i.e.* with 1 min intervals) at the midbody and entry points would be an interesting experiment to carry out.

This brings us to two fundamental questions:

(1) how are the caveolae formed at the furrow, midbody and entry points?

Recycling of caveolae (fission and fusion at the plasma membrane), lateral diffusion, or *de-novo* assembly of caveolae could all contribute to the presence of caveolae at the furrow, midbody and entry points. First, it has been reported that caveolae undergo intensive recycling during cell division [218], with caveolae being internalized during mitotic round up and reappearing at the plasma membrane during telophase, as shown by TIRF microscopy. Second, the specific lipid environment of the intercellular bridge, rich in PI(4,5)P2 [317] could promote the *de-novo* formation and stabilization of caveolae, as it has been shown previously [22, 201, 302, 318-320]. Since the furrow and the intercellular bridge are located

well above the substrate, the latter being approximately 5 µm above the substrate it is not possible to perform TIRF (total internal reflection fluorescence microscopy) to study the formation, fusion and fission of individual caveolae during cytokinesis. However, tracking of Cavin1/CAV1 positive dots at each stage of cytokinesis could prove useful to see appearance of caveolae at the plasma membrane and see if lateral diffusion of caveolae can occur, which could explain local concentration of caveolae in distinct pools. Additionally, one can turn to performing classic PH-sensitive assays of loaded Cholera Toxin B fluorescently tagged to distinguish between the recycling of caveolae from *de-novo* assembly, as performed in *Pelkmans et.al.* [316]

(2) How is the appearance/disappearance of caveolae being controlled?

The midbody proteome revealed the presence of CAV1, EHD2, Pacsin2, Cavin3, and enrichment of Cavin1 (3.5-fold) and Pacsin3 (3-fold). This suggests that EHD2, Pacsin2, Cavin3, and Pacsin3 may be localized at the midbody during cytokinesis. As introduced in Chapter II.2, EHD2, Cavin3 control the dynamics and morphology of caveolae, whereas Pacsins seem to facilitate the formation of caveolae [321]. We have not investigated the localization of these proteins at each step of cytokinesis. However, they might be involved in the regulation of the appearance/disappearance of caveolae at the furrow, midbody and entry points during cytokinesis. It is interesting to speculate that if there is a stable pool of caveolae at the midbody this can be due to the presence of EHD2 to stabilize caveolae at the plasma membrane there. In addition, as 1) the daughter cells undergo severe shape changes and divide under mechanical stress, and 2) EHD2 was described as a mechanotransducer, it is tempting to speculate that EHD2 might actively regulate the transcription of caveolae related genes during cytokinesis. Indeed, it was shown that EHD2 translocates to the nucleus upon mechanical stress (hypo-osmotic shock and cyclic stretch) and regulates the transcription of caveolae regulated genes [223]. However, whether this is possible to occur during the 3-4 h duration of cytokinesis has to be investigated. This would be fairly easy to assay by first checking the endogenous nuclear/cytoplasmic EHD2-ratio in cultured cells in interphase compared to cytokinetic cells in telophase before and after abscission. In contrast, caveolae that are more dynamic and short-lived, as potentially at the entry points for example, might be more enriched in Cavin3 that has been described to bind to Cavin1 and CAV1 and increases the surface dynamics of caveolae [322]. Indeed, Cavin3 down-regulation significantly increases caveolae stability at the plasma membrane (225-300s) and decreases the short-lived caveolae (0-30s). It would be interesting to perform live-cell imaging of

Cavin1 combined with each of the aforementioned proteins to understand the possible differential distribution of these caveolae-associated proteins.

Beside the dynamics of appearance/disappearance of caveolae during cytokinesis, it would be interesting to address the turnover of the caveolae components within caveolae found at the midbody and entry points. In the literature, FRAP experiments of fluorescently-tagged Cavin1 in interphase cells show a slow recovery (in 12 min less than 20% of the signal), in contrast to EHD2 that recovers 60% of the signal in 5 min [10, 170]. Thus, it would be interesting to access the recovery kinetics of at least these two proteins at the bridge and entry points. Finally, the enrichment of Pacsin3 is surprising at first since it is known to be a muscle-specific isoform. However, mRNA levels of Pacsin3 are annotated also in internal, secretory, and reproductive tissues such as in the uterus (https://www.genecards.org/cgibin/carddisp.pl?gene=PACSIN3#protein_expression).

II. Caveolae control the intercellular bridge tension during cytokinesis

a. Depletion of caveolae increases tension the intercellular bridge

During my thesis, I have generated a HeLa ATCC CRISPR/Cas9 Cavin1 knock-out (KO) cell line that has been used recently by our collaborators (Aurélien Roux's Lab, see Annex I for the publication). We reported in Annexe I (Fig. Suppl. 11) the full characterization at the genetic level of this cell line. HeLa cells have three Cavin1 alleles. In the Cavin1 KO cells, the CRISPR/Cas9 was targeted to the *Cavin1* gene and induced the following mutations: two alleles showed a 5-nucleotide deletion (revealed by genomic sequence and TOPO cloning of each allele), and one allele with a 368-nucleotide insertion (Annexe I, Fig. Suppl. 11). Both these mutations led to a predicted premature stop codon in the mRNA. Investigation of the mRNA levels in the Cavin1 KO cells revealed that the Cavin1 mRNA was undetectable, when compared to the control KO cells. This suggests that the Cavin1 mRNA undergoes non-sense mediated decay (NMD), which is in agreement with the loss of Cavin1 protein showed in western blot (Annexe I, Fig. Suppl. 11 and Fig. 3A of the main manuscript). We further confirmed that the Cavin1 expression was abolished in the Cavin1 KO cell line using immunofluorescence (Fig. 3a, S3a), in agreement with previous Cavin1 KO studies [161]. In addition, depletion of Cavin1 led to a decrease in CAV1 protein levels, and of CAV1 at the plasma membrane (Fig. 3a, S3b). This is consistent with previous work from *Liu.et al.,* showing that in Cavin1 KO mice, CAV1 protein levels decreased, but not the mRNA levels, suggesting a strong co-regulation of these proteins. Furthermore, the Cavin1 KO cells did not form caveolae or rosettes at the plasma membrane verified by EM (manuscript Fig 3B). Hence, this cell line is a valuable tool to study effects of the loss of caveolae in HeLa cells. Of note, the levels of protein expression of the other caveolae components, Cavins and Caveolins were not assessed. This could be done in the future using RT-PCR, and western blot.

We found that loss of caveolae in HeLa cells leads to delayed abscission (manuscript Fig. 3D) and increased binucleation (manuscript Fig. 3C). These are hallmarks of cytokinetic defects that are also observed upon depletion of key proteins required for cytokinesis, such as Rab11, CHMP4B or CEP55. This indicates that caveolae are important for successful cytokinesis. What is the exact function of caveolae in cytokinesis? Caveolae are known to

buffer plasma membrane tension in interphase cells (see Introduction Chapter II.5.2). In addition, as summarized in Chapter III.2, tension at the intercellular bridge inhibits ESCRT-III polymerization to the abscission sites. Thus, we hypothesized that if caveolae affect tension during cytokinesis, looking at ESCRT-III localization would be a first good read-out for abnormal intercellular tension. We found that ESCRT-III localization at the abscission site is impaired in caveolae-depleted cells (manuscript Fig.3E, F). Strikingly, laser ablation of Cavin1-depleted cytokinetic bridges leads to a 2-fold increase in tension on the intercellular bridge (manuscript Fig. 4B). These data strongly suggests that the cytokinetic defects observed in caveolae-depleted cells are due to abnormal tension during cytokinesis. As shown previously, laser ablation alone does not allow to distinguish whether this tension is due to an increase in cortical and/or membrane tension. Indeed, laser ablation allows a relative measurement of the cell tension at the bridge, thus we named it intercellular tension. It has been previously measured in HeLa cells that the bridge bears forces of 1.4 ± 0.2 nN using TFM (traction force microscopy) combined with laser ablation of the bridge (see Chapter III) [29]. In addition, attaching a bead to the bridge and pulling a membrane tube with optical tweezers was used to measure membrane tension at the bridge. The authors estimated that membrane tension contributed significantly to the forces being applied at the bridge being in order of 0.4 to 0.8 nN (see Chapter III) [29]. Importantly, reducing global contractility of caveolae-depleted cells rescued the abscission delay (Fig. 33), restored tension on the bridge, as well as ESCRT-III polymerization to the abscission sites, further discussed in section IV. This demonstrated that cytokinetic defects observed are due to increased tension at the bridge. From *Janvore-Lauforie et al.*, laser ablation of cytokinetic bridges on one side of the midbody (to artificially release tension), induces the ESCRT-III-Spastin pathway on the other side of the midbody and subsequent abscission. However, it remains unknown how Spastin and CHMP4B sense tension.

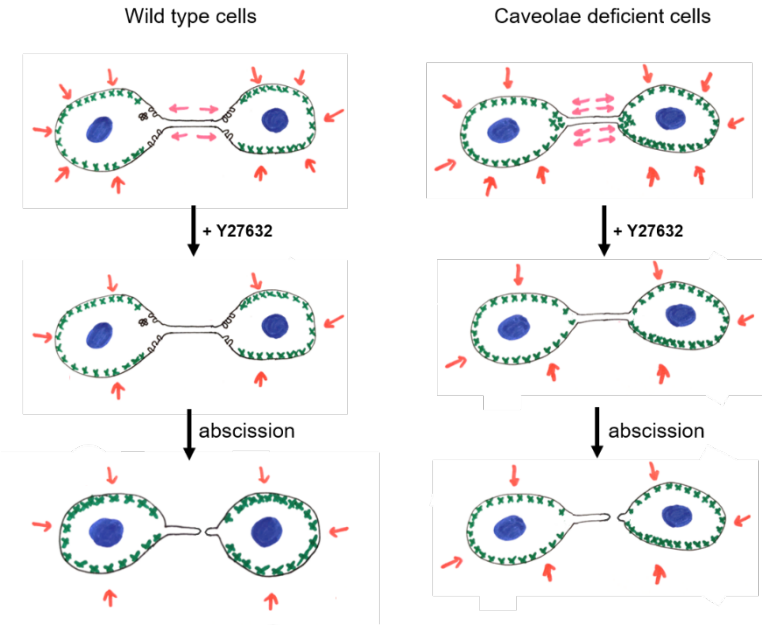

Figure 33 - Schematic of the effect of the ROCK kinase inhibition in the contractility of the cell (red arrows) and tension at the bridge (pink arrows) in wild type and caveolae deficient cells. Adding ROCK inhibitor Y27632 decreases the contractility of the cells (red arrows) as well as the actomyosin II pool at the entry points, especially in caveolae depleted cells. This leads to a decrease in the tension of the bridge, thus restoring normal abscission in caveolae depleted cells. Please note that differences in the arrows size or thickness do not indicate change in tension

In this paper, the authors demonstrated that by decreasing tension in the cells, abscission as well as the ESCRT-III recruitment to the abscission site are accelerated, but did not provide a molecular pathway that controls tension in the bridge. The authors nevertheless described that abscission can be regulated by the spatial confinement of the daughter cells. More specifically, cells dividing in a low-density environment, or growing in micropatterns to set an abnormally high distance between the daughter cells, leads to abscission delay. In these two cases, the authors suggest that the intercellular bridge looks taut because the microtubules at the bridge appear vey straight. In our case, we did not perform such experiments, but if one is to do these experiments with caveolae-depleted cells, I would expect to see an addictive effect, meaning enhanced delay in abscission. Note that in my experiments, I cultured and analysed caveolae-depleted and control cells always at the same cell density (intermediate cell confluency).

In the caveolae field, researchers try to dissociate caveolae functions from CAV1-depedent functions. Depletion of CAV1 in HeLa cells also led to a decrease in ESCRT-III

localization at the abscission sites (data not shown) as well as abscission delay (Fig. S3D). Together these data suggest a caveolae mediated function rather than a CAV1-mediated function is important for cytokinesis. This could be further investigated by laser ablating cytokinetic bridges in CAV1-depleted cells.

In addition, as we have confirmed that Cavin1 is localized at the bridge in other cell types, such as in the primary cells (BMEL), immortalized (RPE) and cancer cells (U2OS), it would be interesting to understand if these cells line exert on the intercellular bridge the same force as HeLa cells. How the localization and the dynamics of caveolae during cytokinesis may vary in cells depending on their specific tension in the bridge remains to be investigated.

III. Caveolae and membrane tension relationship at the intercellular bridge

Caveolae are known to buffer plasma membrane tension in interphase cells. In our work, we have not measured membrane tension, only inferred that the intercellular tension at the bridge is higher in caveolae-depleted cells. As stated above in section II, membrane tension also contributes to the tension at the bridge. Thus, we envisage that, in addition to regulate actomyosin II-dependent tension, as described below, caveolae present at the entry points and in the midbody could play a role in regulating membrane tension at the bridge as well. To test this hypothesis, I have tried to rescue the localization of ESCRT-III at the abscission sites by reducing membrane tension using a hyper-osmotic shock. Indeed, low membrane tension in the Cavin1-depleted cells leads to a normal localization of ESCRT-III at the midbody and abscission site, as quantified by immunofluorescence (manuscript Fig. S4D). This suggests that membrane tension is also increased in caveolae-deficient cells and that it is also important for abscission. It is likely that in wild type cells the disassembly of caveolae at the entry points helps reducing membrane tension at the intercellular bridge (further discussed in the section IV). However, we cannot exclude the possibility that the disassembly of caveolae elsewhere in the cell *(i.e.*, not only at entry points) may help buffering the intercellular tension.

The increase in membrane tension in caveolae-depleted cells could arise from an increase in the cortex contractility, a change in the lipid composition of the membrane, or changes in the osmotic pressure of the cell [256, 323]. In the future, it would thus be important to directly measure membrane tension at the bridge and at the entry points, versus the cell body, both in wild type and caveolae-deficient cells. Probing this parameter could be done by using atomic force microscopy (AFM) or by pulling membrane tethers. Note that in mitotic HeLa cells, it has been empirically measured that the cytoskeleton contributes little or not at all to the membrane tension, thus pulling the tethers measures only the in-plane tension [256]. Another way to measure membrane tension would be to use a recently-developed fluorescent membrane tension probe, the FliptR (Fluorescent LIPid Tension Reporter), to detect membrane tension changes of the plasma membrane in cytokinetic cells, using in live cell imaging [324]. Using the FliptR may be very interesting, as we would be able to distinguish areas of higher and lower membrane tension, for instance in the bridge, entry points and cell body during cytokinesis. It is noteworthy that in interphase cells, upon hypo-

osmotic shock, the Cavin1-depleted cells that I have generated display increased plasma membrane tension measured using the FliptR probe (Annex I Fig. 4C).

IV. Caveolae regulates actin-dependent cortical tension regulation during cytokinesis

a. The strategic localization of caveolae at the entry points could buffer the tension transmitted to the bridge

Unexpectedly, caveolae localize at the entry points and Cavin1 and CAV1 are often enriched there. Interestingly this enrichment disappears when the cells transit to a late stage before abscission (manuscript Fig. 1E, S1E). In addition, live-cell imaging revealed that the intensity of Cavin1-positive dots at the entry points starts to decrease 60 min before abscission and is very low in the 20 min prior to abscission (manuscript Fig. 2B). Adding to the fact that caveolae depletion leads to an increase in tension associated with defects in ESCRT-III localization, these observations argue for a strategic localization of caveolae at the entry points to regulate the tension that is transmitted to the bridge for two reasons:

(i) The spatio-temporal assembly of ESCRT-III at the abscission site is correlated with the loss of Cavin1 at the entry points in wild type cells. The kinetics of the ESCRT-III machinery during cytokinesis has been fairly studied. The formation of cone from the midbody to the abscission sites occurs 30-40 min before abscission, as shown in Fig. 34. In addition, as described in Chapter III, tension at the bridge decreases before abscission. Together, this suggests a mechanical coupling of the ESCRT-III polymerization and the decrease in tension at the intercellular bridge due to caveolae unfolding at the entry points.

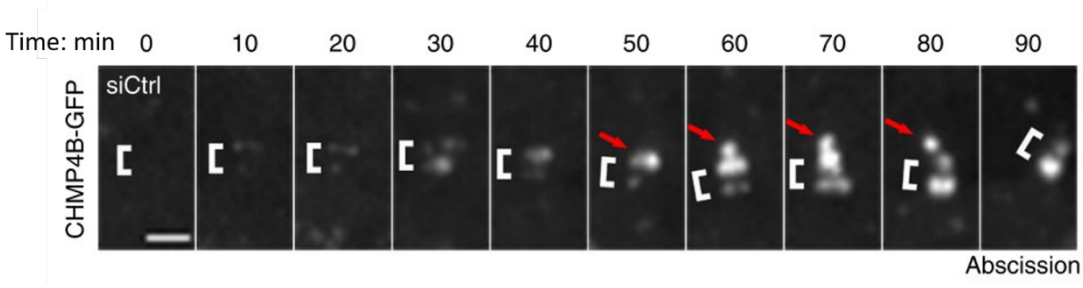

Figure 34 – HeLa cells stably expressing CHMP4B–GFP recorded by spinning-disk confocal time-lapse microscopy every 10 min. Zooms of the intercellular bridge are displayed. Time 0 corresponds to the frame preceding the arrival of CHMP4B at the midbody. Brackets mark the midbody. Arrows point toward pools of CHMP4B on the midbody side. Red arrows correspond to the CHMP4B leading to abscission (last time frame). From [1]

(ii) Caveolae localizing at the entry points inhibits contractility there. In *Janvore-Laufaurie et al.,* the authors proposed that tension on the bridge may come, at least in part, from the daughter cells pulling on the intercellular bridge while they respread on the substrate after furrow ingression. Since the daughter cells move and pull on the substrate, they also pull on the bridge. Interestingly, the authors noticed that the daughter cells stop moving apart 10 min before abscission (Fig. 35a). In addition, the contractile energy of the daughter cells reaches a plateau approximately 60 min before abscission (Fig. 35b), as measured using TFM.

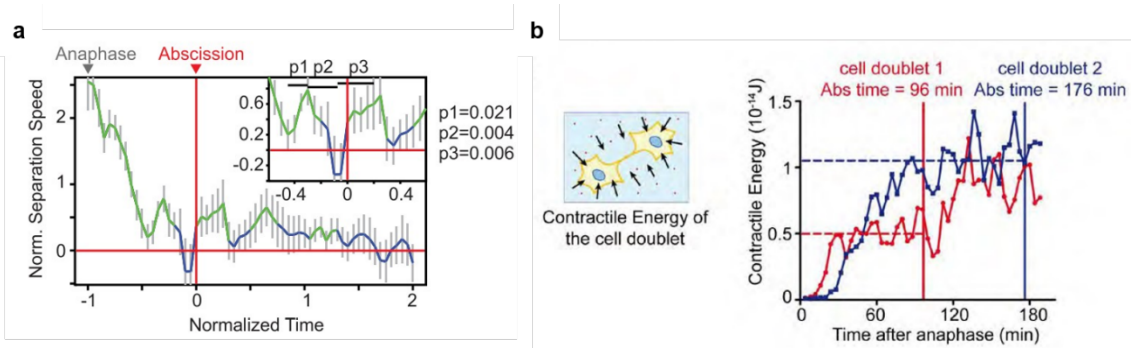

Figure 35 – Movement and contractility of the daughter cells. (a) Separation speed as a function of time (means ± SEM). Green line segments indicate separation speed significantly above 0. (b) Evolution of the Contractile Energy (10-14 Joules) after anaphase for two cell doublets (red and blue). Continuous lines show abscission, dotted lines show the plateau. From [1].

Taken together, the movement and contractility of the daughter cells during cytokinesis observed by *Janvore-Laufaurie et al.* are consistent with the decrease of caveolae at the entry points prior to abscission. More specifically these observations can suggest a role of caveolae at the entry points acting like springs that unfold to alleviate the tension nearby or at the intercellular bridge. This mechanism would buffer the tension on the bridge from the rest of the contractile cell (Fig. 36). The hypothesis of a spring-like caveolae at the entry points predicts that if one is to laser ablate the cytokinetic bridge (to reduce tension at the bridge and entry points), the entry points would become enriched in Cavin1 puncta. If this is not the case, it may suggest that perhaps the reaction of the cell to localize caveolae there may take some time; or that the entry points are no longer needed once the bridge has been cut, hence no increase in Cavin1 locally.

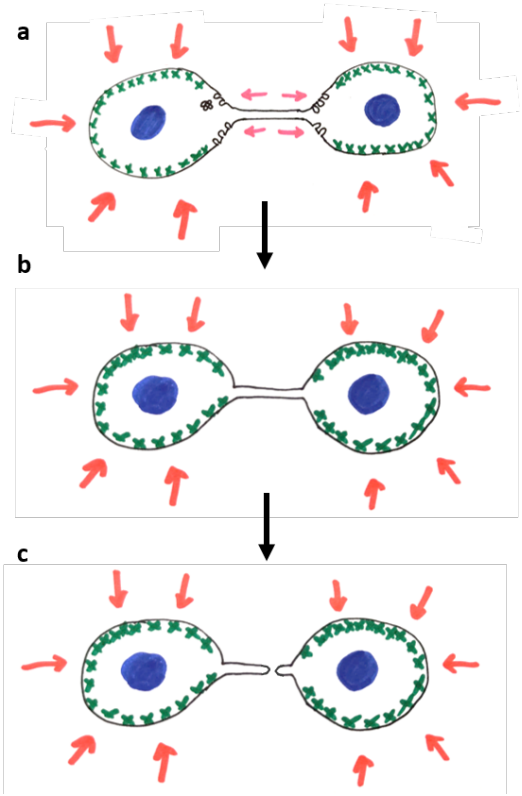

Figure 36 – Model proposed for the localization of caveolae at the entry points of the bridge. After furrow ingression the daughter cells are contractile (red arrows) and pull on the bridge (pink arrows) (a). Caveolae and rosettes stored at the entry points can unfold and reduce tension at the intercellular bridge (b), such that abscission can occur (c). ESCRT-III and midbody at the bridge not shown. Please note that differences in the arrows size or thickness do not indicate change in tension.

In addition, we have observed that the Cavin1- and CAV1-enriched entry points are often associated with a funnel shape of the plasma membrane. Whether this corresponds to a state of high or low local tension should be assessed using biophysical techniques such as membrane tube pulling. In addition, it would be interesting to artificially stretch daughter cells parallel or perpendicular to the intercellular bridge. This would allow us to directly test whether caveolae undergo rapid disassembly (measured by the loss of Cavin1). In addition, when the cells are released from the stretching, we would be able to follow the recovery of budded caveolae at the entry points and midbody.

We have also observed the localization of caveolae rosettes at the entry points using EM (not shown). It has been proposed that rosettes can represent extra membrane storage that is available to use in stress conditions. Interestingly, the rosettes have been proposed to respond to mechanical stress faster than individual caveolae in muscle fibres [325, 326]. As we have not observed rosettes at the intercellular bridge but only at the entry points, this favours a specific localization of these structures there. Thus, rosettes might start localizing

near the entry points of the cells while the cells are spreading to prepare for the subsequent response of caveolae at the entry points to buffer intercellular tension.

b. F-actin and activated myosin II (pMRLC) at the entry points in caveolae-deficient cells may increase the intercellular bridge tension

From the points mentioned above, the entry points seem to be important to control the tension transmitted to the bridge. As the membrane tension and actomyosin II contractility are closely related (Chapter III), what is the impact of caveolae loss on the cytoskeleton architecture? We have observed an increase in the F-actin and pRMLC at the entry points in caveolae-deficient cells (manuscript Fig. 4C, D). In addition, caveolae and activated myosin II were often excluded from each other (manuscript Fig. 4F). Is the increase in actomyosin II at the entry points responsible for the tension increase at the bridge in caveolae-depleted cells? Indeed, inhibition of ROCK kinase in caveolae-deficient cells decreased the number of pRMLC-positive entry points (Fig.33 and manuscript Fig. 5A), and restored normal tension at the bridge measured by laser ablation (manuscript Fig. 5B). First, this strongly suggests that the actomyosin II contractility at the entry points might be responsible for the tension increase in caveolae deficient cells. Second, these data argue for an inhibitory effect of caveolae on the actomyosin II network in wild type cells, to limit the tension transmitted to the bridge. While the overall contractility of the cell has been previously proposed to be the one responsible for the tension at the intercellular bridge, we rather hypothesize a local role of the entry points to regulate (decrease or increase) tension at the intercellular bridge. In agreement with a local regulation of the cytoskeleton at the entry points by caveolae, we did not find a difference on the global levels of actin, pMRLC or MRLC in cytokinetic cells after caveolae depletion (Fig. S4B, C).

Not much has been described about the interplay between caveolae and myosin II, thus how caveolae presence might locally regulate myosin II activation is not known. One study proposed that myosin II may partially associate with CAV1-induced positive tubules in SK-BR-3 breast cancer cells but no caveolae localization with myosin II was shown [327]. Moreover, the caveolae inhibitory effect on the cytoskeleton could suggest that caveolae contain negative regulators of myosin II, such as MRLC phosphatases. Thus, depletion of caveolae could lead to mis-localization of the phosphatases away from the entry points, therefore allowing phosphorylation and activation of myosin II to occur there. It may also be possible that the MRLC kinases preferentially accumulate at the entry points upon

caveolae depletion. To find possible phosphatases localizing in caveolae, one could perform BioID (proximity-dependent biotinylation) studies [328]. The principle of this technique is that by using a promiscuous biotin ligase mutant BirA (R118G), which could be fused to CAV1 or Cavin1, it induces the biotinylation of interacting, or proximal proteins over a period of a few hours [328]. These interactors can then be purified and identified using mass spectrometry.

We are left with an important question: why does the myosin II preferentially accumulates at the entry points upon the loss of caveolae and not in the whole cell? Possibly, the fact that the entry points are an important location for the tension regulation and that during cytokinesis caveolae are abundant there means that loss of caveolae might affect preferentially this area. Or, even if the loss of caveolae first induces a burst of myosin II activation overall in the cell (we did not observe this), the cell body may rapidly compensate and decrease contractility, whereas in the entry points it will not. At the entry points, cortical tension mis-regulation could then translate into lipids' rearrangement, defects on membrane tension, and, eventually, in the activation of the abscission checkpoint. These points will be discussed in more detail bellow in section V.

In addition, arguing for a local effect of caveolae in inhibiting the actomyosin II network is the fact that we observed in wild type cells that the localization of pMRLC at the entry points inversely correlates with ESCRT-III polymerization. This means that as the ESCRT-III polymerize to the abscission site, less pMRLC is localized at the entry points (manuscript Fig. S4E). This result strengthens the hypothesis that the entry points, rather than the whole cell, are responsible for modulating the tension at the bridge. Thus, the fact that caveolae can control intercellular tension and modulate the abscission machinery might represent an active mechanism of the cell to control cytokinesis. It would be interesting to test whether experimentally increasing the local actomyosin II at the entry points in wild type cells would lead to a delay in ESCRT-III recruitment and increased tension at the bridge, as observed in caveolae-depleted cells. This would directly show that the cytoskeleton at the entry points modulates tension at the intercellular bridge. Even though it could be difficult to do, one possibility would be to use live-cell imaging to record bridges where ESCRT-III is localized at the midbody and quantify the time ESCRT-III takes to assemble at the abscission site upon induced actin polymerization at the entry points using optogenetics. Important as well, would be to measure directly the tension in the bridge in caveolae-depleted cells using TFM coupled with laser ablation as done previously in [29]. This would be very informative since

we would be able to analyse in wild type and caveolae-depleted cells whether the entry points are more contractile and exert higher forces in the bridge than the cortex of the daughter cells. However, technical limitations may not allow the measurement of forces specifically at the entry points, because in HeLa cells the bridge and the entry points are approximately 5 μm above the substrate, probably not allowing to access the forces exerted by the entry points. This is because to calculate traction forces exerted on the substrate by the daughter cells using TFM, the cells displace the beads on the substrate, thus if the entry points are above the substrate, we might be missing information. One way to overcome this issue would be to use another cell line in which the intercellular bridge is closer to the substrate. For instance, a research team performed TIRF at the bridge in BSC1 (Monkey African green kidney epithelial) cells, thus it would possible to measure forces at the entry points and may be even at the intercellular bridge directly [329].

Altogether we propose a mechanism where caveolae at the entry points limit the tension at the intercellular bridge (Fig. 37), allowing ESCRT-III recruitment to the midbody and polymerization to the abscission site. Such a mechanism allows successful abscission. Conversely, in caveolae-deficient cells, this buffering mechanism is inexistent and the accumulation of actomyosin II there leads to an increase in tension at the bridge. Consequently, high tension at the intercellular bridge delays the recruitment of the ESCRT-III to the midbody, as well the assembly of the ESCRT-III cone at the abscission site, thus delaying abscission.

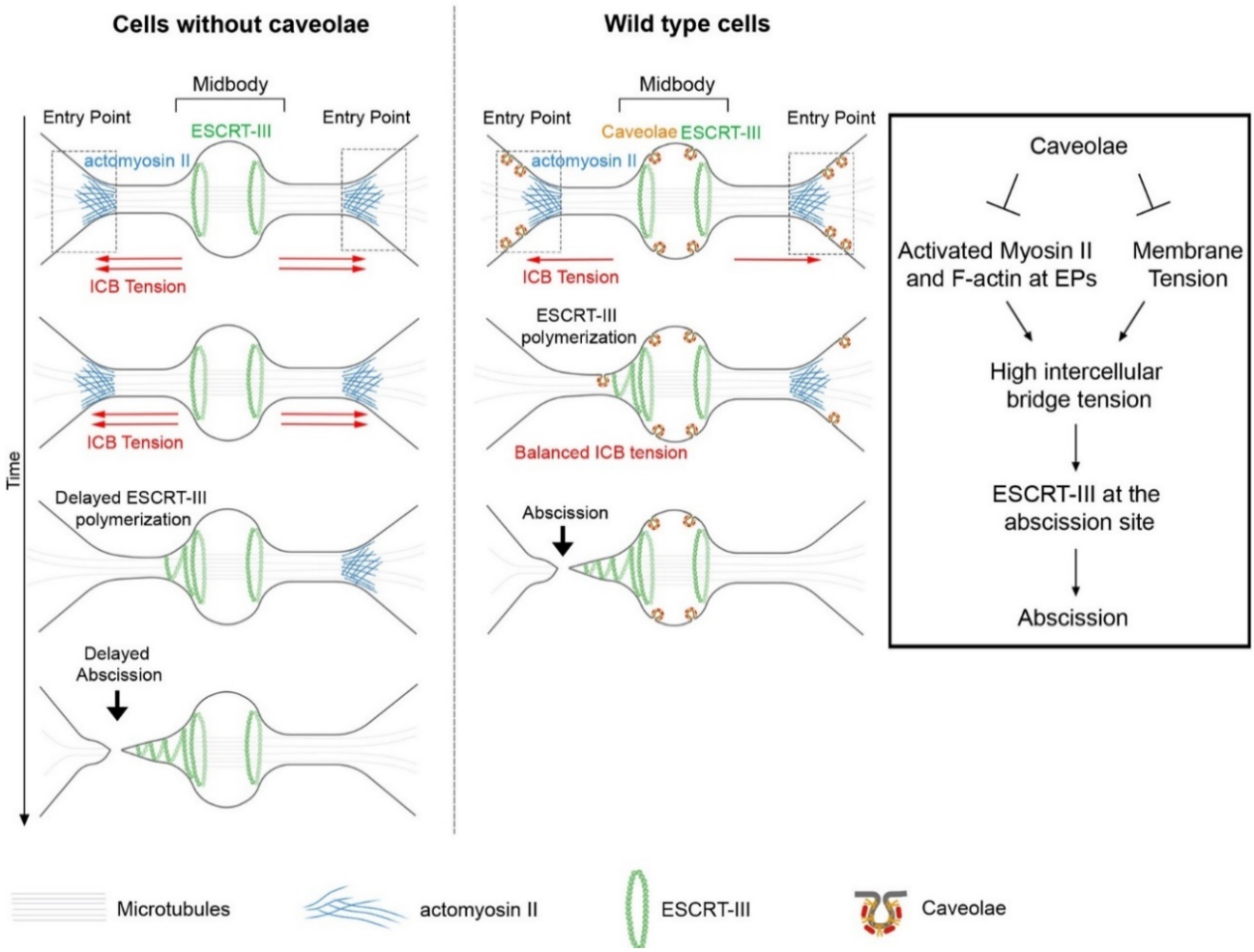

Figure 37 – Model proposed for the regulation of the intercellular tension during cytokinesis**.**

V. Possible mechanisms explaining the caveolae-dependent regulation of membrane and cortical tension during cytokinesis

a. Lipid remodelling could lead to actin accumulation at the entry points

Caveolae have been described to be linked to actin stress fibres [8]. Recently, it was shown that the Abl tyrosine kinases and the formin mDIA1 mediate CAV1 binding to stress fibres [8] (Fig. 38). Indeed, actin depolymerization, or loss of either Abl tyrosine kinases or mDIA1, leads to the clustering of CAV1 at the plasma membrane. Conversely, the overexpression of active mDIA1 that leads to excessive actin polymerization and cell elongation flattens caveolae and the CAV1 puncta at the plasma membrane aligns with stress fibres. Filamin A has also been suggested to link CAV1 at budded caveolae to actin filaments, and seems to dictate the 'stop and go' signals for caveolae lateral diffusion [8] (Fig. 38). Whether these mechanisms happen at the entry points during cytokinesis has not been investigated. In the light of our working model, in which caveolae negatively regulates the cytoskeleton at the entry points, the entry points might inhibit the AbI-mDia-actin pathway in wild type cells.

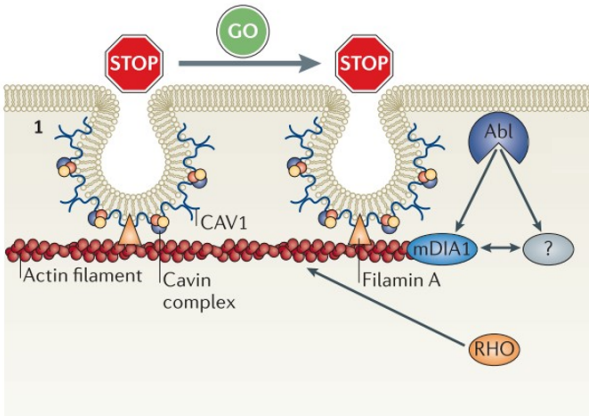

Figure 38 - Schematic showing the actin cytoskeleton association with caveolae. From [8]

A recent paper from the Parton lab revealed that caveolae can control tension in epithelia. In this context, it was found that caveolae negatively regulates F-actin. The authors showed that the depletion of either CAV1 or Cavin1 leads to increased epithelial tension, and this can be rescued by lowering contractility of the tissue by inhibiting ROCK kinases.

Interestingly, the study also described that depleting CAV1 leads to increased PI(4,5)P2 and enhanced recruitment of the formin FMNL2. This mechanism stabilizes actin (Fig. 39), and thus increases tension at adherens junctions. This is physiologically relevant, as the authors showed that increased tension (due to CAV1 depletion) inhibits extrusion of oncogene-expressing cells.

Strikingly, this study reveals a function of caveolae similar to the one described in this thesis. However, the outcomes of the tension regulation are different: during cell division, the loss of caveolae perturbs cytokinesis. Nonetheless, this could suggest a general function of caveolae coupling its plasma membrane tension buffering capacities with the local regulation of actin cortical tension. This study also suggests a possible explanation for the increased contractility at the entry points. We can imagine a similar scenario, in which depletion of caveolae may induce PI(4,5)P2 localization at the entry points and thus accumulation of actomyosin II there. Thus, it would be of interest to test whether formin such as FMNL2 and PI(4,5)P2 are enriched at the entry points in caveolae depleted cells. Increased levels of PI(4,5)P2 could a consequence of the lipid remodelling observed upon the increase of membrane tension, as further discussed in section III. In addition, I would be curious to know if in the case of increased tension in adherens junction in caveolae-depleted cells, myosin II is also more present or more activated.

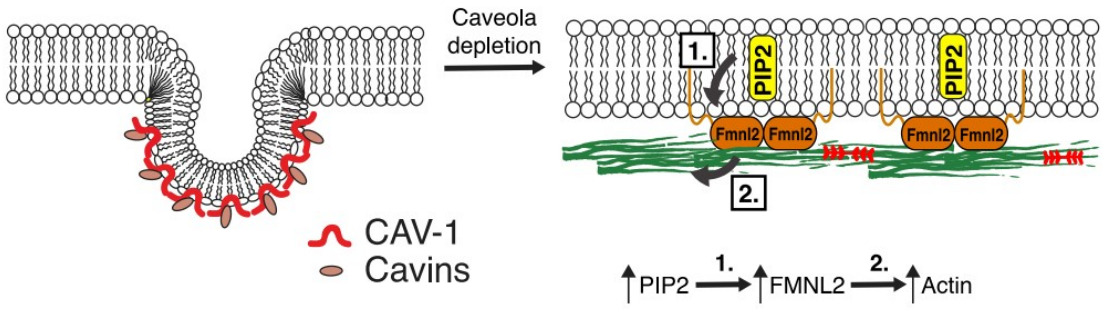

Figure 39 - Schematic diagram: caveola depletion elevates monolayer tension by increasing Ptdlns(4,5)P 2 at the plasma membrane. This induces the recruitment FMNL2 (1), which in turn stabilizes cortical F-actin (2). From [23]

The mechanism just described could be coupled to the triggering of the abscission checkpoint due to increased tension at the intercellular bridge. The increase in F-actin at the entry points and at the bridge has been observed before, when the abscission checkpoint (Introduction Chapter I.4.2) is triggered upon detection of chromatin in the intercellular bridge. When this happens in the context of the abscission checkpoint, high levels of F-actin

at the entry points and at the intercellular bridge are maintained thanks to MSRB2 (human Methionine sulfoxide reductase B2) that reduces oxidized-actin monomers to promote actin polymerization [330]. In caveolae-depleted cells, there is no increase in bridges with chromatin (manuscript Fig. S4A). However, the triggering of the abscission checkpoint may come directly from the sensing of increased tension at the bridge, as reported in [331]. The protein ULK3 (Unc-51-like kinase 3) is one of the proteins triggering the checkpoint, since it phosphorylates IST1 (an ESCRT-III component) to delay abscission. The authors showed that longer abscission times induced by low cell confluency are abolished when ULK3 is depleted. Thus, in caveolae-depleted cells the checkpoint might be activated due to increased membrane tension at the bridge, and arrest temporally abscission until tension is decreased. When the checkpoint is satisfied (low membrane tension), cytokinesis can resume but, overall, it would take more time. Thus, it would be interesting to test whether the increase in F-actin at the entry points is due to the abscission checkpoint in caveolae-depleted cells. Depleting ULK3 in Cavin1-deficient cells and measuring abscission time would show whether the checkpoint is activated or not in these cells. Nobody in the context of checkpoint activation reported the localization of myosin II at the entry points, which thus remains to be investigated.

What would be the physiological purpose of the caveolae pool at the entry points? It could be possible that since no caveolae is localized at the entry points in caveolae-depleted cells, this area is more prone to plasma membrane rupture upon mechanical stress (for instance resulting from the movement of the daughter cells, as reported before [11]). Activation of the checkpoint would protect the plasma membrane from rupturing by promoting actin polymerization at the entry points. However, this may take a bad turn, as the myosin II is also activated at the entry points and pulls on the bridge, and this could possibly be enough to transiently rupture the plasma membrane. This could be tested by looking at cells with cytokinetic bridges and comparing with interphase cells to see whether dividing cells lacking caveolae would take-in fluorescent dyes (demonstrating membrane rupture) as previously shown in interphase cells [332]. This may not be sensitive enough, since transient holes are repaired very fast by the ESCRT-III machinery [70]. Hence, one could perform a hypo-osmotic shock (acute mechanical stress) on cytokinetic bridges and monitor the entry of the dyes by live-cell imaging. This would provide a clearer result.

Finally, a simpler mechanism could be that the increased membrane tension may lead to an increase of actomyosin II levels. As introduced in Chapter III, artificially increasing the

membrane tension by micropipette aspiration in model organisms can lead to a local recruitment of the actomyosin II. However, the molecular mechanisms of how this happens are not known. Nevertheless, this could mean that in our system, when caveolae are depleted, the daughter cells pull on the bridge/entry points and induce accumulation of actomyosin II there.

b. Caveolae may facilitate activation of Akt to activate mTORC2 and regulate membrane tension

Plasma membrane tension has been shown to activate mTORC2 signalling (mammalian target of rapamycin complex 2) while mTORC1 has been more associated with cell volume regulation [21, 333]. However, the mechanism regulating membrane tension and cell volume response to mechanical stress has been understudied. Our collaborators recently showed the tight coupling of cell volume and membrane tension in response to osmotic stress (Annex I). This coupling is primarily regulated by mTORC2, and depends on the membrane area initially stored in the cell, such as in membrane ruffles and caveolae. Specifically, the increase in plasma membrane tension (hypo-osmotic shock) activates mTORC2 signalling (as shown previously), and induces phosphorylation of Akt (also known as Protein kinase B serine/threonine-specific protein kinases). Decreasing membrane tension (hyper-shock) rapidly inhibits mTORC2. In addition, the caveolae deficient cells that I generated displayed higher membrane tension and limited volume changes to hypo-osmotic shock. This is consistent with previous observation that caveolae buffer membrane tension functioning as membrane reservoirs. Thus, in mechanical stress conditions, buffering of membrane area (through caveolae and possibly filopodia and clathrin coated pits) is important for the coupling of membrane tension and cell volume. Moreover, decoupling of cell volume and membrane tension was observed upon inhibition of mTORC1 and mTORC2, respectively. These data suggest caveolae could serve as a signalling hotspot triggering mTORC2 in response to cell volume and membrane tension changes. Indeed, some studies suggested that phosphoinositide 3-kinasePI-3K/Akt activation depends on CAV1 *in vivo* in mice [334], and *in vitro* in vascular smooth muscle cells when cells are mechanically challenged by stretching [335]. In addition, fractionation and purification of caveolar-enriched fractions showed CAV3, Akt, and phosphorylated Akt are in the same fraction, in cardiomyoblasts [336]. Further investigations should be carried out to determine whether Akt associates with non-caveolar CAV1 at the plasma membrane, or specifically

binds to caveolae. In addition, Akt could be localized in caveolae since it interacts with PI(3,4,5)P3, and recently CAV1, Cavin1 or CAV1+Cavin1 have shown to be able to associate with PI(3,4,5)P3 [332]. Overall, one can hypothesize that upon increase in membrane tension, caveolae unfolds and releases Akt that is free to bind to mTORC2 and inhibit plasma membrane tension (Fig. 40).

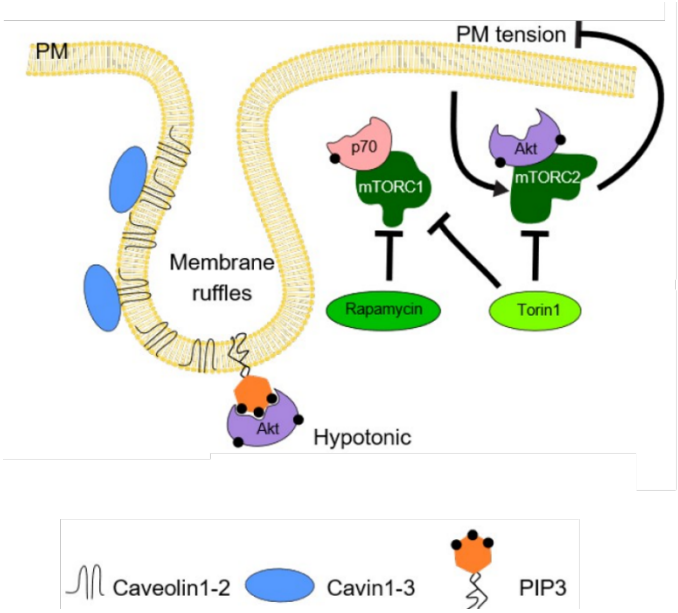

Figure 40 – Proposed mechanosensing model where caveolae links plasma membrane tension sensing to activation of the mTORC2 pathway to reduce plasma membrane tension. Adapted from *Roffay et al.*, in revision (Annex I).

c. Membrane tension can activate the PLD2-mTORC2 pathway to inhibit the actin network.

In the point a. above we have seen that loss of caveolae can lead to lipid remodelling and thus a local accumulation of actin. However, what mechanisms are triggered by increased membrane tension that may lead to actin network increase or lipid remodelling? Recently, it has been demonstrated that the actin network in migrating neutrophils is negatively regulated by a mechanosensory biochemical cascade, by two interdependent mechanisms (Fig 41a): (1) actin polymerization at the leading front increases membrane tension that, via a negative feedback loop, will inhibit actin polymerization; (2) upon increase in membrane tension PLD2 (phospholipase D2) activates mTORC2 that will inhibit new actin polymerization via WAVE complex [21].

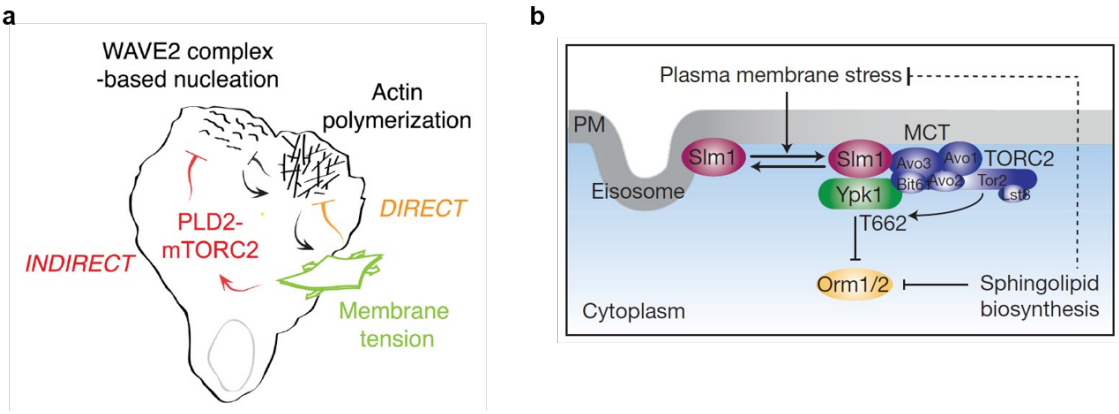

Figure 41 – Membrane tension negatively regulate the cytoskeleton (a) Actin assembly increases membrane tension, which activates two inhibitory links to actin network growth. In the first link, membrane tension directly inhibits actin polymerization by acting as a physical barrier to growth. In the second link, membrane tension acts through the PLD2–mTORC2 pathway to inhibit actin nucleation via the WAVE2 complex. This circuit forms a mechanosensory negative feedback loop that regulates membrane tension and controls the spatial organization of actin assembly during neutrophil polarity and movement. From [21] (b) Schematic illustrating the role of eisosomes, Slm proteins and TORC2 in plasma membrane homeostasis. Plasma membrane stress, due to membrane stretch or inhibition of sphingolipid synthesis, triggers the exit of Slm1 (violet) from eisosomes and thus increases the pool available to associate with and activate TORC2 (blue) towards $Ypk1_{T662}$ (green). Ypk1 in turn phosphorylates Orm proteins (orange) and thus antagonizes their ability to repress serine palmitoyl transferase activity, the rate limiting enzyme for sphingolipid production. Subsequent increase in sphingolipid production ultimately restores plasma membrane homeostasis and thus re-equilibrates eisosomal Slm1 pools. From [31]

Indeed, down-regulation of either mTORC2 or PLD2 leads to an increase in F-actin at the front of neutrophils, concomitantly with an increase in membrane tension which can be measured by Atomic Force Microscopy (AFM). This model was inspired by a similar mechanism that exists in the budding yeast, *S. cerevisiae*. Eisosomes, in yeast, are plasma membrane invaginations that upon increases in membrane tension release Slm1 to activate TORC2 [337]. Furthermore, it was shown in eisosomes that TORC2 activation promotes sphingolipids biosynthesis to reduce membrane tension (Fig 41b). Since no Slm1 orthologues are known in mammalian cells, PLD2 was the most suitable protein that could play such a role. Interestingly, PLD2 has been proposed to localize in caveolae and clathrin-coated-pits.

It is thus tempting to hypothesize a similar mechanism to the one operating in neutrophiles in cytokinetic cells. Taking into account these findings and the above description of Akt, the following hypothesis is proposed: in wild type cells, PLD2 and Akt localize in caveolae at the entry points and upon mechanical stress, Akt/PLD2 activate mTORC2 to decrease membrane tension (possibly with remodelling of the lipids at the membrane) thereby limiting the actomyosin II contractile network in that area. In contras

in caveolae-depleted cells, Akt/PLD2 would be absent from the entry points, thus will not activate mTORC2 locally, resulting in increased membrane tension and actomyosin II network assembly. Further studies should be carried out to clarify whether PLD2 localize in caveolae during cytokinesis, how its localization changes during caveolae disassembly to potentially activate mTORC2, and identify potential downstream effectors of PLD2 upon increase in membrane tension.

VI. Caveolae-dependent tension regulation helps to relocate the ESCRT-III machinery towards the abscission site

Thus far, we have seen that ESCRT-III polymerization can be affected by tension at the bridge. But how could the forces be acting on the bridge control ESCRT-III recruitment to the midbody and assembly at the abscission sites? It has been proposed that high membrane tension and local curvature could inhibit ESCRT-III assembly during cytokinesis [29]. Similarly, the ESCRT-III filaments are recruited to low membrane tension on endosomes [266]. Furthermore, the authors showed *in vitro* that the rate of CHMP4B polymerization in GUV is increased in membranes with low membrane tension. In addition, the ESCRT-II/CHMP6 complex, which helps to recruit the ESCRT-II complex, has been shown to preferentially bind membranes with negative curvatures [338, 339]. Overall, i*n vitro* studies demonstrate that the ESCRT machinery preferentially polymerizes in negative curved membranes [340, 341]. Thus, increased membrane tension in the bridge may impair the binding of the ESCRT machinery to the plasma membrane and thus inhibits ESCRT-III polymerization.

In addition to the pool at the entry points, I have found that Cavin1 and CAV1 are localized in the future abscission sites (manuscript Fig. 2C, S2B). Live-cell imaging revealed that one or a few Cavin1 dots always appear at the tip of the CHMP4B-GFP cone, and then disappear as cells progress toward abscission (manuscript Fig 2D). This suggests that caveolae at the bridge may locally help to decrease membrane tension, favouring ESCRT-III polymerization. Mechanistically, a direct association of CHMP4B with caveolae-associated proteins might be at stake, since CHMP4B has been found in complex with Cavin1, CAV1 and Pacsin3 by mass spectrometry [337]. This could explain the coupling of caveolae and ESCRT-III at the abscission site.

The mechanisms proposed above may explain why ESCRT-III is impaired at the abscission site in caveolae-depleted cells, but do not fully explain why the recruitment of ESCRT-III to the midbody itself also takes longer (manuscript Fig. 3F). Could it be that the curvature of the midbody is different? Or that caveolae affect the trafficking of CHMP4B to the intercellular bridge? This remains to be investigated.

Conclusion

The objective of this study was to investigate whether caveolae play a role in cytokinesis. We have found that caveolae localize at the intercellular bridge and at the cell/bridge interface and are required for the correct timing of abscission in HeLa cells. Caveolae help to decrease tension at the intercellular bridge, which favours subsequent ESCRT-III recruitment to the midbody and abscission site, and therefore promote abscission. We thus revealed a new mechanism by which the daughter cells balance their intercellular tension for successful cytokinesis. This sheds new light on the mechanical regulation of dividing cells during the late stages of cytokinesis, an area that remains understudied.

Though important questions have been addressed in this study, a number of questions remain to be answered in the future to further elucidate the working mechanism of caveolae during cytokinesis. In particular:

- What dictates the localization of caveolae at the ingressing furrow, midbody and entry points?
- How do caveolae regulate membrane and cortical tension at the entry points and intercellular bridge during cytokinesis?
- How the loss of caveolae affects ESCRT-III? Through a tension-only mechanism, a signalling pathway and/or via a direct interaction between the two complexes is required?
- Can dividing cells *in vivo*, for instance in tumours, take advantage of this mechanism to initiate tumorigenesis?

Finally, this work provides a caveolae-dependent mechanism that regulates cytokinesis and thus might have implications in cancer. Caveolae have been described to serve as an oncogene or tumour suppressor depending on the tumour [11, 253]. In a tightly packed environment, such as a tumour microenvironment, cell division occurs. In our study, caveolae depletion leads to binucleated cells (manuscript Fig. 3C), and these are a starting point for tumour formation [118]. Thus, if cells downregulate caveolae, they will be more

prone to become binucleated and tumorigenic. In addition, depletion of CAV1 inhibits the extrusion of oncogene-expressing cells [23] that may lead to the accumulation of these cells *in-situ*. Taking these factors together, we can hypothesize that down-regulation of caveolae could promote tumour cell formation, retention and proliferation. Even though the CAV1 and Cavin1 KO mice have not been reported to develop tumours, this could be explained by compensatory mechanisms, or by the elimination of tetraploid cells in a p53-dependent mechanism. Thus, it would be interesting to investigate whether a double KO $p53^{-/-}$ $Cavin^{-/-}$ would promote tumour formation *in vivo*.

Annex I

Passive coupling of membrane tension and cell volume during active response of cells to osmosis

Chloé Roffay[a], Guillaume Molinard[a], Kyoohyun Kim[b], Marta Urbanska[b], Virginia Andrade[c,d], Victoria Barbarasa[a], Paulina Nowak[a,e], Vincent Mercier[a], José García-Calvo[f], Stefan Matile[c,g], Robbie Loewith[e,g], Arnaud Echard[c], Jochen Guck[b], Martin Lenz[h], and Aurélien Roux[a,g,*]

[a]Department of Biochemistry, University of Geneva, CH-1211 Geneva, Switzerland; [b]Max Planck Institute for the Science of Light & Max-Planck-Zentrum für Physik und Medizin, Staudtstraße 2, DE-91058 Erlangen, Germany; [c]Membrane Traffic and Cell Division Lab, Institut Pasteur, UMR3691, CNRS, 25-28 rue du Dr Roux, F-75015 Paris, France; [d]Sorbonne Université, Collège doctoral, F-75005 Paris, France; [e]Department of Molecular Biology, University of Geneva, CH-1211 Geneva, Switzerland; [f]School of Chemistry and Biochemistry, University of Geneva, CH-1211 Geneva, Switzerland; [g]National Centre of Competence in Research (NCCR) Chemical Biology, University of Geneva, CH-1211 Geneva, Switzerland; [h]Université Paris-Saclay, CNRS, LPTMS, 91405, Orsay, France; PMMH, CNRS, ESPCI Paris, PSL University, Sorbonne Université, Université de Paris, F-75005, Paris, France

This manuscript was compiled on August 3, 2021

During osmotic changes of their environment, cells actively regulate their volume and plasma membrane tension that can passively change through osmosis. How tension and volume are coupled during osmotic adaptation remains unknown, as their quantitative characterization is lacking. Here, we performed dynamic membrane tension and cell volume measurements during osmotic shocks. During the first few seconds following the shock, cell volume varied to equilibrate osmotic pressures inside and outside the cell, and membrane tension dynamically followed these changes. A theoretical model based on the passive, reversible unfolding of the membrane as it detaches from the actin cortex during volume increase, quantitatively describes our data. After the initial response, tension and volume recovered from hypoosmotic shocks but not from hyperosmotic shocks. Using a new fluorescent membrane tension probe (Flipper-TR), we investigated the coupling between tension and volume during these asymmetric recoveries. Caveolae depletion, pharmacological inhibition of ion transporters and channels, mTORCs and of the cytoskeleton all affected tension and volume responses. Treatments targeting mTORC2 and specific downstream effectors caused identical changes to both tension and volume responses, their coupling remaining the same. This supports that the coupling of tension and volume responses to osmotic shocks is primarily regulated by mTORC2.

Plasma membrane tension | Cell volume | Flipper-TR | Osmotic shocks

Lipid membranes are self-assembled viscoelastic bilayers separating cells and their organelles from their environment (1). They are easy to bend but resistant to stretching: their lysis tension - the tension at which they break - is high, in the range of a few mN/m (2). This high value protects cells against lysis upon processes that stretch the cell membrane, still it cannot protect from the huge stretch generate by hypotonic shocks (3). Plasma membrane tension arises from the combined contributions of osmotic pressure, in-plane tension and cytoskeletal forces (4). The cytoskeleton is intimately linked to all processes regulating membrane tension, in particular cell volume regulation (5). For example, hypotonic shocks are not only responsible for increasing membrane tension (6, 7) but also induce the degradation of vimentin (8) and a reorganization of actin filaments (9, 10), without strongly affecting microtubules (8). The cytoskeleton regulates membrane tension by setting its value through active force generation, and by establishing a membrane reservoir that buffers acute changes in tension (11). This membrane reservoir is stored around protruding actin-based structures such as ruffles, filopodia and microvilli.

Part of this membrane reservoir is also stored in caveolae, which are plasma membrane invaginations formed by the assembly of Cavin1-3 and Caveolin1-2, and their disassembly buffers membrane tension increase (6). Cell volume regulation during osmotic changes involves mechano-sensitive ion transporters and channels (12, 13) regulated by membrane tension (14). How their activity is coupled to the cytoskeleton is under debate (15). They comprise volume-regulated anion channels (VRACs), sodium-hydrogen antiporters (NHEs) and Na-K-Cl cotransporters (NKCC1). VRACs are activated by hypotonic stress (16) and are unique in transporting small organic osmolytes – in particular taurine - in addition to anions (17). NHEs inhibition prevents regulatory volume increases of cells (18). Cells have evolved to respond to changes in membrane tension so as to control their impact on many processes essential to cell life (19). The genetic response to an osmotic stress has been studied extensively. This pathway partly consists of activating genes involved in the synthesis

Significance Statement

Tension is the force opposing stretch of lipid membranes. It controls cell functions involving membranes. Membranes rupture above a tension threshold, causing cell death if tension is not properly buffered. However, how cell membrane tension is quantitatively regulated is unknown because it is difficult to measure. Using a new fluorescent membrane tension probe, we explored the coupling between membrane tension and cell volume changes during osmosis. This coupling is described by an equilibrium theory linking tension to folding and unfolding of the membrane. This coupling is nevertheless actively regulated by cell components such as the cytoskeleton, ions transporters and mTOR pathways. Our results highlight that cell volume regulation and membrane tension homeostasis are independent from the regulation of their coupling.

C.R. and A.R. designed the research. C.R. performed all experiments and analysis, except the ones mentioned thereafter. G.M. did the tube pulling and PI experiments and G.M. and C.R. analyzed the data. K.K. did the ODT measurements and analyzed the data. V.B. and C.R. did the GFP tranfected cells experiments and analyzed the data. M.U. did the cell volume measurement on HL-60 using RT-DC and analyzed the data. P.N. did the western blot of mTORCs activities in various conditions. V.A. and A.E. generated the Cavin-1 KO stable cell line. V.M., J.G-C., S.M, A.E., R.L, J.G. contributed with tools and technique. M.L. did the theory and fits to experiments. C.R. M.L. and A.R. wrote the manuscript, with edits from all other co-authors.

Authors declare no competing interests.

*To whom correspondence should be addressed. E-mail: aurelien.roux@unige.ch

different recovery dynamics: it started recovering only 50 min after the shock, but the recovery is fast and complete after 80 min (Supp Fig 4B). These observations show that volume and tension responses after hypertonic shocks can be decoupled on the long term. This uncoupling may be due to reactivation of active cell processes, such as endocytosis or lipid metabolism, which may be triggered by a genetic response to the osmotic shock. Indeed, by reintroducing solutions with physiological osmolarities (315 mOsm, 250 mOsm and 160 mOsm) at the time when volume recovery had started, but not tension recovery (20 min after shock, Supp Fig 4A-B), we observed that volume and tension recoveries had the same dynamics (Supp Fig 4C-F), but only hypotonic medium (160 mOsm) led to a full recovery (Supp Fig 4D). Altogether, these results support the notion that the coupling between cell volume and tension responses to osmotic shocks is kept at least 20 min after the shock.

Quantitative coupling of cell volume to osmotic shocks. To quantitatively capture the relationship between the osmotic pressure of the cell and its volume (Fig 2A-B, Supp Fig 5A-B), we used the PBVH equation of state (34, 42)

$$P(V - V_{\mathrm{OI}}) = P_0(V_0 - V_{\mathrm{OI}}), \qquad [1]$$

where P is the osmotic pressure of the intracellular medium, V the cell volume and P_0 and V_0 are values of P and V under isotonic conditions. Eq. (1) assimilates the contents of the cell to a solution of particles with steric repulsions and otherwise negligible interactions, with the sum of the particles excluded volumes equal to V_{OI}. The cell volume thus cannot be compressed below the 'osmotically inactive volume' V_{OI}. Eq. (1) is in excellent agreement with both our hypertonic and hypotonic data (Fig 2A-B), when the volume is estimated at the time of hypotonic peak (10s after the shock, shown in Fig 1C, Supp Fig 1F). Interestingly, during and after the recovery phase (>10s after shock) volume values diverged from this linear relation only in the hypotonic conditions, reflecting the asymmetry of the recovery (Fig 2A-B). A single-parameter fit yields $V_{\mathrm{OI}} = 300\,\mu m^3$ equal to about 10% of the initial cell volume, smaller than previous estimates (43). Using RT-DC values on HL-60/S4 cells at the peak, we also find a good agreement with $V_{\mathrm{OI}} = 680\mu\mathrm{m}^3$, which is about 30% of its initial cell volume. This difference can be explained by the smaller range of osmotic pressure measured for HL-60/S4 (Supp Fig 5B) or by the intrinsic overestimation of cell volumes in RT-DC. It could also be that HL-60/S4 cells may also have a larger osmotically inactive volume, as it is known to be cell type specific (36).

Estimating the osmotically inactive cell volume. Our verification of the PBVH relation yields two surprising results: first, we find that it holds for a very large range of osmotic pressures in HeLa cells, larger than previously tested. Second, the V_{OI} represents a smaller proportion of V_0 (only 10%, as compared to values between 7% and 50% in other studies (36, 44, 45)). As the V_{OI} is obtained from a linear fit, the range of data, and the formula used for the fit can strongly change the V_{OI}. We tested this possibility by changing the range of data used for the fit, and show that using smaller ranges always provide larger V_{OI} (see Methods). One may argue that the larger range of osmotic shocks we used may artificially give lower values of V_{OI}. To have an independent estimate of the V_{OI}, we ought to measure the protein mass of the cell and compare the hydrated minimal volume of this mass to our V_{OI} values. For this, we used optical diffraction tomography, a 3D tomographic label-free technique, to measure cells refractive index (RI) (46) hence giving a direct access to changes of cell mass and protein concentration. Cells in isotonic conditions had an average RI = 1.37± 0.01. A few seconds after an hypertonic shock (1330 mOsm), cells had an increase in RI to 1.42± 0.01, while under a hypotonic shock (120 mOsm) the RI decreased to 1.35± 0.01 (Fig 2C). RI increases linearly with increasing protein concentration (47). In our experiment, the RI of single cells changed proportionally to the applied osmotic pressure (Supp Fig 5C). This implies that the protein concentration changes proportionally to the osmotic pressure (Fig 2D), which is fully consistent with our finding that cell volume changes proportionally to the osmotic pressure (Fig 2A-B). Extracting the concentration from the RI and knowing the average cell volumes allows for calculation of the dry mass for each osmotic condition (Fig 2E). The average dry mass of single HeLa cells was 305 +/- 98 pg (Supp Fig 5D) and, as expected, is constant throughout all osmotic shocks (Fig 2E). To directly measure changes of concentration for a single protein within the cytoplasm, we measured the relative change of fluorescence intensity of cells overexpressing cytosolic GFP over time. It also varied proportionally to the osmotic pressure (Supplementary information, Supp Fig 5E-G). Thus, no significant amounts of intracellular solutes were exchanged with the environment, in agreement with previous studies (26, 33). Our measurement of the dry mass (Fig 2E) also enabled an estimation of the V_{OI}. Multiplying the average volume of hydrated proteins per unit of dry mass (0.73 ml/g (48)) by the dry mass, we found $V_{\mathrm{OI}} = 223.34 \pm 71.88\mu m^3$ in agreement with our PBVH fit.

Quantitative coupling of membrane tension to volume changes and osmotic pressure. As the cell volume changes, so does the tension and area of its membrane (Fig 1D-1F, Supp Fig 3D-G). To compute the relation between these quantities, we reasoned that the cell membrane is not perfectly flat, but is instead partly folded into tubular protrusions called fillopodia, induced by the action of polymerizing actin. Many other proteins participate in the formation of those membrane protrusions, in particular inverted BAR (I-BAR) domain proteins (49). While other structures than filopodia such as caveolae may contain substantial amounts of surface, in our cells, the largest part of the membrane is stored in filopodia structures as seen from Focused Ion Beam-Scanning Electron Microscopy (FIB-SEM) 3D images (Fig 2F). Protrusions in hypertonic medium (800 mOsm) are longer and larger than protrusions in isotonic medium (Fig 2F). To account for the resulting reduction in apparent membrane area, we use a simple model inspired by (50) (Fig 2G). In the model, the membrane exists in either one of two states: tubulated or flat (Fig 2F), and is at equilibrium with a chemical reservoir of proteins provided by the cell's cytoplasm. When a protein binds to the membrane, one of the tubular protrusions grows. The tubulated membrane area thus increases by a, and the untubulated area decreases by the same amount. Note that the same reasoning can be applied to spherical buds. The free energy of the sys-

tem is reduced by a the binding free energy μ of the protein, and increased by σa equal to the amount of work that must be performed against the membrane tension σ to reduce the untubulated area. The free energy μ regroups the protein entropy loss upon binding, the protein interaction with the membrane as well as the elastic cost of curving a membrane area a into a tube. As each tube contains many proteins, we neglect their translational free energy as well as the energetic cost of curving the membrane at their tip and base. Denoting the total membrane area by $\mathcal{A}$, we can thus represent the membrane by a set of $N = \mathcal{A}/a$ independent patches of area a, each of which can be tubulated or untubulated. The free energy difference between the two states reads $\mu - \sigma a$, implying that the partition function of the membrane reads $Z(\sigma) = z^N$, where the single-patch partition function reads

$$z = 1 + e^{(\mu - \sigma a)/k_B T}, \qquad [2]$$

where $k_B T$ is the thermal energy. Denoting the apparent membrane area by A, the tubulated area is given by $\mathcal{A} - A = -k_B T \partial \ln Z / \partial \sigma$, implying that

$$\frac{\Delta A}{A_0} = \frac{e^{\mu/k_B T}}{e^{\mu/k_B T} + e^{\sigma a/k_B T}} [e^{(\sigma - \sigma_0)a/k_B T} - 1], \qquad [3]$$

Setting the isotonic tension σ_0 to its measured mean $\sigma_0 = 1.2 \times 10^{-4}\,\mathrm{N \cdot m^{-1}}$, the fit of this prediction to the data of Fig. 2H yields a membrane area per protein $a = 53\,\mathrm{nm}^2$ and a binding free energy $\mu = 1.5\,k_B T$, corresponding to a binding free energy per unit area $\mu/a = 0.12\,\mathrm{mN/m}$. This value is in line with estimates obtained for several protein coats (51), and more generally for energies of molecular interactions with surfaces (52). For these parameter values, we estimate that the ratio of total membrane area to membrane area in isotonic state is $e^{\mu/k_B T} + e^{\sigma_0 a/k_B T} \simeq 2.0$. To obtain a further indication of the confidence interval over our fitted values, we estimate the magnitude of the changes in the values of a and μ that lead to a noticeably worse fit of the experimental data (which we formally define as a $\simeq 20\%$ increase of the sum of square residuals). We find that such changes are of the order of 15% for a and 10% for μ.

To relate the change in membrane tension with the applied osmotic pressure, we combine the membrane's tension-strain relation Eq. (3) with the PBVH equation of state Eq. (1) under the assumption that the cell undergoes an approximately homogeneous dilation (contraction) when subjected to a hypoosmotic (hyperosmotic) shock. The last assumption implies that the volume and area of the cell respectively scale like the cube and the square of its typical lateral dimension. This implies $(A/A_0)^{1/2} = (V/V_0)^{1/3}$, which we combine with the aforementioned equations to yield

$$\frac{P}{P_0} = \frac{1 - \frac{V_{OI}}{V_0}}{\left[\frac{1 + e^{(\mu - \sigma_0 a)/k_B T}}{e^{\mu/k_B T} + e^{\sigma a/k_B T}} e^{\sigma a/k_B T}\right]^{3/2} - \frac{V_{OI}}{V_0}} \qquad [4]$$

Eq. (4) yields a prediction for the dependence of the membrane tension on osmotic pressure, which is in good agreement with our data (Fig 2I). These results strongly support the notion that the short-term response of cell volume and membrane tension are predominantly mechanical and thermodynamic, and consists in a passive equalization of the inner and outer osmotic pressures accompanied by an unfolding of membrane ruffles (Fig 2J). To further investigate the role of membrane ruffles in cell osmotic response, we first studied the role of cytoskeleton in the cell response to osmotic shocks.

Actin and microtubule dynamics during cell osmotic response. As in our system, most of the protrusions involved in buffering area expansion seemed to be filopodia-like structures, we ought to test the role of cortical actin in the osmotic shock response. We first imaged the dynamics of the actin cortex during osmotic shocks using SiR-Actin. Upon hypotonic shock, we observed cell blebbing concomitant with cortical actin depolymerization (Fig 3A). Blebs then extended and merged into a large membrane dome (Fig 3A side view). By quantifying cortical actin fluorescence, we observed a complete repolymerization of the cortex four minutes after the shock (Fig 3B), to a value higher than the initial value. Following a hypertonic shock, the actin cytoskeleton appeared more condensed, and its fluorescence intensity gradually increased with time (Fig 3B). We also followed the behavior of microtubules using SiR-Tubulin. After hypotonic shocks, microtubules also depolymerized and appeared more condensed after a hypertonic shock, but to a smaller extent than actin (Fig 3C-D). These results suggested that actin is strongly depolymerized by the unfolding of the membrane upon hypotonic shocks but then repolymerizes to a thicker cortex when cell volume had fully recovered.

Impact of cytoskeleton inhibition or stabilization on cell osmotic response. To test this hypothesis, we used latrunculin A to depolymerize the F-actin or jasplakinolide to stabilize it (Fig 3E). We then followed the cell volume and tension changes with time and compared them to untreated cells. First, we observed that DMSO, the solvent of stock solutions for the drugs we used, reduced the peak of volume after hypotonic shocks without affecting the peak of tension in control experiments, because DMSO increased the osmolarity of hypotonic solutions (see Methods). As described below, none of the drugs used affected the response to hypertonic shocks (Fig 3F, Supp Fig 6A), consistent with the hypertonic response being essentially passive. Similarly, both drugs had little effect on the initial peak in cell volume after hypotonic shock, consistent with the short-term response to hypotonicity being passive and previous report on non-adherent cells (38). However, latrunculin radically modified the later-time recovery compared to non-treated and jasplakinolide-treated cells. Indeed, the volume of latrunculin-treated cells partially recovered after the initial peak, but then diverged a few minutes after shock (Fig 3G). By contrast, the volume of jasplakinolide treated cells evolved similarly to that of non-treated cells (Fig 3F), although over a shorter time scale. Interestingly, the tension dynamics of both latrunculin and jasplakinolide-treated cells were completely decoupled from volume dynamics, as no peak, and thus no recovery, was observed (Fig 3G). Depolymerizing actin leads to smaller initial tension (11) and smaller cell volume (Supp Fig 6B) inducing more membrane reservoir available which could explain the absence of membrane tension increase upon hypotonic shock (Fig 3G). Stabilization of the actin also leads to no increase of membrane tension under hypotonic shocks; we hypothesize that actin stretches to counterbalance the tension instead of stretching the membrane. Thus, the actin

cortex is a major regulator of the coupling between membrane tension and volume dynamics (Fig 3G). Depolymerization of microtubules with nocodazole had limited effects on the volume dynamics after hypotonic shocks but also decoupled tension from volume changes, as no tension changes were observed (Fig 3F-G). Conversely, stabilizing microtubules with taxol clearly affected the dynamics of volume changes, as its peak was significantly smaller than in non-treated cells, and no recovery was observed. The smaller volume increase of taxol treated cells has also been observed in non-adherent cells (38) and could be due to the higher initial volume which would reduce the size of membrane area buffer (Supp Fig 6B). Maybe because of this lower area buffer, taxol treated cells have a higher tension (11) and a stiffer membrane (53), which may explain why cell volume cannot recover after its further moderate increase (Fig 3F). On the opposite, nocodazole-treated cells are softer (53), and have a lower initial volume (Supp Fig 6B), which could be associated with a larger membrane area buffer. Consistent with this, and as seen for cells treated with latrunculin, tension does not change upon hypotonic shock in nocadazole-treated cells (Fig 3G). These results show that tension dynamics can be decoupled from volume dynamics when actin and microtubule turnover is affected. As seen for taxol-treated cells, it is possible to qualitatively change the volume and tension response to osmotic shock, while preserving their coupling. Finally, none of the treatments affected the hypertonic response, supporting further that cells respond passively to this condition, or at least without the involvement of the cytoskeleton (Supp Fig 6C). While these results clearly show that the cytoskeleton is an essential actor of the cell response to osmotic shocks, several questions remained. Since actin was depolymerized during most of the recovery after hypotonic shocks, how is this recovery achieved? Also, the tight coupling between volume and tension responses suggests that it is under the control of a signaling pathway. In particular, we wondered what is the role of caveolae, described as membrane tension buffering structures (6) and mTOR, a master signaling kinase involved in controlling membrane tension and membrane folding (7, 24).

Impact of Cavin-1 knock-out on cell osmotic response. We tested the role of caveolae in cell osmotic response by using HeLa Cavin1-KO, in which we fully invalidated the expression of the essential component of caveolae Cavin1 (Supp Fig 11). In these cells, we observed that maximal cell volume increase under hypotonic shock corresponds to $1.5 * V_0$, similar than for control cells transfected with CRISPR Cas-9 without guide RNA (called CRISPR control in the following) (Fig 4B, Supp Fig 6D). On the other hand, membrane tension increase was significantly higher in Cavin1-KO cells than in CRISPR control cells (Fig 4C, Supp Fig 6E). Using the calibration of lifetime to membrane tension from HeLa cells, a difference of $\Delta\tau = 0.2$ ns in hypotonic shocks corresponds to a doubling of membrane tension (31). The relative volume and membrane tension changes under hypertonic shocks (600 mOsm) were the same between the CRISPR control and the Cavin-1 KO and they were not different from the control. We interpreted these results as caused by a reduced membrane reservoir in Cavin-1 KO cells, hypotonic shocks would rapidly unfold the membrane area buffer, limiting volume expansion and increasing tension massively, as observed in (6).

Role of mTORCs activity during cell osmotic response. The rapid recovery of cell volume and tension during hypotonic shocks shows that these parameters are tightly and actively regulated by the cell. We studied the role of mTORC1 and mTORC2 in this regulation by following their kinase activity through phosphorylation of p70 and Akt respectively (Fig 4A). mTORC2 was quickly activated under hypotonic shock, as previously shown (7) (Fig 4D, Supp Fig 6F). We further observed that mTORC2 was rapidly inhibited under hypertonic shock (Fig 4D). On the contrary, mTORC1 activity remained constant under hypotonic shock and was inhibited under hypertonic shock (Fig 4D) as seen before in (54). The high phosphorylation of Akt found at 0.1s (Fig 4D) was not reproducibly observed, and may come from the fact that these cells were undergoing osmotic shocks in cold buffer, required to block dephosphorylation. Unlike mTORC1, mTORC2 activation has similar dynamics under hypotonic and hypertonic shocks than volume and tension. This correlation suggests a more important role of mTORC2 than mTORC1 in regulating volume and tension response as well as their coupling. To test this hypothesis, we pharmacologically inhibited mTORCs and measured cell volume and tension responses under osmotic shocks.

Both mTORC1 and mTORC2 are organized around the kinase mTOR, whose phosphorylation activity can be fully inhibited using Torin1, which thus inhibits both complexes (55) while rapamycin is a specific, partial inhibitor of mTORC1 (56) (Fig 4A). First, we quantified the kinase activity of mTORC1 and mTORC2 following rapamycin and torin1 treatment. We observed a complete inactivation of both complexes 30 min after torin1 addition, while rapamycin fully inhibited p70 phosphorylation by mTORC1 after 20 min and without inhibiting mTORC2 (Supp Fig 7A) in agreement with (57). We then studied the effect of Torin1 and rapamycin treatments on the cell response to osmotic shocks. Volume changes induced by hypotonic shocks were only mildly affected by rapamycin, while Torin1-treated cells exhibited a significantly reduced volume peak after hypotonic shocks (Fig 4E) when compared to non-treated cells. Rapamycin-treated cells also showed a peak of tension similar to non-treated cells followed by a slower recovery of tension. In Torin1-treated cells, a limited increase of tension, with no recovery, was observed (Fig 4F). Both rapamycin and Torin1-treated cells did not show significant changes of their volume and tension responses to hypertonic shock in comparison to non-treated cells (Fig 1C, Fig 4E-F, Supp Fig 7B), strongly supporting that the cell response to hypertonic shock is essentially passive. These results suggest that mTORC2 controls the initial volume/tension coupling, while mTORC2 and mTORC1 are involved in the long-term recovery of both volume and tension. While mTORC complexes are involved in the regulation of volume and tension responses to osmotic shocks, and actin in the long-term recovery, factors involved in the initial, rapid recovery from hypotonic shocks remained unclear. Since actin was depolymerized during this phase, we postulated that ion transporters may be the primary actors of this fast recovery.

Role of ion transporters during cell osmotic response. Exchangers and ion channels are essential regulators of cell volume. VRACs are involved in the cell response to osmotic shocks while NKCC1 and NHE participate in the osmotic balance of cells in isotonic conditions. Furthermore, NHE1 and

NKCC1 are interacting with F-actin (58, 59) and mTORCs (Fig 5A) (24, 60) while VRAC has weak interactions with F-actin (61) and its link with mTORCs is still discussed (62, 63). We used pharmacological inhibitors of channels and transporters involved in osmotic stress response: DCPIB inhibits VRACs, while EIPA inhibits NHE exchanger and Bumetanide inhibits NKCC1 exchanger (Fig 5A). After hypotonic shocks, we observed a gradual impact of drugs from Bumetanide to DCPIB on the short-term cell swelling. DCPIB-treated cells were instantaneously permeabilized upon strong hypotonic shock, as seen by the instantaneous labelling of intracellular membranes with CellMask (120 mOsm, Fig 5B). Cell volume did not change at all times in milder hypotonic conditions (25% and 50% water, Fig 5C). By contrast, cells treated with Bumetanide had a smaller but significant peak in cell volume (Fig 5C), and EIPA-treated cells showed no peak immediately after hypotonic shock (Fig 5C). In EIPA- and Bumetanide-treated cells, cell volume slowly diverged three minutes after shock (Fig 5C) consistent with the role of NHE and NKCC1 in slow volume homeostasis (18).

All three drugs changed the tension response of cells to hypotonic shocks (Fig 5D). For Bumetanide and EIPA, the response was clearly decoupled from the volume change but while EIPA-treated cells had a tension response equivalent to non-treated cells, in Bumetanide treated cells, tension did not significantly increase in comparaison of the isotonic control, and did not recover. Tension remained constant for DCPIB-treated cells, perfectly matching the volume dynamics, but this may be due to the rapid permeabilization of DCPIB-treated cells (Fig 5B). In all hypertonic conditions, none of the inhibitors tested significantly affected the cell volume and tension responses, again indicating that the hypertonic response is essentially passive (Fig 5C-D, Supp Fig 7C). EIPA has no effect on adaptation from hypertonic shocks while EIPA is known to be an inhibitor of regulatory volume increases (RVI) because we are looking at a timescale when no volume increase had time to take place. Overall, these results show that ion transporters that participate in the osmotic balance of the cell, also participate in the coupling between tension and volume changes during osmotic shocks, and are primarily involved in the initial, large and rapid recovery from hypotonic shocks.

Discussion

Our study highlights the quantitative relation between cell volume changes and cell plasma membrane tension changes. We showed that cell volume changes are mainly due to cytoplasmic volume changes and confirms that cells modulate their volume according to the PBVH relation on a larger scale than previously reported (34). We observed two phases of cell volume response to osmotic shocks: the short-term response - a few seconds after the shock - which was characterized by cell volume variations according to the PBVH relation and the second phase - a few tens of seconds to minutes after the shock - which we called the long-term response, and which was characterized by an asymmetric recovery. Indeed, cell volume recovered fast from hypotonic shocks, but recovered slowly from hypertonic shocks. By measuring cell volume and PM tension for 2h after a mild hypertonic shocks (600 mOsm), we observed that tension fully recovered, faster (30 min) than cell volume (70 min), which only recovered partially. Reactivation of endocytosis a few tens of minutes after the shock (64) might contribute to the faster tension recovery by removing excess membrane area. During those two phases, we observed that membrane tension changes followed cell volume changes. In the short-term response, evolution of tension with volume changes was consistent with a model based on membrane unfolding. Fits to the model yielded an estimate of the size of the membrane area buffer, i.e. the area stored in ruffles, about 1 to 1.5 times the projected area of the cell (maximal area being 2 to 2.5 times the initial projected area). It also gives a value of the binding free energy per unit area, which is of the same order than previous estimates (51). It also enabled inferring the change of tension according to the change of pressure applied outside the cells. This result is qualitatively maintained during the long-term response, as tension dynamically evolves with the same asymmetry as volume after hypotonic and hypertonic shocks. These results establish that tension passively follows volume changes during the entire duration of the response and recovery to osmotic shocks.

One of the essential questions raised by the tight coupling of membrane tension and volume changes during osmotic shocks is what are the determinants of this coupling. When we depleted caveolae, known to participate in buffering membrane tension, we observed a much higher increase of membrane tension under hypotonic shocks, consistent with (6). Cell volume changes, on this other hand, were more limited than in parental cells, supporting the idea that depleting caveolae therefore removes membrane area buffer, limiting the expansion of cells during osmotic shocks. These results led to the notion that the membrane area buffer is a critical determinant of the coupling between cell volume and membrane tension. In further support of this notion, inhibitor of the mTOR pathways decoupled tension and volume responses on the long-term response, consistent with the fact that mTORC1 is proposed to regulate cell volume homeostasis, while mTORC2 is proposed to regulate cell surface homeostasis (22). On the short term response, only the inhibition of mTORC2 led to a reduced volume change while the tension mildly increased and did not recover. Durable mTORC2 inhibition by Torin1 in isotonic medium (Supp Fig 8A) do not lead to PM tension change but cell volume is smaller (Supp Fig 8B). PM tension increase during hypotonic shocks is limited suggesting that cells have a high membrane area buffer (Fig 6A, Fig 4F, Supp Fig 8B). Consistently, a similar response is found when inhibiting NKCC1 which inhibit mTORC2 (24). mTORC2 might be the primary signaling complex coupling cell volume to tension due to its link to caveolae. Indeed, studies highlight a signaling pathway between caveolae and mTORC2 in mammals (7) similar than between eisosomes and TORC2 in yeast (25) suggesting a common mechanism of membrane tension regulation. In mammals, PLD2, interacts with components of membrane invaginations (clathrin-coated pits and caveolae) and the mTORC2 complex (7), similarly than Slm1 shuttles between eisosomes and TORC2 to inhibit its activity when tension increases (27). The feedback loops as mTORC2 regulates the dynamics of caveolin-1 phosphorylation (65) but the link between caveolae and Akt phosphorylation is under debate (66).

Further evidence that the membrane area buffer directly affected the coupling between tension and volume came from studying downstream effectors of mTORC2, and notably the cytoskeleton. When microtubules were stabilized, the volume of cells increased (Supp Fig 6B) as well as the osmotically inactive volume (Supp Fig 8C). As a consequence, during hypotonic shocks, further volume increase was smaller, as well as tension, which did not recover (Fig 3F-G). These results are compatible with the notion that increased initial volume would reduce the membrane area buffer, limiting further changes (Fig 6A). But even if the overall response was changed, the coupling between tension and volume change was preserved (Fig 3F-G, Fig 6B). Altogether, those results support the hypothesis of regulations of cell volume and tension independent from the regulation of their coupling. Similar volume response as in taxol-treated cells was obtained with EIPA, as it completely abrogated the initial volume increase under hypotonic shock. It is surprising since EIPA is known as an inhibitor of regulatory volume increases (RVI) mostly tested in the context of mitosis (67) or adherence (68) but, to our knowledge, cell volume dynamics of EIPA treated-cells undergoing hypotonic shocks has never been done before. As seen for taxol-treated cells, EIPA-treated cells have larger cell volume in isotonic medium (68) (Supp Fig 8B) and a larger osmotically inactive volume (Supp Fig 8D), again supporting the notion that increase in initial volume limits further increase upon hypotonic shocks. Again, these results support the idea that higher initial volume reduces the membrane area buffer (Supp Fig 8B), limiting further changes of volume and tension during osmotic shocks. Consistently, cells with a smaller initial volume, treated with latrunculin A, jasplakinolide or nocodazole (Supp Fig 6B) undergoes swelling under hypotonic shock without increase of their PM tension (Fig 3F-G). This is probably because their membrane area buffer is increased (Fig 6C).

Overall, our results support the notion that a large excess of membrane is stored into ruffles maintained by the cytoskeleton, and that this area buffer sets the coupling of cell volume and membrane tension changes during osmotic shocks (Supp Fig 9). The recovery phase is required to restore this large excess. Any initial modification of this membrane excess will impact the coupling of cell membrane tension and volume. When the cell volume dramatically increases because of hypotonicity, the cell initially responds by depolymerizing the cytoskeleton to drive membrane unfolding, which results in a release of membrane surface area. The initial volume recovery is mediated through ion transporters, as the cytoskeleton is still disrupted, and finalized with actin repolymerization to refold the membrane, under the control of mTOR signaling. Our results show that the coupling between tension and volume is actively regulated by the cytoskeleton, ion transporters and mTOR signaling to maintain a quantitative relation between volume and tension well described by passive physical mechanisms. This coupling is regulated by the excess membrane buffer, and is thus partially independent of specific regulatory mechanisms of tension and volume.

Materials and Methods

A more detailed method is available in supplementary materials.

Cell culture. Human cervical adenocarcinoma cells HeLa-Kyoto were cultured in DMEM, 4.5g/L glucose (61965,Thermofischer) supplemented with 10% FBS (10270-106, Thermofischer) and 1% PS in a 5% CO_2 incubator. HeLa Kyoto EGFP-LaminB1/H2B-mCherry cells from cell lines service (CLS, 330919) were used to image the nuclear membrane. Selection pressure for the stably expressed constructs was kept by adding 0.5mg/mL of G418 and 0.5ug/mL of puromycin in otherwise identical medium as described above. HL-60/S4 cells (ATCC Cat CRL-3306) were cultured in RPMI medium (ATCC-modification) supplemented with 10% FBS and 1% P/S in a 5% CO_2 incubator. HeLa ATCC Cavin1-KO cell line and corresponding control were cultured in DMEM, 4.5g/L glucose supplemented in pyruvate (10569,Thermofischer) supplemented with 10% FBS and 1% PS in a 5% CO_2 (see Supplementary method about the cell line generation). For all cell lines, number of passages was kept under 20. Our cells were authenticated by Microsynth and are mycoplasma-negative, as tested by GATC Biotech and are not on the list of commonly misidentified cell lines maintained by the International Cell Line Authentication Committee.

Image acquisition and analysis for Flipper-TR imaging. Membrane tension measurement were performed on the setup published in (31). Setup used for imaging is a Nikon Eclipse Ti A1R microscope equipped with a time-correlated single-photon counting module from PicoQuant. Excitation was performed using a pulsed 485 nm laser (PicoQuant, LDH-D-C-485) operating at 20 MHz, and the emission signal was collected through a 600/50 nm bandpass filter using a gated PMA hybrid 40 detector and a TimeHarp 260 PICO board (PicoQuant). In order to measure membrane tension changes through time, HeLa Kyoto cells were labelled with Flipper-TR (Spirochrome SC020). Flipper-TR was dissolved in DMSO at 1 mM stock solutions. Cells were labelled with a 1:1000 dilution from the DMSO stock, incubated 37°C for 15 min and slices were acquired every 25 sec for 10 minutes (Fig 3C) without washing the probe. Osmotic shocks were applied 10 seconds before the second timepoint. Quality of imaging is altered in DMEM (with or without FBS, independently of phenol-red), such that all images were acquired in Leibovitz for short-term imaging (less than 2h) or FluoroBrite (A1896701) for longer times. Lifetimes of Flipper-TR were extracted from FLIM images using SymPhoTime 64 software (PicoQuant) by fitting fluorescence decay data from all pixels to a dual exponential model after deconvoluting the instrument response function (calculated by the software). We selected full images instead of choosing region of interest because the fitting was mildly affected and the result were more reproducible. The full-width at half-maximum response of the instrument was measured at 176 ps.

Drug treatment. Concentrations of drugs were kept constant throughout the experiment. Cells were pre-incubated in DMEM with drugs at 37°C (see below for drug concentrations and incubation time). DMEM was replaced by Leibovitz with drugs and CellMask or Flipper-TR. The osmotic shocks were applied as before except that the solution contained the same drug concentration. The following pharmacological inhibitors were pre-incubated as follow: 50 nM Latrunculin A for 1h (SIGMA L5163), 200 nM Jasplakinolide for 30 min (ENZO ALX-350-275), 5 μM Nocodazole for 30 min (SIGMA M1404), 1 μM Taxol for 1h (SIGMA T1912), 100 μM DCPIB for 30 min (TOCRIS 1540), 50 μM EIPA for 30 min (TOCRIS 3378), 100 μM Bumetanide for 30 min (SIGMA B3023), 250 nM Torin1 for 30 min (LC Lab T-7887) and 100 nM Rapamycin for 30 min (LC Lab R-5000). All the drugs were diluted in DMSO.

ACKNOWLEDGMENTS. We thank K. Roux, R. Wimbish for critical reading of the manuscript, and C. Tomba for discussions. AR acknowledges funding from Human Frontier Science Program Young Investigator Grant RGY0076/2009-C, the Swiss National Fund for Research Grants N°31003A_149975 and N°31003A_173087, and Synergia Grant N° CRSII5_189996, the European Research Council Consolidator Grant N° 311536, and Synergy Grant N°951324-R2-TENSION. This work has been supported by Institut Pasteur, CNRS and ANR (SeptScort) to A.E. V.AR. received a fellowship

from the Doctoral School Complexité du Vivant ED515 and La Ligue Contre le Cancer.

1. AL Le Roux, X Quiroga, N Walani, M Arroyo, P Roca-Cusachs, The plasma membrane as a mechanochemical transducer. *Philos. Transactions Royal Soc. B: Biol. Sci.* **374**, 20180221 (2019).
2. JA Nichol, OF Hutter, J PhysiolTensile strength and dilatational elasticity of giant sarcolemmal vesicles shed from rabbit muscle. *J Physiol* **493 (Pt 1)**, 187–198 (1996).
3. N Groulx, F Boudreault, SN Orlov, R Grygorczyk, Membrane reserves and hypotonic cell swelling. *The J. Membr. Biol.* **214**, 43–56 (2006).
4. E Sitarska, A Diz-Muñoz, Pay attention to membrane tension: Mechanobiology of the cell surface. *Curr Opin Cell Biol* **66**, 11–18 (2020).
5. SF Pedersen, EK Hoffmann, JW Mills, The cytoskeleton and cell volume regulation. *Comp. Biochem. Physiol. Part A, Mol. & Integr. Physiol.* **130**, 385–399 (2001).
6. B Sinha, et al., Cells Respond to Mechanical Stress by Rapid Disassembly of Caveolae. *Cell* **144**, 402–413 (2011).
7. A Diz-Muñoz, et al., Membrane Tension Acts Through PLD2 and mTORC2 to Limit Actin Network Assembly During Neutrophil Migration. *PLoS Biol* **14**, e1002474 (2016).
8. L Pan, et al., Hypotonic Stress Induces Fast, Reversible Degradation of the Vimentin Cytoskeleton via Intracellular Calcium Release. *Adv. Sci.* **6**, 1900865 (2019).
9. J Dai, MP Sheetz, X Wan, CE Morris, Membrane Tension in Swelling and Shrinking Molluscan Neurons. *J. Neurosci.* **18**, 6681–6692 (1998).
10. F Guilak, GR Erickson, HP Ting-Beall, The effects of osmotic stress on the viscoelastic and physical properties of articular chondrocytes. *Biophys J* **82**, 720–727 (2002).
11. D Raucher, MP Sheetz, Characteristics of a Membrane Reservoir Buffering Membrane Tension. *Biophys. J.* **77**, 1992–2002 (1999).
12. PG Gillespie, RG Walker, Molecular basis of mechanosensory transduction. *Nature* **413**, 194–202 (2001).
13. OP Hamill, B Martinac, Molecular Basis of Mechanotransduction in Living Cells. *Physiol. Rev.* **81**, 685–740 (2001).
14. D Reeves, T Ursell, P Sens, J Kondev, R Phillips, Membrane mechanics as a probe of ion-channel gating mechanisms. *Phys. Rev. E* **78**, 041901 (2008).
15. B Martinac, The ion channels to cytoskeleton connection as potential mechanism of mechanosensitivity. *Biochimica et Biophys. Acta (BBA) - Biomembr.* **1838**, 682–691 (2014).
16. R Syeda, et al., LRRC8 Proteins Form Volume-Regulated Anion Channels that Sense Ionic Strength. *Cell* **164**, 499–511 (2016).
17. TJ Jentsch, VRACs and other ion channels and transporters in the regulation of cell volume and beyond. *Nat. Rev. Mol. Cell Biol.* **17**, 293–307 (2016).
18. EK Hoffmann, IH Lambert, SF Pedersen, Physiology of Cell Volume Regulation in Vertebrates. *Physiol. Rev.* **89**, 193–277 (2009).
19. A Diz-Muñoz, DA Fletcher, OD Weiner, Use the force: membrane tension as an organizer of cell shape and motility. *Trends Cell Biol.* **23**, 47–53 (2013).
20. S Hohmann, Osmotic Stress Signaling and Osmoadaptation in Yeasts. *Microbiol. Mol. Biol. Rev.* **66**, 300–372 (2002).
21. K Christoph, FX Beck, W Neuhofer, Osmoadaptation of Mammalian Cells – An Orchestrated Network of Protective Genes. *Curr. Genomics* **8**, 209–218 (2007).
22. M Riggi, B Kusmider, R Loewith, The flipside of the TOR coin - TORC2 and plasma membrane homeostasis at a glance. *J. Cell. Sci.* **133** (2020).
23. M Delarue, et al., mTORC1 Controls Phase Separation and the Biophysical Properties of the Cytoplasm by Tuning Crowding. *Cell* **174**, 338–349.e20 (2018).
24. WL Demian, et al., The Ion Transporter NKCC1 Links Cell Volume to Cell Mass Regulation by Suppressing mTORC1. *Cell Reports* **27**, 1886–1896.e6 (2019).
25. M Riggi, et al., Decrease in plasma membrane tension triggers PtdIns(4,5)P2 phase separation to inactivate TORC2. *Nat. Cell Biol.* **20**, 1043–1051 (2018).
26. M Riggi, et al., TORC2 controls endocytosis through plasma membrane tension. *The J. Cell Biol.* **218**, 2265–2276 (2019).
27. D Berchtold, et al., Plasma membrane stress induces relocalization of Slm proteins and activation of TORC2 to promote sphingolipid synthesis. *Nat. Cell Biol.* **14**, 542–547 (2012).
28. E Jacinto, et al., Mammalian TOR complex 2 controls the actin cytoskeleton and is rapamycin insensitive. *Nat. Cell Biol.* **6**, 1122–1128 (2004).
29. A Echarri, MA Del Pozo, Caveolae - mechanosensitive membrane invaginations linked to actin filaments. *J Cell Sci* **128**, 2747–2758 (2015).
30. A Pietuch, BR Brückner, A Janshoff, Membrane tension homeostasis of epithelial cells through surface area regulation in response to osmotic stress. *Biochimica et Biophys. Acta (BBA) - Mol. Cell Res.* **1833**, 712–722 (2013).
31. A Colom, et al., A fluorescent membrane tension probe. *Nat. Chem.* **10**, 1118–1125 (2018).
32. MAA Ayee, E LeMaster, T Teng, J Lee, I Levitan, Hypotonic Challenge of Endothelial Cells Increases Membrane Stiffness with No Effect on Tether Force. *Biophys. J.* **114**, 929–938 (2018).
33. S Boulant, C Kural, JC Zeeh, F Ubelmann, T Kirchhausen, Actin dynamics counteract membrane tension during clathrin-mediated endocytosis. *Nat. Cell Biol.* **13**, 1124–1131 (2011).
34. JD Finan, KJ Chalut, A Wax, F Guilak, Nonlinear Osmotic Properties of the Cell Nucleus. *Annals Biomed. Eng.* **37**, 477–491 (2009).
35. EH Zhou, et al., Universal behavior of the osmotically compressed cell and its analogy to the colloidal glass transition. *Proc. Natl. Acad. Sci.* **106**, 10632–10637 (2009).
36. II Katkov, On proper linearization, construction and analysis of the Boyle-van't Hoff plots and correct calculation of the osmotically inactive volume. *Cryobiology* **62**, 232–241 (2011).
37. O Otto, et al., Real-time deformability cytometry: on-the-fly cell mechanical phenotyping. *Nat. Methods* **12**, 199–202 (2015).
38. AK Fajrial, et al., Characterization of Single-Cell Osmotic Swelling Dynamics for New Physical Biomarkers. *Anal Chem* **93**, 1317–1325 (2021).
39. M Dal Molin, et al., Fluorescent Flippers for Mechanosensitive Membrane Probes. *J. Am. Chem. Soc.* **137**, 568–571 (2015).
40. M Guo, et al., Cell volume change through water efflux impacts cell stiffness and stem cell fate. *Proc. Natl. Acad. Sci.* **114**, E8618–E8627 (2017).
41. SA Serra, et al., LRRC8A-containing chloride channel is crucial for cell volume recovery and survival under hypertonic conditions. *Proc Natl Acad Sci U S A* **118** (2021).
42. E Ponder, Hemolysis and Related Phenomena. *Grune Stratton, New-York* (1948).
43. Y Xu, et al., A single-cell identification and capture chip for automatically and rapidly determining hydraulic permeability of cells. *Anal Bioanal Chem* **412**, 4537–4548 (2020).
44. D Peckys, P Mazur, CryobiologyRegulatory volume decrease in COS-7 cells at 22 ℃ and its influence on the Boyle van't Hoff relation and the determination of the osmotically inactive volume. *Cryobiology* **65**, 74–78 (2012).
45. H Shapiro, J Gen PhysiolThe change in osmotically inactive fraction produced by cell activation. *J Gen Physiol* **32**, 43–51 (1948).
46. K Kim, J Guck, The Relative Densities of Cytoplasm and Nuclear Compartments Are Robust against Strong Perturbation. *Biophys J* (2020).
47. H Zhao, P Brown, P Schuck, On the Distribution of Protein Refractive Index Increments. *Biophys. J.* **100**, 2309–2317 (2011).
48. R Schlüßler, et al., Mechanical Mapping of Spinal Cord Growth and Repair in Living Zebrafish Larvae by Brillouin Imaging. *Biophys. J.* **115**, 911–923 (2018).
49. S Guerrier, et al., The F-BAR domain of srGAP2 induces membrane protrusions required for neuronal migration and morphogenesis. *Cell* **138**, 990–1004 (2009).
50. I Lavi, et al., Cellular blebs and membrane invaginations are coupled through membrane tension buffering. *Biophys. J.* **117**, 1485–1495 (2019).
51. M Saleem, et al., A balance between membrane elasticity and polymerization energy sets the shape of spherical clathrin coats. *Nat Commun* **6**, 6249 (2015).
52. E Evans, Probing the relation between force–lifetime–and chemistry in single molecular bonds. *Annu. Rev Biophys Biomol Struct* **30**, 105–128 (2001).
53. K Mandal, A Asnacios, B Goud, JB Manneville, Mapping intracellular mechanics on micropatterned substrates. *Proc Natl Acad Sci U S A* **113**, E7159–E7168 (2016).
54. M Plescher, AA Teleman, C Demetriades, TSC2 mediates hyperosmotic stress-induced inactivation of mTORC1. *Sci Rep* **5**, 13828 (2015).
55. Q Liu, et al., Discovery of 1-(4-(4-Propionylpiperazin-1-yl)-3-(trifluoromethyl)phenyl)-9-(quinolin-3-yl)benzo[h][1,6]naphthyridin-2(1H)-one as a Highly Potent, Selective Mammalian Target of Rapamycin (mTOR) Inhibitor for the Treatment of Cancer. *J. Medicinal Chem.* **53**, 7146–7155 (2010).
56. F Boutouja, CM Stiehm, HW Platta, mTOR: A Cellular Regulator Interface in Health and Disease. *Cells* **8** (2019).
57. Y Bai, et al., Differential Role of Rapamycin in Epidermis-Induced IL-15-IGF-1 Secretion via Activation of Akt/mTORC2. *Cell Physiol Biochem.* **42**, 1755–1768 (2017).
58. SP Denker, DL Barber, Ion transport proteins anchor and regulate the cytoskeleton. *Curr Opin Cell Biol* **14**, 214–220 (2002).
59. CM Liedtke, M Hubbard, X Wang, Stability of actin cytoskeleton and PKC-delta binding to actin regulate NKCC1 function in airway epithelial cells. *Am J Physiol Cell Physiol* **284**, C487–496 (2003).
60. ME Meima, BA Webb, HE Witkowska, DL Barber, The sodium-hydrogen exchanger NHE1 is an Akt substrate necessary for actin filament reorganization by growth factors. *J Biol Chem* **284**, 26666–26675 (2009).
61. B König, Y Hao, S Schwartz, AJ Plested, T Stauber, A FRET sensor of C-terminal movement reveals VRAC activation by plasma membrane DAG signaling rather than ionic strength. *Elife* **8** (2019).
62. IH Lambert, JV Jensen, PA Pedersen, mTOR ensures increased release and reduced uptake of the organic osmolyte taurine under hypoosmotic conditions in mouse fibroblasts. *Am J Physiol Cell Physiol* **306**, C1028–1040 (2014).
63. A Kumar, et al., SWELL1 regulates skeletal muscle cell size, intracellular signaling, adiposity and glucose metabolism. *Elife* **9** (2020).
64. H De Belly, et al., Membrane Tension Gates ERK-Mediated Regulation of Pluripotent Cell Fate. *Cell Stem Cell* **28**, 273–284 (2021).
65. AM Hau, et al., Dynamic Regulation of Caveolin-1 Phosphorylation and Caveolae Formation by Mammalian Target of Rapamycin Complex 2 in Bladder Cancer Cells. *Am J Pathol* **189**, 1846–1862 (2019).
66. MG Sugiyama, GD Fairn, CN Antonescu, Akt-ing Up Just About Everywhere: Compartment-Specific Akt Activation and Function in Receptor Tyrosine Kinase Signaling. *Front Cell Dev Biol* **7**, 70 (2019).
67. MP Stewart, et al., Hydrostatic pressure and the actomyosin cortex drive mitotic cell rounding. *Nature* **469**, 226–230 (2011).
68. K Xie, Y Yang, H Jiang, Controlling Cellular Volume via Mechanical and Physical Properties of Substrate. *Biophys. J.* **114**, 675–687 (2018).

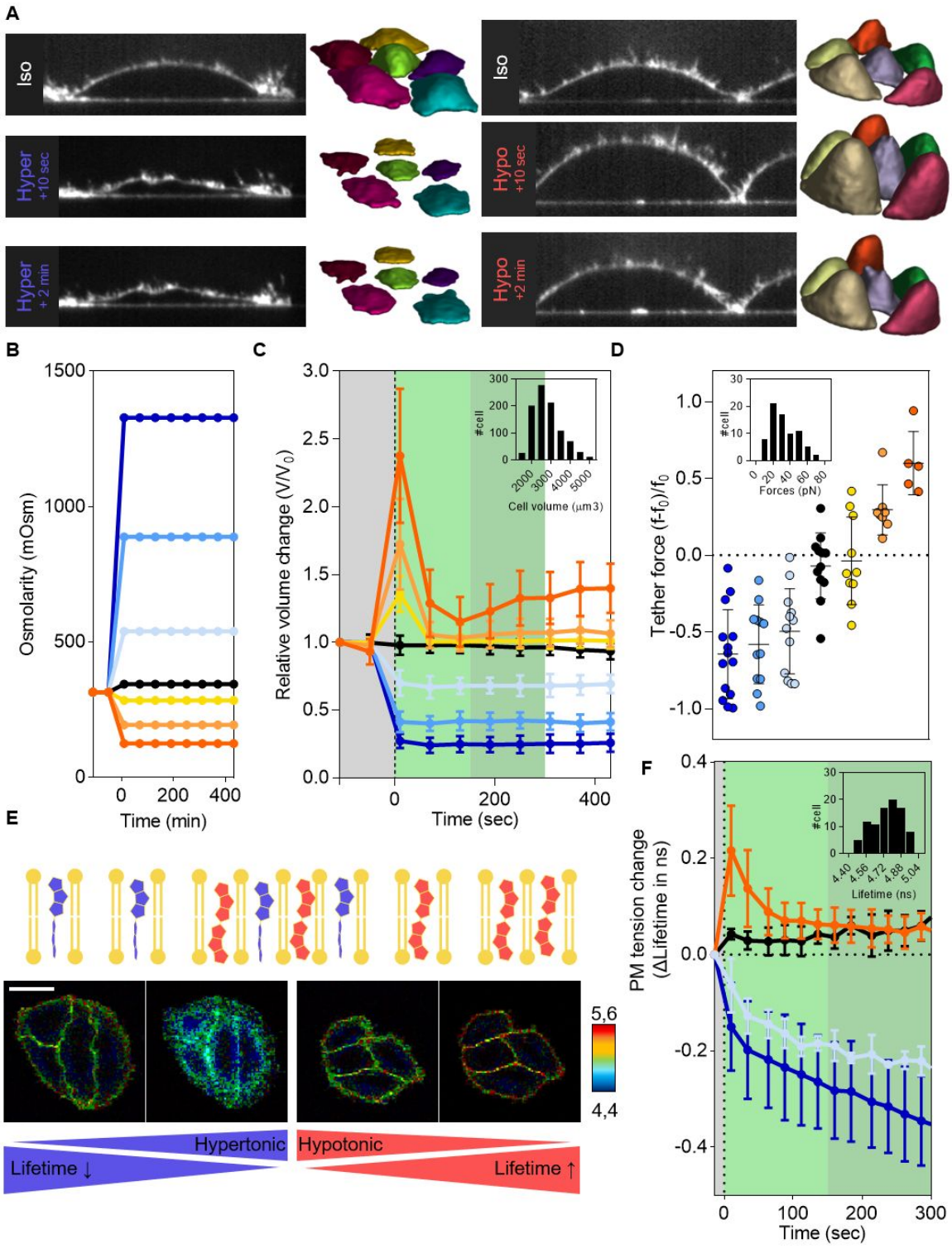

Fig. 1. Osmotic shocks affect cell volume and membrane tension. A, Representative side view of cell with CellMask staining and corresponding 3D reconstruction of cell volume using Limeseg (left hyper, right hypo). **B**, Osmolarities (mOsm) of cell media with time for the different step wise osmotic. Osmotic conditions corresponds to 120 mOsm in dark orange, 190 mOsm is light orange, 285 mOsm in yellow, 315 mOsm in black, 540 mOsm in light blue, 890 mOsm in medium blue and 1330 mOsm in dark blue. Color code is maintained. **C**, Averaged cell volume dynamics under osmotic shock (grey : before shocks; light green : short-term response; dark green : long-term response). Statistics are : dark orange (R>3, N=28), light orange (R>3, N=20), yellow (R>3, N=40), black (R>3, N=66), light blue (R>3, N=62), medium blue (R>3, N=47) and dark blue (R>3, N=43). Insert : Cell volume distribution in isotonic medium before osmotic shocks (R>50, N=959). **D**, Relative change of tether force immediately after osmotic shocks (averaged over 10 sec) for different osmotic shocks. Insert : Tether force distribution in isotonic medium before osmotic shocks (R=N=73). **E**, Fluorescence lifetime of the Flipper-TR probe reports membrane tension changes. FLIM images of Flipper-TR lifetime values (colorscale) of cells subjected to osmotic shocks. **F**, Dynamics of the change of tension as measured by Flipper-TR lifetime (grey : before shock; light green : short-term response; dark green : long-term response). Osmotic conditions corresponds to 120 mOsm in dark orange (R=7, N>28), 315 mOsm in black (R=3, N>12), 600 mOsm in light blue (R=3, N>12) and 1330 mOsm in dark blue (R=5, N>20). Insert : Distribution of the cell average Flipper-TR lifetimes in isotonic medium before osmotic shocks (R>100, N>400).

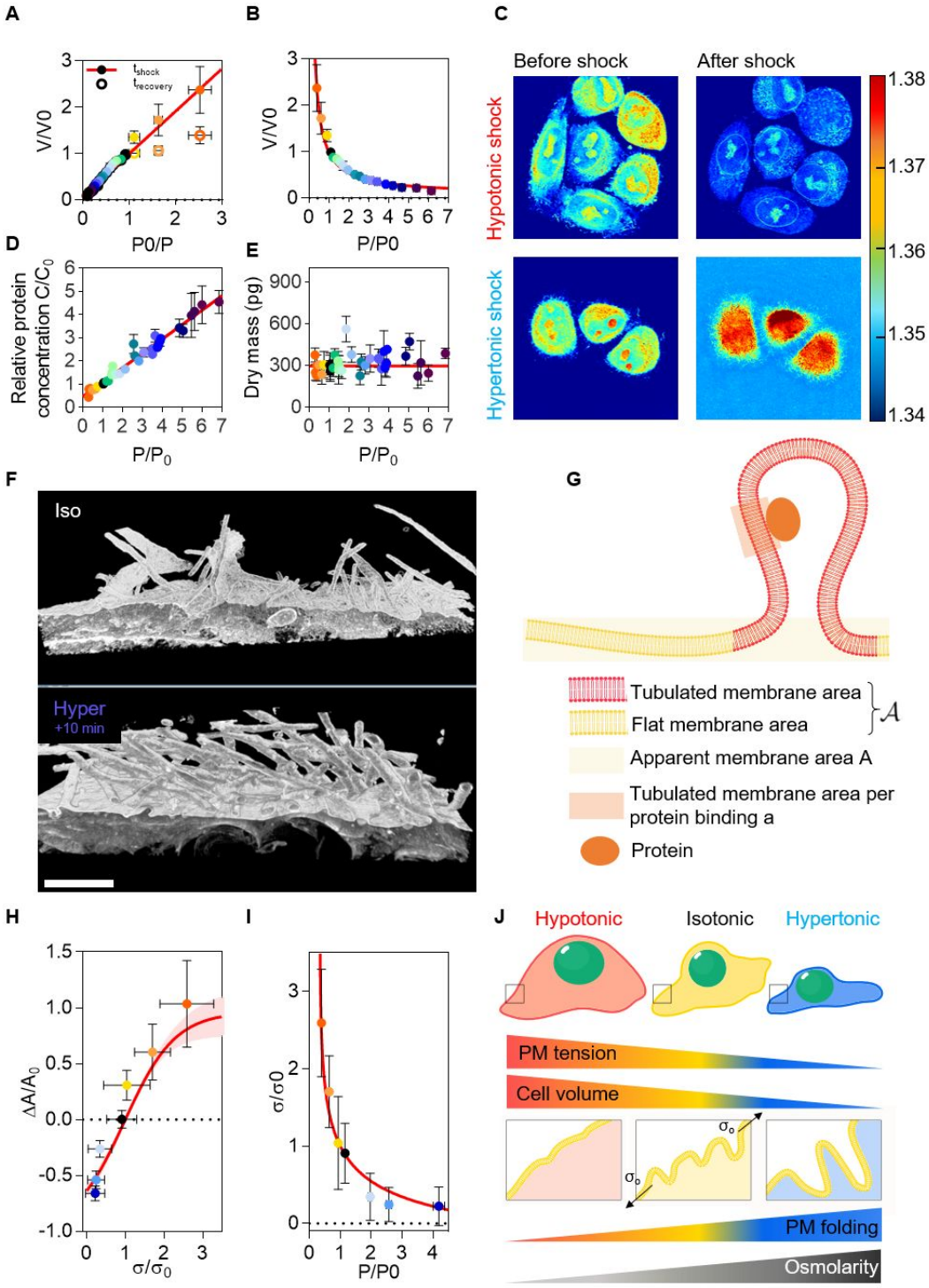

Fig. 2. Quantitative coupling of cell volume and cell membrane tension to osmotic shocks. A, Normalized volume changes (V/V_0) as a function of osmotic pressure ratio (P_0/P) just after osmotic shocks (full circle) and 8 min after the osmotic shock (empty circle, recovery phase) compared to the prediction of Eq. $\mathrm{Eq.}\ (1)$ (red line). Color code is maintained from Fig 1. Statistics are (R>3, N=28) for dark orange, (R>3, N=20) for light orange, (R>3, N=40) for yellow,(R>3, N=66) for black, (R>3, N=62) for light blue, (R>3, N=47) for medium blue and (R>3, N=43) for dark blue. **B**, Normalized volume changes (V/V_0) as a function of osmotic pressure ratio (P/P_0) just after osmotic shocks compared to the prediction of Eq. $\mathrm{Eq.}\ (1)$ (red line). Statistics are the same than A. **C**, Refractive index images of cells under osmotic shocks. **D**, Protein concentration changes (C/C_0) according to pressure applied (P/P_0). Each point corresponds to one experiment containing at least two cells. Analysis is performed on individual cells. **E**, Calculated dry mass of cells versus normalized pressure (P/P_0). Each point corresponds to one experiment containing at least two cells. Analysis is performed on individual cells. **F**, Representative FIB-SEM images of the membrane tubulations in isotonic medium and hypertonic medium. Scale bar : 2μm **G**, Scheme describing the parameters of the theory. **H**, Relative changes of membrane area $(\Delta A/A_0)$ versus relative changes of membrane tension $(\Delta\sigma/\sigma_0)$ compared to the prediction of Eq. $\mathrm{Eq.}\ (??)$ (red line). Color code is maintained from Fig 1. Statistics are (R=N=5 in x, R>3, N=28 in y) for dark orange, (R=N=8 in x, R>3, N=20 in y) for light orange, (R=N=10 in x, R>3, N=40 in y) for yellow,(R=N=12 in x, R>3, N=66 in y) for black, (R=N=12 in x, R>3, N=62 in y) for light blue, (R=N=12 in x, R>3, N=47 in y) for medium blue and (R=N=14 in x, R>3, N=43 in y) for dark blue. **I**, Normalized tension (σ/σ_0) versus normalized pressure (P/P_0) and prediction obtained using $\mathrm{Eq.}\ (4)$. Statistics are the same than in (F). **J**, Scheme describing the theory.

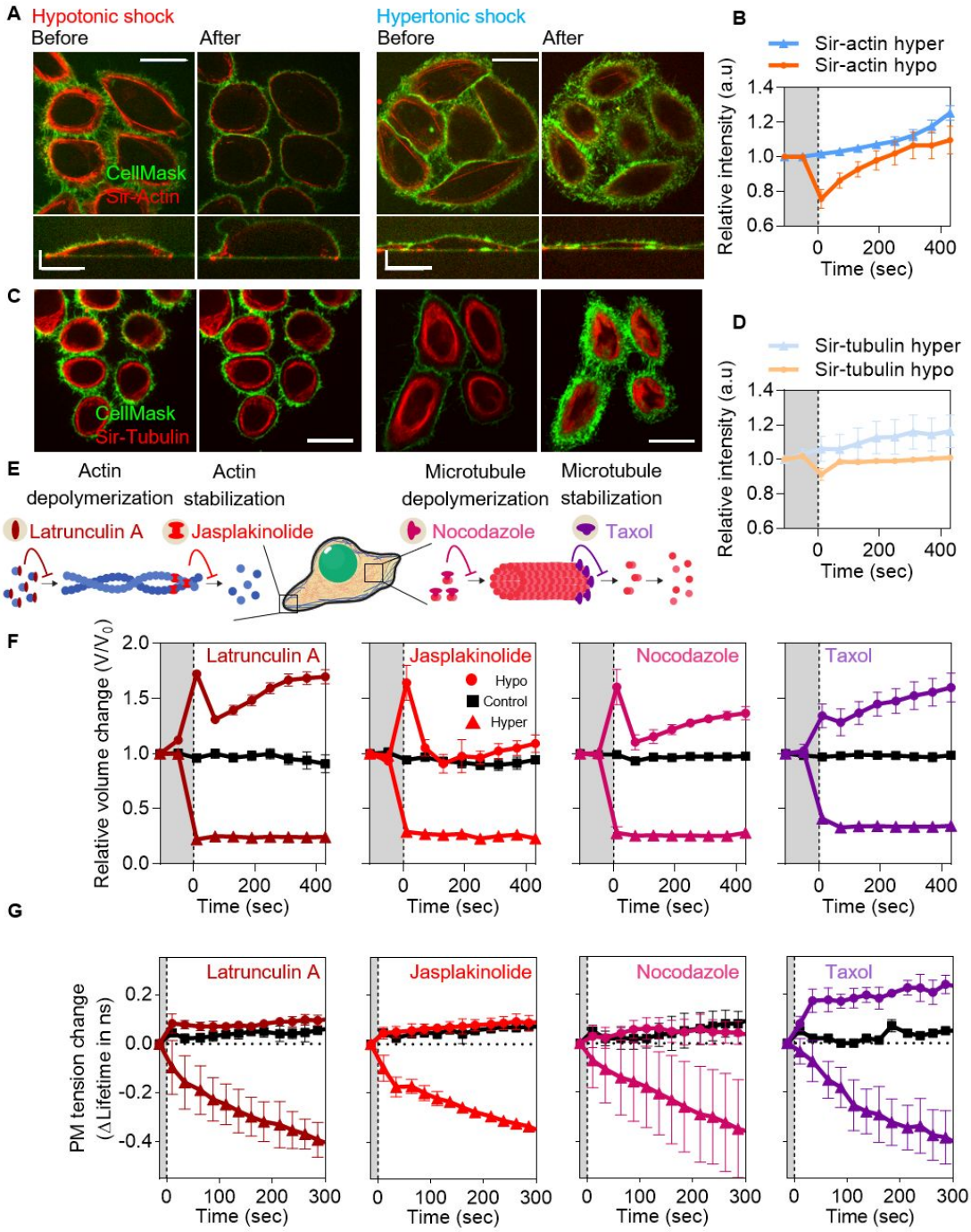

Fig. 3. Cytoskeleton controls the long-term response of cells to osmotic shocks. A, Actin imaging under hypotonic shock (left) and hypertonic shock (right). Scale bar : 20 μm. Bottom panels are y projections. **B**, Quantification of actin fluorescence intensities during shocks (R=3, N>3). **C**, Tubulin imaging under hypotonic shock (left) and hypertonic shock (right). Scale bar : 20 μm. **D**, Quantification of tubulin fluorescence intensities during shocks (R=3, N>3). **E**, Illustrations of cytoskeletal drugs effects. **F**, Single cell volume dynamics of cells treated with latrunculin A, jasplakinolide, nocodazole or taxol during hypotonic shocks (120 mOsm, circle), isotonic condition (315 mOsm, square) and hypertonic shocks (700 mOsm - P/P0 = 2, triangle). Statistics are R>3 for every experiments. For latrunculin A, N=5 for control, N=4 for hypo, N=15 for hyper; for Jasplakinolide, N=6 for control, N=8 for hypo, N=10 for hyper; for nocodazole, N=8 for control, N=8 for hypo, N=6 for hyper; for taxol, N=10 for control, N=19 for hypo, N=12 for hyper. **G**, Membrane tension dynamics of cells treated with latrunculin A, jasplakinolide, nocodazole or taxol during the same shocks as in e. Statistics are N>4 for every experiments. For latrunculin A, R=2 for control, R=6 for hypo, R=4 for hyper; for jasplakinolide, R=4 for control, R=10 for hypo, R=3 for hyper; for nocodazole, R=2 for control, R=6 for hypo, R=4 for hyper; for taxol, R=2 for control, R=3 for hypo, R=4 for hyper

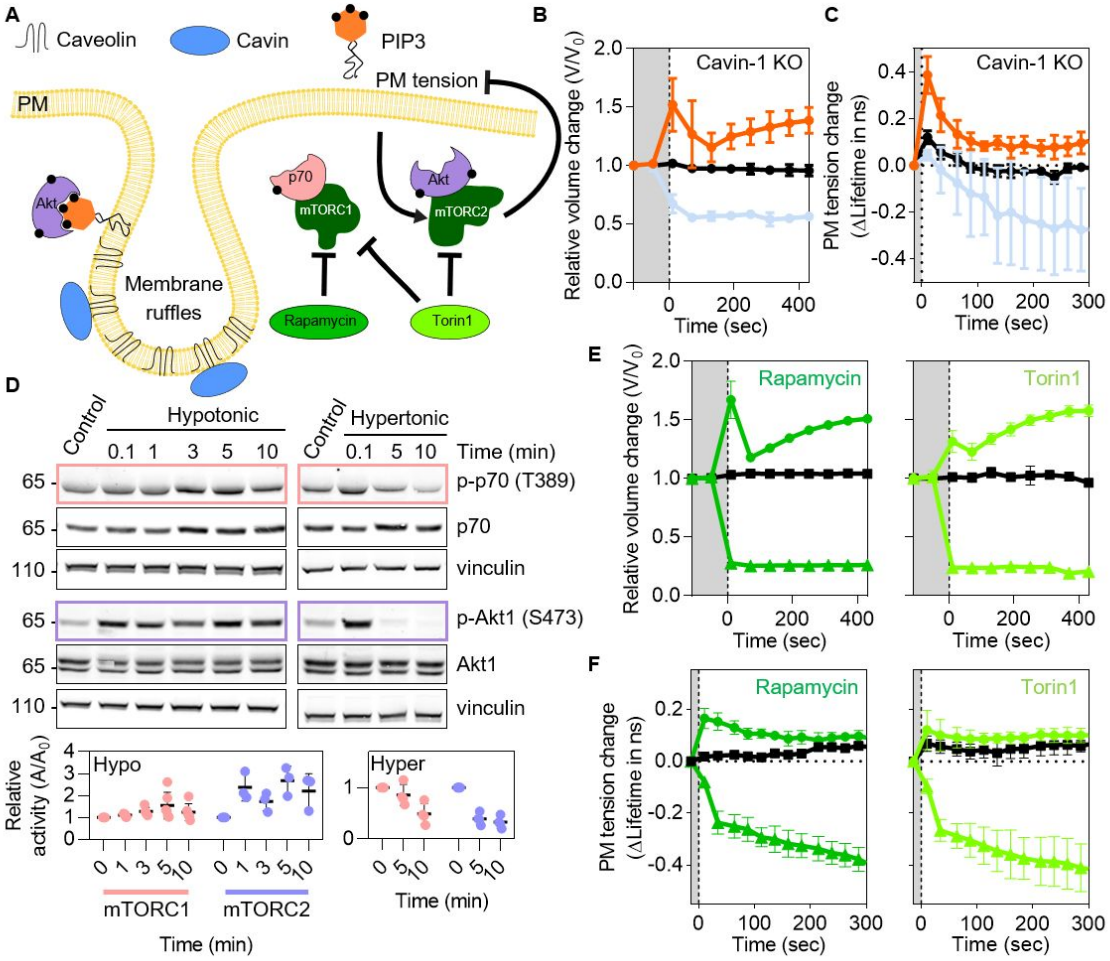

Fig. 4. Caveolae and mTORC2 are involved in membrane tension regulation. A, Schematic of membrane ruffles interactions with caveolin1-2, cavin1-3, PIP3 and Akt phosphorylation as well as the signaling pathways of mTOR complexes inhibited by Torin 1 (mTORC1 and mTORC2) or rapamycin (mTORC1). **B**, Single cell volume dynamics of cells Cavin-1 KO. Statistics are R>3 for every experiments and N=7 for control, N=15 for hypo, N=18 for hyper. **C**, Membrane tension dynamics of cells Cavin-1 KO and their corresponding CRISPR control. Statistics are N>4 for every experiments and R=3 for control, R=4 for hypo, R=2 for hyper. **D**, Activity of mTORC1 and mTORC2 under hypertonic and hypotonic shock. Panels represent activation (phosphorylation) of S6K1 (p-p70) and Akt (pAkt) and loading controls. Longer timepoint are in Supp Fig XX and corresponding quantification. **E**,Single cell volume dynamics of cells treated with rapamycin or Torin1 for hypotonic shocks (120 mOsm, circle), isotonic condition (315 mOsm, square) and hypertonic shocks (700 mOsm - P/P0 = 2, triangle) Statistics are R>3 for every experiments. For rapamycin, N=4 for control, N=5 for hypo, N=4 for hyper; for torin1, N=10 for control, N=9 for hypo, N=7 for hyper. **F**, Membrane tension dynamics of cells treated with rapamycin or Torin1 for identical shocks as in c. Statistics are N>4 for every experiments. For rapamycin, R=2 for control, R=6 for hypo, R=4 for hyper; for torin1, R=7 for control, R=15 for hypo, R=4 for hyper.

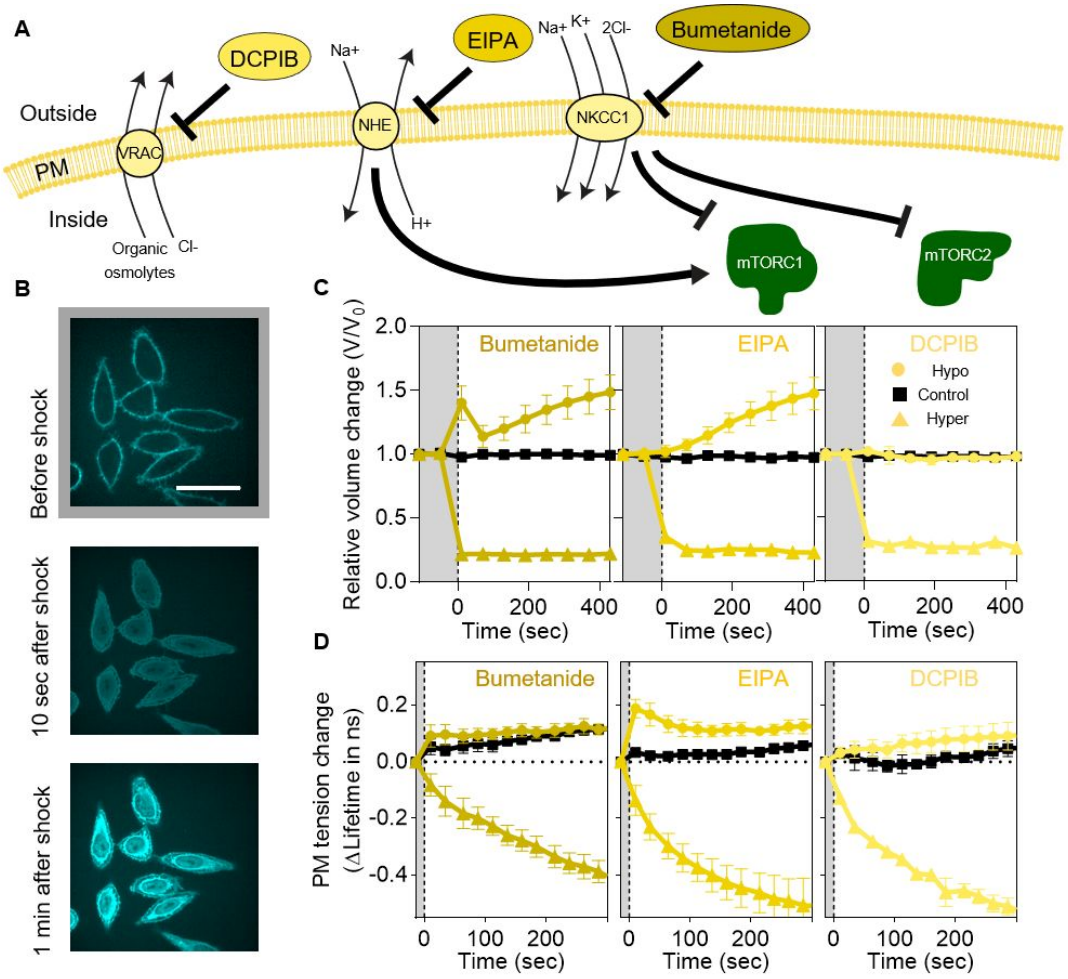

Fig. 5. Ion transporters are responsible for the short-term response of cells to osmotic shocks A, Illustrations of DCPIB, EIPA and Bumetanide pharmacological effects on, respectively, VRACs, NHE and NKCC1 channels. **B**, Confocal images of DCPIB treated cells and response under hypotonic shock. Scale bar = 40μm. **C**, Single cell volume dynamics in cells treated with Bumetanide, EIPA, DCPIB for hypotonic shocks (120 mOsm, circle), isotonic condition (315 mOsm, square) and hypertonic shocks (700 mOsm - P/P0 = 2, triangle) Statistics are R>3 for every experiments. For Bumetanide, N=9 for control, N=66 for hypo, N=8 for hyper; for EIPA, N=12 for control, N=9 for hypo, N=9 for hyper; for DCPIB, N=12 for control, N=31 for hypo, N=14 for hyper. **D**, Membrane tension dynamics in cells treated with Bumetanide, EIPA, DCPIB for identical shocks as in c. Statistics are N>4 for every experiments. For Bumetanide, R=5 for control, R=11 for hypo, R=4 for hyper; for EIPA, R=3 for control, R=12 for hypo, R=3 for hyper; for DCPIB, R=2 for control, R=6 for hypo, R=2 for hyper.

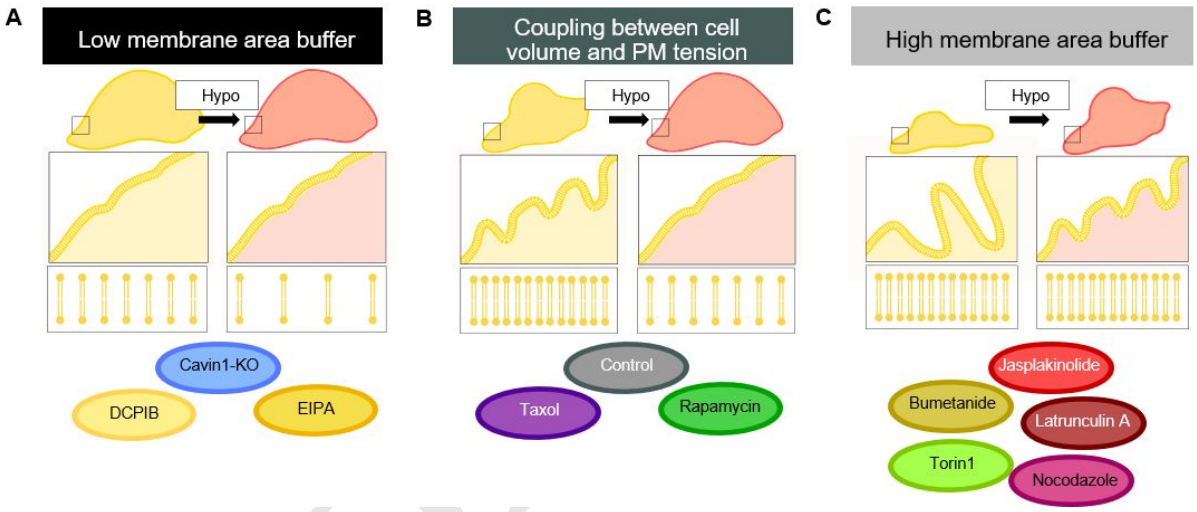

Fig. 6. Recapitulative scheme A, In case of low membrane area buffer, cells have larger initial volumes which remains mostly unchanged during hypotonic shocks. Membrane ruffles are initially unfolded which lead to higher stretching of the membrane and an increase of PM tension in resting conditions. **B**, In case of intermediate membrane area buffer, cell volume increase under hypotonic shocks causing the unfolding of membrane ruffles. Membrane stretches and PM tension increases in a cell volume dependent manner. **C**, In case of high membrane area buffer, cells have smaller initial volume, thus having also more ruffles and therefore cell volume increase under hypotonic shocks. Cell volume increase during hypotonic shock is responsible for unfolding the ruffles without stretching the membrane to its maximum, therefore having limited increase of PM tension.

Supplementary material : Passive coupling of membrane tension and cell volume during active response of cells to osmosis

Chloé Roffay[a], Guillaume Molinard[a], Kyoohyun Kim[b], Marta Urbanska[b], Virginia Andrade[c,d], Victoria Barbarasa[a], Paulina Nowak[a,e], Vincent Mercier[a], José García-Calvo[f], Stefan Matile[c,g], Robbie Loewith[e,g], Arnaud Echard[c], Jochen Guck[b], Martin Lenz[h], and Aurélien Roux[a,g,*]

[a]Department of Biochemistry, University of Geneva, CH-1211 Geneva, Switzerland; [b]Max Planck Institute for the Science of Light & Max-Planck-Zentrum für Physik und Medizin, Staudtstraße 2, DE-91058 Erlangen, Germany; [c]Membrane Traffic and Cell Division Lab, Institut Pasteur, UMR3691, CNRS, 25-28 rue du Dr Roux, F-75015 Paris, France; [d]Sorbonne Université, Collège doctoral, F-75005 Paris, France; [e]Department of Molecular Biology, University of Geneva, CH-1211 Geneva, Switzerland; [f]School of Chemistry and Biochemistry, University of Geneva, CH-1211 Geneva, Switzerland; [g]National Centre of Competence in Research (NCCR) Chemical Biology, University of Geneva, CH-1211 Geneva, Switzerland; [h]Université Paris-Saclay, CNRS, LPTMS, 91405, Orsay, France; PMMH, CNRS, ESPCI Paris, PSL University, Sorbonne Université, Université de Paris, F-75005, Paris, France

This manuscript was compiled on July 30, 2021

Supplementary method

Effect of DMSO on cell volume and plasma membrane tension. To evaluate the effect of DMSO on cell response to osmotic shocks, we added 2 μL of DMSO in DMEM incubated 30 min. DMEM was replaced by Leibovitz with 2 μL of DMSO and CellMask or Flipper-TR. The osmotic shocks were applied as before except that solutions were supplemented with 1uL of DMSO. DMSO affects hypotonic solutions osmolarity. 75% water condition corresponds to 90 mOsm. 75% water + 1% DMSO corresponds to 120 mOsm. 75% water + 2% DMSO corresponds to 130 mOsm. Therefore, cell volume increase was limited (Supp Fig 10A). Cell tension increase was identical to control (Supp Fig 10B). Absolute cell volume with and without additional DMSO (1%) was the same (Supp Fig 10C).

Apply osmotic shock for live cell imaging. Cells were seeded into 35-mm MatTek glass-bottom microwell dishes and were imaged in Leibovitz medium (Thermofischer, 21083027) supplemented with 10% Fetal Bovine Serum and 1% Penicillin Streptomycin. For hypotonic shocks, we simply diluted the cell imaging media with 25%, 50% or 75% of MilliQ water (285 mOsm, 200 mOsm, 120 mOsm). For hypertonic and isotonic shocks, a stock solution of Leibovitz and sucrose (2M) was diluted to obtain a final osmotic pressure of 550 mOsm, 900 mOsm, 1300 mOsm, 2000 mOsm and 3500 mOsm as well as additional intermediate solutions (Supp Fig 1E-F). We chose sucrose over salts to avoid changing specific ion concentrations in the medium. Also, sucrose does not cross the cell membrane, and is not metabolized by HeLa cells. Control hypertonic shocks performed using sorbitol gave identical results (Supp Fig 11A-B). Under the microscope, 1 mL of shock solution was added (1-2s) to the imaging dish containing 1mL of isotonic buffer during imaging. Osmotic shocks were applied 10 seconds before the third time point (0 min). At the end of each experiment, the remaining buffer was collected and its osmotic pressure was measured using an osmometer (Camlab). Since osmotic shocks are applied lived under the microscope, no mixing of the solutions is possible and the entire volume of sucrose solution falls at the bottom. The sucrose concentration perceived by the cells at the moment of the shock $c_{cell} = 2{*}c_f$.

Image acquisition and analysis for cell volume measurement. Z-stacks were acquired through a spinning-disk confocal composed of a Nikon Ti-E system, a Yokogawa CSU-X1 Confocal Scanner Unit, a iXon camera (Andor, Belfast, NIR, UK), a Laser stack by Intelligent Imaging Innovation Inc (3i, Denver, CO, USA), a 37°C incubator (Life Imaging service, Basel, Switzerland). All images were acquired with Slidebook software (3i, Denver, CO, USA). In order to measure single cell volume changes through time, HeLa Kyoto cells were labelled with the plasma membrane marker CellMask (Thermofischer C10046). Dyes were diluted in cell medium at 1:1000, incubated at 37°C for 10 min. Confocal Z-stacks (400 nm steps) were acquired every minute for 10 minutes. Osmotic shocks were applied 10 seconds before the third timepoint. Cell 3D images were segmented using a Matlab homewritten code, validated with GUV measurement (Supp Fig 1A) and cell volume and area were extracted. Cells were segmented using a 3D watershed with an intensity threshold automatically determined according to the stack pixel distribution of the entire stack. The tracking in time was straightforward since cells are not moving. Code available on https://github.com/ChloeRoffay/3D-segmentation-time-tracking. Extracting cell volume from confocal stack requires post measurement correction since RI of the cell media is different from the RI of the objective/oil/glass bottom dish as explained in (1). RI of the cell media also changes for the different osmotic shocks applied (Supp Fig 11C). Using a simplified equation from (1)

$$\frac{d}{d'} = \frac{\tan\left(sin^{-1}\frac{0.5NA}{n_1}\right)}{\tan\left(sin^{-1}\frac{0.5NA}{n_2}\right)} \qquad [1a]$$

We calculated the axial correction according to P/P_0 (Supp Fig 11D) with NA = 1.3 and $n_1 = 1.518$ while n_2 are the RI of the medium (Supp Fig 5C). The correction never exceed 6%. The correction to apply on absolute cell volume in isotonic medium is equal to 0.86. In order to verify the validity of the correction, we compared GUV volume measured G_m with our algorithm and GUV volume calculated G_cal. Assuming that GUV are spherical, we measured the bigger GUV surface and extracted the corresponding radius. Using the radius, we calculated the GUV volume G_cal. $G_corr = 0.86{*}G_m$. G_m has 11% error compared to G_cal while G_corr has 4.5% error

(Supp Fig 1A). Since we are looking at relative volume changes, we calculated the corresponding correction to apply on V/V_0 (Supp Fig 11E) which never exceed 1.07.

High-throughput 2D imaging of HL-60/S4 cells for volume estimation. HL-60/S4 cells were collected by centrifugation for 5 min at 180g and resuspended in an osmolarity-adjusted measurement buffer (MB). MB was based on Leibovitz's L15 medium (no. 21083027, Thermo Fisher Scientific) supplemented with 10% heat-inactivated FBS, 1% penicillin–streptavidin and 0.6% (wt/vol) methyl cellulose (4,000 cPs; Alfa Aesar) for increased viscosity that prevents cell sedimentation during the measurements. The osmolarity of MB was adjusted by addition of sucrose or by mixing Leibovitz's/FCS-based MB with water-based MB of same viscosity, and measured before each experiment using a freezing point osmometer (Fiske 210 Micro-Sample Osmometer, Advanced Instruments). 2D bright-field cell images were acquired at high throughput using real-time deformability cytometry (2) according to previously published procedures (3). In brief, the cells suspended in MB were introduced to the microfluidic chip with a syringe pump. The total flow rate was set to 0.16 μLs^{-1} (0.04 μLs^{-1} sample flow together with 0.12 μLs^{-1} focusing sheath flow). The time between resuspension of cells and start of the measurement amounted to roughly 2 min, after that few thousand events were recorded every minute to follow the cell volume response over time. Cell images were acquired at the end of a 300-μm-long channel with a 30x30 μm^2 square cross-section at 2,000 frames per second using stroboscopic illumination with a pulse duration <3 μs to avoid motion blurring. The cell contours were detected in real time and cell area and further parameters were estimated online. Acquired events were filtered for area between 50–500 μm^2 to excluded debris and area ratio between 1.00–1.05 to excluded rough or incomplete contours (3). Volume of the cells was estimated offline by 360° rotation of upper and lower halves of the 2D cell contours around the symmetry axis, and averaging the two obtained values (4) using ShapeOut version 1.0.1 (available at https://github.com/ZELLMECHANIK-DRESDEN/ShapeOut).

Refractive index measurement and processing. The three-dimensional (3D) refractive index (RI) distribution of samples was measured using a custom-made ODT (Optical Diffraction Tomography) microscope. The optical setup of ODT employs Mach-Zehnder interferometry in order to measure complex optical fields of light scattered by samples from various incident angles, as shown in (5). A coherent laser beam (wavelength = 532 nm, frequency-doubled Nd-YAG laser, Torus, Laser Quantum, Inc., UK) is divided into two beams by a 2x2 single-mode fiber optic coupler. One beam is used as a reference beam and the other beam illuminates the specimen on the stage of a custom-made inverted microscope through a tube lens (f = 175 mm) and a high numerical aperture (NA) objective lens (NA = 1.2, 63x, water immersion, Carl Zeiss AG, Germany). To reconstruct a 3D RI tomogram of samples in a field-of-view, the samples are illuminated with 150 various incident angles scanned by a dual-axis galvanomirror (GVS012/M, Thorlabs Inc., USA). The diffracted beam from a sample is collected by a high NA objective lens (NA = 1.3, 100x, oil immersion, Carl Zeiss AG) and a tube lens (f = 200 mm). The total magnification is set to be 90.5x. The beam diffracted by the sample interferes with the reference beam at the image plane, and generates a spatially modulated hologram. The hologram is recorded with a CCD camera (FL3-U3-13Y3M-C, FLIR Systems, Inc., USA). From measured holograms, the 3D RI tomograms are reconstructed by the Fourier diffraction theorem employing the first-order Rytov approximation (6, 7). Cells were manually segmented based on the epifluorescence image of the membrane (CellMask staining as previously described). Cell's basis was automatically detected to correct the z-drift. By applying the segmented ROI to the projection of the RI tomogram onto the cell's basis plane, pixels value of RI were extracted, averaged over the entire cell, and averaged over many cells for each osmotic condition.

Osmotically inactive volume measurement. The osmotically inactive volume V_{OI} of the cell is extracted from the plot $V/V_0(P_0/P)$ (Fig 2A-B and Supp 5A-D). It cannot be directly measured because mathematically it corresponds to the cell volume when the osmotic pressure applied is infinite. The linear fit is $V/V_0 = (1\text{-m})(P_0/P) + m$ with $m = V_{OI}/V_0$. A commune mistake is to apply $V/V_0 = q(P_0/P) + m$ considering that m and q are independent parameters (8). To understand the discrepancy with the previous results in the litterature we extracted the V_{OI} from different sets of point. Taking into account all the osmotic conditions ($0<P_0/P<3$) or only the hypertonic shocks ($0<P_0/P<1$) (Supp Fig 12A-B), we extracted a non significantly different osmotically inactive volume below $10\%*V_0$. If an intermediate range of osmotic conditions is considered including both hypotonic and hypertonic conditions ($0.5<P_0/P<2$) (Supp Fig 12C), $V_{OI} = 17\%*V_0$. Our V_{OI} value is in agreement with the litterature when we only consider hypertonic conditions in a range $0.5<P_0/P<1$ which leads to $V_{OI} = 27\%*V_0$ (Supp Fig 12D). Indeed, including extreme hypertonic shocks ($0<P_0/P<0.5$), $V_{OI} = 7\%*V_0$ leads to the smallest osmotically inactive volume extracted (Supp Fig 12E). The decisive criterion is not the number of hypertonic conditions considered but the range of pressure applied (Supp Fig 12F).

Tube pulling experiment. Membrane nanotube pulling experiments were performed on the setup published in (9) allowing simultaneous optical tweezer application, spinning disc confocal and brightfield imaging based on an inverted Nikon eclipse Ti microscope and a 5W 1064nm laser focused through a 100 × 1.3 NA oil objective (ML5-CW-P-TKS-OTS, Manlight). A membrane nanotube was formed by displacing the cell's observation chamber away from a concanavalin-A-coated bead (3.05 mm diameter, Spherotec) held the optical trap, and previously in contact with the cell to adhere to the cell membrane. The force F exerted on the bead was calculated from Hooke's law: F = k.x, where k is the stiffness of the trap (k = 8.58 $pN.pix^{-1}.W^{-1}$) and x is the displacement of the bead from its initial zero-force position.

Cell porosity measurement. HeLa Kyoto cells were incubated for 5 min with Propidium Iodide 160 g/mL during the osmotic shock, and then checked under the microscope for fluorescence. Permeabilization with 1% Saponin was used as a positive control.

Cell viability measurement. Cell viability was measured using the CCK-8 test. HeLa cells were cultured in 96-well plates,

with three duplicated wells for each group. When 80–90% confluence was reached, cells were treated with osmotic shocks for 1h, and CCK-8 solution (10 L) at a 1:10 dilution was added to each well followed by a further 1h incubation under 5% CO_2 at 37 °C. Absorbance was measured at 450 nm with a microplate reader. The mean optical density (OD, absorbance) of three wells in the indicated groups was used to calculate the percentage of cell viability as follows: percentage of cell viability = (Atreatment Ablank)/(Acontrol Ablank) × 100% (where, A = absorbance). Values plotted are averages of duplicates.

Image acquisition and analysis of the cytoskeleton. In order to measure actin or tubulin intensity changes through time, HeLa Kyoto cells were labelled with the plasma membrane marker Cell Mask orange (Thermofischer C10045) and SiR-actin (SC001, Spirochrome) or SiR-tubulin (SC002, Spirochrome). Dyes were dissolved in DMSO at a stock concentration of 1mM, and diluted 1:1000 in cell's medium, incubated at 37°C for 20 min to label cells. Cells were then imaged as described above. Cells were manually segmented and average intensity was extracted using ImageJ.

GFP experiments. pGFP was transfected using FuGENE®6 Transfection Reagent (E2691,Promega) with OptiMEM (31985088, Thermofischer). Transfected Hela Kyoto cells were image with the same spinning disk confocal set-up, single confocal planes being acquired every second for 10 minutes. Nikon's Perfect Focusing System was used to keep focus during the entire osmotic shock. Cells were manually segmented using ImageJ and the mean fluorescence was extracted through time. For each cell, values were normalized to the initial value.

Focused-Ion Beam Scanning Electron Microscopy (FIB-SEM). Cells were fixed immediately or treated for 10 min at 37°C with hypertonic medium (0.5M sucrose). Cells were washed once with PBS and fixed for 3h on ice using 2.5% glutaraldehyde and 2% PFA in buffer A containing 0.15M cacodylate and 2mM $CaCl_2$. Then, cells were processed for FIB-SEM as described (10). At the end of the sample preparation, a small block was cut using an electric saw and incubated for approximately 30 min in 100% xylene to remove the leftover plastic. Finally, the ROI was processed using a HELIOS 660 Nanolab DualBeam SEM/FIB (FEI Company). The ROI size was about 20 µm wide and the thickness of the FIB slice was 10 nm, depending on the experiment. Image processing was done with ImageJ and Icy. Briefly, stacks were aligned using StackReg plugin before being rescaled and a median filter was applied to the whole stack. Images were inverted, the brightness and contrast were adjusted and the 3D image was displayed using the 3D VTK viewer of Icy software.

Control and Cavin1 KO cell lines. Control and Cavin1 KO clones were generated using CRISPR/Cas9. A gRNA targeting the 5'-GCTCACCGTATTGCTCGTGG-3' of the Cavin1 non-coding strand, as proposed in https://chopchop.cbu.uib.no/ was used (Supp Fig 13A). This sequence has been inserted in the plasmid pSpCas9(BB)-2A-Puro (PX459) V2.0 (Addgene, http://addgene.org/62988; RRID:Addgene 6298866), a kind gift from Feng Zhang. HeLa ATCC cells were transfected using X-tremeGENE 9 DNA reagent (Roche) with pSpCas9(BB)-2A-Puro containing the target sequence described above for Cavin1 KO, or with empty pSpCas9(BB)-2A-Puro for Control KO. After 24 h, cells were selected with 2 mg / mL of puromycin and clones were isolated. Each clone was then tested by PCR on genomic DNA using the following primers 5'-CGGACGTGGCTCGAGTTTCC-3' and 5'-CCGCTCCCTCCCTAATTGGC-3' to amplify approximately 600 bp upstream and 600 bp downstream the target sequence. PCR products were cloned into a TOPO vector (Invitrogen) and 37 individual clones were sequenced. For RT-PCR, polyA+ RNAs were extracted using NucleoSpin RNA (Macheray-Nagel) and amplified using MMLV reverse transcriptase (Superscript II, ThermoFisher) and the following primers: 5'-CTATATTGTCGAGCGGCCGC-3' and 5'-CGCAGTGCAGAGCATCCAG-3' primers for Cavin1, and 5'-AGCCACATCGCTCAGACAC-3' and 5'GCCCAATACGACCAAATCC-3' for GAPDH. Western blots were used to ascertain the loss of Cavin1 at the protein level (Supp Fig 13B). Control and Cavin1 KO cells were lysed in 1x Laemmli (Bio-Rad Laboratories) with Benzonase nuclease. Lysates were migrated in a 12% SDS-PAGE (Bio-Rad Laboratories), transferred onto PVDF membranes (Millipore) and incubated overnight with primary antibodies in 50 mM Tris-HCl pH 8.0, 150 mM NaCl, 0.1% Tween20, 5% milk followed by HRP-coupled secondary antibodies (1:10,000, Jackson Immuno Research) and revealed by chemiluminescence (GE Healthcare). The following primary antibodies were used: rabbit anti-Cavin1 (1/4000 Proteintech 18892-1-AP), mouse anti-GAPDH (1/40000 Proteintech 60004-1-Ig) (Supp Fig 13C).

Western blot. 200,000-250,000 cells were seeded on 6-well plates or 3.5cm Nunc Cell culture dishes (Thermo Fisher Scientific) a day prior to the experiment. For the inhibition test, cells were treated for the indicated time with 100nM Rapamycin, 250nM Torin1 (LC Laboratories, USA) or DMSO (mock control, Sigma Aldrich). For osmotic shocks, the following solutions were used: 300mM sorbitol (Sigma Aldrich) in DMEM containing 10% fetal bovine serum (hypertonic shock), 50% water in DMEM containing 10% fetal bovine serum (hypotonic shock). Cells were treated with solutions for the indicated time and washed with ice-cold PBS of corresponding osmolarity to block dephosphorylation quickly before lysis. Cells were lysed in lysis buffer (40mM HEPES, 10mM Na-PPi, 10mM Na--glycerophosphate, 4mM EDTA 1% Triton X-100, pH 7.4) supplemented with 1× Halt Protease Phosphatase Inhibitor Cocktail (Thermo Fisher Scientific) and kept at -20°C until further analysis. A Pierce BCA Protein Assay (Thermo Fisher Scientific) was used to determine protein concentration in the samples. After addition of sample buffer (312.5mM Tris, 10% SDS, 50% glycerol, 25% -mercaptoethanol, 0.1% bromophenol blue, pH 6.8) and protein denaturation at 95°C for 5min, samples were loaded on SDS-PAGE 10% acrylamide gels and resolved in 1× SDS-PAGE running buffer at 60-110V. After electrophoresis, proteins were transferred to a nitrocellulose membrane using the iBlot2 Gel Transfer System (Thermo Fisher Scientific). Subsequently, membranes were blocked for 1h in 5% bovine serum albumin (BSA, US Biological Life Sciences) in TBST buffer. Incubation with primary antibodies diluted in 5% BSA in TBST was done overnight at 4°C with gentle shaking. The following day, membranes were washed three times in TBST and incubated with secondary antibodies in 5% BSA in TBST for 1h at room tempera-

ture. After three subsequent washes in TBST, membranes were imaged with Odyssey CLx Imaging System (LI-COR Biosciences). The following antibodies were used for Western blotting: mouse anti-pan-Akt-1 monoclonal (Cell Signaling Technology 2920; 1:1,000), rabbit anti-phospho-Akt-1Ser473 (Cell Signaling Technology 4060; 1:750), muse anti-pan-p70 S6 Kinase (Santa Cruz 8418; 1:1,000), rabbit anti-phospho-p70 S6 KinaseThr389 (Cell Signaling Technology 9234; 1:750). Secondary antibodies were IRDye 680RD donkey anti-rabbit IgG (LI-COR Biosciences) and IRDye 800CW goat anti-mouse IgG (LI-COR Biosciences) used at 1:10,000.

All images were constructed using ImageJ, Picoqwant or Matlab. All graphs were constructed with GraphPad Prism 8.

1. EE Diel, JW Lichtman, DS Richardson, Tutorial: avoiding and correcting sample-induced spherical aberration artifacts in 3D fluorescence microscopy. *Nat Protoc* **15**, 2773–2784 (2020).
2. O Otto, et al., Real-time deformability cytometry: on-the-fly cell mechanical phenotyping. *Nat. Methods* **12**, 199–202 (2015).
3. M Urbanska, P Rosendahl, M Kr?ter, J Guck, High-throughput single-cell mechanical phenotyping with real-time deformability cytometry. *Methods Cell Biol* **147**, 175–198 (2018).
4. M Herbig, et al., Real-time Deformability Cytometry: Label-free functional characterization of cells. *Flow Cytom. Protoc. (Human Press.*, 347–369 (2017).
5. K Kim, J Guck, The Relative Densities of Cytoplasm and Nuclear Compartments Are Robust against Strong Perturbation. *Biophys J* (2020).
6. E Wolf, Three-dimensional structure determination of semi-transparent objects from holographic data. *Opt. Commun* **1**, 153–156 (1969).
7. Y Sung, et al., Optical diffraction tomography for high resolution live cell imaging. *Opt Express* **17**, 266–277 (2009).
8. II Katkov, On proper linearization, construction and analysis of the Boyle-van't Hoff plots and correct calculation of the osmotically inactive volume. *Cryobiology* **62**, 232–241 (2011).
9. N Chiaruttini, et al., Relaxation of Loaded ESCRT-III Spiral Springs Drives Membrane Deformation. *Cell* **163**, 866–879 (2015).
10. P Nunes-Hasler, et al., STIM1 promotes migration, phagosomal maturation and antigen cross-presentation in dendritic cells. *Nat Commun* **8**, 1852 (2017).

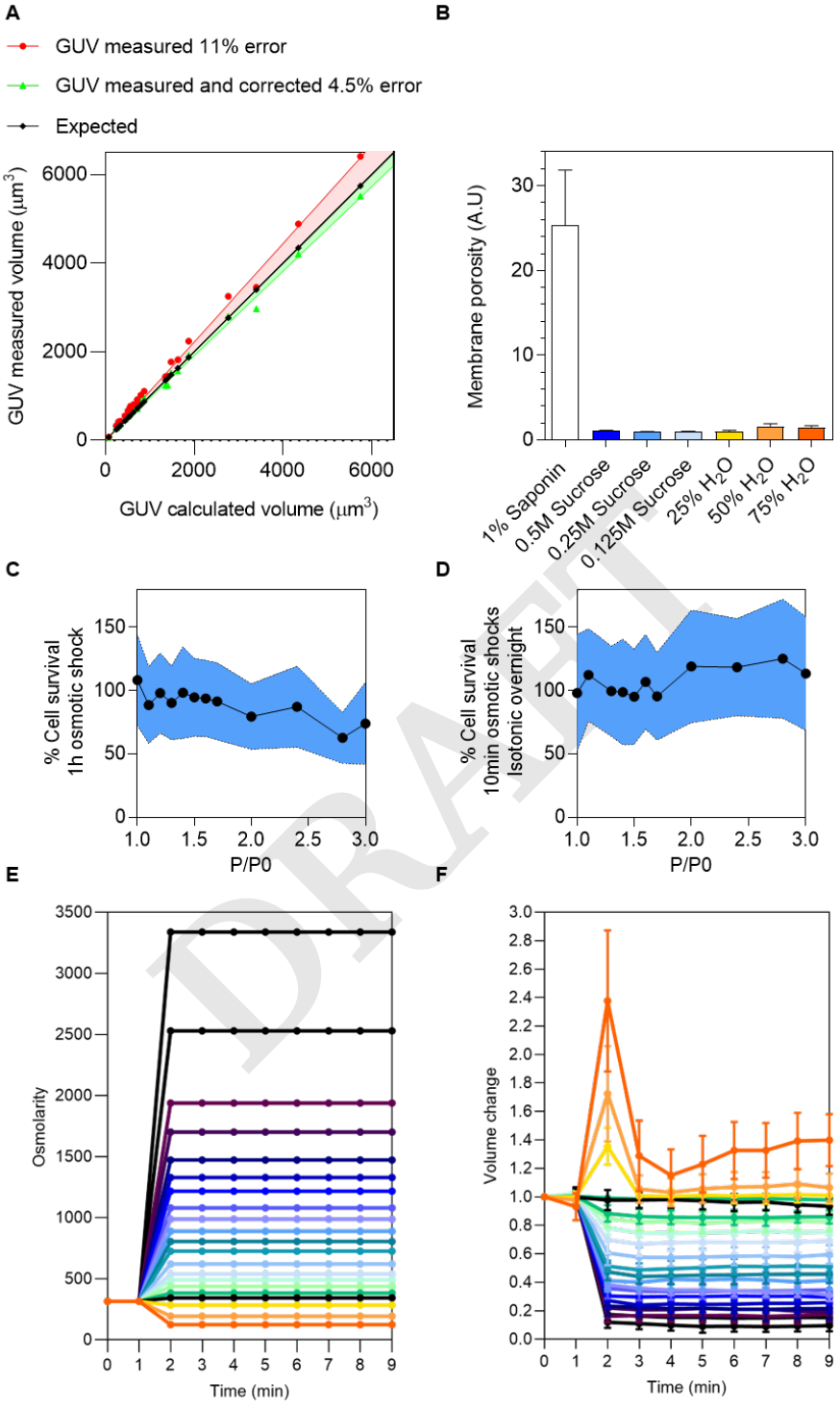

Fig. 1. Supplementary || Cell volume changes under osmotic pressure. A, Estimation of the 3D segmentation error using GUV. In red, the GUV volume measured with 11% error from the expected volume of GUV (calculated from the measured radius) and in green the corrected volume measurement using the ref ??. **B**, Cell membrane porosity measured using propidium iodide for different osmotic conditions (hypotonic and hypertonic). **C**, Cell survival rate measured using CCK-8 salt after 1h of hypertonic shocks. **D**, Cell survival rate measured using CCK-8 salt after 10 min of hypertonic shocks and overnight in isotonic medium. **E**, Osmolarity changes during time of all the osmotic conditions used for the Ponder relation. **F**, Volume changes during time of all the osmotic conditions used for the Ponder relation.

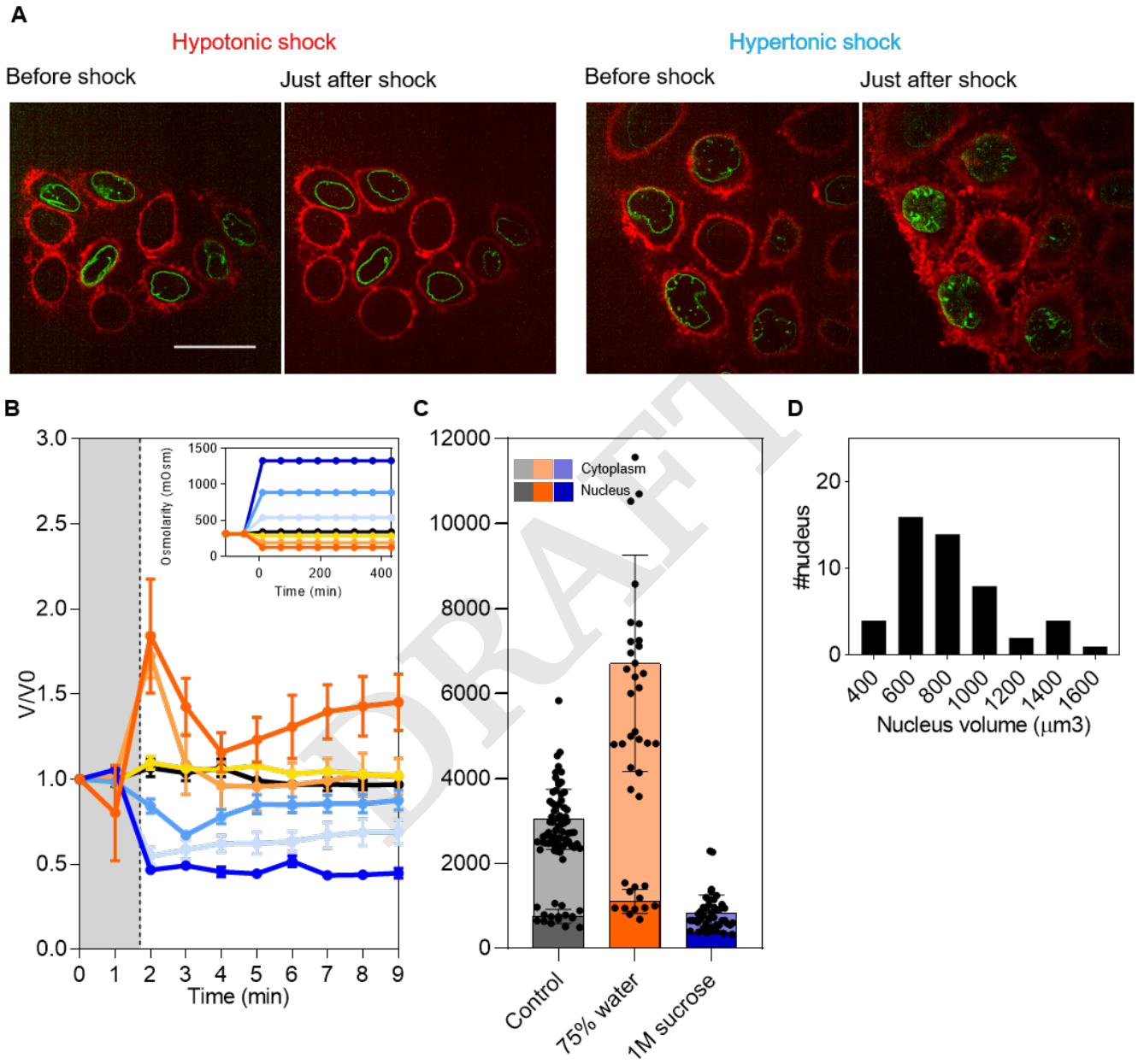

Fig. 2. Supplementary || Nucleus volume changes under osmotic pressure. A, Representative confocal images of plasma membrane (CellMask) and nuclear membrane (Lamin-B1) under hypotonic (120 mOsm) and hypertonic shocks (800 mOsm). **B**, Single nucleus volume dynamic under osmotic shock. **C**, Relative contribution of nucleus and cytoplasm to cell volume changes under hypotonic shock (120 mOsm - orange) and hypertonic shock (1M sucrose - blue). **D**, Distribution of nucleus size in isotonic medium.

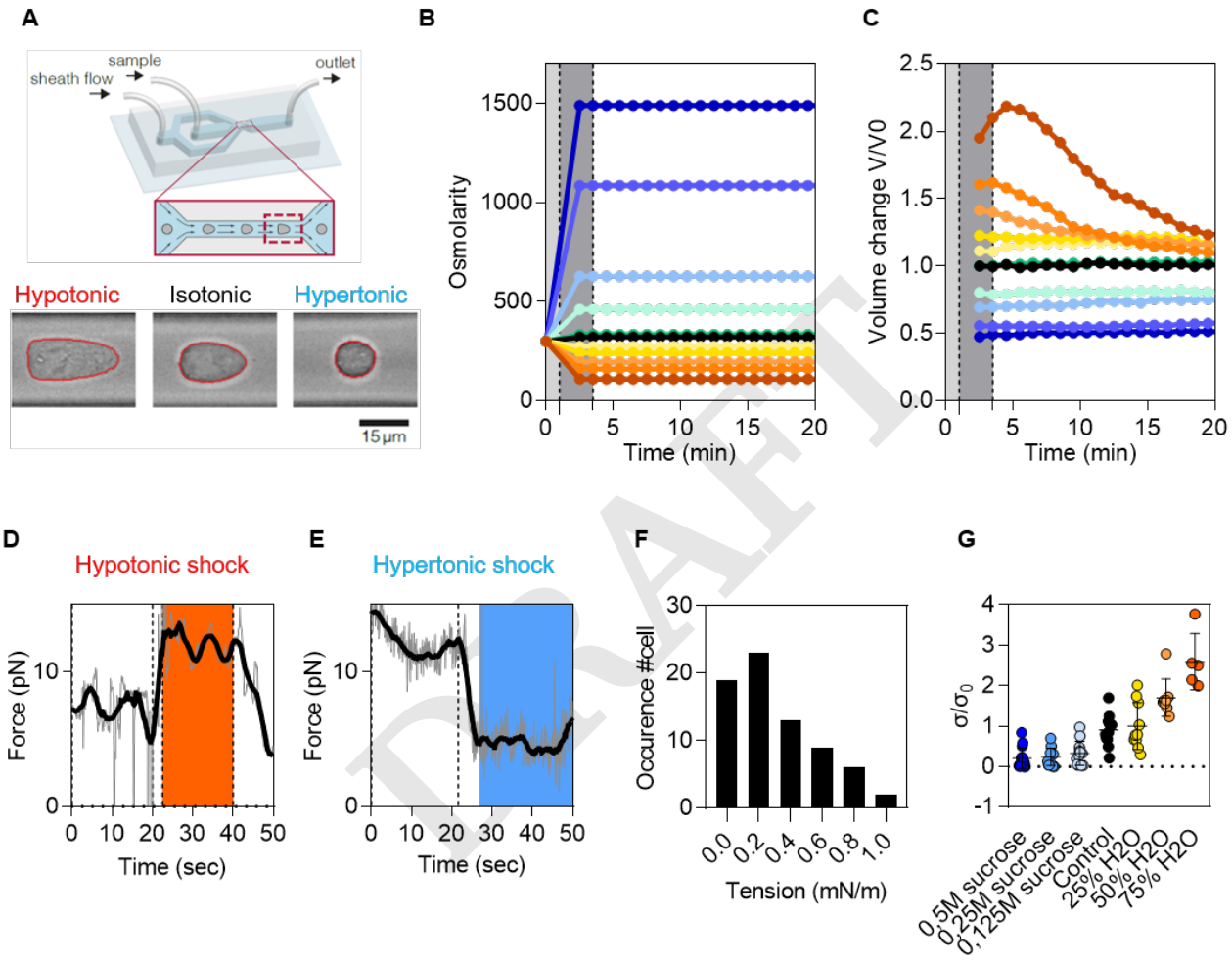

Fig. 3. Supplementary || HL-S4 cell volume changes under osmotic shocks using RT-DC and membrane tension changes. **A**, RT-DC principles. **B**, Osmolarity changes under osmotic shocks with RT-DC measurement. **C**, Cell volume dynamic under osmotic shocks with RT-DC measurement. For P = 110 mOsm, the number of event n = 3000; for P = 162 mOsm n = 3312; for P = 196 mOsm n = 4002; for P = 243 mOsm n = 2846; for P = 274 mOsm n = 3002; for P = 322 mOsm n = 3351; for P = 334 mOsm n = 3005; for P = 462 mOsm n = 3458; for P = 628 n = 5046; for P = 1086 mOsm n = 3348; for P = 1491 n = 449. **D**, Representative tether force measurement under hypotonic shock. **E**, Representative tether force measurement under hypertonic shock. **F**, Distribution of initial tether force to pull a cell membrane tube (isotonic condition). **G**, Relative tension measurement under osmotic conditions.

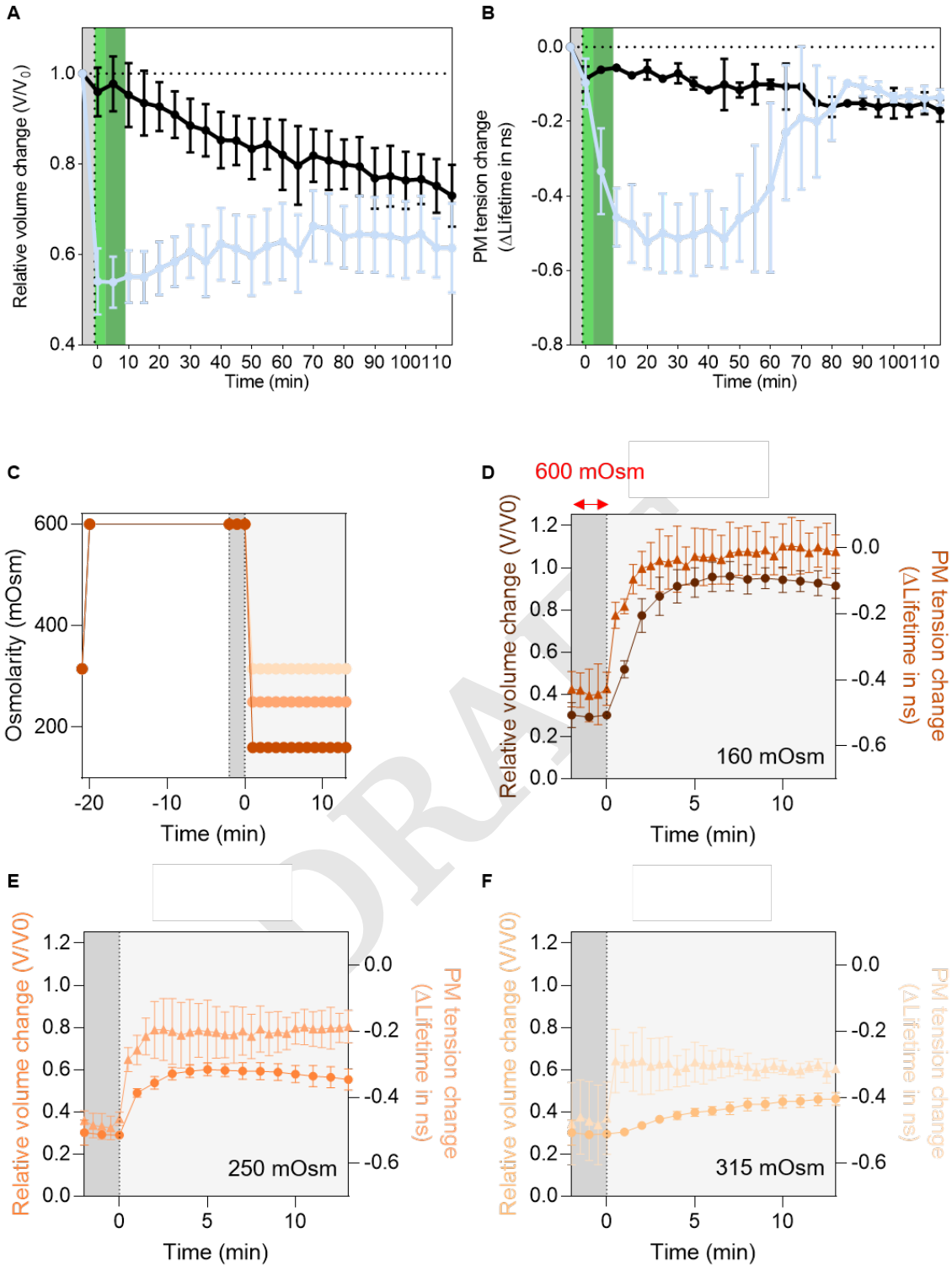

Fig. 4. Supplementary || Long term recovery after hypertonic shocks and active cell recovery after consecutive shocks (hypertonic then hypotonic). **A**, Relative volume change under isotonic shock and hypertonic shock of 600 mOsm. For isotonic shock (black), R = 4 and N = 21. For hypertonic shock (light blue), R = 5 and N = 19. **B**, PM tension change under isotonic shock and hypertonic shock of 600 mOsm. For each experiment N>4. For isotonic shock (black), R = 2. For hypertonic shock (light blue), R = 3. **C**, Osmolarities (mOsm) of cell media with time for the different shocks. **D**, Relative volume change (round) and PM tension change (triangle) after a 20 min long hypertonic shock (600 mOsm) followed by an hypotonic shock (160 mOsm). For cell volume measurement, R>3 and N = 8. For PM tension measurement, N>4 and R = 3. **E**, Relative volume change (round) and PM tension change (triangle) after a 20 min long hypertonic shock (600 mOsm) followed by an hypotonic shock (250 mOsm). For cell volume measurement, R>3 and N = 12. For PM tension measurement, N>4 and R = 4. **F**, Relative volume change (round) and PM tension change (triangle) after a 20 min long hypertonic shock (600 mOsm) followed by a return to an isotonic medium (315 mOsm). For cell volume measurement, R>3 and N = 10. For PM tension measurement, N>4 and R = 3.

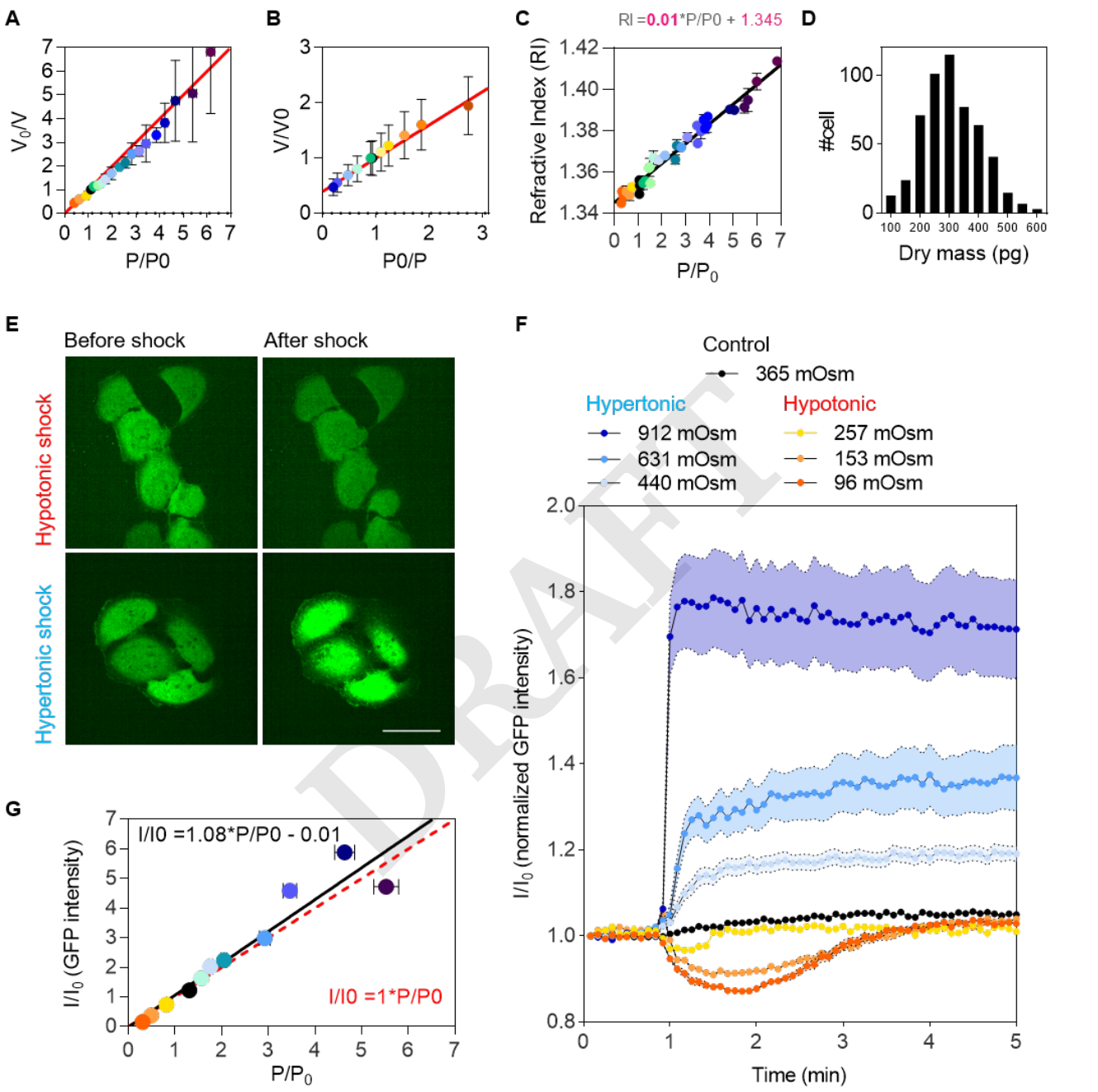

Fig. 5. Supplementary || Measure GFP diffusion changes under osmotic shocks. A, Inverse of volume change (V0/V) according to pressure change (P/P0) in HeLa cells. **B**, Ponder's relation measuring volume with RT-DC in HL-60/S4 cells. For P = 110 mOsm, the number of event n = 3000; for P = 162 mOsm n = 3312; for P = 196 mOsm n = 4002; for P = 243 mOsm n = 2846; for P = 274 mOsm n = 3002; for P = 322 mOsm n = 3351; for P = 334 mOsm n = 3005; for P = 462 mOsm n = 3458; for P = 628 n = 5046; for P = 1086 mOsm n = 3348; for P = 1491 n = 449. **C**, Refractive index of cell according to change of pressure (P/P0). Each point corresponds to R = 1 with N > 4 for each. **D**, Distribution of dry mass (pg) in isotonic medium. **E**, Representative images of GFP tranfected cells under hypotonic shock (top) and hypertonic shock (down). **F**, Relative change of intensity (I/I0) in time for various osmolarities. **G**, Relative change of intensity (I/I0) according to pressure changes (P/P0).

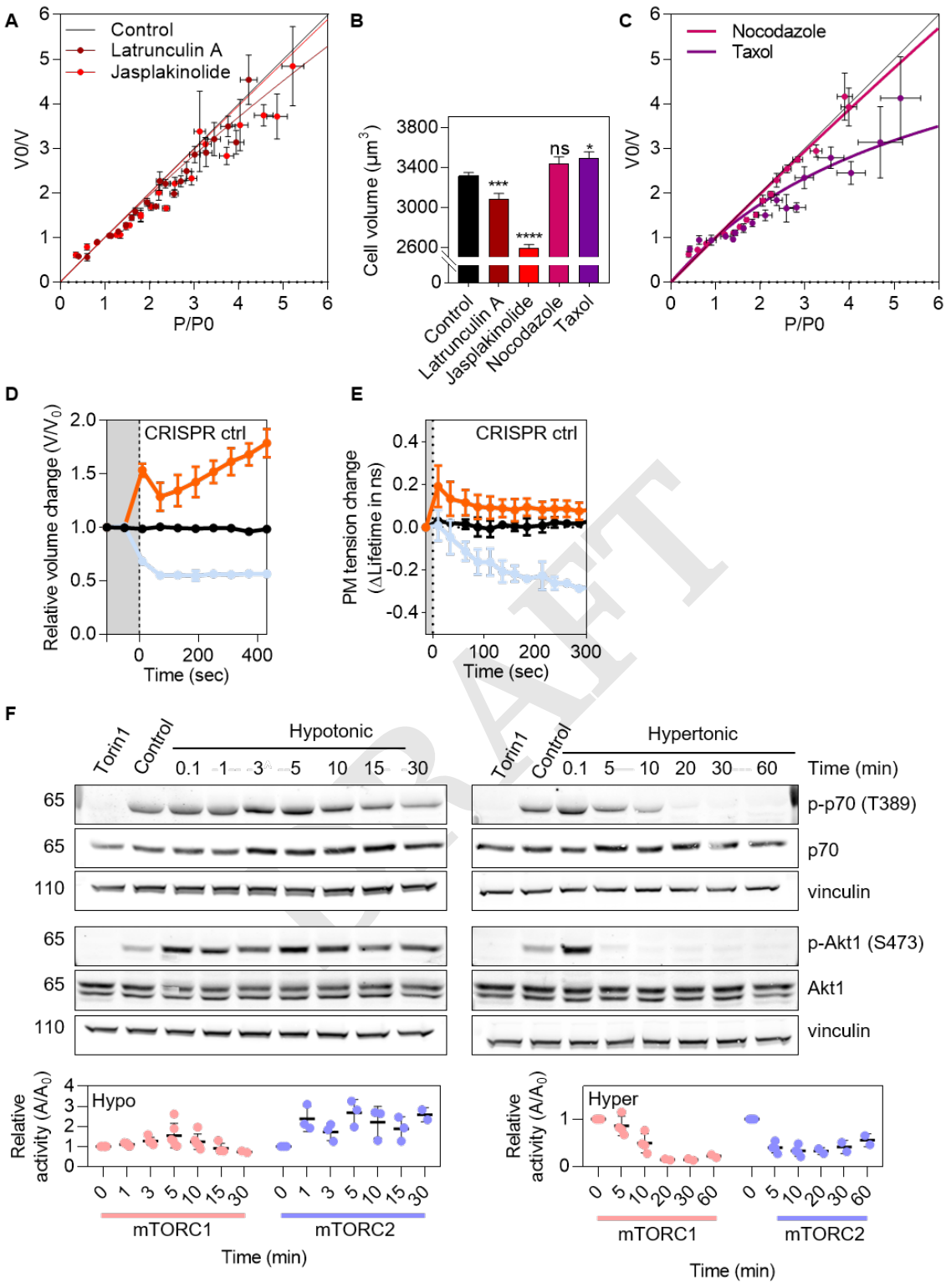

Fig. 6. Supplementary || Cell response to osmotic shocks under drug treatment and mTOR activity under osmotic shocks. A, Ponder's relation for latrunculin A or jasplakinolide treated cells. **B**, Cell volume in isotonic medium. R > 20 for every drug conditions and N = 959 for control, N = 267 for latrunculin A, N = 287 for jasplakinolide, N = 147 for nocodazole, N = 244 for taxol. **C**, Ponder's relation for nocodazole or taxol treated cells. **D**, Single cell volume dynamics of cells CRISPR control. Statistics are R>3 for every experiments. For CRISPR control, N=5 for control, N=18 for hypo, N=12 for hyper. **E**, Membrane tension dynamics of cells CRISPR control. Statistics are N>4 for every experiments. For CRISPR control, R=2 for control, R=5 for hypo, R=2 for hyper. **F**, Activity of mTORC1 and mTORC2 under hypertonic and hypotonic shock. Panels represent activation (phosphorylation) of S6K1 (p-p70) and Akt (pAkt) and loading controls. **E**, Quantification of the western blot in (C).

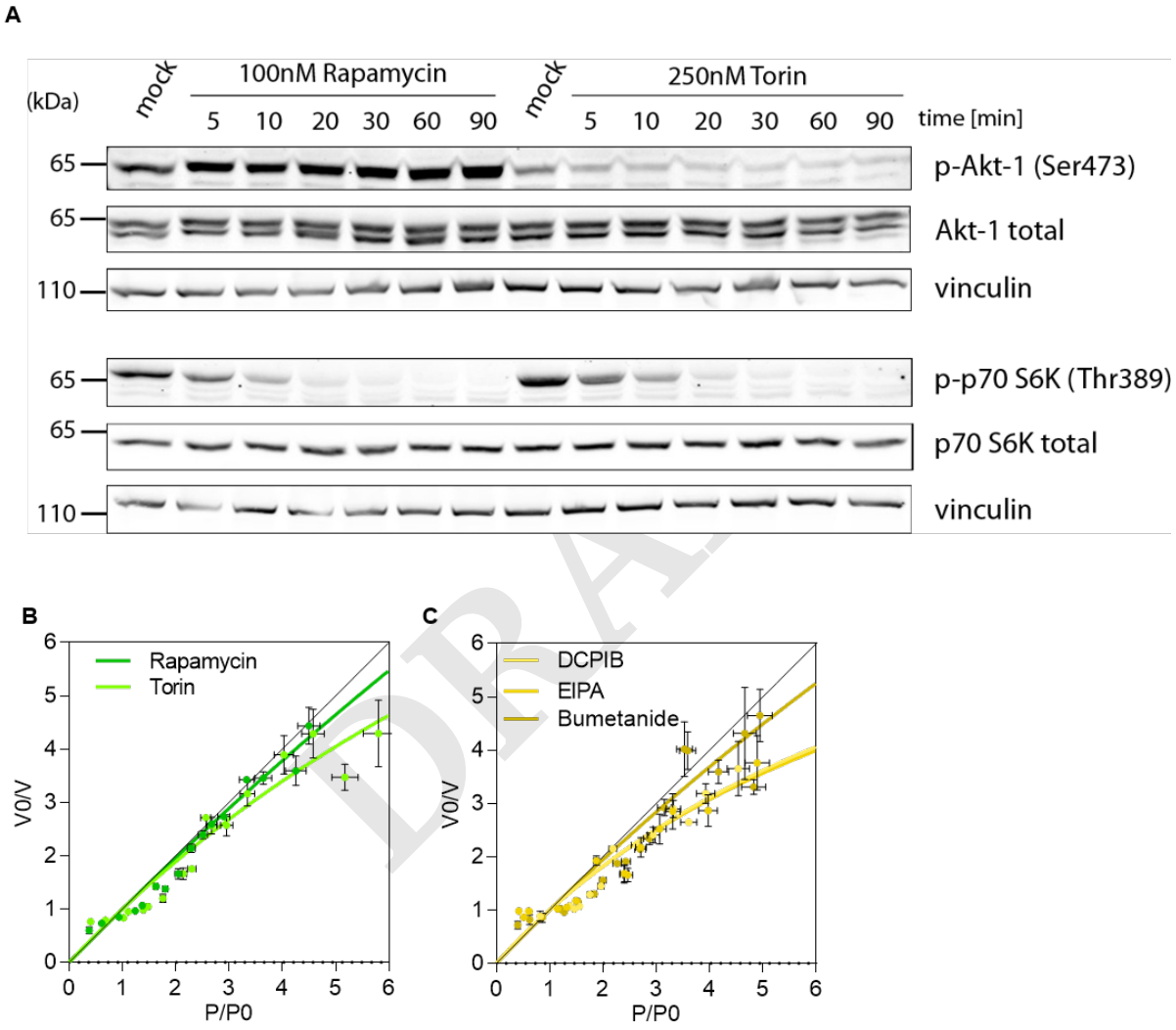

Fig. 7. Supplementary || Cell response to osmotic shocks under drug treatment and kinetic of inhibition of mTOR. A, Dynamics of mTOR inhibition under rapamycin and torin1 treatment. Panels represent activation (phosphorylation) of S6K1 (p-p70) and Akt (pAkt) and loading controls. **B**, Ponder's relation for rapamycin or Torin1 treated cells. **C**, Ponder's relation for DCPIB or EIPA or Bumetanide treated cells.

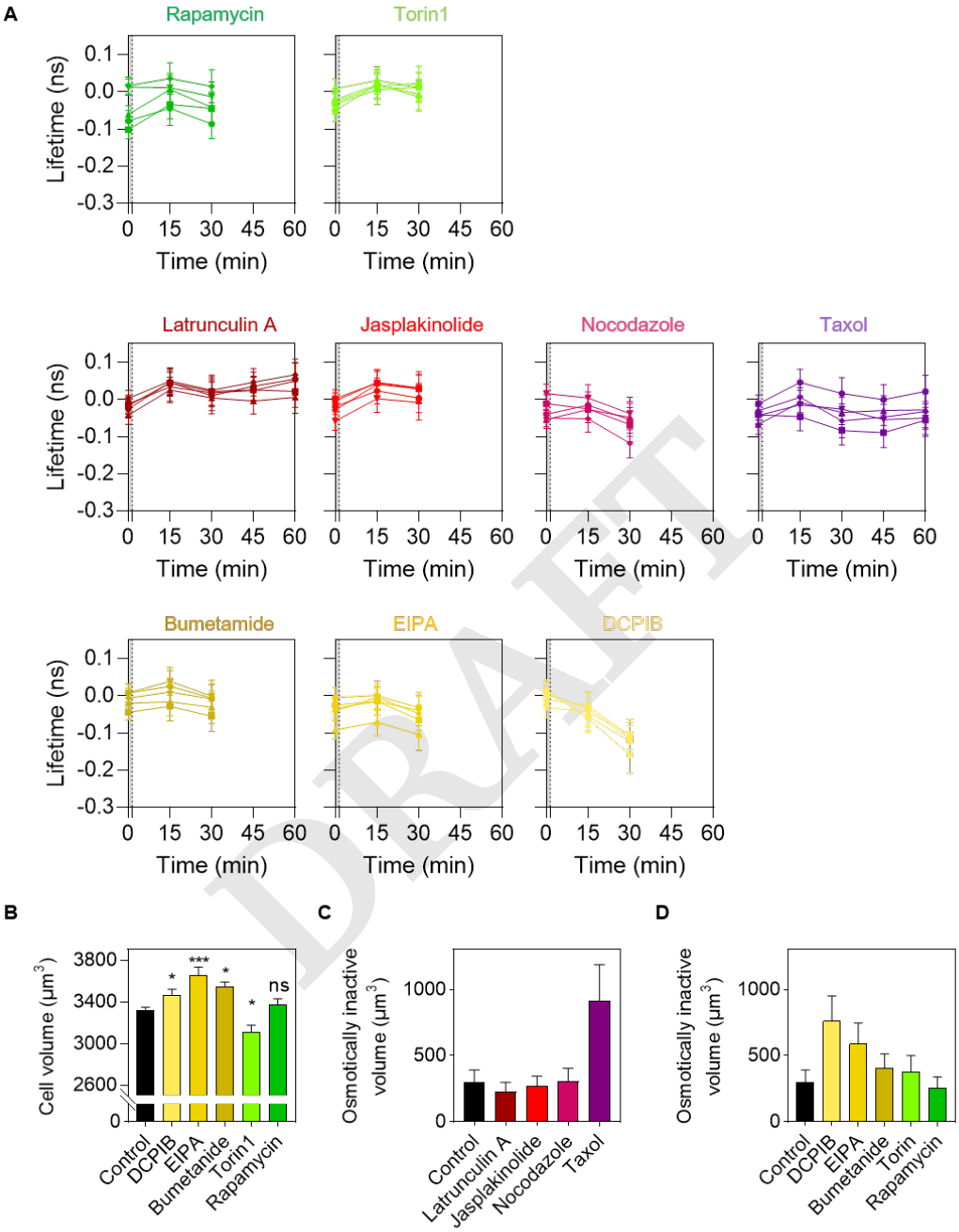

Fig. 8. Supplementary || Lifetime changes during drug treatment and cell volume after drug treatment. A, PM tension changes as a function of time as the drugs are added. For every drug condition, N>3 and R=5. **B**, Cell volume in isotonic medium. R > 20 for every drug conditions and N = 959 for control, N = 210 for DCPIB, N = 125 for EIPA, N = 296 for bumetanide, N = 164 for torin1, N = 185 for rapamycin. **C**, Osmotically inactive volume extracted from the Ponder's relation (Supp Fig 6A-C). The error is extracted from the fit uncertainty. **D**, Osmotically inactive volume extracted from the Ponder's relation (Supp Fig 7B-C). The error is extracted from the fit uncertainty.

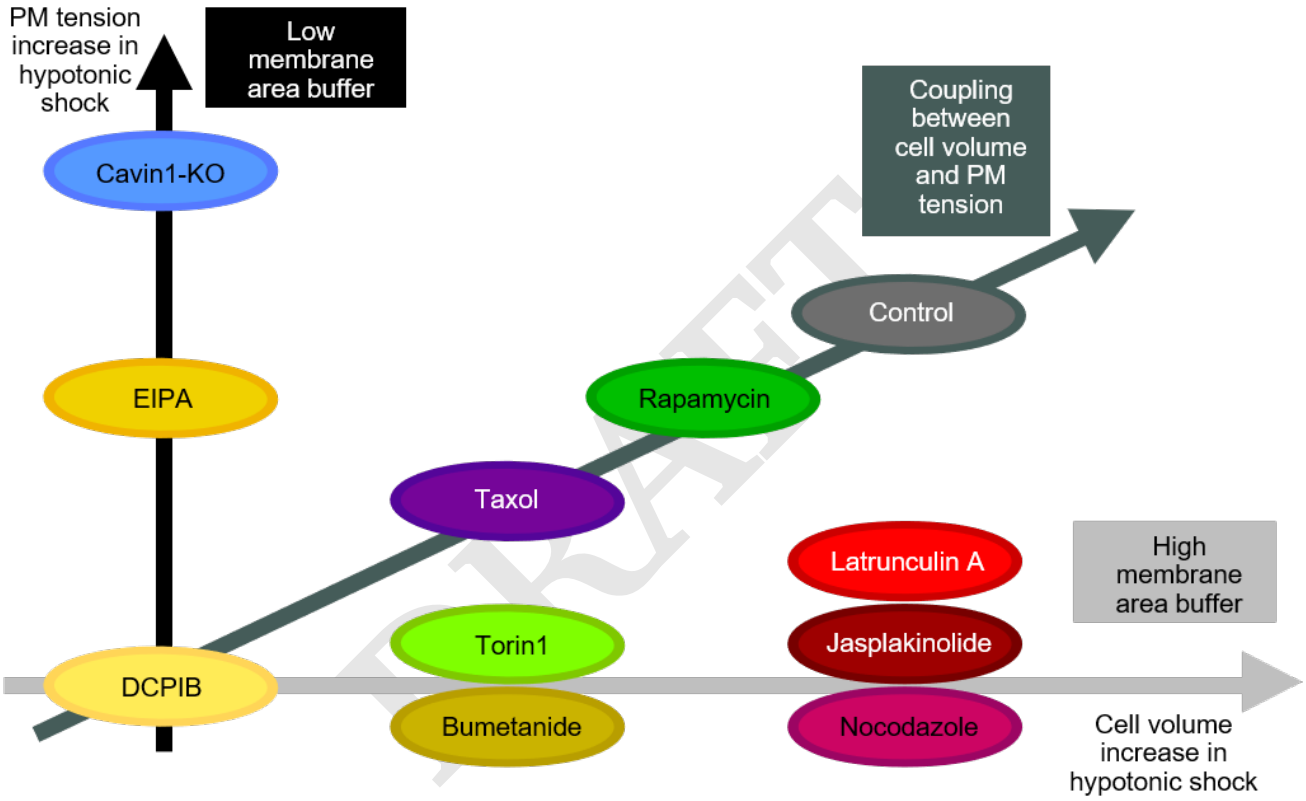

Fig. 9. Supplementary || Recapitulative scheme Coupling between PM tension increase and cell volume increase in hypotonic shocks (along the dark grey line) is verified for cells treated with taxol and rapamycin and control cells suggesting that cells have an intermediate membrane area buffer and for DCPIB which has no increase of cell volume neither PM tension. EIPA and Cavin1-KO have PM tension increase without cell volume increase under hypotonic shocks suggesting that those cells have a low membrane area buffer. Torin1, bumetanide, latrunculinA, jasplakinolide and nocodazole treated cells have cell volume increase without PM tension increase under hypotonic shocks suggesting that those cells have increased membrane area buffer.

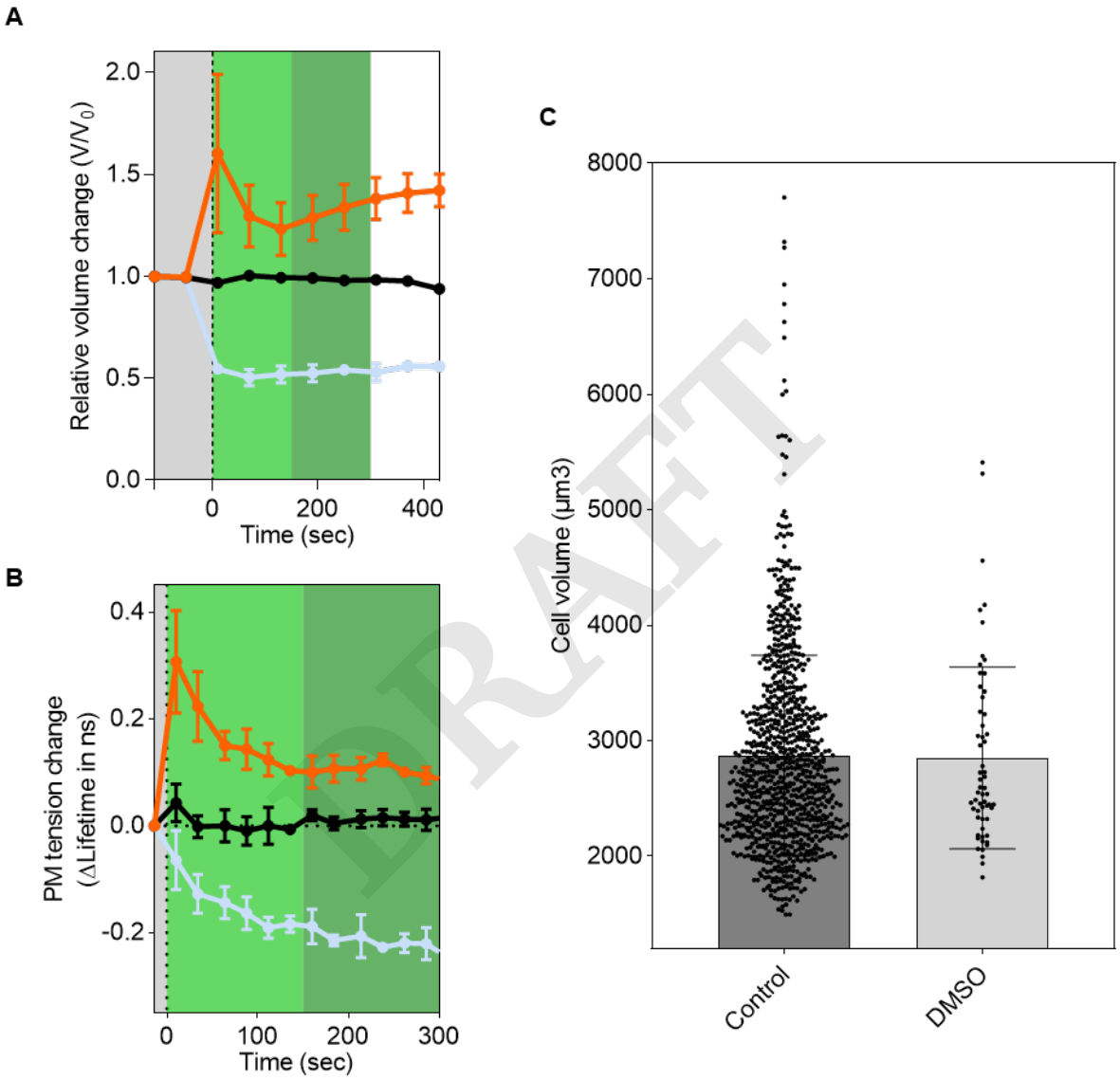

Fig. 10. Supplementary || PM tension and cell volume changes under DMSO treatment. A,Relative volume change under hypotonic shocks (120 mOsm), isotonic shock (315 mOsm) and hypertonic shock (600 mOsm). For each experiments, R>3. For hypotonic shock (orange) N = 37, for isotonic shock (black) N = 14 and for hypertonic shock (light blue) N = 8. **B**,PM tension change under hypotonic shocks (120 mOsm), isotonic shock (315 mOsm) and hypertonic shock (600 mOsm). For each experiment, N>4 and R = 3. **C**, Absolute cell volume of control cell and cells with DMSO.

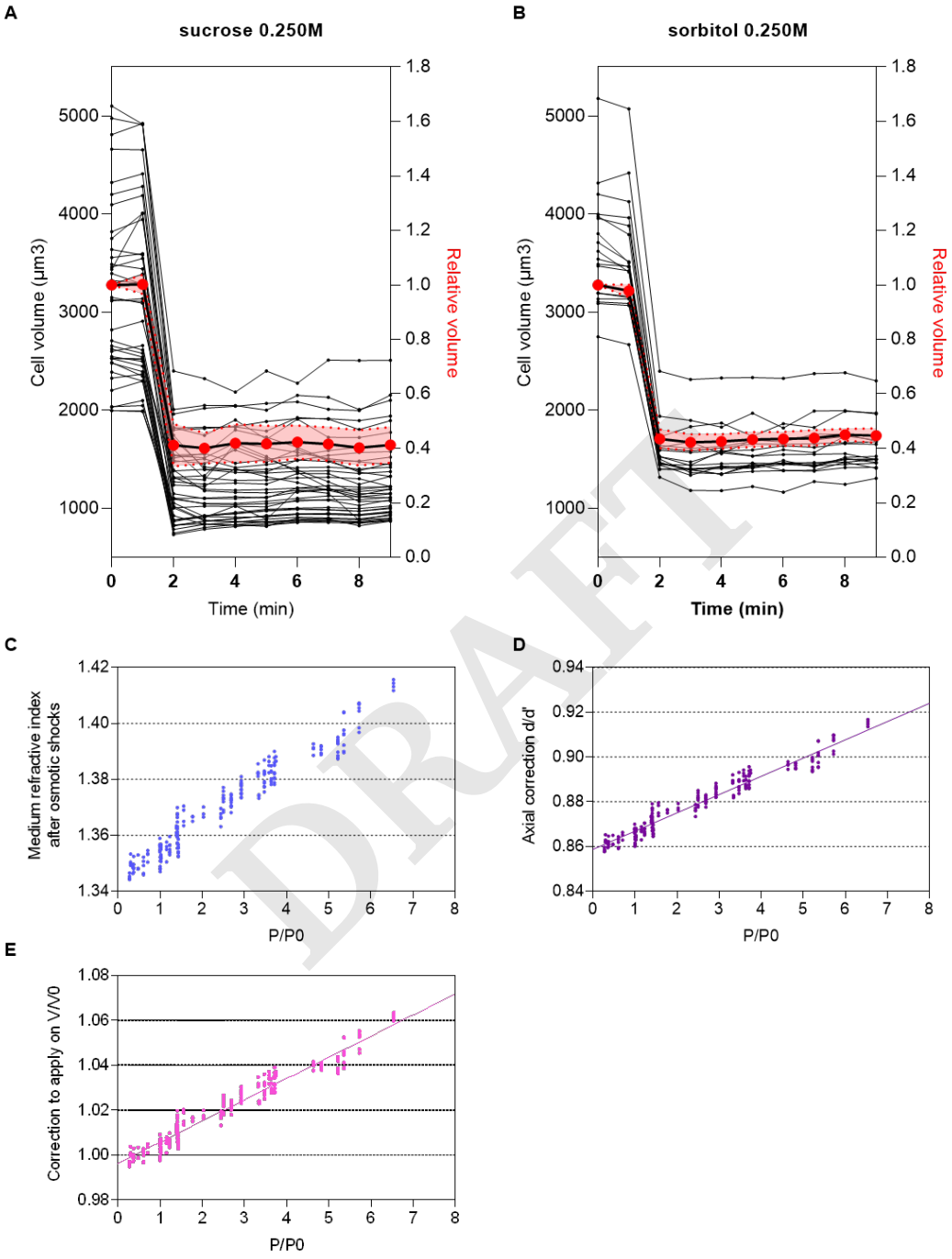

Fig. 11. Supplementary || Comparaison of the effect between sucrose and sorbitol and calculation of axial correction necessary for volume measurement. **A**, Absolute volume of cells undergoing a sucrose hypertonic shocks 0.250M (each black line are individual cells) and relative volume changes of all the cells. **B**, Absolute volume of cells undergoing a sorbitol hypertonic shocks 0.250M (each black line are individual cells) and relative volume changes of all the cells. **C**, Refractive index of the medium after osmotic shocks. **D**, Axial correction d/d' calculated (see Methods). **E**, Relative cell volume correction required.

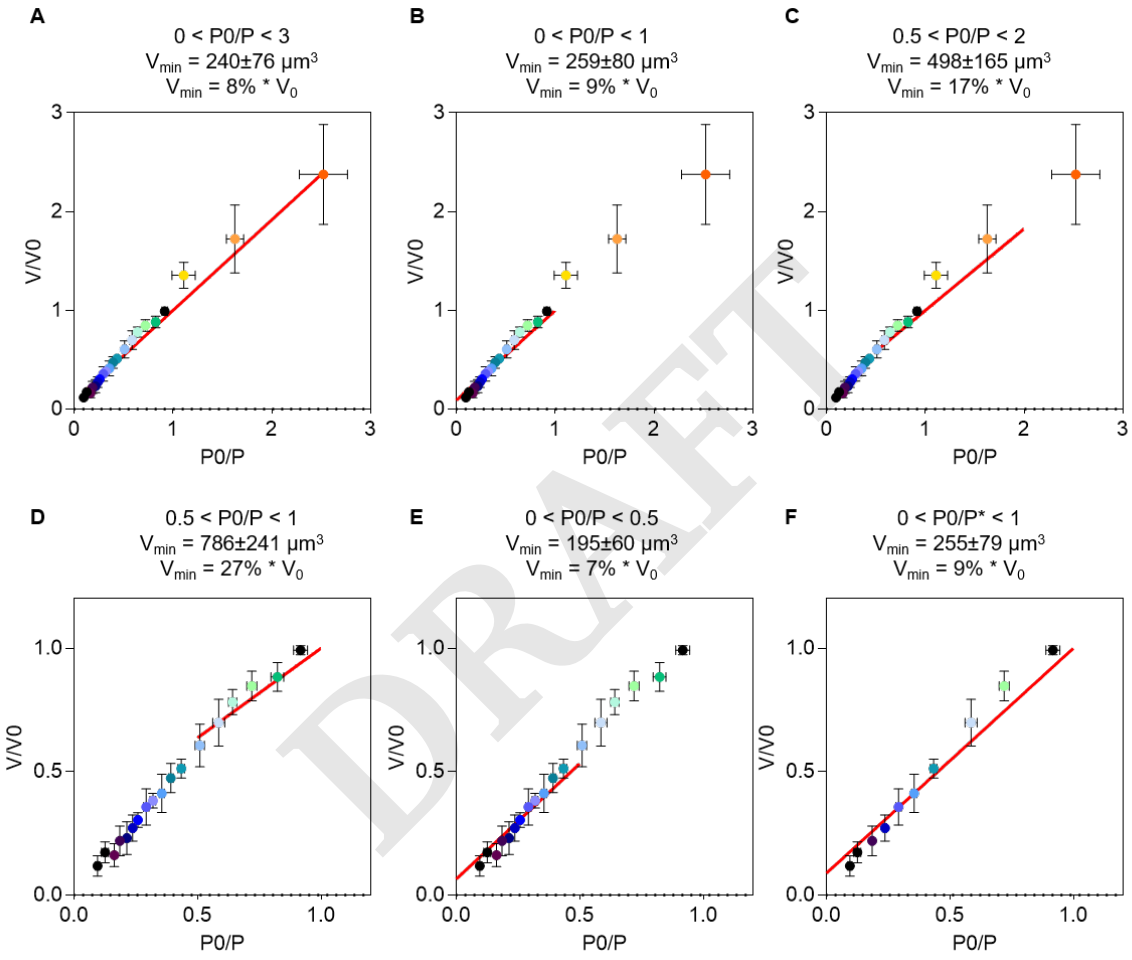

Fig. 12. Supplementary || Calculation of the osmotically inactive volume. **A**, Ponder's relation and extraction of the osmotically inactive volume for $0<P_0/P<3$. **B**, Ponder's relation and extraction of the osmotically inactive volume for $0<P_0/P<1$. **C**, Ponder's relation and extraction of the osmotically inactive volume for $0.5<P_0/P<2$. **D**, Ponder's relation and extraction of the osmotically inactive volume for $0.5<P_0/P<1$. **E**, Ponder's relation and extraction of the osmotically inactive volume for $0<P_0/P<0.5$. **F**, Ponder's relation and extraction of the osmotically inactive volume for $0<P_0/P<1$.

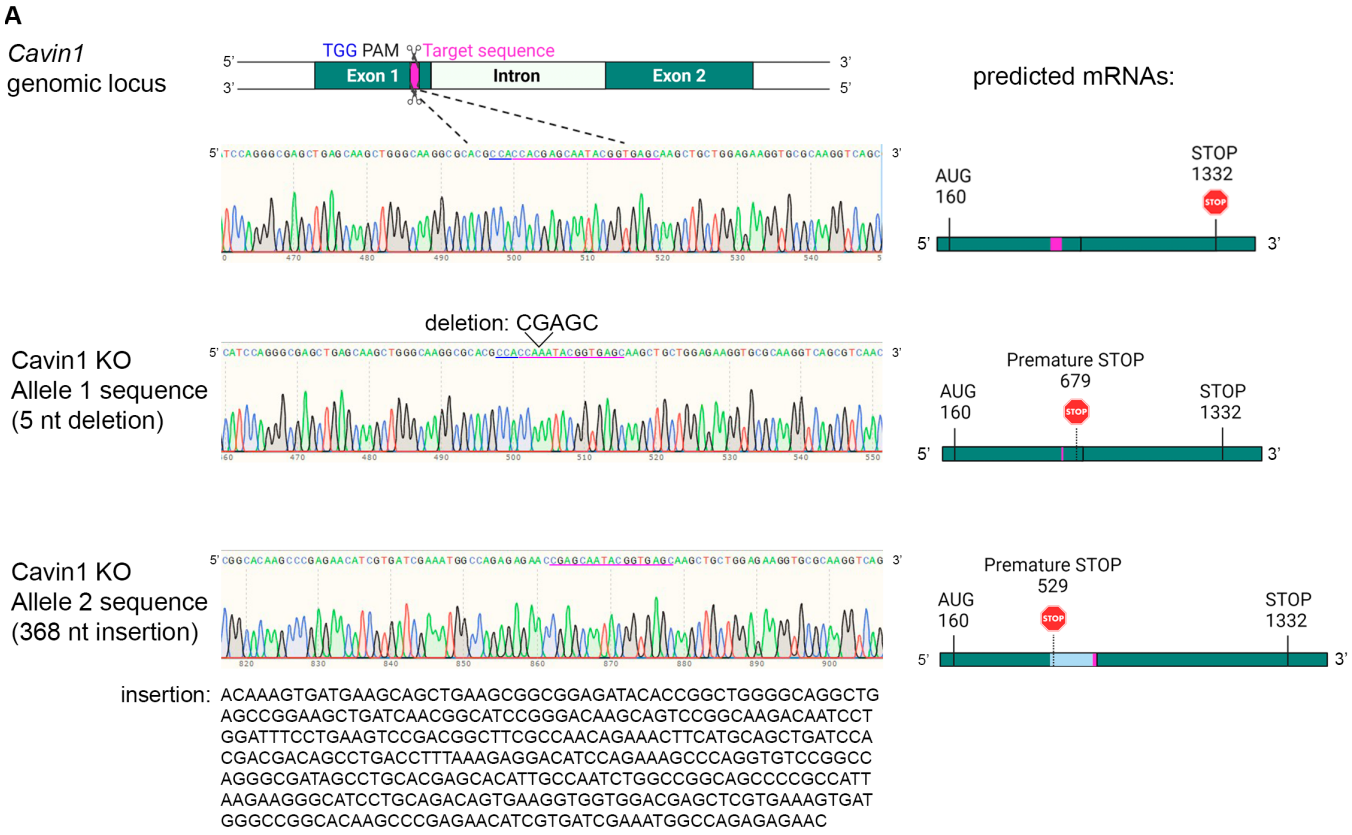

Fig. 13. Supplementary || Characterization of Cavin1 KO cells. **A**, Left panels: A CRISPR/Cas9 guide RNA was designed to target the first Exon of Cavin1 with the indicated PAM and target sequence (blue and magenta, respectively), as indicated in the material and methods. Below the schematic representation of the genomic Cavin1 locus, are successively displayed the sequences of the DNA sequence around the PAM region for the Control KO clone (corresponding to the expected wt allele), for the mutant Allele 1 found in the Cavin1 KO clone (this allele corresponds to a 5 nucleotide (nt) deletion) and for the mutant Allele 2 also found in the Cavin1 KO clone (this allele corresponds to a 368 indel in the PAM region, whose sequence is provided). Random sequencing of 37 topo-cloned PCR products spanning 1200 nt centred on the PAM region revealed that Allele 1 was found 26 times and Allele 2 11 times in the Cavin1 KO cells. Since HeLa cells are triploid for Chromosome 17 that bears the Cavin1 locus, we conclude that the Cavin1 KO clone contains two alleles 1 and one allele 2 per genome. Right panels: predicted mRNAs resulting from the transcription of the Cavin1 alleles. The positions of the Start codons (AUG) and STOP codons are displayed (numbers correspond to nucleotides). Note the apparition of a premature STOP codon for each mutant allele in Cavin1 KO cells as a result of frameshifts. **B**, RT-PCR in Control KO and Cavin1 KO with Cavin1 specific primers positioned in unmodified parts of exon 1 (see material and methods). RT-PCR with GAPDH specific primers is used as a loading control. The absence of Cavin1 RT-PCR product in Cavin1 KO cells indicate an absence of detectable Cavin1 mRNA, likely due to non-sense mediated decay (NMD). **C**, Westernblot of cells lysates from Control KO (first 6 lanes) and Cavin1 KO (last lane), revealed with anti-Cavin1 antibodies. GAPDH is used as a loading control. 100% loadings correspond to equivalent amounts of Control KO and Cavin1 KO lysates (equivalent GAPDH intensity). Serial dilutions of Control KO lysates (1/2, 1/3, 1/4, 1/5 and 1/6 of 100%) have been included to visualize the sensitivity of the Cavin1 antibody. The absence of detectable signal in the Cavin1 KO lane shows the absence of the Cavin1 protein.

References

1. Addi, C., et al., *The Flemmingsome reveals an ESCRT-to-membrane coupling via ALIX/syntenin/syndecan-4 required for completion of cytokinesis.* Nat Commun, 2020. **11**(1): p. 1941.
2. Kogo, H. and T. Fujimoto, *Concentration of caveolin-1 in the cleavage furrow as revealed by time-lapse analysis.* Biochem Biophys Res Commun, 2000. **268**(1): p. 82-7.
3. Feng, B., H. Schwarz, and S. Jesuthasan, *Furrow-Specific Endocytosis during Cytokinesis of Zebrafish Blastomeres*. 2002. p. 14-20.
4. Goliand, I., et al., *Resolving ESCRT-III Spirals at the Intercellular Bridge of Dividing Cells Using 3D STORM.* Cell Rep, 2018. **24**(7): p. 1756-1764.
5. Guizetti, J., et al., *Cortical Constriction During Abscission Involves Helices of ESCRT-III-Dependent Filaments*. Science, 2011. **331**: p. 1616-20.
6. Mierzwa, B.E., et al., *Dynamic subunit turnover in ESCRT-III assemblies is regulated by Vps4 to mediate membrane remodelling during cytokinesis.* Nat Cell Biol, 2017. **19**(7): p. 787-798.
7. Lamaze, C. and S. Torrino, *Caveolae and cancer: A new mechanical perspective.*, in *Biomedical journal*. 2015. p. 367-79.
8. Parton, R.G. and M.A. del Pozo, *Caveolae as plasma membrane sensors, protectors and organizers*, in *Nature Reviews Molecular Cell Biology*. 2013, Nature Publishing Group. p. 98-112.
9. Goody, R.S., M.P. Müller, and Y.W. Wu, *Mechanisms of action of Rab proteins, key regulators of intracellular vesicular transport*, in *Biological Chemistry*. 2017. p. 565-575.
10. Moren, B., et al., *EHD2 regulates caveolar dynamics via ATP-driven targeting and oligomerization*, in *Molecular Biology of the Cell*. 2012. p. 1316-1329.
11. Nassoy, P. and C. Lamaze, *Stressing caveolae new role in cell mechanics*, in *Trends in Cell Biology*. 2012, Elsevier Ltd. p. 381-389.
12. Green, R.A., E. Paluch, and K. Oegema, *Cytokinesis in Animal Cells*, in *Annual Review of Cell and Developmental Biology*. 2012. p. 29-58.
13. Lamaze, C., et al., *The caveolae dress code: structure and signaling*, in *Current Opinion in Cell Biology*. 2017. p. 117-125.
14. Goliand, I., et al., *Resolving ESCRT-III Spirals at the Intercellular Bridge of Dividing Cells Using 3D STORM*, in *Cell Reports*. 2018, ElsevierCompany. p. 1756-1764.
15. Lacroix, B. and A.S. Maddox, *Cytokinesis, ploidy and aneuploidy*, in *Journal of Pathology*. 2012. p. 338-351.
16. Bruns, R.R. and G.E. Palade, *the fine structure of blood capillaries*, in *Jurnal of applied Physiology*. 1968. p. 244-276.
17. Mierzwa, B.E., et al., *Dynamic subunit turnover in ESCRT-III assemblies is regulated by Vps4 to mediate membrane remodelling during cytokinesis*. 2017.
18. Pfitzner, A.K., et al., *An ESCRT-III Polymerization Sequence Drives Membrane Deformation and Fission*, in *Cell*. 2020. p. 1140-1155.e18.
19. Hurley, J.H., *ESCRTs are everywhere.* EMBO J, 2015. **34**(19): p. 2398-407.
20. Sinha, B., et al., *Cells respond to mechanical stress by rapid disassembly of caveolae*, in *Cell*. 2011. p. 402-413.
21. Diz-Muñoz, A., et al., *Membrane Tension Acts Through PLD2 and mTORC2 to Limit Actin Network Assembly During Neutrophil Migration.* PLOS Biology, 2016. **14**(6): p. e1002474.

22. Hubert, M., et al., *Lipid accumulation controls the balance between surface connection and scission of caveolae.* eLife, 2020. **9**: p. e55038.
23. Teo, J.L., et al., *Caveolae Control Contractile Tension for Epithelia to Eliminate Tumor Cells*, in *Developmental Cell*. 2020, Elsevier Inc. p. 75-91.e7.
24. Matsumura, S., et al., *Interphase adhesion geometry is transmitted to an internal regulator for spindle orientation via caveolin-1.* Nature Communications, 2016. **7**(1): p. ncomms11858.
25. Parton, R.G., *Caveolae: Structure, Function, and Relationship to Disease*, in *Annual Review of Cell and Developmental Biology*. 2018, Annual Reviews. p. 111-136.
26. Quan, A. and P.J. Robinson, *Syndapin – a membrane remodelling and endocytic F-BAR protein.* The FEBS Journal, 2013. **280**(21): p. 5198-5212.
27. Senju, Y. and S. Suetsugu, *Possible regulation of caveolar endocytosis and flattening by phosphorylation of F-BAR domain protein PACSIN2/ Syndapin II*, in *BioArchitecture*. 2015. p. 70-77.
28. Elia, N., et al., *Computational Model of Cytokinetic Abscission Driven by ESCRT-III Polymerization and Remodeling*, in *Biophysj*. 2012, Biophysical Society. p. 2309-2320.
29. Lafaurie-Janvore, J., et al., *ESCRT-III assembly and cytokinetic abscission are induced by tension release in the intercellular bridge.* Science, 2013. **339**(6127): p. 1625-9.
30. Maity, S., et al., *VPS4 triggers constriction and cleavage of ESCRT-III helical filaments*, in *Science Advances*. 2019.
31. Berchtold, D., et al., *Plasma membrane stress induces relocalization of Slm proteins and activation of TORC2 to promote sphingolipid synthesis.* Nature Cell Biology, 2012. **14**(5): p. 542-547.
32. Paweletz, N., *Walther Flemming : pioneer of mitosis research*. 2001, Nat Rev Mol Cell Biol. p. 72-75.
33. Flemming, W., *Kern und Zelltheilung* 1882.
34. Schroeder, T.E., *Actin in dividing cells: contractile ring filaments bind heavy meromyosin.* Proc Natl Acad Sci U S A, 1973. **70**(6): p. 1688-92.
35. Maupin, P. and T.D. Pollard, *Arrangement of actin filaments and myosin-like filaments in the contractile ring and of actin-like filaments in the mitotic spindle of dividing HeLa cells.* Journal of Ultrastructure and Molecular Structure Research, 1986. **94**(1): p. 92-103.
36. Wang, Y.L. and D.L. Taylor, *Distribution of fluorescently labeled actin in living sea urchin eggs during early development.* J Cell Biol, 1979. **81**(3): p. 672-9.
37. Jantsch-Plunger, V., et al., *Cyk-4: A Rho Family Gtpase Activating Protein (Gap) Required for Central Spindle Formation and Cytokinesis.* Journal of Cell Biology, 2000. **149**(7): p. 1391-1404.
38. Longtine, M.S., et al., *The septins: roles in cytokinesis and other processes.* Current Opinion in Cell Biology, 1996. **8**(1): p. 106-119.
39. Adams, R.R., et al., *pavarotti encodes a kinesin-like protein required to organize the central spindle and contractile ring for cytokinesis.* Genes Dev, 1998. **12**(10): p. 1483-94.
40. Eggert, U.S., et al., *Parallel chemical genetic and genome-wide RNAi screens identify cytokinesis inhibitors and targets*, in *PLoS Biology*. 2004.
41. Skop, A.R., et al., *Dissection of the mammalian midbody proteome reveals conserved cytokinesis mechanisms.* Science, 2004. **305**(5680): p. 61-6.
42. Echard, A., et al., *Terminal Cytokinesis Events Uncovered after an RNAi Screen.* Curr Biol, 2004. **14**(18): p. 1685-93.
43. Echard, A. and P.H. O'Farrell, *The degradation of two mitotic cyclins contributes to the timing of cytokinesis.* Curr Biol, 2003. **13**(5): p. 373-83.
44. Castro, A., et al., *The anaphase-promoting complex: a key factor in the regulation of cell cycle.* Oncogene, 2005. **24**(3): p. 314-325.

45. Mierzwa, B. and D.W. Gerlich, *Cytokinetic Abscission: Molecular Mechanisms and Temporal Control*, in *Developmental Cell*. 2014, Elsevier Inc. p. 525-538.
46. Crowell, E.F., et al., *Engulfment of the midbody remnant after cytokinesis in mammalian cells*. 2014. p. 3840-3851.
47. Mollinari, C., et al., *PRC1 is a microtubule binding and bundling protein essential to maintain the mitotic spindle midzone*. J Cell Biol, 2002. **157**(7): p. 1175-86.
48. Jiang, W., et al., *PRC1: a human mitotic spindle-associated CDK substrate protein required for cytokinesis*. Mol Cell, 1998. **2**(6): p. 877-85.
49. Bieling, P., I.A. Telley, and T. Surrey, *A Minimal Midzone Protein Module Controls Formation and Length of Antiparallel Microtubule Overlaps*. Cell, 2010. **142**(3): p. 420-432.
50. Mierzwa, B. and D.W. Gerlich, *Review Cytokinetic Abscission : Molecular Mechanisms and Temporal Control*, in *Developmental Cell*. 2014, Elsevier Inc. p. 525-538.
51. Pavicic-Kaltenbrunner, V., Mishima, M., Glotzer, M.,, *Cooperative Assembly of CYK-4/MgcRacGAP and ZEN-4/MKLP1 to Form the Centralspindlin Complex*. *Molecular Biology of the Cell*. 2007. **18**: p. 4992–5003.
52. Mishima, M., S. Kaitna, and M. Glotzer, *Central spindle assembly and cytokinesis require a kinesin-like protein/RhoGAP complex with microtubule bundling activity*. Dev Cell, 2002. **2**(1): p. 41-54.
53. Hümmer, S. and T.U. Mayer, *Cdk1 Negatively Regulates Midzone Localization of the Mitotic Kinesin Mklp2 and the Chromosomal Passenger Complex*. Current Biology, 2009. **19**(7): p. 607-612.
54. Gruneberg , U., et al., *Relocation of Aurora B from centromeres to the central spindle at the metaphase to anaphase transition requires MKlp2*. Journal of Cell Biology, 2004. **166**(2): p. 167-172.
55. Douglas, M.E., et al., *Aurora B and 14-3-3 coordinately regulate clustering of centralspindlin during cytokinesis*. Curr Biol, 2010. **20**(10): p. 927-33.
56. Burkard, M.E., et al., *Plk1 Self-Organization and Priming Phosphorylation of HsCYK-4 at the Spindle Midzone Regulate the Onset of Division in Human Cells*. PLOS Biology, 2009. **7**(5): p. e1000111.
57. Nishimura, Y. and S. Yonemura, *Centralspindlin regulates ECT2 and RhoA accumulation at the equatorial cortex during cytokinesis*. Journal of Cell Science, 2006. **119**(1): p. 104-114.
58. Benink, H.A. and W.M. Bement, *Concentric zones of active RhoA and Cdc42 around single cell wounds*. J Cell Biol, 2005. **168**(3): p. 429-39.
59. Piekny, A.J. and M. Glotzer, *Anillin Is a Scaffold Protein That Links RhoA, Actin, and Myosin during Cytokinesis*, in *Current Biology*. 2008. p. 30-36.
60. Addi, C., J. Bai, and A. Echard, *Actin, microtubule, septin and ESCRT filament remodeling during late steps of cytokinesis*, in *Current Opinion in Cell Biology*. 2018, Elsevier Ltd. p. 27-34.
61. Karasmanis, E.P., et al., *A Septin Double Ring Controls the Spatiotemporal Organization of the ESCRT Machinery in Cytokinetic Abscission*. Current Biology, 2019. **29**(13): p. 2174-2182.e7.
62. Mullins, J.M. and J.J. Biesele, *Terminal phase of cytokinesis in D 98S cells*, in *Journal of Cell Biology*. 1977. p. 672-684.
63. Buck, R.C. and J.M. Tisdale, *The fine structure of the mid-body of the rat erythroblast*. J Cell Biol, 1962. **13**: p. 109-15.
64. Allenspach, A.L. and L.E. Roth, *Structural variations during mitosis in the chick embryo*. J Cell Biol, 1967. **33**(1): p. 179-96.
65. Morita, E., et al., *Human ESCRT and ALIX proteins interact with proteins of the midbody and function in cytokinesis*, in *EMBO Journal*. 2007. p. 4215-4227.

66. Carlton, J.G. and J. Martin-Serrano, *Parallels Between Cytokinesis and Retroviral Budding: A Role for the ESCRT Machinery*. Science, 2007. **316**(5833): p. 1908-1912.
67. Katzmann, D.J., M. Babst, and S.D. Emr, *Ubiquitin-dependent sorting into the multivesicular body pathway requires the function of a conserved endosomal protein sorting complex, ESCRT-I*. Cell, 2001. **106**(2): p. 145-55.
68. Garrus, J.E., et al., *Tsg101 and the vacuolar protein sorting pathway are essential for HIV-1 budding*. Cell, 2001. **107**(1): p. 55-65.
69. Elia, N., et al., *Dynamics of endosomal sorting complex required for transport (ESCRT) machinery during cytokinesis and its role in abscission*, in *Proceedings of the National Academy of Sciences*. 2011. p. 4846-4851.
70. Jimenez, A.J., et al., *ESCRT Machinery Is Required for Plasma Membrane Repair*. 2014.
71. Raab, M., et al., *ESCRT III repairs nuclear envelope ruptures during cell migration to limit DNA damage and cell death*. Science, 2016. **352**(6283): p. 359-62.
72. Zhu, L., et al., *ESCRTs function directly on the lysosome membrane to downregulate ubiquitinated lysosomal membrane proteins*. Elife, 2017. **6**.
73. Vietri, M., et al., *disassembly and nuclear envelope sealing*. 2015.
74. Zhou, F., et al., *Rab5-dependent autophagosome closure by ESCRT*. J Cell Biol, 2019. **218**(6): p. 1908-1927.
75. Loncle, N., et al., *An ESCRT module is required for neuron pruning*. Sci Rep, 2015. **5**: p. 8461.
76. Deo, R.A. and W.A. Prinz, *ESCRTs got your Bac!* Cell, 2021. **184**(14): p. 3591-3592.
77. Liu, J., et al., *Bacterial Vipp1 and PspA are members of the ancient ESCRT-III membrane-remodeling superfamily*. Cell, 2021. **184**(14): p. 3660 - 3673.e18.
78. Pfitzner, A.-K., J. Moser von Filseck, and A. Roux, *Principles of membrane remodeling by dynamic ESCRT-III polymers*. Trends in Cell Biology, 2021.
79. Vietri, M., M. Radulovic, and H. Stenmark, *The many functions of ESCRTs*. Nature Reviews Molecular Cell Biology, 2020. **21**(1): p. 25-42.
80. Bastos, R.N. and F.A. Barr, *Plk1 negatively regulates Cep55 recruitment to the midbody to ensure orderly abscission*, in *Journal of Cell Biology*. 2010. p. 751-760.
81. Fabbro, M., et al., *Cdk1/Erk2- and Plk1-dependent phosphorylation of a centrosome protein, Cep55, is required for its recruitment to midbody and cytokinesis*, in *Developmental Cell*. 2005. p. 477-488.
82. Martinez-Garay, I., et al., *The novel centrosomal associated protein CEP55 is present in the spindle midzone and the midbody*. Genomics, 2006. **87**(2): p. 243-53.
83. Goliand, I., T. Dadosh, and N. Elia, *Resolving ESCRT-III spirals at the intercellular bridge of dividing cells using 3D STORM imaging*. 2017.
84. Lee, H.H., et al., *Midbody targeting of the ESCRT machinery by a noncanonical coiled coil in CEP55*. Science, 2008. **322**(5901): p. 576-80.
85. Christ, L., et al., *ALIX and ESC RT-I/II function as parallel ESC RT-III recruiters in cytokinetic abscission*, in *Journal of Cell Biology*. 2016. p. 499-513.
86. Carlton, J.G., M. Agromayor, and J. Martin-Serrano, *Differential requirements for Alix and ESCRT-III in cytokinesis and HIV-1 release*. Proc Natl Acad Sci U S A, 2008. **105**(30): p. 10541-6.
87. Christ, L., et al., *ALIX and ESCRT-I/II function as parallel ESCRT-III recruiters in cytokinetic abscission*. J Cell Biol, 2016. **212**(5): p. 499-513.
88. Schiel, J.A., et al., *FIP3-endosome-dependent formation of the secondary ingression mediates ESCRT-III recruitment during cytokinesis*, in *Nature Cell Biology*. 2012, Nature Publishing Group. p. 1068-1078.
89. Baietti, M.F., et al., *Syndecan-syntenin-ALIX regulates the biogenesis of exosomes*. Nat Cell Biol, 2012. **14**(7): p. 677-85.

90. Ghossoub, R., et al., *Syntenin-ALIX exosome biogenesis and budding into multivesicular bodies are controlled by ARF6 and PLD2*. Nat Commun, 2014. **5**: p. 3477.
91. Guizetti, J., et al., *Cortical Constriction During Abscission Involves Helices of ESCRT-III–Dependent Filaments*, in *Science*. 2011.
92. Han, H., et al., *The AAA ATPase Vps4 binds ESCRT-III substrates through a repeating array of dipeptide-binding pockets*. eLife, 2017. **6**: p. e31324.
93. Fabrikant, G., et al., *Computational Model of Membrane Fission Catalyzed by ESCRT-III*. PLOS Computational Biology, 2009. **5**(11): p. e1000575.
94. Nguyen, H.C., et al., *Membrane constriction and thinning by sequential ESCRT-III polymerization*, in *Nature Structural and Molecular Biology*. 2020, Springer US. p. 392-399.
95. Chavrier, P., et al., *Localization of low molecular weight GTP binding proteins to exocytic and endocytic compartments*. Cell, 1990. **62**(2): p. 317-329.
96. Stenmark, H., *Rab GTPases as coordinators of vesicle traffic*. Nature Reviews Molecular Cell Biology, 2009. **10**(8): p. 513-525.
97. Eggert, U.S., et al., *Parallel chemical genetic and genome-wide RNAi screens identify cytokinesis inhibitors and targets*. PLoS Biol, 2004. **2**(12): p. e379.
98. Fremont, S. and A. Echard, *Membrane Traffic in the Late Steps of Cytokinesis*. Curr Biol, 2018. **28**(8): p. R458-R470.
99. Gromley, A., et al., *Centriolin anchoring of exocyst and SNARE complexes at the midbody is required for secretory-vesicle-mediated abscission*, in *Cell*. 2005. p. 75-87.
100. Saurin, A.T., et al., *The regulated assembly of a PKCepsilon complex controls the completion of cytokinesis*. Nat Cell Biol, 2008. **10**(8): p. 891-901.
101. Zhou, Q., et al., *14-3-3 coordinates microtubules, rac, and myosin II to control cell mechanics and cytokinesis*, in *Current Biology*. 2010. p. 1881-1889.
102. Terry, S.J., et al., *Capping protein regulates actin dynamics during cytokinetic midbody maturation*. Proceedings of the National Academy of Sciences, 2018. **115**(9): p. 2138.
103. Kouranti, I., et al., *Rab35 Regulates an Endocytic Recycling Pathway Essential for the Terminal Steps of Cytokinesis*, in *Current Biology*. 2006. p. 1719-1725.
104. Dambournet, D., et al., *Rab35 GTPase and OCRL phosphatase remodel lipids and F-actin for successful cytokinesis*, in *Nature Cell Biology*. 2011, Nature Publishing Group. p. 981-988.
105. Logan, M.R. and C.A. Mandato, *Regulation of the actin cytoskeleton by PIP2 in cytokinesis*. Biol Cell, 2006. **98**(6): p. 377-88.
106. Frémont, S., et al., *Oxidation of F-actin controls the terminal steps of cytokinesis*, in *Nature Communications*. 2017. p. 1-16.
107. Fielding, A.B., et al., *Rab11-FIP3 and FIP4 interact with Arf6 and the exocyst to control membrane traffic in cytokinesis*. Embo J, 2005. **24**(19): p. 3389-99.
108. Skop, A.R., et al., *Completion of cytokinesis in C. elegans requires a brefeldin A- sensitive membrane accumulation at the cleavage furrow apex*. Curr Biol, 2001. **11**(10): p. 735-46.
109. Riggs, B., et al., *Actin cytoskeleton remodeling during early Drosophila furrow formation requires recycling endosomal components Nuclear-fallout and Rab11*. J Cell Biol, 2003. **163**(1): p. 143-54.
110. Wilson, G.M., et al., *The FIP3-Rab11 protein complex regulates recycling endosome targeting to the cleavage furrow during late cytokinesis*, in *Molecular Biology of the Cell*. 2005. p. 849-860.
111. Simon, G.C., et al., *Sequential Cyk-4 binding to ECT2 and FIP3 regulates cleavage furrow ingression and abscission during cytokinesis*, in *EMBO Journal*. 2008. p. 1791-1803.
112. Iannantuono, N.V.G. and G. Emery, *Rab11FIP1 maintains Rab35 at the intercellular bridge to promote actin removal and abscission*. Journal of Cell Science, 2021. **134**(12).
113. Piperno, G., M. LeDizet, and X.J. Chang, *Microtubules containing acetylated alpha-tubulin in mammalian cells in culture*. Journal of Cell Biology, 1987. **104**(2): p. 289-302.

114. Ferreira, J.G., et al., *Aurora B spatially regulates EB3 phosphorylation to coordinate daughter cell adhesion with cytokinesis*. J Cell Biol, 2013. **201**(5): p. 709-24.
115. Hu, C.-K., M. Coughlin, and T.J. Mitchison, *Midbody assembly and its regulation during cytokinesis*, in *Molecular Biology of the Cell*. 2012. p. 1024-1034.
116. Connell, J.W., et al., *Spastin couples microtubule severing to membrane traffic in completion of cytokinesis and secretion*, in *Traffic*. 2009. p. 42-56.
117. Yang, D., et al., *Structural basis for midbody targeting of spastin by the ESCRT-III protein CHMP1B*. Nat Struct Mol Biol, 2008. **15**(12): p. 1278-86.
118. Fujiwara, T., et al., *Cytokinesis failure generating tetraploids promotes tumorigenesis in p53-null cells*, in *Nature*. 2005. p. 1043-1047.
119. Iwamori, T., et al., *TEX14 interacts with CEP55 to block cell abscission*. Mol Cell Biol, 2010. **30**(9): p. 2280-92.
120. Greenbaum, M.P., et al., *TEX14 is essential for intercellular bridges and fertility in male mice*. Proc Natl Acad Sci U S A, 2006. **103**(13): p. 4982-7.
121. Giansanti, M.G., et al., *Cytokinesis in Drosophila male meiosis*. Spermatogenesis, 2012. **2**(3): p. 185-196.
122. Mathieu, J., et al., *Aurora B and cyclin B have opposite effects on the timing of cytokinesis abscission in Drosophila germ cells and in vertebrate somatic cells*. Dev Cell, 2013. **26**(3): p. 250-65.
123. Lens, S.M.A. and R.H. Medema, *Cytokinesis defects and cancer*, in *Nature Reviews Cancer*. 2019, Springer US. p. 32-45.
124. Carlton, J.G., et al., *ESCRT-III governs the Aurora B-mediated abscission checkpoint through CHMP4C*. Science, 2012. **336**(6078): p. 220-5.
125. Thoresen, S.B., et al., *ANCHR mediates Aurora-B-dependent abscission checkpoint control through retention of VPS4*. Nat Cell Biol, 2014.
126. Sadler, J.B.A., et al., *A cancer-associated polymorphism in ESCRT-III disrupts the abscission checkpoint and promotes genome instability*. Proc Natl Acad Sci U S A, 2018. **115**(38): p. E8900-E8908.
127. Bai, J., et al., *Actin reduction by MsrB2 is a key component of the cytokinetic abscission checkpoint and prevents tetraploidy*. Proceedings of the National Academy of Sciences of the United States of America, 2020. **117**(8): p. 4169-4179.
128. Tedeschi, A., et al., *Cep55 promotes cytokinesis of neural progenitors but is dispensable for most mammalian cell divisions*. Nature Communications, 2020. **11**(1): p. 1746.
129. Bondeson, M.L., et al., *A nonsense mutation in CEP55 defines a new locus for a Meckel-like syndrome, an autosomal recessive lethal fetal ciliopathy*. Clin Genet, 2017. **92**(5): p. 510-516.
130. Frosk, P., et al., *A truncating mutation in CEP55 is the likely cause of MARCH, a novel syndrome affecting neuronal mitosis*. J Med Genet, 2017. **54**(7): p. 490-501.
131. Little, J.N., et al., *Loss of Coiled-Coil Protein Cep55 Impairs Neural Stem Cell Abscission and Results in p53-Dependent Apoptosis in Developing Cortex*. J Neurosci, 2021. **41**(15): p. 3344-3365.
132. Hayashi, M.T. and J. Karlseder, *DNA damage associated with mitosis and cytokinesis failure*. Oncogene, 2013. **32**(39): p. 4593-601.
133. Choudhary, A., et al., *Interphase cytofission maintains genomic integrity of human cells after failed cytokinesis*. Proc Natl Acad Sci U S A, 2013. **110**(32): p. 13026-31.
134. Gupta, D.K., et al., *Tension-induced cytokinetic abscission in human fibroblasts*, in *Oncotarget*. 2018. p. 8999-9009.
135. Pohl, C. and S. Jentsch, *Midbody ring disposal by autophagy is a post-abscission event of cytokinesis*. Nat Cell Biol, 2009. **11**(1): p. 65-70.
136. Kuo, T.C., et al., *Midbody accumulation through evasion of autophagy contributes to cellular reprogramming and tumorigenicity*. Nat Cell Biol, 2011. **13**(10): p. 1214-23.

137. Dionne, L.K., X.J. Wang, and R. Prekeris, *Midbody: from cellular junk to regulator of cell polarity and cell fate*. Curr Opin Cell Biol, 2015. **35**: p. 51-8.
138. Peterman, E., et al., *The post-abscission midbody is an intracellular signaling organelle that regulates cell proliferation.* Nature Communications, 2019. **10**(1): p. 3181.
139. Presle, A., et al., *The viral restriction factor tetherin/BST2 tethers cytokinetic midbody remnants to the cell surface.* Current Biology, 2021. **31**(10): p. 2203-2213.e5.
140. Chai, Y., et al., *Apoptotic regulators promote cytokinetic midbody degradation in C. elegans*. J Cell Biol, 2012. **199**(7): p. 1047-55.
141. Fazeli, G., et al., *C. elegans midbodies are released, phagocytosed and undergo LC3-dependent degradation independent of macroautophagy*. J Cell Sci, 2016. **129**(20): p. 3721-3731.
142. Peterman, E., et al., *The post-abscission midbody is an intracellular signaling organelle that regulates cell proliferation.* Nat Commun, 2019. **10**(1): p. 3181.
143. Crowell, E.F., et al., *Midbody remnant engulfment after cytokinesis abscission in mammalian cells*. J Cell Sci, 2014. **127**(17): p. 3840-51.
144. Dubreuil, V., et al., *Midbody and primary cilium of neural progenitors release extracellular membrane particles enriched in the stem cell marker prominin-1*. J Cell Biol, 2007. **176**(4): p. 483-95.
145. McNeely, K.C. and N.D. Dwyer, *Cytokinesis and postabscission midbody remnants are regulated during mammalian brain development.* Proc Natl Acad Sci U S A, 2020. **117**(17): p. 9584-9593.
146. Ettinger, A.W., et al., *Proliferating versus differentiating stem and cancer cells exhibit distinct midbody-release behaviour*, in *Nature Communications*. 2011, Nature Publishing Group.
147. Labat-de-Hoz, L., et al., *A Model for Primary Cilium Biogenesis by Polarized Epithelial Cells: Role of the Midbody Remnant and Associated Specialized Membranes.* Frontiers in Cell and Developmental Biology, 2021. **8**(1738).
148. Singh, D. and C. Pohl, *Coupling of Rotational Cortical Flow, Asymmetric Midbody Positioning, and Spindle Rotation Mediates Dorsoventral Axis Formation in C. elegans*. Developmental Cell, 2014. **28**(3): p. 253-267.
149. Palade, G.E., *The fine structure of blood capillaries*. J Appl Phys, 1953. **24**: p. 1424.
150. YAMADA, E., *The fine structure of the gall bladder epithelium of the mouse*, in *The Journal of biophysical and biochemical cytology*. 1955. p. 445-58.
151. Rothberg, K.G., et al., *Caveolin , a Protein Component of Caveolae Membrane Coats*. 1992. p. 673-682.
152. Dupree, P., et al., *Caveolae and sorting in the trans-Golgi network of epithelial cells*, in *EMBO Journal*. 1993. p. 1597-1605.
153. Kurzchalia, T.V., et al., *VIP21, a 21-kD membrane protein is an integral component of trans-Golgi-network-derived transport vesicles.* Journal of Cell Biology, 1992. **118**(5): p. 1003-1014.
154. Glenney, J.R. and D. Soppet, *Sequence and expression of caveolin, a protein component of caveolae plasma membrane domains phosphorylated on tyrosine in Rous sarcoma virus-transformed fibroblasts.* Proceedings of the National Academy of Sciences, 1992. **89**(21): p. 10517.
155. Scherer, P.E., et al., *Identification, sequence, and expression of caveolin-2 defines a caveolin gene family.* Proceedings of the National Academy of Sciences of the United States of America, 1996. **93**(1): p. 131-135.
156. Tang, Z., et al., *Molecular Cloning of Caveolin-3, a Novel Member of the Caveolin Gene Family Expressed Predominantly in Muscle (*)*. Journal of Biological Chemistry, 1996. **271**(4): p. 2255-2261.
157. Way, M. and R.G. Parton, *M-caveolin, a muscle-specific caveolin-related protein.* FEBS Letters, 1995. **376**(1): p. 108-112.

158. Fra, A.M., et al., *De novo formation of caveolae in lymphocytes by expression of VIP21-caveolin.* Proceedings of the National Academy of Sciences, 1995. **92**(19): p. 8655-8659.
159. Hill, M.M., et al., *PTRF-Cavin, a Conserved Cytoplasmic Protein Required for Caveola Formation and Function*, in *Cell*. 2008. p. 113-124.
160. Liu, L. and P.F. Pilch, *A critical role of cavin (polymerase I and transcript release factor) in caveolae formation and organization*, in *Journal of Biological Chemistry*. 2008. p. 4314-4322.
161. Liu, L., et al., *Deletion of Cavin / PTRF Causes Global Loss of Caveolae , Dyslipidemia , and Glucose Intolerance*. 2008. p. 310-317.
162. Vinten, J., et al., *A 60-kDa protein abundant in adipocyte caveolae*, in *Cell and Tissue Research*. 2001. p. 99-106.
163. Aboulaich, N., et al., *Vectorial proteomics reveal targeting, phosphorylation and specific fragmentation of polymerase I and transcript release factor (PTRF) at the surface of caveolae in human adipocytes*, in *Biochemical Journal*. 2004. p. 237-248.
164. Hansen, C.G., et al., *SDPR induces membrane curvature and functions in the formation of caveolae.* Nature Cell Biology, 2009. **11**(7): p. 807-814.
165. McMahon, K.-A., et al., *SRBC/cavin-3 is a caveolin adapter protein that regulates caveolae function.* The EMBO Journal, 2009. **28**(8): p. 1001-1015.
166. Bastiani, M., et al., *MURC/Cavin-4 and cavin family members form tissue-specific caveolar complexes.* Journal of Cell Biology, 2009. **185**(7): p. 1259-1273.
167. Hansen, C.G., G. Howard, and B.J. Nichols, *Pacsin 2 is recruited to caveolae and functions in caveolar biogenesis*, in *Journal of Cell Science*. 2011. p. 2777-2785.
168. Senju, Y., et al., *Essential role of PACSIN2/syndapin-II in caveolae membrane sculpting*, in *Journal of Cell Science*. 2011. p. 2032-2040.
169. Seemann, E., et al., *Deciphering caveolar functions by syndapin III KO-mediated impairment of caveolar invagination*, in *eLife*. 2017. p. 1-37.
170. Stoeber, M., et al., *Oligomers of the ATPase EHD2 confine caveolae to the plasma membrane through association with actin*. 2012. p. 2350-2364.
171. Kirkham, M., et al., *Ultrastructural identification of uncoated caveolin-independent early endocytic vehicles.* J Cell Biol, 2005. **168**(3): p. 465-76.
172. Oh, P., D.P. McIntosh, and J.E. Schnitzer, *Dynamin at the neck of caveolae mediates their budding to form transport vesicles by GTP-driven fission from the plasma membrane of endothelium*, in *Journal of Cell Biology*. 1998. p. 101-114.
173. Vinten, J., et al., *Identification of a major protein on the cytosolic face of caveolae*, in *Biochimica et Biophysica Acta - Biomembranes*. 2005. p. 34-40.
174. Sun, X.-H., et al., *A conserved sequence in caveolin-1 is both necessary and sufficient for caveolin polarity and cell directional migration.* FEBS Letters, 2009. **583**(22): p. 3681-3689.
175. Murata, M., et al., *VIP21 / caveolin is a cholesterol-binding protein*. 1995. p. 10339-10343.
176. Epand, R.M., B.G. Sayer, and R.F. Epand, *Caveolin Scaffolding Region and Cholesterol-rich Domains in Membranes.* Journal of Molecular Biology, 2005. **345**(2): p. 339-350.
177. Sargiacomo, M., et al., *Oligomeric structure of caveolin: Implications for caveolae membrane organization*, in *Proceedings of the National Academy of Sciences of the United States of America*. 1995. p. 9407-9411.
178. Monier, S., et al., *VIP21-caveolin, a membrane protein constituent of the caveolar coat, oligomerizes in vivo and in vitro.* Molecular Biology of the Cell, 1995. **6**(7): p. 911-927.
179. Root, K.T., S.M. Plucinsky, and K.J. Glover, *Recent Progress in the Topology, Structure, and Oligomerization of Caveolin: A Building Block of Caveolae*, in *Current Topics in Membranes*. 2015, Elsevier Ltd. p. 305-336.
180. Fujimoto, T., et al., *Isoforms of caveolin-1 and caveolar structure*. 2000. p. 3509-3517.
181. Glenney, J.R. and D. Soppet, *Sequence and expression of caveolin, a protein component of caveolae plasma membrane domains phosphorylated on tyrosine in Rous sarcoma virus- transformed*

fibroblasts, in *Proceedings of the National Academy of Sciences of the United States of America*. 1992. p. 10517-10521.
182. Nystrom, F.H., et al., *Caveolin-1 Interacts with the Insulin Receptor and Can Differentially Modulate Insulin Signaling in Transfected Cos-7 Cells and Rat Adipose Cells*. Molecular Endocrinology, 1999. **13**(12): p. 2013-2024.
183. Li, S., R. Seitz, and M.P. Lisanti, *Phosphorylation of Caveolin by Src Tyrosine Kinases: THE α-ISOFORM OF CAVEOLIN IS SELECTIVELY PHOSPHORYLATED BY v-Src IN VIVO(∗)*. Journal of Biological Chemistry, 1996. **271**(7): p. 3863-3868.
184. Place, A.T., et al., *Cooperative role of caveolin-1 and C-terminal Src kinase binding protein in C-terminal Src kinase-mediated negative regulation of c-Src*. Molecular pharmacology, 2011. **80**(4): p. 665-672.
185. Monier, S., et al., *Oligomerization of VIP21-caveolin in vitro is stabilized by long chain fatty acylation or cholesterol*. FEBS Letters, 1996. **388**(2-3): p. 143-149.
186. Dietzen, D.J., W.R. Hastings, and D.M. Lublin, *Caveolin Is Palmitoylated on Multiple Cysteine Residues: PALMITOYLATION IS NOT NECESSARY FOR LOCALIZATION OF CAVEOLIN TO CAVEOLAE (*)*. Journal of Biological Chemistry, 1995. **270**(12): p. 6838-6842.
187. Volonte, D., et al., *Caveolin-1 and caveolin-3 form heterooligomeric complexes in atrial cardiac myocytes that are required for doxorubicin-induced apoptosis*. American Journal of Physiology-Heart and Circulatory Physiology, 2008. **294**(1): p. H392-H401.
188. Scherer, P.E., et al., *Cell-type and Tissue-specific Expression of Caveolin-2: CAVEOLINS 1 AND 2 CO-LOCALIZE AND FORM A STABLE HETERO-OLIGOMERIC COMPLEX IN VIVO **. Journal of Biological Chemistry, 1997. **272**(46): p. 29337-29346.
189. Walser, Piers J., et al., *Constitutive Formation of Caveolae in a Bacterium*. Cell, 2012. **150**(4): p. 752-763.
190. Lahtinen, U., et al., *Involvement of caveolin-2 in caveolar biogenesis in MDCK cells*, in *FEBS Letters*. 2003. p. 85-88.
191. Kovtun, O., et al., *Cavin family proteins and the assembly of caveolae*. 2015. p. 1269-1278.
192. Tillu, V.A., et al., *A phosphoinositide-binding cluster in cavin1 acts as a molecular sensor for cavin1 degradation*. 2015. p. 3561-3569.
193. Kovtun, O., et al., *Structural insights into the organization of the cavin membrane coat complex*, in *Developmental Cell*. 2014, Elsevier Inc. p. 405-419.
194. Stoeber, M., et al., *Model for the architecture of caveolae based on a flexible , net-like assembly of Cavin1 and Caveolin discs*. 2016. p. 8069-8078.
195. Tillu, V.A., et al., *A variable undecad repeat domain in cavin1 regulates caveola formation and stability*, in *EMBO reports*. 2018. p. 1-12.
196. McMahon, K.A., et al., *SRBC/cavin-3 is a caveolin adapter protein that regulates caveolae function*, in *EMBO Journal*. 2009, Nature Publishing Group. p. 1001-1015.
197. Burgener, R., et al., *Purification and characterization of a major phosphatidylserine-binding phosphoprotein from human platelets*. Biochem J, 1990. **269**(3): p. 729-34.
198. Naslavsky, N. and S. Caplan, *EHD proteins: key conductors of endocytic transport*. Trends in Cell Biology, 2011. **21**(2): p. 122-131.
199. Daumke, O., et al., *Architectural and mechanistic insights into an EHD ATPase involved in membrane remodelling*. Nature, 2007. **449**(7164): p. 923-927.
200. Quan, A. and P.J. Robinson, *Syndapin - A membrane remodelling and endocytic F-BAR protein*, in *FEBS Journal*. 2013. p. 5198-5212.
201. Örtegren, U., et al., *Lipids and glycosphingolipids in caveolae and surrounding plasma membrane of primary rat adipocytes*, in *European Journal of Biochemistry*. 2004. p. 2028-2036.

202. Wanaski, S.P., B.K. Ng, and M. Glaser, *Caveolin scaffolding region and the membrane binding region of Src form lateral membrane domains*, in *Biochemistry*. 2003. p. 42-56.
203. Hirama, T., et al., *Phosphatidylserine dictates the assembly and dynamics of caveolae in the plasma membrane*, in *Journal of Biological Chemistry*. 2017, Â© 2017 ASBMB. Currently published by Elsevier Inc; originally published by American Society for Biochemistry and Molecular Biology. p. 14292-14307.
204. Westermann, M., F. Steiniger, and W. Richter, *Belt-like localisation of caveolin in deep caveolae and its re-distribution after cholesterol depletion*, in *Histochemistry and Cell Biology*. 2005. p. 613-620.
205. Hayer, A., et al., *Biogenesis of caveolae: Stepwise assembly of large caveolin and cavin complexes*, in *Traffic*. 2010. p. 361-382.
206. Pol, A., et al., *Cholesterol and fatty acids regulate dynamic caveolin trafficking through the Golgi complex and between the cell surface and lipid bodies*. Mol Biol Cell, 2005. **16**(4): p. 2091-105.
207. Shvets, E., et al., *Dynamic caveolae exclude bulk membrane proteins and are required for sorting of excess glycosphingolipids*, in *Nature Communications*. 2015, Nature Publishing Group.
208. Hayer, A., et al., *Caveolin-1 is ubiquitinated and targeted to intralumenal vesicles in endolysosomes for degradation*, in *Journal of Cell Biology*. 2010. p. 615-629.
209. Andreone, B.J., et al., *Blood-Brain Barrier Permeability Is Regulated by Lipid Transport-Dependent Suppression of Caveolae-Mediated Transcytosis*, in *Neuron*. 2017, Elsevier Inc. p. 581-594.e5.
210. Han, B., et al., *Assembly and Turnover of Caveolae: What Do We Really Know?*, in *Frontiers in Cell and Developmental Biology*. 2016. p. 1-7.
211. Ludwig, A., B.J. Nichols, and S. Sandin, *Architecture of the caveolar coat complex*. 2016. p. 3077-3083.
212. Gambin, Y., et al., *Single-molecule analysis reveals self assembly and nanoscale segregation of two distinct cavin subcomplexes on caveolae*. 2014. p. 1-18.
213. Pelkmans, L. and M. Zerial, *Kinase-regulated quantal assemblies and kiss-and-run recycling of caveolae*, in *Nature*. 2005. p. 128-133.
214. Khater, I.M., et al., *Caveolae and scaffold detection from single molecule localization microscopy data using deep learning*. 2019.
215. Tillu, V.A., et al., *Cavin1 intrinsically disordered domains are essential for fuzzy electrostatic interactions and caveola formation*, in *Nature Communications*. 2021, Springer US. p. 1-18.
216. Hoernke, M., et al., *EHD2 restrains dynamics of caveolae by an ATP- dependent , membrane-bound , open conformation*. 2017.
217. Yeow, I., et al., *Article EHD Proteins Cooperate to Generate Caveolar Clusters and to Maintain Caveolae during Repeated Article EHD Proteins Cooperate to Generate Caveolar Clusters and to Maintain Caveolae during Repeated Mechanical Stress*, in *Current Biology*. 2017, Elsevier Ltd. p. 1-12.
218. Boucrot, E., et al., *Redistribution of caveolae during mitosis.*, in *Journal of cell science*. 2011. p. 1965-1972.
219. Henley, J.R., et al., *Dynamin-mediated Internalization of Caveolae*. 1998. p. 85-99.
220. Stoeber, M., et al., *Oligomers of the ATPase EHD2 confine caveolae to the plasma membrane through association with actin*, in *EMBO Journal*. 2012. p. 2350-2364.
221. Matthaeus, C. and J.W. Taraska, *Energy and Dynamics of Caveolae Trafficking*, in *Frontiers in Cell and Developmental Biology*. 2021.
222. Mohan, J., et al., *Cavin3 interacts with cavin1 and caveolin1 to increase surface dynamics of caveolae*, in *Journal of Cell Science*. 2015. p. 979-991.
223. Torrino, S., et al., *EHD2 is a mechanotransducer connecting caveolae dynamics with gene transcription*, in *Journal of Cell Biology*. 2018. p. 4092-4105.

224. Wickström, S.A., et al., *Integrin-linked kinase controls microtubule dynamics required for plasma membrane targeting of caveolae*. Dev Cell, 2010. **19**(4): p. 574-88.
225. Echarri, A. and M.A. Del Pozo, *Caveolae - mechanosensitive membrane invaginations linked to actin filaments.*, in *Journal of cell science*. 2015. p. 2747-2758.
226. Hernandez, V.J., et al., *Cavin-3 dictates the balance between ERK and Akt signaling*, in *eLife*. 2013. p. 10-12.
227. Pelkmans, L., et al., *Caveolin-stabilized membrane domains as multifunctional transport and sorting devices in endocytic membrane traffic.* Cell, 2004. **118**(6): p. 767-80.
228. Dulhunty, A.F. and C. Franzini-Armstrong, *The relative contributions of the folds and caveolae to the surface membrane of frog skeletal muscle fibres at different sarcomere lengths*. J Physiol, 1975. **250**(3): p. 513-39.
229. Prescott, L. and M.W. Brightman, *The sarcolemma of Aplysia smooth muscle in freeze-fracture preparations*, in *Tissue and Cell*. 1976. p. 241-258.
230. Gervásio, O.L., et al., *Caveolae respond to cell stretch and contribute to stretch-induced signaling*, in *Journal of Cell Science*. 2011. p. 3581-3590.
231. Lim, Y.-w., et al., *Caveolae Protect Notochord Cells against Catastrophic Mechanical Failure during Article Caveolae Protect Notochord Cells against Catastrophic Mechanical Failure during Development*, in *Current Biology*. 2017, Elsevier Ltd. p. 1968-1981.e7.
232. García-Cardeña, G., et al., *Dissecting the Interaction between Nitric Oxide Synthase (NOS) and Caveolin: FUNCTIONAL SIGNIFICANCE OF THE NOS CAVEOLIN BINDING DOMAININ VIVO **.* Journal of Biological Chemistry, 1997. **272**(41): p. 25437-25440.
233. Couet, J., M. Sargiacomo, and M.P. Lisanti, *Interaction of a Receptor Tyrosine Kinase, EGF-R, with Caveolins: CAVEOLIN BINDING NEGATIVELY REGULATES TYROSINE AND SERINE/THREONINE KINASE ACTIVITIES**. Journal of Biological Chemistry, 1997. **272**(48): p. 30429-30438.
234. Song, K.S., et al., *Co-purification and Direct Interaction of Ras with Caveolin, an Integral Membrane Protein of Caveolae Microdomains: DETERGENT-FREE PURIFICATION OF CAVEOLAE MEMBRANES (*)*. Journal of Biological Chemistry, 1996. **271**(16): p. 9690-9697.
235. Nystrom, F.H., et al., *Caveolin-1 interacts with the insulin receptor and can differentially modulate insulin signaling in transfected Cos-7 cells and rat adipose cells.* Molecular Endocrinology, 1999. **13**(12): p. 2013-2024.
236. Strippoli, R., et al., *Caveolin-1 deficiency induces a MEK-ERK1/2-Snail-1-dependent epithelial–mesenchymal transition and fibrosis during peritoneal dialysis.* EMBO Molecular Medicine, 2015. **7**(1): p. 102-123.
237. Bernatchez, P.N., et al., *Dissecting the molecular control of endothelial NO synthase by caveolin-1 using cell-permeable peptides.* Proc Natl Acad Sci U S A, 2005. **102**(3): p. 761-6.
238. Trane, A.E., et al., *Deciphering the binding of caveolin-1 to client protein endothelial nitric-oxide synthase (eNOS): scaffolding subdomain identification, interaction modeling, and biological significance.* J Biol Chem, 2014. **289**(19): p. 13273-83.
239. Blouin, C.M., et al., *Glycosylation-Dependent IFN-γR Partitioning in Lipid and Actin Nanodomains Is Critical for JAK Activation.* Cell, 2016. **166**(4): p. 920-934.
240. Ariotti, N., et al., *Caveolae regulate the nanoscale organization of the plasma membrane to remotely control Ras signaling*, in *Journal of Cell Biology*. 2014. p. 777-792.
241. Best, J.M. and T.J. Kamp, *Different subcellular populations of L-type Ca2+ channels exhibit unique regulation and functional roles in cardiomyocytes.* J Mol Cell Cardiol, 2012. **52**(2): p. 376-87.
242. Huang, H., et al., *Caveolae Regulation of Mechanosensitive Channel Function in Myotubes.* PLOS ONE, 2013. **8**(8): p. e72894.

243. Domingues, L., et al., *Coupling of melanocyte signaling and mechanics by caveolae is required for human skin pigmentation*, in *Nature Communications*. 2020, Springer US.
244. McMahon, K.A., et al., *Identification of intracellular cavin target proteins reveals cavin-PP1alpha interactions regulate apoptosis*, in *Nature Communications*. 2019, Springer US.
245. Hetmanski, J.H.R., et al., *Membrane Tension Orchestrates Rear Retraction in Matrix-Directed Cell Migration*, in *Developmental Cell*. 2019. p. 460-475.e10.
246. Dewulf, M., et al., *Dystrophy-associated caveolin-3 mutations reveal that caveolae couple IL6/STAT3 signaling with mechanosensing in human muscle cells*, in *Nature Communications*. 2019, Springer US. p. 1-13.
247. Cao, H., et al., *Heterozygous CAV1 frameshift mutations (MIM 601047) in patients with atypical partial lipodystrophy and hypertriglyceridemia.* Lipids Health Dis, 2008. **7**: p. 3.
248. Schrauwen, I., et al., *A Frame-Shift Mutation in CAV1 Is Associated with a Severe Neonatal Progeroid and Lipodystrophy Syndrome.* PLoS One, 2015. **10**(7): p. e0131797.
249. Kim, C.A., et al., *Association of a Homozygous Nonsense Caveolin-1 Mutation with Berardinelli-Seip Congenital Lipodystrophy.* The Journal of Clinical Endocrinology & Metabolism, 2008. **93**(4): p. 1129-1134.
250. Hayashi, Y.K., et al., *Human PTRF mutations cause secondary deficiency of caveolins resulting in muscular dystrophy with generalized lipodystrophy.* J Clin Invest, 2009. **119**(9): p. 2623-33.
251. Razani, B., et al., *Caveolin-1 Null Mice Are Viable but Show Evidence of Hyperproliferative and Vascular Abnormalities **. 2001. p. 38121-38138.
252. Matthaeus, C., et al., *EHD2-mediated restriction of caveolar dynamics regulates cellular fatty acid uptake*, in *Proceedings of the National Academy of Sciences of the United States of America*. 2020. p. 7471-7481.
253. Singh, V. and C. Lamaze, *Membrane tension buffering by caveolae: a role in cancer?*, in *Cancer and Metastasis Reviews*. 2020, Cancer and Metastasis Reviews. p. 505-517.
254. Goetz, J.G., et al., *Biomechanical remodeling of the microenvironment by stromal caveolin-1 favors tumor invasion and metastasis.* Cell, 2011. **146**(1): p. 148-63.
255. Yu, H., J.K. Mouw, and V.M. Weaver, *Forcing form and function: biomechanical regulation of tumor evolution.* Trends Cell Biol, 2011. **21**(1): p. 47-56.
256. Sens, P. and J. Plastino, *Membrane tension and cytoskeleton organization in cell motility.*, in *Journal of physics. Condensed matter : an Institute of Physics journal*. 2015, IOP Publishing. p. 273103.
257. Clark, Andrew G., et al., *Stresses at the Cell Surface during Animal Cell Morphogenesis.* Current Biology, 2014. **24**(10): p. R484-R494.
258. Chugh, P., et al., *Actin cortex architecture regulates cell surface tension*, in *Nature Cell Biology*. 2017. p. 689-697.
259. Cheffings, Thomas H., Nigel J. Burroughs, and Mohan K. Balasubramanian, *Actomyosin Ring Formation and Tension Generation in Eukaryotic Cytokinesis.* Current Biology, 2016. **26**(15): p. R719-R737.
260. Matzke, R., M. Jacobson K Fau - Radmacher, and M. Radmacher, *Direct, high-resolution measurement of furrow stiffening during division of adherent cells.* (1465-7392 (Print)).
261. Houk, Andrew R., et al., *Membrane Tension Maintains Cell Polarity by Confining Signals to the Leading Edge during Neutrophil Migration.* Cell, 2012. **148**(1): p. 175-188.
262. Effler, J.C., et al., *Mitosis-specific mechanosensing and contractile-protein redistribution control cell shape.* Curr Biol, 2006. **16**(19): p. 1962-7.
263. Mueller, J., et al., *Load Adaptation of Lamellipodial Actin Networks.* Cell, 2017. **171**(1): p. 188-200.e16.
264. Taneja, N., et al., *Precise Tuning of Cortical Contractility Regulates Cell Shape during Cytokinesis*, in *Cell Reports*. 2020, ElsevierCompany. p. 107477.

265. Bennabi, I., et al., *Artificially decreasing cortical tension generates aneuploidy in mouse oocytes*, in *Nature Communications*. 2020, Springer US. p. 1-14.
266. Mercier, V., et al., *Endosomal membrane tension regulates ESCRT-III-dependent intra-lumenal vesicle formation*, in *Nature Cell Biology*. 2020, Springer US. p. 947-959.
267. Fujiwara, T., et al., *Cytokinesis failure generating tetraploids promotes tumorigenesis in p53-null cells.* Nature, 2005. **437**(7061): p. 1043-7.
268. Green, R.A., E. Paluch, and K. Oegema, *Cytokinesis in Animal Cells.* Annu Rev Cell Dev Biol, 2012.
269. Addi, C., J. Bai, and A. Echard, *Actin, microtubule, septin and ESCRT filament remodeling during late steps of cytokinesis.* Curr Opin Cell Biol, 2018. **50**: p. 27-34.
270. Dambournet, D., et al., *Rab35 GTPase and OCRL phosphatase remodel lipids and F-actin for successful cytokinesis.* Nat Cell Biol, 2011. **13**(8): p. 981-8.
271. Schiel, J.A., et al., *FIP3-endosome-dependent formation of the secondary ingression mediates ESCRT-III recruitment during cytokinesis.* Nat Cell Biol, 2012. **14**: p. 1068-78.
272. Fremont, S., et al., *Oxidation of F-actin controls the terminal steps of cytokinesis.* Nat Commun, 2017. **8**: p. 14528.
273. Mierzwa, B. and D.W. Gerlich, *Cytokinetic Abscission: Molecular Mechanisms and Temporal Control.* Dev Cell, 2014. **31**(5): p. 525-538.
274. D'Avino, P.P. and L. Capalbo, *Regulation of midbody formation and function by mitotic kinases.* Semin Cell Dev Biol, 2016. **53**: p. 57-63.
275. Stoten, C.L. and J.G. Carlton, *ESCRT-dependent control of membrane remodelling during cell division.* Semin Cell Dev Biol, 2017.
276. Scourfield, E.J. and J. Martin-Serrano, *Growing functions of the ESCRT machinery in cell biology and viral replication.* Biochem Soc Trans, 2017. **45**(3): p. 613-634.
277. Parton, R.G., *Caveolae: Structure, Function, and Relationship to Disease.* Annu Rev Cell Dev Biol, 2018. **34**: p. 111-136.
278. Parton, R.G., et al., *Caveolae: The FAQs.* Traffic, 2020. **21**(1): p. 181-185.
279. Ariotti, N., et al., *Caveolae regulate the nanoscale organization of the plasma membrane to remotely control Ras signaling.* J Cell Biol, 2014. **204**(5): p. 777-92.
280. Sens, P. and M.S. Turner, *Budded membrane microdomains as tension regulators.* Phys Rev E Stat Nonlin Soft Matter Phys, 2006. **73**(3 Pt 1): p. 031918.
281. Sinha, B., et al., *Cells respond to mechanical stress by rapid disassembly of caveolae.* Cell, 2011. **144**(3): p. 402-13.
282. Gervásio, O.L., et al., *Caveolae respond to cell stretch and contribute to stretch-induced signaling.* J Cell Sci, 2011. **124**(Pt 21): p. 3581-90.
283. Del Pozo, M.A., F.N. Lolo, and A. Echarri, *Caveolae: Mechanosensing and mechanotransduction devices linking membrane trafficking to mechanoadaptation.* Curr Opin Cell Biol, 2021. **68**: p. 113-123.
284. Lo, H.P., et al., *The caveolin-cavin system plays a conserved and critical role in mechanoprotection of skeletal muscle.* J Cell Biol, 2015. **210**(5): p. 833-49.
285. Garcia, J., et al., *Sheath Cell Invasion and Trans-differentiation Repair Mechanical Damage Caused by Loss of Caveolae in the Zebrafish Notochord.* Curr Biol, 2017. **27**(13): p. 1982-1989.e3.
286. Lim, Y.W., et al., *Caveolae Protect Notochord Cells against Catastrophic Mechanical Failure during Development.* Curr Biol, 2017. **27**(13): p. 1968-1981.e7.
287. Dewulf, M., et al., *Dystrophy-associated caveolin-3 mutations reveal that caveolae couple IL6/STAT3 signaling with mechanosensing in human muscle cells.* Nat Commun, 2019. **10**(1): p. 1974.
288. Teo, J.L., et al., *Caveolae Control Contractile Tension for Epithelia to Eliminate Tumor Cells.* Dev Cell, 2020. **54**(1): p. 75-91.e7.

289. Matsumura, S., et al., *Interphase adhesion geometry is transmitted to an internal regulator for spindle orientation via caveolin-1*. Nat Commun, 2016. **7**: p. ncomms11858.
290. Boucrot, E., et al., *Redistribution of caveolae during mitosis*. J Cell Sci, 2011. **124**(Pt 12): p. 1965-72.
291. Feng, B., H. Schwarz, and S. Jesuthasan, *Furrow-specific endocytosis during cytokinesis of zebrafish blastomeres*. Exp Cell Res, 2002. **279**(1): p. 14-20.
292. Elia, N., et al., *Dynamics of endosomal sorting complex required for transport (ESCRT) machinery during cytokinesis and its role in abscission*. Proc Natl Acad Sci U S A, 2011. **108**(12): p. 4846-51.
293. Crowell, E.F., J.Y. Tinevez, and A. Echard, *A simple model for the fate of the cytokinesis midbody remnant: implications for remnant degradation by autophagy: modeling remnant production and degradation enables re-interpretation of published data and improves design of future experiments*. Bioessays, 2013. **35**(5): p. 472-81.
294. Montagnac, G., A. Echard, and P. Chavrier, *Endocytic traffic in animal cell cytokinesis*. Curr Opin Cell Biol, 2008. **20**: p. 454-461.
295. Hill, M.M., et al., *PTRF-Cavin, a conserved cytoplasmic protein required for caveola formation and function*. Cell, 2008. **132**(1): p. 113-24.
296. Liu, L., et al., *Deletion of Cavin/PTRF causes global loss of caveolae, dyslipidemia, and glucose intolerance*. Cell Metab, 2008. **8**(4): p. 310-7.
297. Sens, P. and J. Plastino, *Membrane tension and cytoskeleton organization in cell motility*. J Phys Condens Matter, 2015. **27**(27): p. 273103.
298. Steigemann, P., et al., *Aurora B-mediated abscission checkpoint protects against tetraploidization*. Cell, 2009. **136**(3): p. 473-84.
299. Dandoulaki, M., et al., *Src activation by Chk1 promotes actin patch formation and prevents chromatin bridge breakage in cytokinesis*. J Cell Biol, 2018. **217**(9): p. 3071-3089.
300. Presle, A., et al., *The viral restriction factor tetherin/BST2 tethers cytokinetic midbody remnants to the cell surface*. Curr Biol, 2021. **31**(10): p. 2203-2213.e5.
301. Ng, M.M., F. Chang, and D.R. Burgess, *Movement of membrane domains and requirement of membrane signaling molecules for cytokinesis*. Dev Cell, 2005. **9**(6): p. 781-90.
302. Atilla-Gokcumen, G.E., et al., *Dividing cells regulate their lipid composition and localization*. Cell, 2014. **156**(3): p. 428-39.
303. Cauvin, C. and A. Echard, *Phosphoinositides: Lipids with informative heads and mastermind functions in cell division*. Biochim Biophys Acta, 2015. **1851**(6): p. 832-43.
304. Ortegren, U., et al., *Lipids and glycosphingolipids in caveolae and surrounding plasma membrane of primary rat adipocytes*. Eur J Biochem, 2004. **271**(10): p. 2028-36.
305. Hubert, M., et al., *Lipid accumulation controls the balance between surface connection and scission of caveolae*. Elife, 2020. **9**.
306. Zhou, Y., et al., *Caveolin-1 and cavin1 act synergistically to generate a unique lipid environment in caveolae*. J Cell Biol, 2021. **220**(3).
307. Mercier, V., et al., *Endosomal membrane tension regulates ESCRT-III-dependent intra-lumenal vesicle formation*. Nat Cell Biol, 2020. **22**(8): p. 947-959.
308. Hein, M.Y., et al., *A human interactome in three quantitative dimensions organized by stoichiometries and abundances*. Cell, 2015. **163**(3): p. 712-23.
309. Grande-García, A., et al., *Caveolin-1 regulates cell polarization and directional migration through Src kinase and Rho GTPases*. J Cell Biol, 2007. **177**(4): p. 683-94.
310. Echarri, A. and M.A. Del Pozo, *Caveolae - mechanosensitive membrane invaginations linked to actin filaments*. J Cell Sci, 2015. **128**(15): p. 2747-58.
311. Hetmanski, J.H.R., et al., *Membrane Tension Orchestrates Rear Retraction in Matrix-Directed Cell Migration*. Dev Cell, 2019. **51**(4): p. 460-475.e10.

312. Domingues, L., et al., *Coupling of melanocyte signaling and mechanics by caveolae is required for human skin pigmentation*. Nat Commun, 2020. **11**(1): p. 2988.
313. Singh, V. and C. Lamaze, *Membrane tension buffering by caveolae: a role in cancer?* Cancer Metastasis Rev, 2020. **39**(2): p. 505-517.
314. Lens, S.M.A. and R.H. Medema, *Cytokinesis defects and cancer*. Nat Rev Cancer, 2019. **19**(1): p. 32-45.
315. Mullins, J.M. and J.J. Biesele, *Terminal phase of cytokinesis in D-98s cells*. J Cell Biol, 1977. **73**(3): p. 672-84.
316. Pelkmans, L. and M. Zerial, *Kinase-regulated quantal assemblies and kiss-and-run recycling of caveolae*. Nature, 2005. **436**(7047): p. 128-33.
317. Atilla-Gokcumen, G.E., et al., *Dividing cells regulate their lipid composition and localization*, in *Cell*. 2014, The Authors. p. 428-439.
318. Ng, M.M., F. Chang, and D.R. Burgess, *Movement of membrane domains and requirement of membrane signaling molecules for cytokinesis*, in *Developmental Cell*. 2005. p. 781-790.
319. Cauvin, C. and A. Echard, *Phosphoinositides: Lipids with informative heads and mastermind functions in cell division*, in *Biochimica et Biophysica Acta - Molecular and Cell Biology of Lipids*. 2015, Elsevier B.V. p. 832-843.
320. Zhou, Y., et al., *Caveolin-1 and cavin1 act synergistically to generate a unique lipid environment in caveolae*. 2021.
321. Parton, R.G., K.A. McMahon, and Y. Wu, *Caveolae: Formation, dynamics, and function*, in *Current Opinion in Cell Biology*. 2020, Elsevier Ltd. p. 8-16.
322. Mohan, J., et al., *Cavin3 interacts with cavin1 and caveolin1 to increase surface dynamics of caveolae*. 2015.
323. Diz-Muñoz, A., D.A. Fletcher, and O.D. Weiner, *Use the force: Membrane tension as an organizer of cell shape and motility*, in *Trends in Cell Biology*. 2013. p. 47-53.
324. Colom, A., et al., *A fluorescent membrane tension probe*. Nature chemistry, 2018. **10**(11): p. 1118-1125.
325. Lo, H.P., et al., *The caveolin–cavin system plays a conserved and critical role in mechanoprotection of skeletal muscle*. Journal of Cell Biology, 2015. **210**(5): p. 833-849.
326. Echarri, A., et al., *An Abl-FBP17 mechanosensing system couples local plasma membrane curvature and stress fiber remodeling during mechanoadaptation*, in *Nature Communications*. 2019, Springer US.
327. Verma, P., A.G. Ostermeyer-fay, and D.A. Brown, *Caveolin-1 Induces Formation of Membrane Tubules That Sense Actomyosin Tension and Are Inhibited by Polymerase I and Transcript Release Factor / Cavin-1*. 2010. p. 2226-2240.
328. Roux, K.J., et al., *A promiscuous biotin ligase fusion protein identifies proximal and interacting proteins in mammalian cells*. J Cell Biol, 2012. **196**(6): p. 801-10.
329. Goss, J.W. and D.K. Toomre, *Both daughter cells traffi c and exocytose membrane at the cleavage furrow during mammalian cytokinesis*. 2006. p. 1047-1054.
330. Bai, J., *Actin reduction by MsrB2 is a key component of the cytokinetic abscission checkpoint and prevents tetraploidy*, in *Proceedings of the National Academy of Sciences of the United States of America*. 2020. p. 4169-4179.
331. Caballe, A., et al., *ULK3 regulates cytokinetic abscission by phosphorylating ESCRT-III proteins*. Elife, 2015. **4**: p. e06547.
332. Zhou, Y., et al., *Dissecting the nanoscale lipid profile of caveolae*. bioRxiv, 2020: p. 2020.01.16.909408.
333. Delarue, M., et al., *mTORC1 Controls Phase Separation and the Biophysical Properties of the Cytoplasm by Tuning Crowding*. Cell, 2018. **174**(2): p. 338-349.e20.

334. Matthews, L.C., M.J. Taggart, and M. Westwood, *Modulation of caveolin-1 expression can affect signalling through the phosphatidylinositol 3-kinase/Akt pathway and cellular proliferation in response to insulin-like growth factor I.* Endocrinology, 2008. **149**(10): p. 5199-208.
335. Zhang, B.C., et al., *PI-3K/AKT signal pathway modulates vascular smooth muscle cells migration under cyclic mechanical strain.* Vasa, 2011. **40**(2): p. 109-16.
336. Ha, H. and Y. Pak, *Modulation of the caveolin-3 and Akt status in caveolae by insulin resistance in H9c2 cardiomyoblasts.* Experimental & molecular medicine, 2005. **37**: p. 169-78.
337. Hein, M.Y., et al., *Article A Human Interactome in Three Quantitative Dimensions Organized by Stoichiometries and Article A Human Interactome in Three Quantitative Dimensions Organized by Stoichiometries and Abundances*. 2015. p. 712-723.
338. Fyfe, I., et al., *Association of the endosomal sorting complex ESCRT-II with the Vps20 subunit of ESCRT-III generates a curvature-sensitive complex capable of nucleating ESCRT-III filaments.* The Journal of biological chemistry, 2011. **286**(39): p. 34262-34270.
339. Lee, I.-H., et al., *Negative membrane curvature catalyzes nucleation of endosomal sorting complex required for transport (ESCRT)-III assembly.* Proceedings of the National Academy of Sciences, 2015. **112**(52): p. 15892.
340. De Franceschi, N., et al., *The ESCRT protein CHMP2B acts as a diffusion barrier on reconstituted membrane necks.* Journal of Cell Science, 2018. **132**(4).
341. Schöneberg, J., et al., *ATP-dependent force generation and membrane scission by ESCRT-III and Vps4.* Science, 2018. **362**(6421): p. 1423.